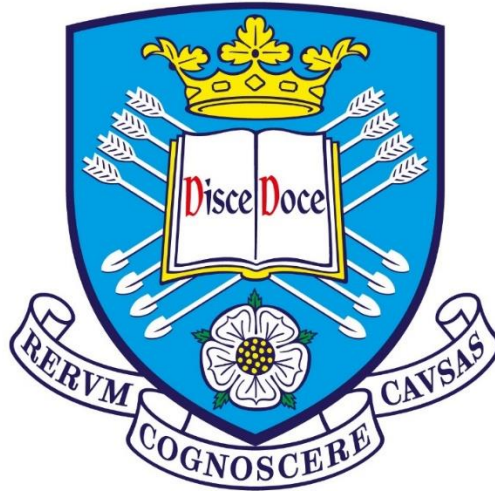


# The University of Sheffield



## Ultra-high-speed Three-phase Permanent Magnet Motors

**Tianran He**

**A thesis submitted for the degree of Doctor of Philosophy**

Department of Electronic and Electrical Engineering

The University of Sheffield

Mapping Street, Sheffield, S1 3JD, UK

**October 2021**

## ABSTRACT

This thesis analyses the electromagnetic performance and mechanical stress of three-phase permanent magnet (PM) motors for ultra-high-speed (180krpm) application, together with investigation on the influence of rotor eccentricity and winding circulating current.

Firstly, 6-slot/2-pole (6s/2p) high-speed permanent magnet (HSPM) motors with 1, 2, and 3 slot-pitch windings are designed, optimized, and compared, accounting for their different winding factors, end-winding lengths, and end-winding axial lengths. It shows that for high-speed applications, compared with 1 and 3 slot-pitch windings, the motor with 2 slot-pitch windings has a good trade-off between winding factor and end-winding axial length, and is attractive for improving torque density. In addition, 6s/2p HSPM motors with alternate layouts of 2 slot-pitch windings are analyzed and compared with a 3-slot/2-pole (3s/2p) HSPM motor with non-overlapping windings due to same winding factor. It indicates that compared with the 3s/2p PM motor, the 6s/2p PM motors with 2 slot-pitch windings have advantages, e.g. high torque, small phase inductance, low rotor loss, and no unbalanced magnetic force (UMF), which are desirable for high-speed operation.

Secondly, the influence of rotor eccentricity on electromagnetic performances of the 2-pole PM motors is investigated. For 3s/2p motors, static rotor eccentricity leads to unbalanced magnitudes and phase angles of fundamental back electromotive forces (back-EMFs) of three phases, while dynamic rotor eccentricity results in asymmetric positive and negative half-periods in the phase back-EMF waveform. For 6s/2p motors with 1, 2, and 3 slot-pitch windings, when strong magnetic saturation exists, the static rotor eccentricity leads to slight unbalanced back-EMFs of three phases. In addition, the circulating currents in the parallel-connected windings due to rotor eccentricity are analyzed. It is shown that with the circulating currents, the various loss components are increased, and the average torque and torque ripple remain almost unchanged, but the average UMF and cogging torque are reduced.

Finally, several prototype motors have been manufactured and successfully operated up to 180krpm, and particularly, the influence of rotor eccentricity is experimentally validated.

## ACKNOWLEDGEMENTS

I would like to express my sincere gratitude to my supervisor, Professor Z. Q. Zhu, for his invaluable guidance, insightful suggestion, and continuous encouragement at every stage of my PhD study. His immense knowledge and plentiful experience have encouraged me in all the time of my academic research and daily life.

I would like to thank the following people who have helped me complete this research.

- All members of the Electrical Machines and Drives Group.
- Miss F. Xu, Dr. Y. Wang, Mr. D. W. Liang, and Dr. Y. X. Li, for their support and inspired suggestions.
- Mr. H. Bin, Mr. J. K. Jiang, Miss X. L. Xu, Mr. J. Q. Zhao, Dr. D. Wu, Dr. L. M. Gong, and Dr. J. T. Chen, from Midea Welling Motor Technology (Shanghai) Co., Ltd., China, which sponsored the project.

Finally, I would like to express special thanks to my parents. From them, I have learned that one person can really make a difference. I will never forget their constant support and love.

# CONTENTS

<b>ABSTRACT.....</b>	<b>I</b>
<b>ACKNOWLEDGEMENTS.....</b>	<b>II</b>
<b>CONTENTS.....</b>	<b>III</b>
<b>NOMENCLATURE.....</b>	<b>VII</b>
<b>CHAPTER 1 GENERAL INTRODUCTION.....</b>	<b>1</b>
1.1. Introduction.....	1
1.2. Various Machine Types.....	2
1.2.1. Induction Machines.....	2
1.2.2. Switched Reluctance Machines.....	3
1.2.3. Permanent Magnet Machines.....	4
1.2.4. Summary.....	16
1.3. Stator Structures and Winding Configurations.....	18
1.3.1. Stator Structures.....	18
1.3.2. Winding Configurations.....	27
1.4. Rotor Structures.....	39
1.4.1 IPM.....	39
1.4.2 SPM.....	43
1.4.3 Solid PM.....	46
1.4.4 Summary.....	47
1.5. Parasitic Effect.....	48
1.5.1 Stator Iron Loss.....	48
1.5.2 AC Copper Loss.....	49
1.5.3 Rotor Eddy Current Loss.....	50
1.5.4 Windage Loss.....	51
1.5.5 Rotor Dynamic and Vibration.....	52
1.5.6 Thermal Aspect.....	52
1.6. Scope and Contributions.....	52
<b>CHAPTER 2 COMPARATIVE STUDY OF 6-SLOT/2-POLE HIGH-SPEED PERMANENT MAGNET MOTORS WITH DIFFERENT WINDING CONFIGURATIONS.....</b>	<b>56</b>
2.1 Introduction.....	56
2.2 Machine Topologies.....	57
2.2.1 Winding Factor.....	58
2.2.2 End-winding Length.....	59

2.2.3	End-winding Axial Length .....	60
2.3	Optimal Designs .....	61
2.3.1	Fixed Current Density .....	61
2.3.2	Fixed Copper Loss.....	66
2.3.3	Fixed Total Stator Loss.....	80
2.4	Electromagnetic Performance of Optimized Motors.....	85
2.4.1	Open-circuit Air-gap Field.....	87
2.4.2	Back-EMF.....	87
2.4.3	Electromagnetic Torque.....	90
2.4.4	Winding Inductances .....	90
2.4.5	Loss Analysis .....	92
2.5	Influence of End-windings.....	100
2.6	Experimental Validation .....	103
2.7	Conclusion .....	107
<b>CHAPTER 3 Electromagnetic Performance Analysis of 6-Slot/2-Pole High-Speed Permanent Magnet Motors with Two Slot-pitch Windings.....</b>		<b>108</b>
3.1	Introduction .....	108
3.2	Motor Topology .....	110
3.2.1	Winding Configuration.....	110
3.2.2	End-winding Length.....	111
3.2.3	Axial Length of End-winding .....	111
3.3	Design Optimization.....	113
3.4	Performance Evaluation.....	117
3.4.1	Open-circuit Analysis .....	117
3.4.2	Torque Analysis .....	118
3.4.3	Loss Analysis .....	122
3.4.4	Winding Inductances .....	126
3.5	Comparison of 3s/2p and 6s/2p HSPM Motors .....	128
3.5.1	Open-circuit Analysis .....	129
3.5.2	Torque Analysis .....	131
3.5.3	Unbalanced Magnetic Force .....	131
3.5.4	Loss Analysis .....	132
3.5.5	Winding Inductances .....	133
3.6	Experimental Validation .....	133
3.7	Conclusion .....	138

APPENDIX 3. A .....	139
APPENDIX 3. B.....	140
<b>CHAPTER 4 INFLUENCE OF ROTOR ECCENTRICITIES ON ELECTROMAGNETIC PERFORMANCE OF 2-POLE PERMANENT MAGNET MOTORS .....</b>	<b>142</b>
4.1. Introduction.....	142
4.2. Motor Topologies and Rotor Eccentricity Types.....	143
4.2.1 Motor Topologies.....	143
4.2.2 Rotor Eccentricity Types .....	144
4.3. 2-Pole Asymmetric Motor with Rotor Eccentricity .....	146
4.3.1 Open-circuit Air-gap Field.....	146
4.3.2 Back-EMF.....	148
4.3.3 Electromagnetic Torque.....	160
4.3.4 Cogging Torque.....	164
4.3.5 Unbalanced Magnetic Force .....	168
4.4. 2-Pole Symmetrical Motor with Rotor Eccentricity.....	169
4.4.1 Open-circuit Air-gap Field.....	170
4.4.2 Back-EMF.....	171
4.4.3 Electromagnetic Torque and Cogging Torque.....	183
4.4.4 Unbalanced Magnetic Force .....	185
4.5. Prototyping and Experimental Validation .....	187
4.5.1 Back-EMF.....	188
4.5.2 Static Torque.....	194
4.6. Conclusion .....	196
APPENDIX 4. A .....	196
<b>CHAPTER 5 Influence of Rotor Eccentricities on Electromagnetic Performance of 6-Slot/2-Pole Permanent Magnet Motors .....</b>	<b>199</b>
5.1 Introduction.....	199
5.2 Machine Topologies and Rotor Eccentricity Types .....	202
5.2.1 Machine Topology and Winding Connection.....	202
5.2.2 Rotor Eccentricity Types .....	202
5.3 Effect of Rotor Eccentricity on Back-EMF and Circulating Current.....	203
5.3.1 Influence of Rotor Eccentricity.....	204
5.3.2 Influence of Rotor Eccentricity Ratio.....	210
5.4 Steady-state Circulating Currents and Effect due to Rotor Eccentricities.....	214
5.4.1 Open-circuit Condition .....	214

5.4.2	On-load Condition.....	221
5.5	Conclusion .....	229
	Appendix 5. A.....	229
	<b>CHAPTER 6 GENERAL CONCLUSIONS AND FUTURE WORK .....</b>	<b>242</b>
6.1.	General Conclusions.....	242
6.1.1	Stator Structure and Winding Configuration .....	242
6.1.2	Rotor Eccentricity.....	245
6.2.	Future Work .....	247
	<b>REFERENCES.....</b>	<b>249</b>
	<b>APPENDIX I PUBLICATION RESULTED FROM PHD STUDY.....</b>	<b>272</b>

## NOMENCLATURE

### *Symbol*

$a$	Number of parallel paths	
$A_g$	Air-gap area	$\text{mm}^2$
$A_{iron}$	Stator iron core area	$\text{mm}^2$
$B$	Flux density	T
$B_{ave}$	Average air-gap flux density	T
$B_g$	Air-gap flux density	T
$B_m$	Flux density magnitude	T
$B_{max}$	Maximum stator iron core flux density	T
$B_r$	Magnet remanence	T
$B_{ra}$	Radial flux density component of air-gap flux density	T
$B_{rk}$	Magnitude of the kth order radial flux density component	T
$B_{ta}$	Tangential flux density component of air-gap flux density	T
$B_{tk}$	Magnitude of the kth order tangential flux density component	T
$B_{rn}$	Nth harmonic magnitude	T
$B_{r\_slotless}$	Radial component of air-gap field	T
$B_{r\_slotted}$	Radial component of air-gap field	T
$C_f$	Friction coefficient	
$D_g$	Air-gap diameter	mm
$D_i$	Stator inner diameter	mm
$D_o$	Stator outer diameter	mm
$e_a$	Back-EMF of phase A	V
$e_b$	Back-EMF of phase B	V
$e_c$	Back-EMF of phase C	V
$E_{ave}$	Average peak value of three phase back-EMF	V
$E_{ph}$	Peak value of phase back-EMF	V
$E_1$	Back-EMF of coil 1	V
$E_2$	Back-EMF of coil 2	V
$\Delta E$	Back-EMF difference between two coils	V
$f$	Frequency	Hz
$g$	Air-gap length	mm
$h$	Overall thermal heat transfer coefficient	$\text{W}/^\circ\text{Cm}^2$



$H$	Magnetic field strength	A/m
$h_t$	Tooth-tip height	mm
$h_t$	Tooth-tip height	mm
$h_y$	Yoke height	mm
$I$	Peak phase current	A
$I_A$	Peak current of phase A	A
$i_a$	Current of phase A	A
$I_B$	Peak current of phase B	A
$i_b$	Current of phase B	A
$I_c$	Peak current of phase C	A
$i_c$	Current of phase C	A
$I_{max}$	Maximum phase current	A
$i$	Integer	
$j$	Integer	
$J_{max}$	Maximum allowed current density	A/mm <sup>2</sup>
$k_a$	Additional loss coefficient	
$k_e$	Eddy current loss coefficient	
$k_h$	Hysteresis loss coefficient	
$k_p$	Slot packing factor	
$k_w$	Winding factor	
$k_{dk}$	Distribution factor	
$k_{pk}$	Pitch factor	
$k$	Harmonic order	
$l_a$	Rotor length	mm
$l_{con}$	Connection part length of end-winding	mm
$l_e$	End-winding length	mm
$l_{ea}$	End-winding axial length	mm
$l_{ex}$	Extension part length of end-winding	mm
$l_g$	Equivalent air-gap length including a non-magnetic sleeve	mm
$l_{ma}$	Motor axial length	mm
$L_{coil}$	Inductance	H
$LOSS_{max}$	Maximum loss	W
$l_{RI}$	Arc distance between point-A and adjacent tooth	mm

$l_{R2}$	Arc distance between point-B and adjacent tooth	mm
$l_s$	Stator active length	mm
$m_w$	Number of full-pitch coils connected in series	
$m$	Odd number	
$n$	Original field harmonic	
$N_{ph}$	Number of series turns per phase	
$N_s$	Slot number	
$O_r$	Center of the rotor	
$O_s$	Center of the stator bore	
$p$	Number of pole pairs	
$P_a$	Anomalous loss of stator iron core	W/kg
$P_{cu}$	Copper loss	W
$P_e$	Eddy current loss of stator iron core	W/kg
$P_h$	Hysteresis loss of stator iron core	W/kg
$P_{iron}$	Stator iron loss	W
$P_{limit}$	Stator thermal limitation	W
$P_{rotor}$	Rotor eddy current loss	W
$P_{stator}$	Total stator loss	W
$r$	Radial position	mm
$R_{coil}$	Resistance	$\Omega$
$R_{AC}$	AC resistance	$\Omega$
$R_{DC}$	DC resistance	$\Omega$
$R_g$	Air-gap radius	mm
$R_{in}$	Stator bore radius	mm
$R_m$	Magnet radius	mm
$R_r$	Rotor radius	mm
$R_{sh}$	Shaft radius	mm
$R_{si}$	Stator inner radius	mm
$R_u$	Unbalanced ratio	
$S_{slot}$	Slot area	mm <sup>2</sup>
$T_{ck}$	Cogging torque associated with the kth order air-gap flux density harmonic	Nm
$T_{em}$	Electromagnetic torque	Nm

$v$	Integer	
$V_m$	Maximum motor operation temperature	°C
$w_t$	Tooth width	mm
$X$	Rotor offset distance	mm
$y$	Slot-pitch number	
$Z_{coil}$	Impedance	$\Omega$
$\alpha$	Eccentricity angle	Elec. Deg.
$\alpha_a$	Circumferential position	Elec. Deg.
$\alpha_p$	Pole arc coefficient	
$\alpha_{rk}$	Phase angle of the kth order radial flux density component	Elec. Deg.
$\alpha_y$	Coil-pitch angle	Elec. Deg.
$\alpha_{tk}$	Phase angle of the kth order tangential flux density component	Elec. Deg.
$\alpha_s$	Shortened angle compared to the pole pitch	Elec. Deg.
$\beta$	Rotor initial angle	Elec. Deg.
$\delta$	Skin depth	mm
$\delta_{\alpha\beta}$	Angle difference between eccentricity and rotor initial angles	Elec. Deg.
$\varepsilon$	Eccentricity ratio	
$\theta$	Rotor position	Elec. Deg.
$\theta_{end}$	Angle between extend and connection part of end-winding	Mech. Deg.
$\theta_i$	Position of the ith coil	Elec. Deg.
$\lambda$	Split ratio	
$\lambda_g$	Relative air-gap permeance	
$\lambda_{g1}$	The 1st harmonic magnitude	
$\mu$	Permeability	H/m
$\mu_0$	Permeability of free space	H/m
$\mu_r$	Relative permeability of permanent magnet	H/m
$\rho_{air}$	Air gap density	kg/m <sup>3</sup>
$\rho_{cu}$	Resistivity of copper	$\Omega/m$
$\chi$	1 and 0 for dynamic and static rotor eccentricities	
$\psi$	Flux linkage	Wb
$\omega$	Rotor mechanical speed	rad/s
$\sigma$	Electrical angle between adjacent full-pitch coils	Elec. Deg.

### ***Abbreviation***

3s/2p	3-slot/2-pole
6s/2p	6-slot/2-pole
6s/4p	6-slot/4-pole
AC	Alternating current
Back-EMF	Back electromotive force
BLDC	Brushless direct current
CF	Carbon fibre
CFD	Computational fluid dynamic
DC	Direct current
DE	Dynamic eccentricity
DFIM	Doubly-fed induction machine
DVD	Digital versatile disc
EAT	Electrically assisted turbocharger
ETC	Electric turbocharger
FEM	Finite element method
FRPM	Flux-reversal permanent magnet
FSPM	Flux switching permanent magnet
GF	Glass fibre
HDD	Hard disk drive
HEV	Hybrid electric vehicle
HSPM	High-speed permanent magnet
IEEE	Institute of Electrical and Electronics Engineers
IM	Induction machine
IPM	Interior permanent magnet
krpm	Kilo revolutions per minute
L/D	Rotor length/diameter ratio
LCR	Inductance, capacitance, and resistance
LPTN	Lumped-parameter thermal network
MMF	Magnetomotive force
NEMA	National electrical manufacturers association
ORC	Organic rankine cycle
PM	Permanent magnet

PMM	Permanent magnet machine
PMSM	Permanent magnet synchronous machine
PWM	Pulse width modulation
RMS	Root mean square
SE	Static eccentricity
SPM	Surface-mounted permanent magnet
SRM	Switched reluctance machine
T/V	Torque/Volume
UMF	Unbalanced magnetic force
UHSPM	Ultra-high-speed permanent magnet
VPMSM	Vernier permanent magnet synchronous machine

# CHAPTER 1

## GENERAL INTRODUCTION

### 1.1. Introduction

In the last few decades, high-speed electrical machines have been intensively and extensively researched and are popular in industrial and domestic applications, including compressors, vacuum pumps, turbine generators, machine tools, flywheel energy storages, and so on [BIA04] [BOR12] [GER14] [SHE18]. Compared with low-speed and moderate-speed conventional electrical machines, high-speed electrical machines offer advantages such as high power density, small size, and light weight. More importantly, high-speed electrical machines can be directly connected to high-speed loads, and conventional gear boxes are no longer needed, which avoids complex gear box systems, improves system efficiency and reliability, and reduces system vibration, noise, and cost [BIA04] [ARK05] [LIS16] [GER14] [SHE18]. With the revolution in the field of power electronics converters, the problem of high frequency caused by high-speed operation is no longer a restriction. Meanwhile, the development of high-speed electrical machines is also supported by the development of high-speed bearing systems with high robustness, less loss, and long lifetime.

In general, there is no specific speed that can be a widely accepted standard for high-speed electrical machines [SHE18]. However, a ‘guide number’ is proposed to define high-speed electrical machines in [MIL91] [GER14], which is a product of the rated rotating speed and the square root of rated output power, i.e.  $\text{rpm} \cdot \sqrt{\text{kW}}$ . This value can also describe the difficulty degree for the design of high-speed electrical machines. Since the dynamic problems can be neglected when the electrical machines operate below  $100,000 \text{ rpm} \cdot \sqrt{\text{kW}}$ , the electrical machines with a value of more than  $100,000 \text{ rpm} \cdot \sqrt{\text{kW}}$  could be defined as high-speed machines. In [LIS16], the tip speed, i.e. the rotor surface line speed, is presented as a better way to define the high-speed electrical machines since the rotor surface speeds can be used as the critical speeds under different design considerations, such as the constraints of rotor mechanical stress and rotor dynamic characteristic.

This thesis investigates 2-pole ultra-high-speed (180 krpm) permanent magnet (UHSPM) motors with different winding configurations for domestic appliance applications, e.g. vacuum cleaners, focusing on electromagnetic performance with due account for rotor eccentricity.

This chapter reviews the development of high-speed electrical machines, especially for three-

phase permanent magnet machines. Section 1.2 analyses the characteristics of different high-speed electrical machine technologies, i.e. induction machines (IMs), switched reluctance machines (SRMs), and permanent magnet machines (PMMs). The stator structures, winding configurations, and rotor constructions of three-phase high-speed permanent magnet machines are summarised in sections 1.3 and 1.4. Then, section 1.5 discusses several parasitic effects due to high-speed operation, such as stator iron loss, alternating current (AC) copper loss, rotor eddy current loss, windage loss, rotor dynamics, vibration, and thermology. Finally, the scope and contribution are shown in section 1.6.

It is worth noting that “high-speed electrical machines” will be simplified as “high-speed machines” throughout this thesis.

## **1.2. Various Machine Types**

In general, three machine types are often employed for high-speed applications, i.e. IMs, SRMs, and PMMs. In this section, their advantages, disadvantages, and applications will be reviewed and compared.

### **1.2.1. Induction Machines**

With simple rotor structure and high mechanical strength, IMs are potential candidates for high-speed applications, especially for the IMs with solid rotor structures [ARK05] [GER14], Fig. 1. 1.

In general, with conventional laminated rotor structures, the highest surface speed of IMs is around 185 m/s [ZHA16b]. Beyond 185 m/s, the high strength lamination or solid rotor structure, Fig. 1. 1 (a), should be used to improve the rotor structural integrity. Due to the inherent robustness of solid rotor structure, the limitation of the tip speed can be larger than 400 m/s [ARK05]. [PYR10] designs an 8-MW 6.6-kV 12 krpm IM with a slitted solid rotor structure for gas compressors, Fig. 1. 1 (b). Slitting can increase the flux into the rotor and decrease the rotor eddy current loss, but it increases friction coefficients of the rotor surface, which leads to large air-gap friction loss, especially for high-speed operation. In addition, the mechanical strength of the rotor is decreased due to slitting, which results in a relatively low critical speed, e.g. 204 m/s. In [SHA96], a copper layer is employed to improve the mechanical strength of the solid rotor, Fig. 1. 1 (c). Compared with the smooth solid rotor, the copper layer not only improves the rotor stiffness but also increases the efficiency since it is equivalent to rotor bars and end-rings. However, the copper layer results in large air-gap and small air-gap

flux density, which leads to relatively low power factor and power density. In [LHA02], the slitted solid rotor with a squirrel cage is proposed to balance the power density and mechanical strength, Fig. 1. 1 (d). Compared with the solid rotor with a copper layer, the squirrel cage rotor has higher power density and efficiency but less mechanical strength. In [FOD14], an induction machine, a switched reluctance machine, and a permanent magnet machine are designed and compared for high-speed applications under the same output performance, i.e. 20 kW @ 26 krpm. However, the conclusion in [FOD14] is doubtful since it shows that the IM has the highest power factor, while the IM has the lowest power density and efficiency compared with both SRM and PMM.

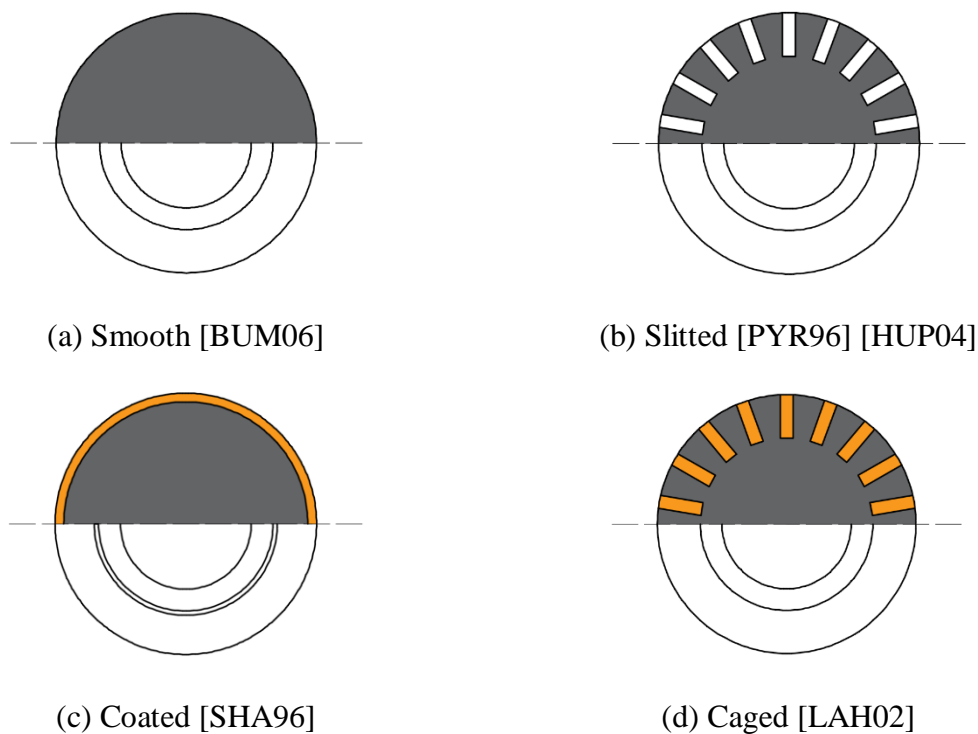


Fig. 1. 1. Four solid rotor constructions of IMs.

### 1.2.2. Switched Reluctance Machines

Due to simple structure, high robustness, low cost, and high temperature resistance, the switched reluctance motors have received much attention in high-speed applications. In literature, the highest power of high-speed SRMs is 250 kW @ 22 krpm [RIC97], and the highest rated speed is 200 krpm with 1.0 kW rated power [MOR00]. In [FOD14], compared with IM and PMM, the SRM with the longest stack length has the largest stator iron loss, and its efficiency and power density are lower than those of PMM. However, the rotor of SRM without copper and magnets play an important role for several specific applications, especially



for high temperature high-speed operation. [BOR14a] designs a 45 kW 32 krpm 6s/4p switched reluctance machine with a novel rotor geometry for aerospace applications, which is a harsh environment with high temperature and strong radiation, Fig. 1. 2 (a). [IKA14] designs a 100 kW 20 krpm 36-slot/2-pole synchronous reluctance machine with a novel rotor construction including Cu-Al alloy and iron bars, Fig. 1. 2 (b).

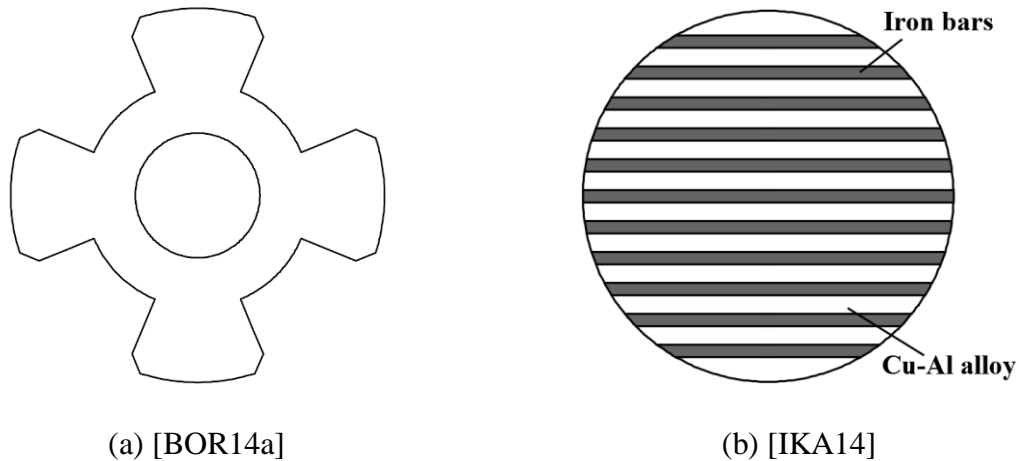


Fig. 1. 2. Novel rotor constructions of reluctance machines.

### 1.2.3. Permanent Magnet Machines

Compared with IMs and SRMs, PMMs have the highest power density and efficiency, lowest mass, and shortest stator active length. In [ARK05], the solid-rotor IMs are compared with the PMs, and the results show that under different operation points, i.e. 30 krpm @ 540 kW, 60 krpm @ 95 kW, and 100 krpm @ 30 kW, and similar constraints, the permanent magnet machines always have higher efficiency and almost 50% larger torque density than the solid-rotor induction machines. Meanwhile, compared with IMs and SRMs, PMMs are much less sensitive to air-gap length, which is desirable for high-speed operation. Therefore, the PMMs are the most attractive machine type for high-speed applications.

In general, the high-speed permanent magnet (HSPM) machines include single-phase and three-phase HSPM machines. The former has been employed in low-power household applications due to simple motor structure and low cost. However, it has self-starting issue, and needs special design for starting. The latter has high power density, high power factor, and large output torque, which can be employed in industrial and domestic drives. In this section, the single-phase and three-phase HSPM machines are reviewed in detail.

## A. Single-phase

Based on the conventional single-phase induction motor, the single-phase capacitor-start permanent-magnet (PM) AC line-start motor is designed and analyzed in [MIL85]. The stator remains the same structure as that of the conventional induction motor, and the rotor structure consists of permanent magnets and cage windings, Fig.1. 3. The permanent magnet can improve the efficiency, power factor, and power density, but it may decrease the starting torque. Therefore, the cage windings are used to provide sufficient starting torque. Although the single-phase capacitor-start PM AC line-start motor can be employed for pumps, air conditions, and fans [KUR04], the complex rotor design and low mechanical strength results in low critical speed.

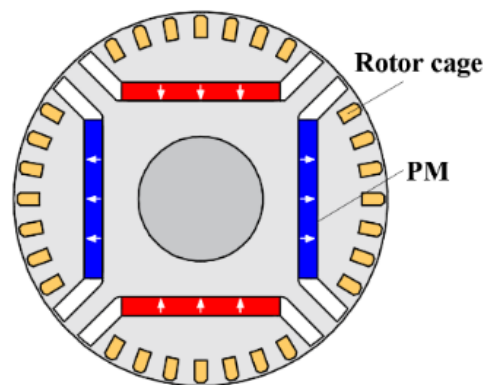


Fig. 1. 3. Rotor structure of single-phase capacitor-start PM AC line-start motor [MIL85].

[MAY89] develops a single-phase brushless direct current (BLDC) motor with a bifilar stator winding and asymmetric stator pole faces, and [HUA99] designs a single-phase BLDC spindle motor for digital versatile disc (DVD) and hard disk drive (HDD) applications. In those single-phase BLDC motors, the salient poles of the stator are reshaped to reduce cogging torque, and an automatic phase adjuster is used to increase torque and efficiency. Compared with the three-phase motor, the single-phase motor offers advantages in terms of low cost and simple manufacturing. However, in [MAY89] and [HUA99], the single-phase BLDC motor employs an outer rotor structure, which has a large rotor surface speed and is limited for high-speed applications.

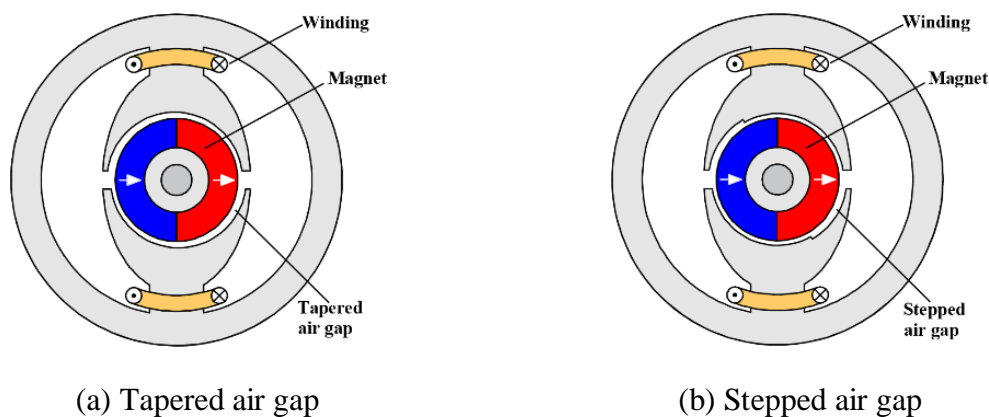
In [BEN99], a universal motor, a three-phase PM BLDC motor, and a single-phase PM BLDC motor are designed and compared for vacuum cleaner. Due to the self-starting problems caused by the null-points in the torque waveform, various asymmetric stators, i.e. asymmetric air-gaps, including tapered air gap, stepped air gap, asymmetric auxiliary slot, asymmetric tooth-tips, are designed to provide a sufficient starting torque and a smooth torque waveform due to low

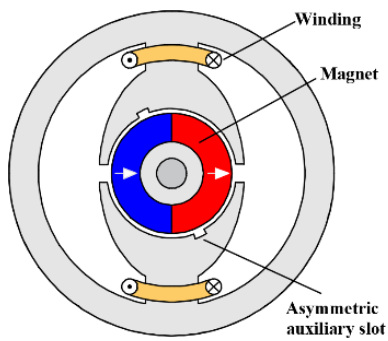
cogging torque [BEN00], Fig. 1. 4. The results show that compared with the universal motor, both PM BLDC motors have better torque/speed and efficiency/speed performance and less noise and electromagnetic emissions. Although the single-phase motor with lower cost is more suitable for consumer products which are extremely sensitive to the cost, the three-phase motor with larger torque and higher efficiency is more attractive. Due to the inner rotor structure, the PM motors with low rotor surface speed are desirable for high-speed applications [ZHO06].

For high-speed FSPM motors [WON06] [JAN05] [CHE06], the asymmetric rotor, i.e. tapered air gap, is also employed to meet the requirement of large starting torque. In [CHE06], the rotor pole-arc and asymmetric rotor pole surface are optimized to improve the starting torque and decrease the cogging torque of a high-speed single-phase FSPM motor, Fig. 1. 5.

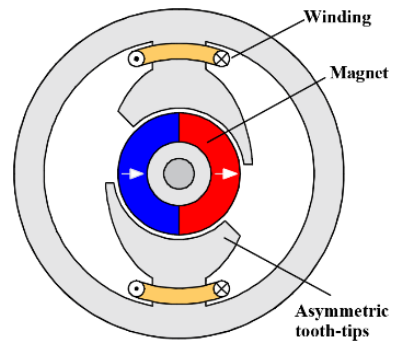
It is worth noting that the mentioned single-phase PM motors employ cylindrical stator and cylindrical rotor, while the single-phase PM motors with U-shape stator and cylindrical rotor are also developed to ease manufacturing and reduce cost [ERT05], Fig. 1. 6. In high-speed applications, Dyson Company designs a 105 krpm 4-pole single-phase PM BLDC motor with double U-shape stators and cylindrical rotor for vacuum cleaners and hair dryers [DYS11], Fig. 1. 7, which is a well-known stator structure for single-phase HSPM motor due to light weight, low cost, and high efficiency. Due to easy manufacturing, the E-shape stator structure is employed in a 200 krpm three-phase UHSPM motors for drilling applications where the space in the tool head is limited [TUY14], Fig. 1. 8.

Overall, although the single-phase PM motor has several advantages, especially low cost, it has lower power density and efficiency compared with the three-phase PM motor. In addition, the non-uniform air-gap distribution may lead to vibration and noise under high-speed operation.





(c) Asymmetric auxiliary slot



(d) Asymmetric tooth-tips

Fig. 1. 4. Different stator structures for self-starting [BEN00].

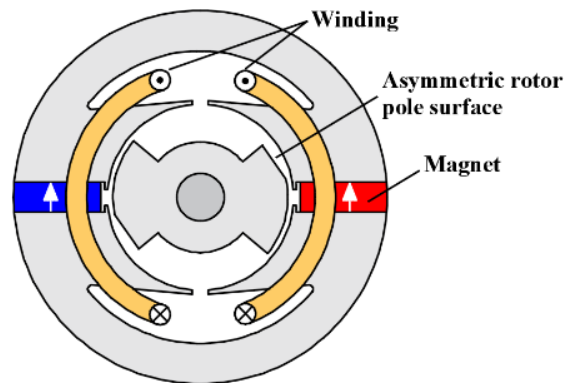


Fig. 1. 5. Single-phase FSPM machine topology [CHE06].

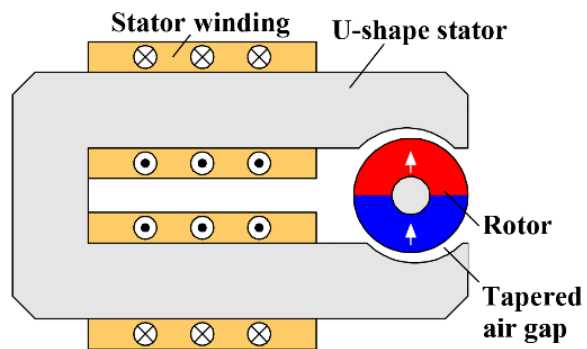


Fig. 1. 6. Single-phase PM motor with U-shape stator structure [ERT05].

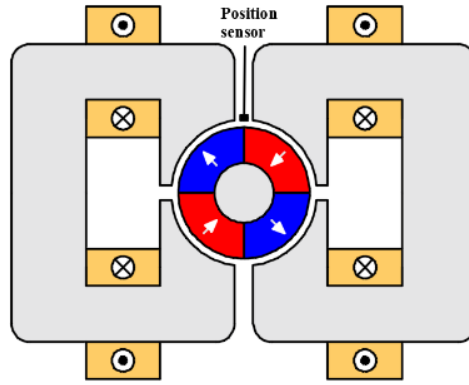


Fig. 1. 7. Single-phase PM motor with double U-shape stator structure [DYS11].

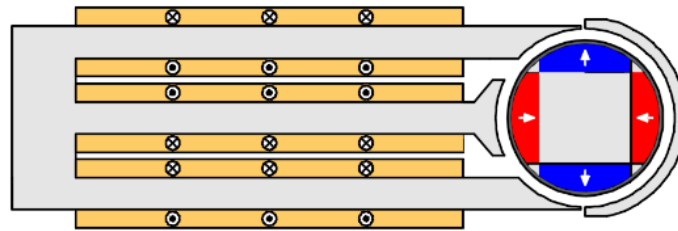


Fig. 1. 8. Three-phase PM motor with E-shape stator structure [TUY14].

## B. Three-phase

As mentioned before, three-phase PM BLDC motors offer advantages in high power density, high efficiency, and no self-starting issue. For the state-of-the-art vacuum cleaners, e.g. Dyson V15™, Midea Z7™, and Philips Speed-Pro Max, etc., the requirements of high-speed motor mainly focus on high power density, high efficiency, low vibration and noise, small size, and lightweight. Therefore, three-phase PM BLDC motors may be more competitive than single-phase motors for state-of-the-art vacuum cleaners.

Besides PM BLDC motors, PMSMs are strongly recommended for high-speed applications. In general, the main differences between the BLDC motor and PMSM include (a) excitation current waveforms, square waveform is essential for BLDC motors and sinusoidal waveform for PMSMs, and (b) the back-electromotive-force (back-EMF) waveforms, i.e. trapezoidal waveform is desirable for BLDC motors and sinusoidal waveform for PMSMs in order to reduce torque ripples. However, employing a 2-pole parallel magnetized rotor structure, the PM BLDC motor has sinusoidal air-gap flux density and back-EMF waveforms [ZHU97].

Three-phase HSPM motors have various machine topologies and winding configurations. Firstly, for high-speed operation, 2-pole and 4-pole rotors are widely employed to limit the fundamental frequency and reduce the stator iron losses and switching losses in the power electronics converter. Secondly, the slotted and slotless stator structures are selected to meet

the design requirements. In general, for high-power, large-size HSPM machines, the slotted stator is appropriate, while the slotless stator structure is more suitable for low-power, small-size, UHSPM machines. Therefore, the slot/pole number combination should be considered, which affects the winding factor, rotor loss, and UMF. Thirdly, the overlapping and non-overlapping winding configurations have different characteristics when combining with different stator structures. The overlapping winding configurations include full-pitched and short-pitched windings, Fig. 1. 14, while the non-overlapping windings can be divided into concentrated, toroidal, and skewed slotless windings, Figs. 1. 18 and 1. 19. All the winding configurations can be employed in slotted and slotless stator structures, except for the skewed slotless windings, which can only combine with the slotless stator. Fourthly, with high-speed operation, the centrifugal force leads to huge mechanical stress in the rotor and may destroy the magnets and rotor laminations. Therefore, various rotor constructions in interior PM (IPM), surface-mounted PM (SPM), and solid PM are designed to withstand the centrifugal force, Fig. 1. 21. For IPM machines, a solid stainless-steel rotor [ARU16] or a combination of silicon-steel and stainless-steel [ZHA15d] is employed to improve the rotor mechanical strength. For SPM machines, a non-magnetic high-strength sleeve is employed to improve the rotor mechanical strength [ZHU97] [BIA04] [SHI04], and the materials include non-magnetic stainless steel, Inconel, Titanium, glass fibre (GF), and carbon fibre (CF). The maximum surface speed of the GF sleeve is 150 m/s, but that of the CF sleeve can reach 210 m/s [BIN06]. The solid PM rotor structure can be classified into the solid PM with sleeve [HES87] [WAN03] [ZWY05] and the solid PM with hollow shaft [ZHE05]. It is worth noting that both sleeve and hollow shaft increase the effective air-gap length, decrease the air-gap flux density, and affect the output performance. Therefore, the rotor design should consider the trade-off between the electromagnetic performance and the constraint of mechanical stress.

Table 1. 1 lists several three-phase HSPM machines, including rated power/speed, slot/pole number combination, winding configuration, rotor structure, and applications. They are all published on IEEE/IET Electronic Library and sorted by the rated power. It can be seen that the rated power of the three-phase HSPM machine in [ZHA18b] is the highest, 2000 kW @ 20 krpm, whose value of  $\text{rpm} \cdot \sqrt{\text{kW}}$  is also the largest, and the rated speed of the three-phase HSPM machine in [ISM18] is the highest, 1200 krpm. In general, multi-slot stator structure, i.e. the number of slots larger than 6 ( $N_{slot} > 6$ ), is employed in high-power machines, while for low-power machines, minimal-slot, i.e. the number of slots less than or equal to 6 ( $N_{slot} \leq 6$ ), and slotless stator structures are widely used.

Table 1. 1

## Three-phase High-speed Permanent Magnet Machines in Literature

<b>Reference</b>	<b>Power (kW)</b>	<b>Speed (krpm)</b>	<b>Slot/pole</b>	<b>Winding</b>	<b>Rotor</b>	<b>Application</b>
[ZHA18b]	2000	20	48s/8p	Overlapping (Full-pitched)	SPM	-
[ZHA15a]	1120	18	27s/4p	Overlapping (Full-pitched)	SPM	Pump Drive
[ZHA16a]	1120	18	27s/4p	Overlapping (Full-pitched)	SPM	Compressor
[CHE19]	800	2.5	24s/4p	Overlapping (Full-pitched)	SPM	Prototype
[DUG20]	400	10	48s/4p	Overlapping (Full-pitched)	SPM	Prototype
[DON16a]	300	13.3	12s/14p	Concentrated	IPM	Aircraft Gas Turbine
[FAN17]	200	40	24s/2p	Overlapping (Full-pitched)	SPM	-
[DON14b]	150	24	24s/2p	Toroidal	Solid PM	Turbo Blowers
[ZHA17a]	150	17	36s/4p	Overlapping (Full-pitched)	SPM	Prototype
[DON16c]	140	24	24s/4p	Overlapping (Full-pitched)	Inter-SPM /Spoke-IPM	-
[LEE20]	124	36	24s/2p	Overlapping (Full-pitched)	SPM	Generator
[LIW14]	117	60	36s/2p	Toroidal	SPM	Micro Gas Turbine

[ZHA16c]	117	60	36s/2p	Toroidal	Solid PM	Prototype
[ZWY05]	100	500	Slotless/2p	Toroidal	Solid PM	Mesoscale Gas Turbines
[BEN18]	100	50	36s/4p	Overlapping (Full-pitched)	SPM	Turbo Generator
[HUA16b]	100	32	24s/4p	Overlapping (Full-pitched)	SPM	Centrifugal Air Blower
[JAN18]	82	12.5	24s/2p	Overlapping (Full-pitched)	SPM	Centrifugal Pump
[DON14]	75	36	24s/2p	Toroidal	Solid PM	Prototype
[JAS17]	57	30	6s/4p	Concentrated	SPM/Inset-PM	Pumps, Compressors, Blower
[JUM14]	50	100	Slotless/2p	Concentrated / Toroidal /Skewed	Solid PM	-
[JAN07]	50	70	12s/2p	Overlapping (Full-pitched)	SPM	Centrifugal Turbo-Compressors
[MUN10]	40	40	36s/4p	Overlapping (Full-pitched)	SPM	Prototype
[DAM16]	40	30	18s/2p	Overlapping (Full-pitched)	SPM	Light Duty Electric Vehicle
[ZHA15e]	30	96	18s/2p	Overlapping (Full-pitched)	SPM	Prototype
[JAN11b]	30	20	36s/6p	Overlapping (5/6 short-pitched)	IPM	Compressor
[BER16]	25	30	18s/2p	Overlapping (Full-pitched)	SPM	Prototype
[WAN10a]	22	120	6s/2p	Concentrated	SPM	Prototype
[FOD14]	20	26	18s/2p	Overlapping (Full-pitched)	SPM	Electric Vehicle



[LIU18]	15.7	125	12s/2p	Overlapping (Full-pitched)	IPM	Prototypes
[GIL16]	15	150	6s/2p	Concentrated	SPM	Electrically-assisted Turbocharger (EAT)
[GIL16]	15	150	Slotless/2p	Toroidal	SPM	EAT
[HON09]	15	120	12S/2P	Overlapping (5/6 short-pitched)	Solid PM	Air Blower
[CHE11]	15	30	24s/2p	Toroidal	Solid PM	Prototype
[ZHA21]	15	120	12s/2p	Toroidal	Solid PM/SPM	Gas Compressor
[MIR08]	11.8	15	36s/4p	Overlapping (Full-pitched)	IPM	-
[HON97]	11	50	36s/2p	Overlapping (Full-pitched)	IPM	Spindle Machine Tool
[UZH16]	11	31.2	6s/2p	Concentrated	Solid PM	Generator
[JUN18]	10	70	18s/2p	Overlapping (Full-pitched)	SPM	Electric-turbo
[SHE13]	10	70	12s/2p	Overlapping (Full-pitched)	SPM	Prototype
[XUE12]	7.5	30	24s/2p	Overlapping (4/6 short-pitched)	SPM	-
[OYA03]	5	240	6s/2p	Concentrated	SPM	-
[SHI04]	5	240	6s/2p	Concentrated	SPM	Electrical Drive System
[LIM17]	4	150	6s/2p	Concentrated	SPM	Electric Turbocharger
[GIL17]	4	75	6s/4p	Concentrated	SPM	-

[GIL17]	4	75	Slotless/2p	Toroidal	SPM	-
[BOR14]	3.7	240	Slotless/2p	Toroidal	SPM	Gas-turbine Generator
[UZH16]	3.5	45	6s/2p	Concentrated	Solid PM	Gas Blower
[HUY15]	3	150	24s/2p	Overlapping (Full-pitched)	Solid PM	Prototype
[ZHO06]	3	150	6s/2p	Concentrated	SPM	-
[HON18]	3	100	12S/2P	Overlapping (Full-pitched)	SPM	Electric Turbocharger
[GIL15]	3	80	6s/2p	Concentrated	SPM	Compressor
[ZHA15H]	3	80	6s/4p	Concentrated	SPM	Prototype
[IID20]	2.5	100	6s/2p,4p	Concentrated	SPM	Prototype
[PFI10]	2	200	Slotless/2p	Overlapping (Full-pitched)	Solid PM	Prototype
[ZHE05]	2	200	Slotless/2p	Overlapping (15/18 short-pitched)	Hollow shaft	Cryogenic
[NOG05]	2	120	6s-3s/2p	Concentrated	SPM	Turbocharger
[NOG09]	1.5	150	6s/2p	Concentrated	SPM	Automotive Supercharger
[HWA14]	1.5	60	3s/2p	Concentrated	SPM	Spindle Machine Tool
[JAN09]	1.5	20	slotless /2p	Overlapping (Full-pitched)	SPM	Flywheel
[ZHA15d]	1.5	18	36s/4p	Overlapping (Full-pitched)	IPM	Prototype

[KRA17]	1.5	12	3s/2p	Concentrated	SPM	Small Prototype Urban-Type Vehicle
[ZHU01]	1.3	120	3s/2p	Concentrated	SPM	Prototype
[BIA04]	1.3	20	Slotless/2p	Overlapping (Full-pitched)	SPM	Friction Welding Unit
[ZHU97]	1.3	20	3s/2p	Concentrated	SPM	Electric Drives
[BIA05]	1	40	3s/2p	Concentrated	SPM	Hand-tool
[BIA05]	1	40	Slotless/2p	Overlapping (Full-pitched)	SPM	Hand-tool
[WAN09]	0.75	60	24s/2p	Toroidal	Solid PM	Prototype
[XUJ11]	0.5	100	12s/4p; 2p	Overlapping (Full-pitched)	SPM	Miniature Turbojet
[HON13]	0.4	200	6s/2p	Concentrated	Solid PM	Micro Turbine Generator (MTG)
[ISM18]	0.15	1200	Slotless/2p	Toroidal	Solid PM	Prototype
[BOR14]	0.15	200	Slotless/2p	Toroidal	SPM	Micro-milling Spindle
[BUR19]	0.1	500	Slotless/2p	Concentrated	SPM	Micro Gas Turbines
[LUO09]	0.1	500	Slotless/2p	Overlapping (Full-pitched)	Solid PM	Prototype
[BIA04]	0.05	150	3s/2p	Concentrated	SPM	Hand-tool
[BUR19]	0.04	400	Slotless/2p	Concentrated	SPM	Micro Gas Turbines

[BOR14]	0.03	90	Slotless/2p	Toroidal	SPM	Air Compressor
[HES87]	0.01	150	3s/2p	Concentrated	Solid PM	Hand-tool
[SCH17]		160	Slotless/2p	Toroidal	Solid PM	Electrical Drive Systems
[WAL09]		40	Slotless/2p	Overlapping (Full-pitched)	SPM	Hand-tool

#### 1.2.4. Summary

In this section, IMs, SRMs, single-phase and three-phase PMMs have been introduced for high-speed applications. Their applications, advantages, and disadvantages have been summarized in Table 1. 2.

In general, the high-speed induction machines employing solid rotor structures with copper sleeves or copper cages have significant copper losses and rotor eddy current losses, which leads to low efficiency and power factor. The switched reluctance machines with simple and robust rotors have high temperature capability and can withstand harsh environments. However, low power density due to large air-gap, high windage loss due to salient pole rotor structure, high iron loss due to non-sinusoidal magnetic field distribution, large vibration and consequent noise, low efficiency, and low power factor result in the limitation of high speed operation. The single-phase PM machines with an inherent self-starting problem have lower power density, lower efficiency, and higher torque ripple than the three-phase PM machines. With a low-cost and simple rotor structure, single-phase PM machines are suitable for applications with the low-cost requirement. Three-phase PM machines with the highest power density and efficiency, highest critical speed, and lowest vibration and noise are the best choice for high-performance, high-speed applications. Therefore, three-phase HSPM machines will be researched in this thesis.

Table 1. 2  
Comparison of Various High-Speed Machines

	<b>Advantages</b>	<b>Disadvantages</b>
<b>Induction machine</b>	<ul style="list-style-type: none"> <li>• Low cost</li> <li>• Sensorless open-loop speed control</li> </ul>	<ul style="list-style-type: none"> <li>• Large copper loss</li> <li>• Low efficiency</li> <li>• Low power factor</li> <li>• Low strength of laminated rotor core</li> <li>• Large eddy current loss in solid rotor</li> </ul>
<b>Switched reluctance machine</b>	<ul style="list-style-type: none"> <li>• Simple and robust rotor</li> <li>• High temperature capability</li> </ul>	<ul style="list-style-type: none"> <li>• High windage loss</li> <li>• High iron loss</li> <li>• Low efficiency</li> <li>• Low power factor</li> <li>• Large vibration and noise</li> </ul>
<b>Single-phase PM machine</b>	<ul style="list-style-type: none"> <li>• Low cost</li> <li>• Higher power density and efficiency than universal motors</li> <li>• Simple rotor structure</li> </ul>	<ul style="list-style-type: none"> <li>• Additional design for self-starting</li> <li>• Demagnetization risk</li> <li>• Lower power density and efficiency than three-phase motors</li> <li>• Constraints of mechanical stress and thermal</li> <li>• Sleeve design for high-speed</li> </ul>
<b>Three-phase PM machine</b>	<ul style="list-style-type: none"> <li>• High power density</li> <li>• High efficiency</li> <li>• High power factor</li> <li>• Low vibration and noise</li> <li>• Sensorless control</li> </ul>	<ul style="list-style-type: none"> <li>• Relatively high cost</li> <li>• Demagnetization risk</li> <li>• Sleeve design for high-speed</li> </ul>

### 1.3. Stator Structures and Winding Configurations

In this section, the stator structures and winding configurations of HSPM machines are reviewed. The stator structures can be classified into slotted and slotless topologies, and the winding configurations can be divided into overlapping and non-overlapping layouts. The outline is illustrated in Fig. 1. 9.

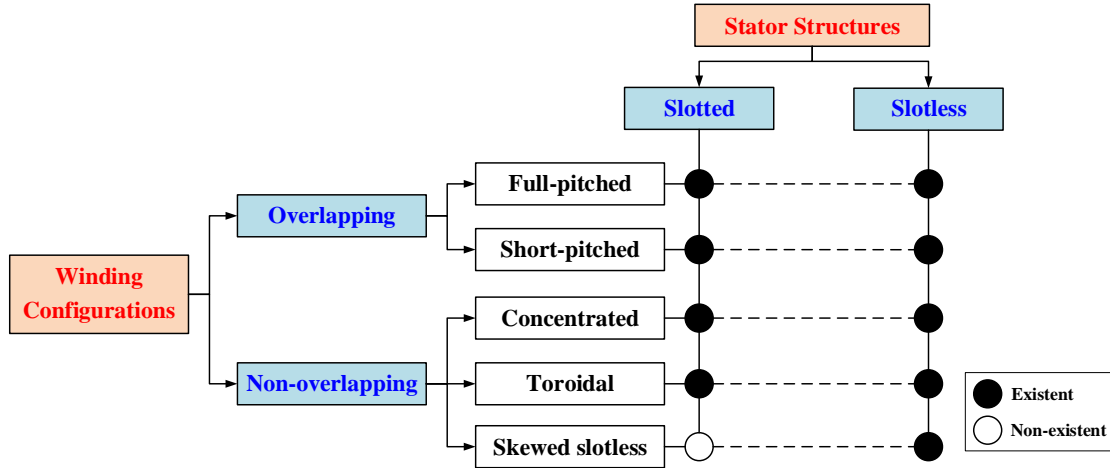


Fig. 1. 9. Outline of stator structures and winding configurations.

#### 1.3.1. Stator Structures

In HSPM machines, the slotted and slotless stator structures are employed for different applications.

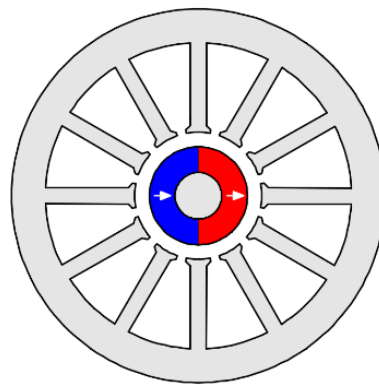
It is worth noting that “i-slot/j-pole” will be simplified as “is/jp” throughout this thesis.

##### A. Slotted

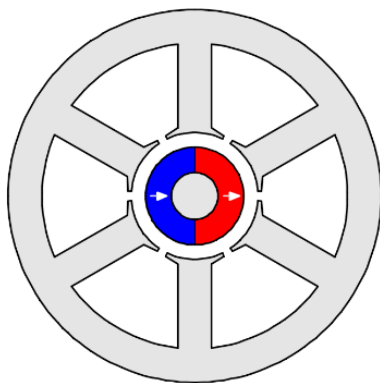
In general, the slotted HSPM motors can be separated into multi-slot (>6-slot) and minimal-slot (6-slot; 3-slot) HSPM motors [WAN03], Fig. 1. 10. The multi-slot stator structure is widely used for high power (>10 kW) requirements.

[ZHA18b] designs a 48s/8p high-speed SPM machine with a rating of 2 MW @ 20 krpm by multi-physics and multi-objective optimization. The optimal goal is the maximum torque per loss per mass, with a trade-off between power density and efficiency. For aircraft turbo-generator applications, the 36s/4p stator structure is employed for two high-speed SPM machines, and their rated power and speed are 150 kW @ 17 krpm [ZHA17a] and 100 kW @ 60 krpm [BEN18]. The former mainly analyses the various loss components, and the latter focuses on thermal analysis by the FE method. With toroidal windings, one 36s/2p HSPM machine [ZHA16c] and three 24s/2p HSPM machines are designed and analyzed, including

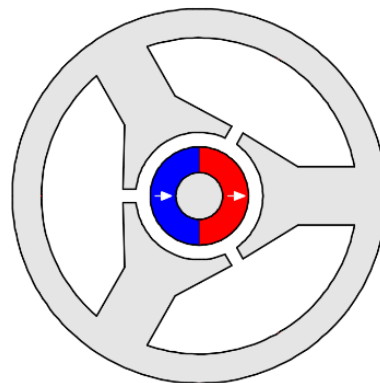
various loss components, mechanical stress, temperature distributions, and rotor dynamics [DON14] [CHE11] [WAN09]. In [ZHA15e] [BER16] [FOD14] [JUN18], 18s/2p HSPM machines are researched for different applications, such as electric vehicles and electric-turbo compounding systems. In addition, 12s/2p HSPM machines are employed in industrial applications. For centrifugal turbo-compressors, a 50 kW, 70 krpm 12s/2p HSPM machine is designed and analyzed by an analytical approach [JAN07]. [HON09] shows that the sleeve thickness affects the performances of a 15 kW, 120 krpm 12s/2p HSPM machine for air blower cooling fuel cells, such as rotor loss, von-Mises stress, unbalance vibration response, and critical speed. Then, [HON18] proposes a 3 kW 100 krpm HSPM machine for electric turbochargers (ETC), and the influence of the rotor length/diameter (L/D) ratio on the response time of the ETC is analyzed.



(a) Multi-slot (12-slot)



(b) Minimal-slot (6-slot)



(c) Minimal-slot (3-slot)

Fig. 1. 10. HSPM machines with multi-slot and minimal-slot stator structures [WAN03].

Overall, for various applications and requirements, the slot number should be optimized for different optimization objectives in the design of HSPM machines. [ZHA16a] analyses the performances of high power HSPM machines with different slot and pole number combination,



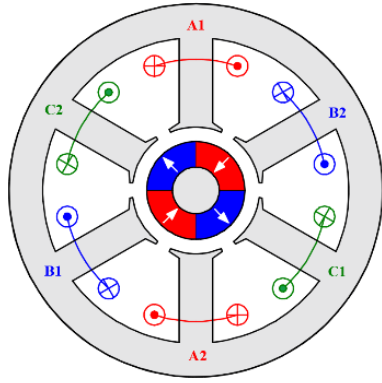
including 12-/24-/27-/36-slot and 2-/4-pole. The results show that compared with the machine with a 2-pole rotor, the machine with a 4-pole rotor has larger stator iron loss but smaller copper loss due to shorter end-winding length. In addition, the 4-pole rotor can reduce the motor axial length and improve the rotor dynamic characteristic. With a 4-pole rotor structure, the 27-slot is selected due to the lowest cogging torque and small PM eddy current loss.

For low-power HSPM machines, the minimal-slot stator structure is employed to simplify the winding process and avoid the physics limitation of small size. In literature, three typical slot/pole number combinations are selected in low-power small size HSPM machines, i.e. 6s/4p, 6s/2p, and 3s/2p, Fig. 1. 11, which will be reviewed as follows.

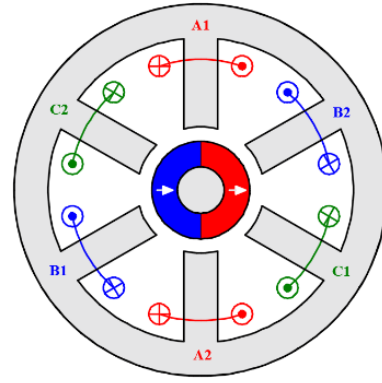
#### 1) 6s/4p

As mentioned before, the 4-pole rotor is adopted to reduce the end-winding length, copper loss, and stator yoke thickness in several multi-slot HSPM machines [MIR08] [ZHA16a] [DUG20]. With the same design considerations, a 4-pole rotor is selected for 6-slot HSPM machines [ZHA15H] [GIL17] [WAN18] [IID20].

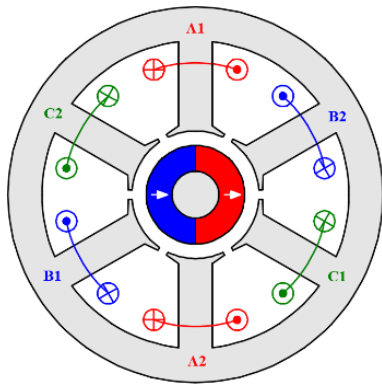
[ZHA15H] designs a 3 kW 80 krpm 6s/4p HSPM machine with concentrated windings for generators. The tooth shoe shape is optimized for the minimum sleeve loss and maximum efficiency. [WAN18] optimizes a 6s/4p HSPM motor considering stator iron loss and mechanical constraints. It found that both stator iron loss and mechanical constraints decrease the optimal split ratio, i.e. the ratio of stator inner to outer diameter. In [IID20], the 6s/4p and 6s/2p HSPM motors with a rating of 2.5 kW @ 100 krpm are compared to enhance output power density. With the same loss density, cooling capability, packing factor, and motor axial length (including end-winding), the 4-pole motor can increase 1.5 times the output power density by decreasing the motor size by 33% (stator outer diameter), compared with the 2-pole motor. However, this research neglects the switching loss in the power electronics converter, which has a close relationship with fundamental frequency and should be considered.



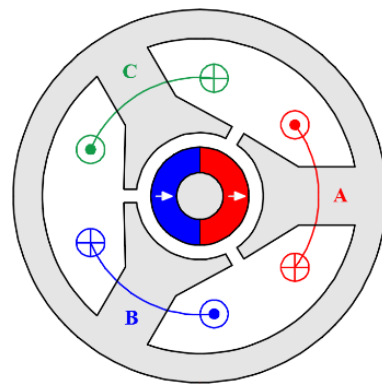
(a) 6s/4p [WAN18]



(b) 6s/2p with straight teeth [NOG05]



(c) 6s/2p with semi-closed [ZHO06]



(d) 3s/2p [ZHU97]

Fig. 1. 11. Low-power small size HSPM machine topologies with minimal-slot stator structures.

## 2) 6s/2p

For low-power, small-size HSPM machines, the frequency of the 4-pole motor is twice that of the 2-pole motor, which leads to large stator iron loss and switching losses in the power electronic converters. More importantly, for ultra-high-speed operation, 2-pole magnets can be designed as a magnet ring or a solid PM, Fig. 1. 21, which have high mechanical strength and simple manufacturing processes. Therefore, the 2-pole rotor is widely employed in low-power, small-size HSPM machines [WAN03] [NOG05] [NOG07] [NOG09] [NOG15] [ZHO06] [WAN10K] [NIU12] [HON13] [UZH16] [GIL15] [GIL16] [LIM17]

[WAN03] analyses several design features of HSPM machines for microturbines, including stator structures, winding configurations, rotor constructions, and bearing systems. It shows that compared with the multi-slot structure, the 6s/2p motor with full-pitched overlapping windings has the largest winding factor, i.e. '1'. [SHI04] designs a 5 kW 240 krpm 6s/2p

UHSPM motor with concentrated windings. The Inconel-718 sleeve is adopted to protect the rotor, and the magnet rings are magnetized radially. Although the winding factor decreases from '1' to '0.5' due to the concentrated winding, the reduced end-winding axial length leads to the decreased motor axial length and improved rotor dynamic characteristic. In [NOG05], for turbocharger applications, the 6s/2p and 3s/2p number combinations are compared for a 2 kW HSPM motor with a rated speed of 120 krpm and the maximum speed of 220 krpm. According to the loss analysis, the 6-slot motor with significantly smaller overall motor losses is more suitable for high-speed applications. Therefore, [NOG07] [NOG09] design a 6s/2p 1.5 kW 150 krpm HSPM motor with parallel magnetized magnets for automotive superchargers and 'b'-shaped copper-bar windings are employed for ease of manufacture. [NOG15] analyses the eddy current losses in copper-bar windings due to proximity effect caused by high-speed operation and reduce the AC copper losses by different tooth-tip shapes and segmentation of the conductors.

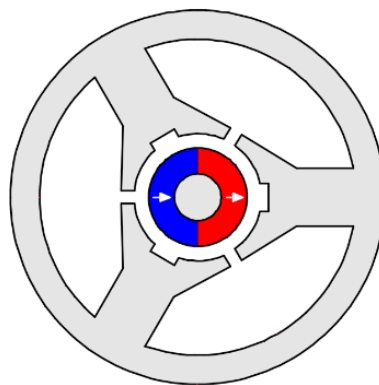
In [GIL15], for compressor applications, a 3 kW, 80 krpm 6s/2p HSPM motor is optimized for the highest efficiency by the FE method. Then, for a 15 kW 150 krpm electrically assisted turbocharger (EAT), [GIL16] compares three HSPM motor topologies, i.e. 2-pole slotless motor with toroidal windings, Fig. 1. 13 (b), 6s/2p motor with straight teeth, Fig. 1. 11 (a) and 6s/2p motor with semi-closed slot, Fig. 1. 11 (b). The result indicates that the 6s/2p slotted motors have a better compromise between efficiency and torque. More importantly, in terms of rotor dynamic, the 6s/2p motor with a semi-closed slot is the best choice due to the shortest motor axial length. [UZH16] designs two 6s/2p HSPM machines with a rating of 11 kW @ 31.2 krpm for gas blower applications and 3.5 kW @ 45 krpm for micro-organic Rankine cycle (ORC) power plants, respectively. Meanwhile, a multidisciplinary design process is proposed, and it indicates that considering the constraints of electromagnetic, mechanical, thermal, and dynamic, the design of high-speed machines cannot have a single optimum solution but can have different solutions for different requirements.

### 3) 3s/2p

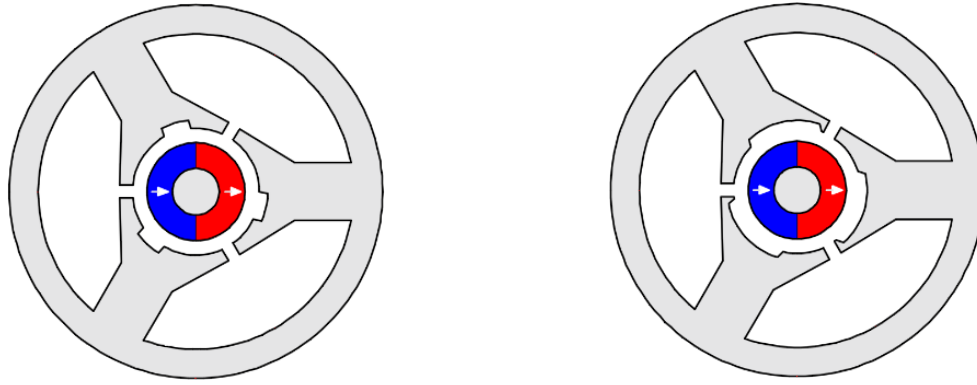
3s/2p number combination is the simplest structure for three-phase slotted HSPM machines. [HES87] designs a 3s/2p 10 W 150 krpm HSPM motor for a precision handpiece (or hand-tool) and analyses several challenges and constraints of high-speed operation. [ZHU97] designs a 1.3 kW 20 krpm HSPM motor for a friction welding unit, and the stator iron loss is analyzed under different maximum stator iron flux densities and lamination materials. In [ZHU01],

considering the sensorless operation based on the detection of the zero-crossing of the back-EMF waveform, the design criteria of a 1.26 kW 120 krpm 3s/2p HSPM motor is investigated. It shows that under the same overall size (including end-winding) and the similar efficiency, the motor with a lower stator iron flux density has smaller inductances and lower diode conduction angles, which is more suitable for high-speed sensorless operation. In [EDE01], a 3s/2p HSPM motor is optimized by finite element method for maximum efficiency considering stator iron loss. [BIA05] analyses and designs two 1.0 kW, 2-pole HSPM motors with a speed range of 20–40 krpm. One is a 3s/2p slotted HSPM motor, and the other one is a 2-pole slotless HSPM motor. In [BIA04], based on the 3s/2p slotted and 2-pole slotless motors, the potentials and limits of low power HSPM motors are discussed in terms of electromagnetic, mechanical, and thermal aspects.

However, compared with the 6s/2p PM motor, the 6s/4p, and 3s/2p PM motors have inherent UMF due to the diametrically asymmetric stator structure. In [PAN14], the influence of motor dimensions on no-load UMF is investigated, and the method of reducing the no-load UMF is proposed, i.e. adding extra notches in the middle of each stator tooth, Fig. 1. 12 (a). Then, in [MAJ18] and [MAJ19a], the extra notches are optimized to reduce the UMF considering no-load condition, Fig. 1. 12 (b), and rotor eddy current losses of 3s/2p PM motors, respectively, Fig. 1. 12 (c). It shows that the rated on-load UMF is removed and the rotor losses are reduced significantly. However, the elimination and reduction highly depend on load conditions, and the electromagnetic torque is decreased slightly.



(a) Extra notches for reducing the no-load UMF [PAN14]



(b) Extra notches for reducing the on-load UMF [MAJ18]

(c) Extra notches for reducing the eddy current loss [MAJ19a]

Fig. 1. 12. Extra notches for reducing no-load/on-load UMFs and rotor eddy current loss.

#### 4) *Optimal design of slotted machines*

As mentioned before, there is no single optimum design with multidisciplinary designs, and thus this section only shows the optimal design in terms of electromagnetic performance.

For high-speed slotted stator structure, the split ratio can be optimized since it affects not only the electromagnetic performance but also the mechanical stress of the rotor due to high rotor surface speed [HES87] [ZHU97] [PAN06] [WAN18]. For the maximum torque, the optimal split ratio depends on the remanence of the magnet ( $B_r$ ) and the maximum stator iron flux density ( $B_{max}$ ) [ZHU97]. For the maximum efficiency considering the stator iron loss, the optimal split ratio depends on the stator active length, output torque, and  $B_{max}$  [EDE01]. [BIA05] focuses on two design variables for the maximum torque, i.e. the stator inner diameter and the open circuit maximum stator iron flux density. With the fixed stator outer diameter, the first design variable is equivalent to the split ratio. In addition, the stator thermal limitation is introduced to avoid the thermal issue of the stator, which means the total stator loss is restricted, including iron core loss and copper loss. Considering the stator iron loss and mechanical constraints, [WAN18] investigates the optimal split ratio of a 6s/4p HSPM motor for the maximum torque by the influence of air-gap length and rotor pole pairs. The results show that the considered mechanical constraints decrease the optimal split ratio. Furthermore, the limitations of stator total loss and rotor loss are considered in [MAJ19b] since the rotor losses in small-size HSPM motors are difficult to reduce, and the cooling capability of the rotor is relatively poor.

For the minimum torque ripple and maximum efficiency, a ‘Tanguchi’ method is used in

[HWA14] accounting for various loss components. The ‘Tanguchi’ method is a simplified version of the global optimization, and different design variables with different suitable variation ranges are adopted. This method can avoid the calculation of maximum stator iron flux density but can only be used by FEM.

## B. Slotless

The slotless stator structures with large air-gap and flux leakage have relatively small output torque, which is rarely seen in conventional low-speed and moderate-speed PM machines. For high-power, large-size HSPM machines, although the high speed can increase the power, the critical speed is limited by the rotor mechanical strength and dynamic characteristics. Therefore, the relatively large torque is required in high-power large-size HSPM machines, and thus the slotless stator structure is not the suitable choice. For low-power, small-size HSPM machines, the critical speed is higher than that of high-power, large-size HSPM machines due to smaller rotor diameter. Therefore, the slotless stator structures with relatively small torque can be accepted in low-power, small-size HSPM machines, Fig. 1. 13.

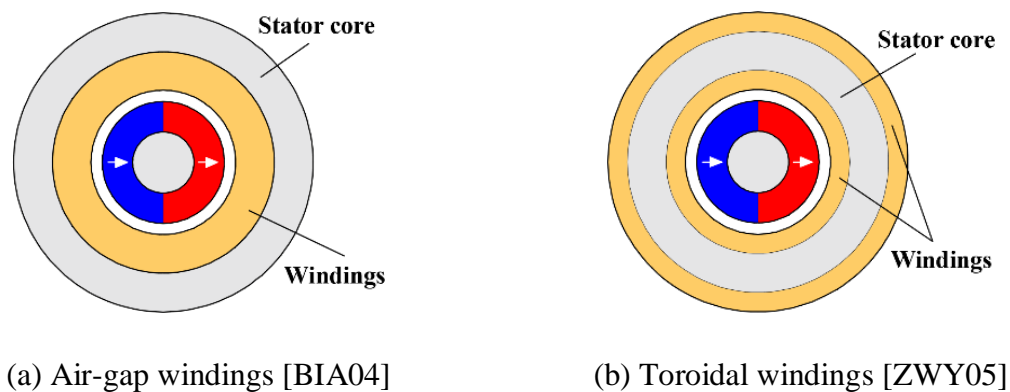


Fig. 1. 13. Slotless HSPM machines.

[HES82] proposes a 2-pole slotless PM motor for speeds in excess of 100 krpm, and it is compared with a slotted HSPM motor with the same external size. The analysis shows that the slotless stator structure with a simple construction is extremely attractive, especially for ultra-high-speed operation. The toroidal windings are employed in this slotless motor. In [WAN03], the multi-slot, minimal-slot, and slotless motors are discussed. It shows that compared with the slotted motor, the slotless motor has a smaller  $B_g$  due to larger flux leakage and lower rotor loss due to the uniform air gap. To compensate for the reduction of flux density, the stator active length of the slotless motor is relatively long.

The comparison in [HES82] and [WAN03] mainly focuses on electromagnetic performance. However, in [BIA04] and [BIA05], the comparison of a 3s/2p slotted HSPM motor and a 2-pole slotless HSPM motor includes electromagnetic performance, temperature distribution, mechanical stress, and PM demagnetization. The results show that for slotless motors, the effect of armature reaction is restricted, and the PM demagnetization is avoided due to the reduced rotor eddy current loss.

[GIL17] compares a 6s/4p HSPM motor and a 2-pole slotless motor for the reduction of noise emissions. It shows that the slotless motor has 38% smaller open-circuit power loss and 12dB lower noise due to significantly less armature reaction.

In literature, the slotless stator structure is popular for ultra-high-speed applications, such as 1200 krpm microsize machines [ISM18], 1000 krpm starter of gas turbine [ZWY09], 500 krpm mesoscale gas turbines [ZWY05] [LUO09], 400 krpm centrifugal compressor [BUR19] [AHN17]. Most importantly, the slotless stator may be the only solution for micro-scale HSPM machines. [SCH17] presents a millimeter-scale 2-pole slotless bearingless HSPM motor with a rated speed of 160 krpm for electrical drive systems. The measured overall motor losses at 160 krpm are below 1W and the measured temperature below 45°C.

The 2-pole slotless UHSPM motors are designed and optimized for the minimum power losses by analytical methods in [LUO09], [PFI10], and [BUR19]. However, their constraints are different, the  $B_{max}$  in [LUO09], the dimensions of the rotor in [PFI10], and the  $J_{max}$  in [BUR19].

### C. Summary

In this section, the applications, advantages, and disadvantages of slotted and slotless stator structures are summarised in Table 1. 3. The main consideration for the selection of slotted or slotless stator structures is the requirement of large torque, low rotor loss, or ultra-high-speed, respectively. In this thesis, the UHSPM motor is designed for a vacuum cleaner application, which has an extra torque requirement due to the drag force of the blades. Therefore, the slotted stator structure is a more suitable solution.

Table 1. 3

## Applications, Advantages, and Disadvantages of Slotted and Slotless Stator Structures

	Slotted	Slotless
Application	<ul style="list-style-type: none"> <li>• All power classes and size levels, except millimeter-scale</li> <li>• Especially for large torque requirement</li> </ul>	<ul style="list-style-type: none"> <li>• Low power and small size</li> <li>• Especially for low rotor loss requirement</li> <li>• Ultra-high-speed application</li> </ul>
Advantages	<ul style="list-style-type: none"> <li>• Large air-gap flux density</li> <li>• High overall thermal heat transfer coefficient, with forced-air cooling</li> <li>• Small current density or short stator active length</li> </ul>	<ul style="list-style-type: none"> <li>• Simple stator structure</li> <li>• Uniform air-gap distribution</li> <li>• Low rotor loss without slotting effect</li> <li>• Less PM demagnetization</li> <li>• Small windage loss</li> <li>• Low vibration and noise</li> </ul>
Disadvantages	<ul style="list-style-type: none"> <li>• Large rotor loss due to slotting effect and large armature reaction harmonics</li> <li>• PM demagnetization</li> <li>• With special slot/pole number combination, e.g. 3s/2p, UMF exists</li> </ul>	<ul style="list-style-type: none"> <li>• Small air-gap flux density</li> <li>• Low output torque</li> <li>• Large AC winding copper loss</li> <li>• Poor overall thermal heat transfer</li> </ul>

## 1.3.2. Winding Configurations

With slotted and slotless stator structures, various winding configurations can be combined for different applications. In general, the winding configuration can be divided into overlapping and non-overlapping windings, which have a close relationship with the winding factor, end-winding length, and motor axial length.

## A. Overlapping winding

For integer-slot motor, the overlapping winding includes full-pitched and short-pitched windings according to the coil span angle ( $\theta_s$ ), i.e.  $\theta_s = \pi$  elec. deg. and  $\theta_s < \pi$  elec. deg.,



respectively. When the coil span angle equals to the pole pitch, i.e. full-pitched winding, the winding factor ( $k_w$ ) is equal to the distribution factor ( $k_{dk}$ ), which can be calculated by (1.2). When the coil span angle is less than the pole pitch ( $k_{pk}$ ), i.e. short-pitched winding, the winding factor is equal to the product of distribution factor and pitch factor, which can be calculated by (1.3).

$$k_w = k_{dk} \times k_{pk} \quad (1.1)$$

$$k_{dk} = \frac{\sin\left(\frac{m_w k \sigma}{2}\right)}{m_w \sin\left(\frac{k \sigma}{2}\right)} \quad (1.2)$$

$$k_{pk} = \cos\left(\frac{k \alpha_s}{2}\right) \quad (1.3)$$

where  $k$  is the harmonic order,  $m_w$  is the number of full-pitch coils connected in series,  $\sigma$  is the electrical angle between adjacent full-pitch coils,  $\alpha_s$  is the shortened angle of the span angle of a coil compared with the pole pitch.

### 1) Slotted motor

In high-power multi-slot ( $> 6$ -slot) HSPM machines, the full-pitched overlapping winding is widely employed, Fig. 1. 14 (a), [BEN18] [BER16] [DON16c] [FOD14] [HON09] [HON18] [HUA16b] [HUY15] [JAN07] [MUN10] [ZHA15e] [ZHA17a]. Although the full-pitched overlapping winding has a long end-winding length and axial length, the output torque is usually large since the winding factor is ‘1’.

In [JAN11b], a 36s/6p 30kW 20 krpm high-speed interior permanent magnet machine employs a 5/6 short-pitched overlapping winding to reduce the space harmonic components of magnetomotive force (MMF) and minimize the rotor loss. However, the decreased winding factor (from 0.966 to 0.933) results in the reduction of the fundamental component and output torque. [HES82] [HON09] also employs 5/6 short-pitched windings for a 12s/2p HSPM motor to reduce the rotor loss, Fig. 1. 14 (b). In [XUE12], a 24s/2p HSPM motor with 4 slot-pitch windings, i.e. 4/12 short-pitched windings, is designed and analyzed. The 4/12 short-pitched windings can not only reduce the rotor loss but also decrease the end-winding length in axial direction, while the winding factor is only ‘0.48’.

For low-power minimal-slot HSPM machines, the full-pitched overlapping winding can only

be used in 6-slot motors. In general, the 6s/2p low-power small-size HSPM motor with full-pitched overlapping windings has long end-winding length and axial length, which leads to long motor axial length, low torque density, and low rotor mechanical natural frequency. In [ZHO07], the 3s/2p HSPM motor with concentrated non-overlapping windings and two 6s/2p HSPM motors with full-pitched overlapping and concentrated non-overlapping windings are compared for the rotor loss. With sine-wave currents and unmagnetized magnets, i.e. only considering stator MMF space harmonics, the 3s/2p motor has the largest rotor eddy current loss, and two 6s/2p motors have almost the same rotor loss. The influence of full-pitched overlapping and concentrated non-overlapping windings under on-load condition is not discussed, which will be investigated in this thesis.

For 6s/2p HSPM motors, 3 slot-pitch (full-pitched) windings [WAN03] [ZHO07] and 1 slot-pitch (concentrated) windings [OYA03] [SHI04] [NOG05] have been employed for high-speed applications, Figs. 1. 15 (a) and (c). However, 2 slot-pitch (short-pitched) winding is attractive for improving the power density since it has a good trade-off between winding factor and end-winding axial length, which will be the main research of this thesis, Fig. 1. 15 (b).

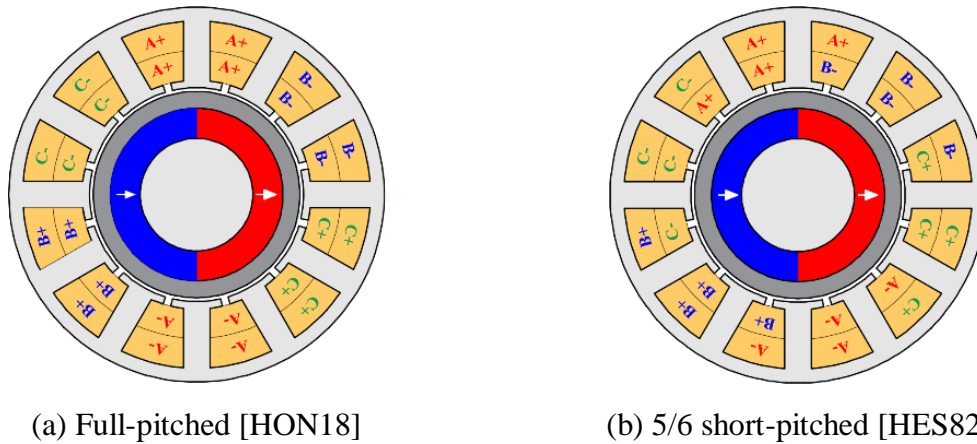
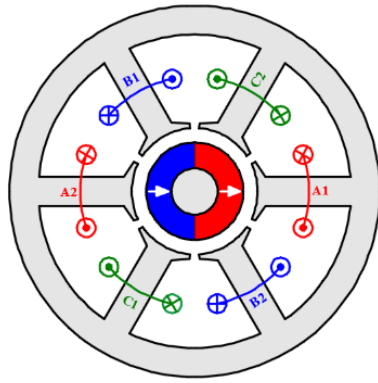
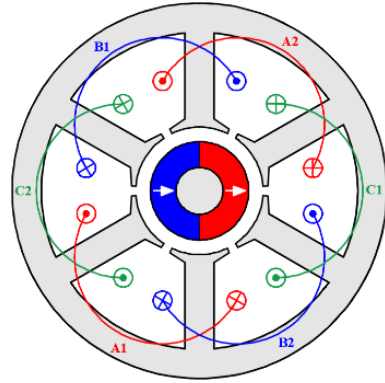


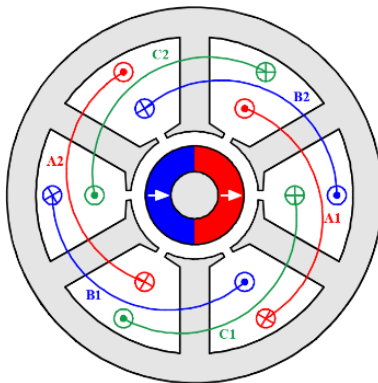
Fig. 1. 14. Full-pitched and short-pitched overlapping windings for 12s/2p HSPM machines.



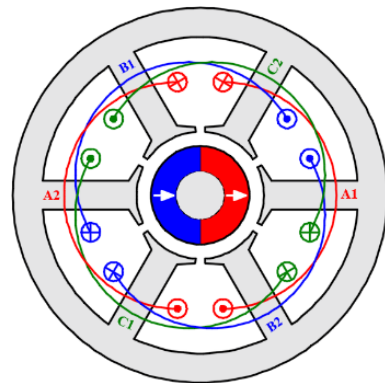
(a) 1 slot-pitch winding [NOG05]



(b) 2 slot-pitch winding, MA



(b) 2 slot-pitch winding, MB

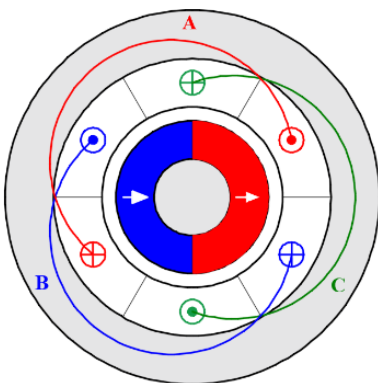


(c) 3 slot-pitch winding [WAN03]

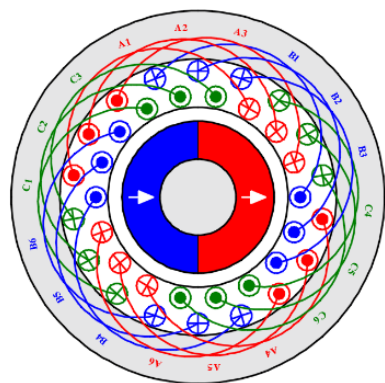
Fig. 1. 15. 6s/2p HSPM motors with 1, 2, and 3 slot-pitch windings.

## 2) Slotless motor

For slotless HSPM machines, the overlapping winding is widely employed since the large winding factor can compensate for the low flux linkage caused by large air-gap, Fig. 1.16 (a), [CHE99] [BIA04] [BIA05] [WAL09] [CHE09] [KOL13] [AHN17].



(a) Full-pitched [BIA04]



(b) Short-pitched [ZHE05]

Fig. 1. 16. 2-pole slotless HSPM motors with different winding configurations.

[CHE99] compares the overlapping and non-overlapping windings for slotless PM brushless motors. It shows that the conventional overlapping windings can offer large power density and are more suitable for medium and large motors where the power density is an important criteria. However, it also points out that the overlapping windings may be difficult to wind, and their relatively long end-winding may not be acceptable for high-speed applications. [WAL09] designs a 2-pole slotless HSPM motor for hand-tool applications. With full-pitched overlapping windings, the axial leakage is analyzed by a 2-D analytical model and a 3-D FE model. It shows that at the axial ends of the motor, the reduction of flux density is substantial, but that in back-EMF is minor due to the motor dimensions for hand-tool applications. In [LUO09], a 100W 500 krpm slotless HSPM machine adopts full-pitched overlapping windings, and its winding factor is calculated by

$$k_w = \frac{6}{\pi} \sin\left(\frac{\pi}{6}\right) \quad (1.4)$$

Compared with the slotted motor with full-pitched overlapping windings, i.e.  $k_w=1$ , the slotless motor with full-pitched overlapping windings has a relatively lower winding factor, i.e.  $k_w=0.955$ .

However, although the full-pitched overlapping winding has a large winding factor, the long end-winding length and axial length may decrease the torque density, increase the copper loss, and reduce the rotor mechanical natural frequency. Therefore, the short-pitched overlapping winding with a relatively large winding factor and relatively short end-winding axial length is attractive for improving torque density. In [ZHE05] and [ZHA07], a 2-pole slotless UHSPM motor with a rating of 2 kW @ 200 krpm is designed for cryogenic compressor applications. The motor employs 15/18 short-pitched overlapping windings to reduce the end-winding length and copper loss, Fig. 1. 16 (b).

## B. Non-overlapping winding

In this section, different non-overlapping winding configurations are discussed, including concentrated windings, toroidal windings, and skewed slotless windings.

### 1) Slotted motor

In high-power multi-slot (>6-slot) HSPM machines with 2-/4-pole rotors, the concentrated winding results in a low winding factor. Take 2-pole motors with 12-/18-/24-slot as examples.

The fundamental winding factors of three motors with full-pitched overlapping windings are 0.966, 0.960, and 0.958, respectively, while those of three motors with concentrated windings are 0.5, 0.5, and 0.5, respectively. Therefore, the concentrated non-overlapping winding is not desirable for high-power multi-slot HSPM machines.

Compared with full-pitched overlapping windings, toroidal windings with the same winding factor have shorter end-winding axial length, which improves the rotor stiffness and avoids rotor dynamic issues. More importantly, the airspace of outside slots can be used as cooling channels, which increases the motor cooling capability. Therefore, the toroidal winding replaces the overlapping winding in high-power multi-slot HSPM machines to reduce the end-winding axial length [DON14] [CHE11] [WAN09]. However, the outside conductors of toroidal windings cannot produce the back-EMF but can be a part of the end-winding length and consequently increase the copper loss. In addition, the flux leakage caused by outside conductors leads to eddy current loss in the motor frame [BOR14], which may account for about 50% of overall losses in a particular design and decreases the motor efficiency. Although the heat dissipation in the frame is not difficult, the eddy current loss in the frame caused by toroidal windings decreases the efficiency and should be paid attention in design.

In [WAN09] and [XIN10], the windage losses and anti-demagnetization of the 75 kW 60 krpm 24s/2p HSPM motor with toroidal windings are studied by 3D FE method, Fig. 1. 17. The predicted windage losses and rotor temperature are verified by the measured results. It also shows that the toroidal winding can reduce windage loss, which has a close relationship with the rotor axial length. For anti-demagnetization of PM, i.e. protecting the PM from overheating demagnetization, two strategies can be employed, one is the reduction of rotor losses, and the other one is the improvement of the cooling condition of rotor. In [XIN10], a 24-slot stator structure is employed to reduce the rotor eddy current loss and a low roughness height of rotor surface is used to decrease the air friction loss of rotor. In addition, the stator core with outer and inner cooling vents can improve the cooling condition of rotor and reduce the maximum temperature of PM. [CHE11] proposes a design method of HSPM machines considering electromagnetic performance, mechanical strength, rotor dynamic characteristics, and temperature distributions. Then, a 15 kW 30 krpm 24s/2p HSPM machine with toroidal windings is designed and prototyped. [DON14] designs a 24s/2p air-cooled HSPM motor with Gramme ring windings, i.e. toroidal windings. The electromagnetic performance is analyzed by the FEA model, and the thermal properties with air-cooling are analyzed by computational fluid dynamic (CFD) thermal model and LPTN model. By optimising the stator dimensions,

especially outer slot, the loss density is reduced, and cooling capability is improved [DON14a].

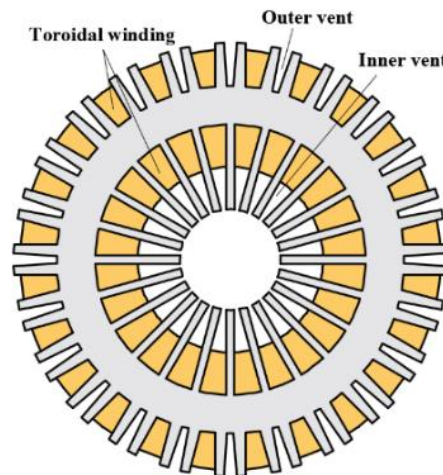
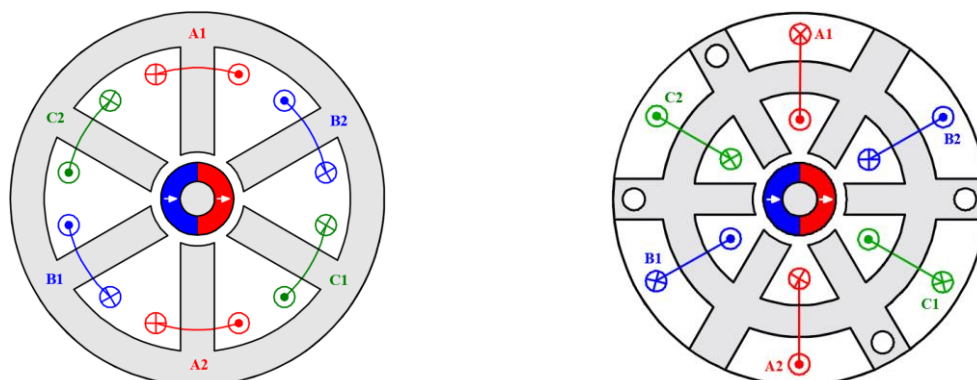


Fig. 1. 17. 24s/2p HSPM motor with toroidal windings.

Therefore, in multi-slot HSPM machines, toroidal windings are more suitable than concentrated non-overlapping windings. However, both toroidal windings [WAN03] [XU20] [FER20] and concentrated windings [NOG09] [GIL15] [GIL16] [HON13] [LIM17] [MAJ19b] [NIU12] [UZH16] [NOG07] [SHI04] [OYA03] [WAN10K] [ZHO06] are widely used in 6-slot HSPM machines, Fig. 1. 18. [UZH16] shows that although the fundamental winding factor of the concentrated winding is '0.5', doubling the number of turns may not lead to large copper loss compared with the long end-winding of the full-pitched overlapping winding. In addition, the short end-winding axial length of the concentrated non-overlapping winding leads to the short rotor axial length, which increases the first mechanical natural frequency and critical speed of the rotor.



(a) Concentrated winding [NOG05]

(b) Toroidal winding [XU20]

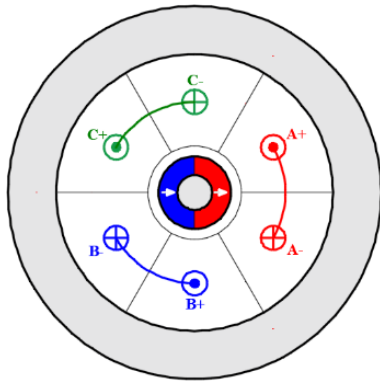
Fig. 1. 18. Different non-overlapping windings.

In 3s/2p HSPM motors, the concentrated winding is a conventional winding configuration [BIA05] [BIA04] [EDE01] [HES87] [HWA14] [KRA17] [ZHU01] [ZHU97], while the toroidal winding is rarely mentioned. [XU20] analyses the electromagnetic performance of 2-pole HSPM motors with toroidal windings and different slot numbers, including 3-slot, 6-slot, 9-slot, and 12-slot. It shows that compared with concentrated windings ( $k_w=0.866$ ), toroidal windings result in a smaller winding factor for 3s/2p motor ( $k_w=0.5$ ). In addition, the 3s/2p motor with toroidal windings cannot eliminate the 3<sup>rd</sup> harmonic in the flux linkage waveform caused by the associated 3<sup>rd</sup> air-gap field harmonic or local magnetic saturation. However, the corresponding 3<sup>rd</sup> harmonic will disappear in the line back-EMF waveform and has no influence on the torque. Therefore, in 3s/2p HSPM motors, the concentrated winding is a better solution than the toroidal winding with a smaller winding factor.

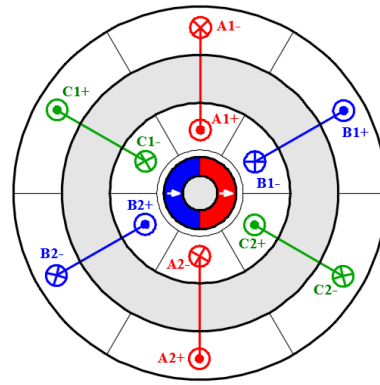
## 2) *Slotless motor*

In slotless motors, three non-overlapping winding configurations can be used [CHE98] [CHE99], such as concentrated windings [BUR19], toroidal windings [ZWY05] [BOR14], skewed slotless windings [MAX] [JUM16a] [JUM16b], Fig. 1. 19.

In [HES82], a multilayer basket winding, i.e. skewed slotless winding, and a ring winding, i.e. toroidal winding, are compared for a 50 W 150 krpm slotless HSPM motor. It shows that the skewed slotless winding has almost no end-windings and all conductors are in the air-gap and magnetic field caused by PMs, which means the winding axial length is almost the same as the stator active length. However, this kind of winding with a relatively complex structure requires specialist equipment and a special manufacturing process. In literature, there are three skewed slotless winding configurations, i.e. helical windings, rhombic windings, and diamond windings, Fig. 1. 20, [KEN85] [MAX] [JUM16b]. [LOO10] investigates the 3D torques and forces of two skewed slotless winding configurations, i.e. helical windings and rhombic windings, and their potential for high-speed applications is also analyzed. For skewed slotless windings, three-phase coils are overlapped radially, which increases the winding thickness in the air-gap, but almost no end-winding, which decreases the rotor axial length and increases the rotor mechanical natural frequency. However, since the coil is skewed by  $\pi$  elec. deg., the current direction is not ideal and may lead to extra undesired transverse torque and force.

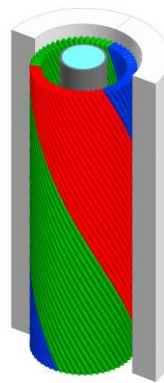


(a) Concentrated winding [CHE99]



(b) Toroidal winding [CHE98][ZWY05]

[BUR19]



(c) Skewed slotless winding [KEN85] [MAX]

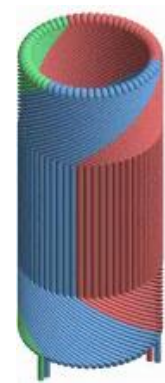
Fig. 1. 19. 2-pole slotless HSPM motors with different non-overlapping windings.



(a) Helical



(b) Rhombic



(c) Diamond

Fig. 1. 20. Three skewed slotless winding configurations [JUM14].

By 2D and 3D analytical and FE models, [JUM14] compares three slotless winding configurations in a 2-pole slotless HSPM machine, such as concentrated windings, toroidal



windings, and helical windings. The results show that with the same power and phase current, the motor with concentrated windings has the highest rotor loss due to the 3-coil rotational asymmetric winding distribution, and the motors with helical and toroidal windings have almost the same rotor loss. Although with higher rotor loss, the non-overlapping windings with 3 coils per 2 poles are employed in a 2-pole 400 krpm slotless HSPM motor due to their simplicity [BUR19]. [CHE98] and [CHE99] review the winding topologies for slotless PM machines and investigate the influence of winding topologies on the optimal design. It shows that the winding configurations slightly affect the optimal ratio of magnet thickness to winding thickness for minimum copper loss, since it only changes the coefficient in the calculation of copper loss. Several slotless motors with toroidal windings have been mentioned before and are widely employed in UHSPM motors due to the simple winding process, short end-winding axial length, modular design, and improved cooling capability, such as 150 W @ 1200 krpm in [ISM18], 100 W @ 500 krpm in [ZWY05], 150 W @ 200 krpm in [BOR14], 15 kW @ 150 krpm in [GIL16], and 160 krpm in [SCH17].

### C. Summary

In this section, the applications, advantages, and disadvantages of overlapping and non-overlapping are summarised in Table 1. 4.

As mentioned before, the overlapping winding includes full-pitched and short-pitched windings, while the non-overlapping winding includes concentrated, toroidal, and skewed slotless windings. They have their own suitable stator structures and applications, which depend on the design requirements and motor dimensions.

- 1) For high-power, multi-slot HSPM machines, overlapping winding and toroidal non-overlapping winding are employed. The main difference between the two winding configurations is the end-winding axial length.
- 2) For low-power minimal-slot HSPM machines, the concentrated non-overlapping winding is a dominant winding configuration due to short end-winding axial length. With the same advantage, the toroidal winding needs additional volume radially for the outside windings, which increases the end-winding copper loss but offers additional cooling channels.
- 3) For slotless HSPM machines, both overlapping and non-overlapping windings are employed. The full-pitched overlapping winding with the largest winding factor can offer the maximum output torque but has the longest end-winding axial length, while

the short-pitched overlapping winding with a relatively small winding factor not only decreases the rotor losses but also improves the rotor mechanical stiffness.

- 4) The toroidal non-overlapping winding with short end-winding axial length and the simple winding process is popular for slotless stator applications.
- 5) The skewed slotless winding, i.e. helical, rhombic, and diamond windings, with compact structure, self-support construction, and no end-winding, is an attractive solution for slotless HSPM motors. However, the non-idealized skewed current direction leads to undesirable torque and force. In addition, the skewed slotless winding needs a 3D model to analyse and requires a special manufacturing process.

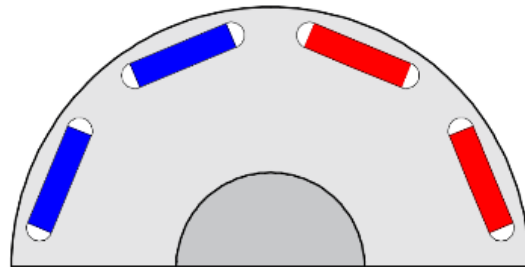
Table 1. 4

Applications, Advantages, and Disadvantages of Overlapping and Non-overlapping Windings

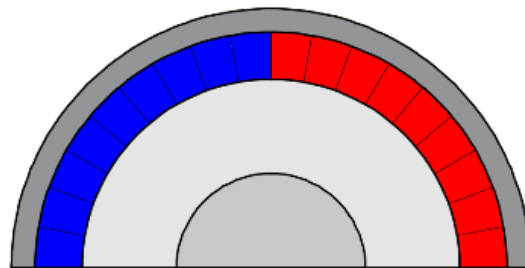
	Overlapping		Non-overlapping		
	Full-pitched	Short-pitched	Concentrated	Toroidal	Skewed
Applications	Multi-slot; Slotless	Multi-slot; Slotless	Multi-slot; Minimal-slot; Slotless	Multi-slot; Minimal-slot; Slotless	Slotless
Advantages	<ul style="list-style-type: none"> <li>• Large winding factor</li> <li>• Large torque</li> </ul>	<ul style="list-style-type: none"> <li>• High torque density</li> <li>• Relatively large winding factor</li> <li>• Reduced space harmonic and rotor losses.</li> <li>• Less copper loss</li> </ul>	<ul style="list-style-type: none"> <li>• Short end-winding length and axial length</li> <li>• Low copper loss</li> <li>• Modular design</li> </ul>	<ul style="list-style-type: none"> <li>• Short end-winding length and axial length</li> <li>• Improved cooling capability</li> <li>• Modular design</li> </ul>	<ul style="list-style-type: none"> <li>• Almost no end-winding</li> <li>• Self-support structure</li> </ul>
Disadvantages	<ul style="list-style-type: none"> <li>• Long end-winding length and axial length</li> <li>• Long rotor shaft axial length</li> <li>• Low rotor mechanical nature frequency</li> <li>• Large copper loss</li> </ul>	<ul style="list-style-type: none"> <li>• Similar to full-pitched windings</li> </ul>	<ul style="list-style-type: none"> <li>• Low winding factor</li> <li>• Low torque</li> <li>• Large rotor loss</li> </ul>	<ul style="list-style-type: none"> <li>• Low winding factor</li> <li>• Large copper loss</li> <li>• Frame loss due to external leakage of outer slot windings</li> </ul>	<ul style="list-style-type: none"> <li>• Complex structure</li> <li>• Undesired axial torque and force</li> </ul>

## 1.4. Rotor Structures

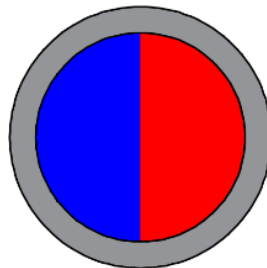
In general, HSPM machines mainly employ three various rotor structures, i.e. IPM, SPM, and solid PM, Fig. 1. 21. Those rotor designs affect the electromagnetic performance, thermal aspect, mechanical strength, and dynamic characteristic of HSPM machines.



(a) IPM [BIN06]



(b) SPM [BIN06]



(c) Solid PM [HES97]

Fig. 1. 21. High-speed PM machines with IPM, SPM, and solid PM rotor structures.

### 1.4.1 IPM

In conventional PM machines, IPM rotor structure can offer reluctance torque and reduction of PM amount. The limitation is the contradiction between the rotor flux leakage and the stress of IPM rotor iron bridges [BIN06] [DON16c].

Although the solid steel rotor may be used to withstand high centrifugal force due to high rotor

surface speed, the edges of magnets and rotor slots suffer high mechanical stress, which may destroy the PMs and rotor iron core [MIR08] [DON16c]. Therefore, the mechanical stress in high-speed IPM machines should be computed carefully. [HIP92] proposes an IPM rotor design for a 24s/4p HSPM machine, which consists of a solid steel rotor, four rectangular samarium-cobalt magnets, and four flux barriers to reduce the leakage flux. The optimized rotor structure can operate at 40 krpm considering mechanical constraints. [BIN06] compares two 40 kW, 40 krpm high-speed machines with SPM and IPM rotor constructions. Fig. 1. 21.

For IPM rotors, the magnets are inserted into the rotor slots without interference fit and no prestress between the rotor iron and magnets. Therefore, during high-speed operation, the outer iron bridge suffers not only its own centrifugal forces but also the force from the magnet. In addition, compared with SPM, the magnets are distributed unevenly in radial direction in the rotor, leading to local peak stress in the irons at the edges of rotor slots. Therefore, the critical speed of the IPM machine is limited by mechanical stress and is far less than that of the SPM machine if it has a carbon-fibre retaining sleeve. To reduce the PM volume and save the cost, [MIR08] analyses one SPM rotor and two IPM rotor constructions for high-speed applications. With the same speed (15 krpm) and torque (7.5 Nm), the IPM rotor with two-layer magnets has a larger reduction of PM volume and a higher safety factor for mechanical stress compared with the IPM rotor with one layer magnet.

In [DON16c], two 24s/4p HSPM motors with SPM and IPM rotor structures are compared with a rating of 140 kW @ 24 krpm and the same key dimensions, Fig. 1. 22. Both of them are not the conventional SPM and IPM rotors, the compared SPM rotor having four bread-shape magnets and four inter-pole fillets, which are bandaged by an alloy sleeve (Inconel 718) to withstand the centrifugal force, while the compared IPM rotor having a spoke-type IPM rotor with the C-shaped iron laminations and trapezoidal PMs. The results show that the SPM rotor structure has higher mechanical strength and efficiency, but the IPM rotor can offer a relatively low cost.

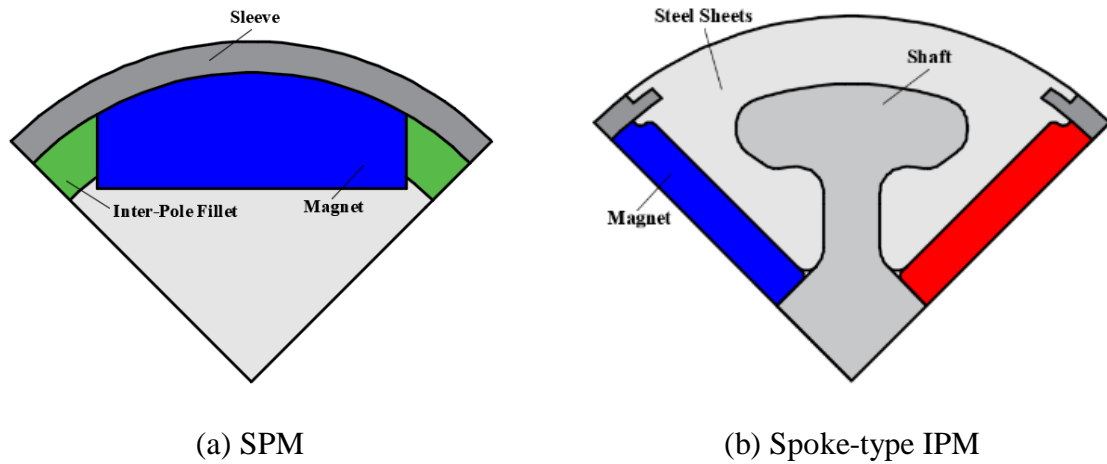
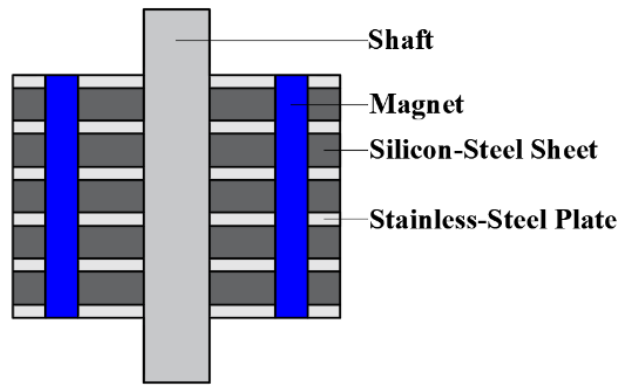


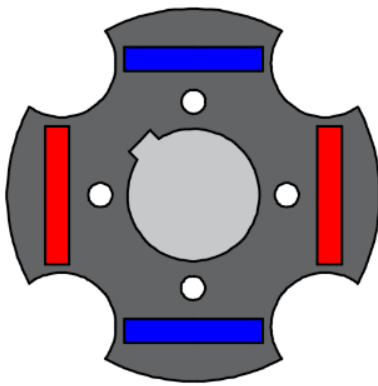
Fig. 1. 22. High-speed PM machines with SPM and spoke-type IPM rotor structures [DON16c].

In literature, several methods have been proposed in IPM rotor structures to improve the mechanical strength for high-speed applications. In [ZHA15d], a retaining shield rotor construction is proposed to improve the mechanical strength of high-speed IPM rotors. This novel rotor structure is a combination of silicon-steel sheet and stainless-steel plate, Fig. 1. 23. The former with a small flux iron bridge can reduce the flux leakage, and the latter with large tensile yield strength can withstand the centrifugal forces. The research focuses on the influence of the axial proportions of stainless-steel plates on the mechanical stress and electromagnetic performance, especially on the torque and rotor losses, and a trade-off should be satisfied.

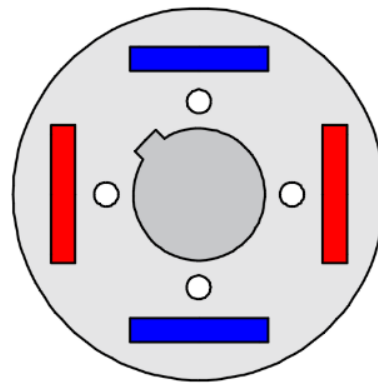
[ARU16] employs solid semi-magnetic stainless steel to improve the mechanical strength of the high-speed IPM rotor rather than the combination of silicon-steel and stainless-steel in [ZHA15d]. Without rotor lamination, the large rotor loss is a challenge for solid rotor design, and thus the axially segmented and circumferentially slitted solid rotors for reducing the rotor losses are proposed, optimized, and compared in [ARU16]. The results show that with the same condition, the circumferentially slitted rotor structure has significantly smaller eddy current loss than the axially segmented solid rotor. In addition, for a 2-pole rotor, [HON97] employs the 6 iron ribs between magnets to reduce the rotor maximum stress and protect the rotor core and magnets, Fig. 1. 24. Meanwhile, the radial, Halbach, and parallel magnetized rotors are compared in a 36s/2p high-speed IPM machine. The results show that the Halbach magnet array can not only produce the sinusoidal air-gap flux density waveform but also reduce the torque ripple and roughly remain the output torque.



(a) Retaining shield rotor construction



(b) Silicon-steel



(c) Stainless-steel

Fig. 1. 23. A retaining shield rotor construction for high-speed IPM machines [ZHA15d].

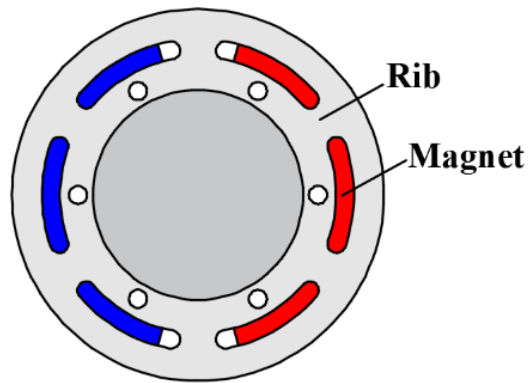


Fig. 1. 24. 2-pole rotor structure with 6 iron ribs between magnets [HON97].

### 1.4.2 SPM

As mentioned before, compared with IPM rotor constructions, the SPM rotor constructions with retaining sleeves have better mechanical strength and higher critical speed. In general, the SPM rotor design for high-speed applications mainly focuses on the trade-offs of electromagnetic performance and mechanical, thermal, and dynamic constrains.

#### A. Sleeve design

For high-speed applications, the sleeve is the most important part and has a close relationship with motor performance. Firstly, although the increased sleeve thickness improves mechanical strength, the increased effective air-gap length leads to the decrease of  $B_g$  and output torque due to non-magnetic material sleeve. Secondly, non-conductivity material sleeves with high mechanical strength have higher critical speed. However, their low thermal conductivity may lead to high maximum temperature concentration in the rotor and thus increase the demagnetization risk. Therefore, the sleeve thickness and sleeve material are widely researched in the rotor design for HSPM machines.

[LIW14] compares 36s/2p HSPM machines with different sleeve materials for a 117 kW 60 krpm micro gas turbine application, such as stainless steel, carbon fibre, copper iron alloy, and copper. The comparison focuses on the electromagnetic performance and temperature distribution. The results show that the copper iron alloy sleeve increases the flux leakage, and three non-magnetic sleeves have the same flux linkage. More importantly, although the rotor with a carbon-fibre sleeve has the smallest rotor losses, the rotor with a copper sleeve has the lowest maximum temperature due to high thermal conductivity and relatively small eddy current losses. In [BIN06], the carbon fibre and glass fibre sleeves for SPM high-speed motors are compared. It shows that the glass fibre sleeve cannot withstand the centrifugal force when the rotor surface speed is larger than 150m/s, and the carbon fibre sleeve can allow higher critical speed. With different materials of magnets and sleeves, the rotor mechanical stress is computed by the analytical model and verified by the FEM model in [DAM16]. The results show that the combination of Titanium sleeve and NdFeB magnet has high mechanical strength.

Apart from the sleeve material, the sleeve shape can also be designed to reduce the rotor loss. [SHE13] proposes a new sleeve design, i.e. grooving retaining sleeve, Fig. 1. 25. The circumferential, axial, and comprehensive grooves are compared, and the results show that the Titanium sleeve with circumferential grooving has the lowest eddy current losses and the



smallest maximum stress in the sleeve. In [JUN15], a new sleeve design is employed for sleeve loss reduction by decreasing the sleeve volume and splitting the eddy current loop, Fig. 1. 26. However, the mechanical stress is significantly reduced and should be checked carefully.

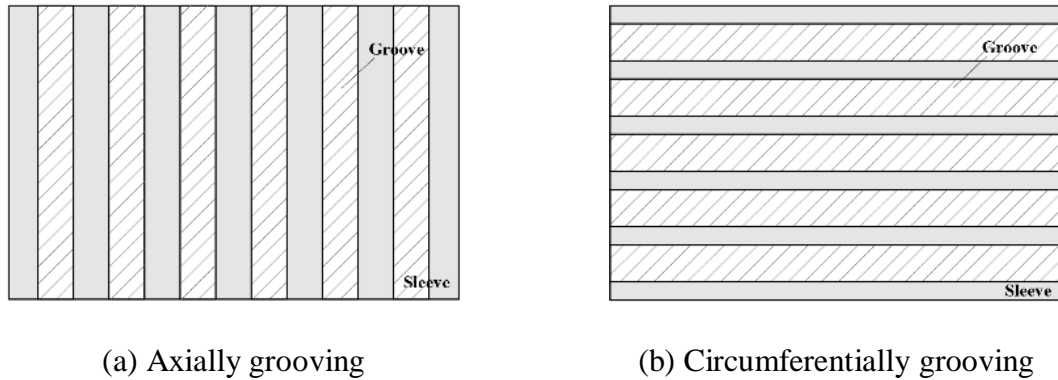


Fig. 1. 25. Sleeve design with axial and circumferential groovings [SHE13].

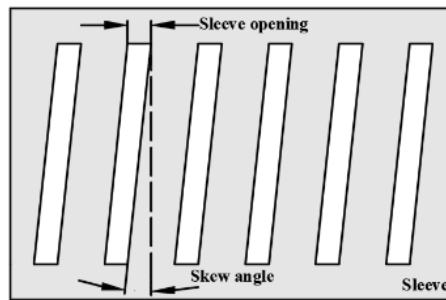


Fig. 1. 26. A new sleeve design for reducing eddy current loss [JUN15].

In [ZHO06], a copper shield between the retaining sleeve and magnets is employed to reduce the total rotor eddy currents due to the shielding effect, which is proposed by [VEE97]. The results show that with the increase of shield thickness, the total rotor loss decreases due to stronger shielding effect. In addition, according to the thermal analysis, with a copper shield, the maximum rotor temperature is reduced from 240 °C to 70 °C. However, the  $B_g$  is reduced due to the increased effective air-gap. With the increase of the copper shield thickness, the sleeve loss decreases firstly and then remains almost the same since the thickness is beyond the skin depth of the copper shield [SHA09]. In addition, with and without copper shield, the effect of sleeve axial segmentation on sleeve losses is investigated. The results show that the sleeve without segment and with a copper shield is the most effective solution to reduce sleeve losses. [FAN17] employs a radial multilayer sleeve to decrease the rotor losses and PM temperature under the same output performance and mechanical strength. [ZHA15a] proposes a hybrid protective measure consists of Titanium alloy and carbon fibre. The Titanium alloy

shield can not only improve the mechanical strength but also reduce the losses of the carbon fibre sleeve and magnets. Although large losses exist in the Titanium alloy shield, the maximum temperature of the sleeve with Titanium alloy is almost the same as that of the sleeve without Titanium alloy due to the high thermal conductivity of the Titanium alloy shield.

#### B. Pole arc to pole pitch

[ZHA16a] investigates the influence of the ratio of pole arc to pole pitch, i.e. pole arc coefficient ( $\alpha_p$ ), on electromagnetic performance. With the increase of pole arc coefficient, the PM loss, cogging torque, and no-load current increase [ZHA17a]. The increased pole arc coefficient results in the increased magnetic flux and the decreased stator active length for the same back-EMF. Therefore, a trade-off should be satisfied based on the requirements.

When the pole arc coefficient is less than '1', the inter-pole air-gap exists, Fig. 1. 27 (a), which may lead to large local stress in the sleeve due to the uneven distribution of magnets [BEN18]. Therefore, [ZHA15a] compares different materials of inter-pole filler to reduce the sleeve stress and improve the rotor stiffness, Fig. 1. 27 (b), such as plastics, carbon fibre, and Titanium alloy. In [BEN18], the materials of inter-pole filler are PMs, i.e.  $\alpha_p=1$ , air, glass fibre, and iron. The results show that the Titanium alloy and iron inter-pole fillers have the lowest sleeve stress. However, the high electrical conductivities of Titanium alloy and iron inter-pole fillers result in high rotor eddy current losses. Therefore, [ZHA15a] [ZHA16a] employs non-magnetic non-conductive plastics inter-pole filler and [BEN18] [BIN06] [LIW14] [WAN21] adopt SPM without pole gap, i.e.  $\alpha_p=1$ , for their different design requirements. In addition, the iron inter-pole filler, i.e. the inter-PM rotor, is employed by [DON16c] and [JAS17]. It is worth noting that without pole gap, [WAN21] analyses the rotor stress for a HSPM motor with segmented magnets retained by a carbon-fibre sleeve. It shows that magnet edging effect caused by segmentation leads to sleeve stress concentration but reduces the magnet tangential stress, and thus the number of PM segments should be optimized to avoid stress concentration.

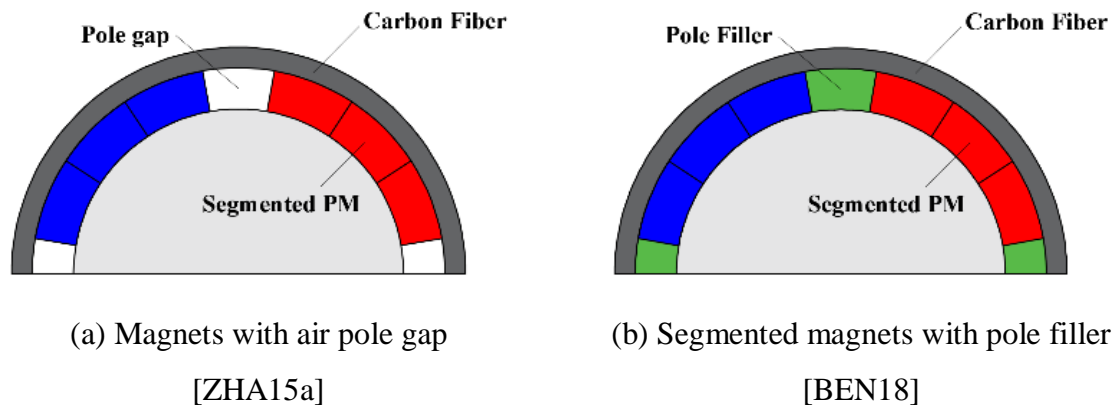


Fig. 1. 27. Two SPM rotor structures with different pole gap materials.

### 1.4.3 Solid PM

There are two solid PM rotor structures, i.e. solid PM with sleeve and solid PM with hollow shaft. The mechanical stress is the design consideration of solid PM rotor structure.

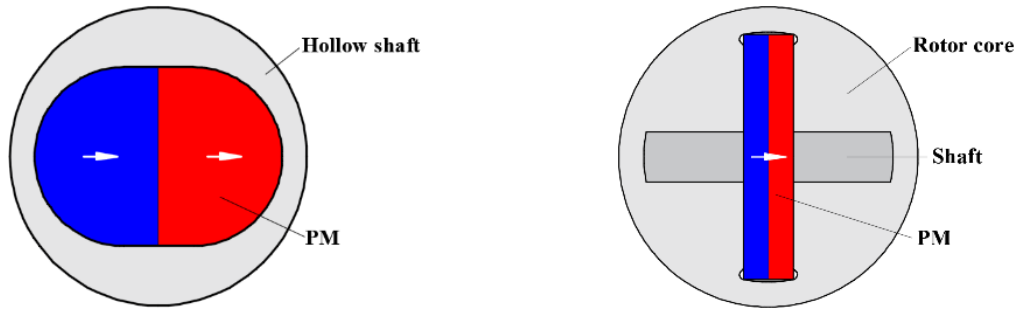
#### A. Solid PM with sleeve

The solid PM with sleeve is widely employed in the HSPM motors with small size rotor [HES87] [ZWY05] [CHE11] [AHN18]. In [WAN03], the 2-pole solid PM is used and magnetized in whole, leading to the symmetry of mechanical strength and electromagnetic performance. In addition, the solid PM is segmented axially to reduce the rotor loss and simplify the assembly process of magnets. Meanwhile, the high rotor mechanical strength and electromagnetic performance are remained [CHE11]. [AHN18] compares different materials of magnets and sleeves for a 500 W 400 krpm 2-pole slotless HSPM motor with a solid PM rotor. The magnet materials are NdFeB and Sm<sub>2</sub>Co<sub>17</sub>, and the sleeve materials include Titanium alloy, SUS304, Inconel718, and carbon fiber. The results show that the combination of Inconel718 sleeve and NdFeB (N42SH) magnet has high mechanical strength and the largest rotor dynamic safety factor. In addition, the SUS304 sleeve is the worst since it cannot meet the mechanical stress requirement.

#### B. Solid PM with hollow shaft

In [ZHE05], a 2 kW 200 krpm slotless HSPM motor is designed for a centrifugal compressor drive application. This design employs a solid PM rotor structure, and the magnets are located inside a hollow shaft (Titanium), Fig. 1. 28 (a). This rotor structure can improve the rotor stiffness and significantly increase the first critical speed. [HUY15] modifies the equation of natural frequency calculation considering the solid PM with hollow shaft, and the analytical

prediction shows that the first natural frequency is well above the rated operation frequency. [LIU18b] proposes a novel solid PM rotor design with a hollow shaft, which consists of an amorphous rotor core, solid PM, and a hollow shaft, Fig. 1. 28 (b). It should be noticed that epoxy is employed in the gaps between PMs and rotor core to improve the rotor mechanical strength. The advantage of the novel rotor structure is that since the PM is inserted into the rotor core, the manufacture and assembly are simple. However, this rotor structure will lead to large shaft loss, which may increase the rotor temperature and demagnetization risk.



(a) Conventional hollow shaft [ZHE05]

(b) Novel hollow shaft [LIU18b]

Fig. 1. 28. Solid PM with hollow shaft rotor structure.

#### 1.4.4 Summary

In this section, the applications, advantages, and disadvantages of IPM, SPM, and solid PM rotor structures are summarised in Table 1. 5. The selection of rotor structure depends on the constraints of mechanical stress and motor size. In general, the solid PM rotor structure has the highest mechanical strength, and the IPM rotor structure has the lowest mechanical strength, while the cost is the lowest. The SPM with sleeve rotor structure has a better trade-off between electromagnetic performance and mechanical stress, which is widely employed in HSPM machines and is also selected in this thesis.

Table 1. 5

Applications, Advantages, and Disadvantages of Different Rotor Structures

	IPM	SPM	Solid PM
Application	<ul style="list-style-type: none"> <li>• Large torque requirement</li> <li>• Low cost requirement</li> </ul>	<ul style="list-style-type: none"> <li>• All HSPM machines</li> </ul>	<ul style="list-style-type: none"> <li>• Ultra-high-speed PM machines</li> <li>• Small size rotor</li> </ul>
Advantages	<ul style="list-style-type: none"> <li>• Large output torque</li> <li>• Low cost</li> </ul>	<ul style="list-style-type: none"> <li>• High mechanical strength</li> <li>• High critical speed</li> <li>• Low rotor loss</li> </ul>	<ul style="list-style-type: none"> <li>• High mechanical strength</li> <li>• Ultra-high critical speed</li> <li>• Simple structure for small size rotor</li> </ul>
Disadvantages	<ul style="list-style-type: none"> <li>• Low mechanical strength</li> <li>• Low critical speed</li> <li>• Large rotor loss with solid rotor</li> </ul>	<ul style="list-style-type: none"> <li>• Low thermal conductive sleeves lead to high temperature</li> <li>• Demagnetization risk</li> </ul>	<ul style="list-style-type: none"> <li>• High cost</li> <li>• Large effective air-gap</li> </ul>

### 1.5. Parasitic Effect

The high-speed operation results in an increased number of parasitic effects which do not exist or are not important in the low-speed and moderate-speed operation, such as stator iron loss, AC copper loss, rotor loss, windage loss, rotor dynamic characteristic, rotor vibration, and thermal aspect.

#### 1.5.1 Stator Iron Loss

Compared with low-/moderate-speed conventional machines, the stator iron loss becomes the dominant loss in HSPM machines. Therefore, the calculation of stator iron loss should be included in the analysis and design of high-speed machines. In general, the Bertotti model [BER88] is employed in the analytical computation of stator iron loss. There are three losses

included in the classic Bertotti model, namely, hysteresis loss ( $P_h$ ), eddy current loss ( $P_e$ ), and anomalous loss ( $P_a$ ), as shown by

$$P_{fe} = P_h + P_e + P_a = k_h f B_m^2 + k_e f^2 B_m^2 + k_a f^{1.5} B_m^{1.5} \quad (1.5)$$

In this thesis, the lamination material is JFE\_Steel\_20JNEH1200, whose hysteresis ( $k_h$ ), eddy current ( $k_e$ ), and anomalous loss ( $k_a$ ) coefficients are 173.296, 0.086, and 2.068 W/m<sup>3</sup>, respectively.

[ATA92] develops a method to predict the iron loss in a PM BLDC motor under on-load condition. It indicates that the on-load iron losses is markedly higher than open-circuit iron losses. In addition, [ATA93] calculates the rotational stator iron loss caused by the angle of lag between magnetic field strength (H) and flux density (B), i.e. non-circular flux density loci. In [ZHA17b], the magnetic flux variation at each point of the iron core is obtained, and meanwhile, the fundamental and harmonics of flux density are analyzed by Fourier analysis. Moreover, the additional iron loss due to rotational magnetic flux in the iron core is considered. The results show that for HSPM machines, the stator iron loss is affected not only by the alternating flux effect but also by the rotational flux effect. In [DON14a], the skin effect is considered when the frequency is above 2 kHz, and the accuracy of analytically predicted results is improved. In [BER16], the additional losses due to magnetic anomalies, manufacturing processes, and rotational fields are considered.

### 1.5.2 AC Copper Loss

The copper losses in HSPM machines include two basic components, DC and AC copper losses. The DC copper loss component has a close relationship with output torque, and its thermal dependence is well understood. The AC copper loss caused by the skin effect and proximity effect should be analyzed due to the high frequency current and large slot leakage flux in HSPM machines [MEL06].

Skin effect is a tendency for alternating current to flow mostly near the outer surface of the conductor. The effect becomes more and more apparent with the increase of frequency, and thus it should be considered in HSPM machines. Proximity effect is a tendency for alternating current to flow in a smaller region due to the magnetic field caused by nearby conductors. In general, the skin effect can be eliminated when the conductor diameter is smaller than the skin depth under the rated frequency. [UZH14] divides each winding turn into several parallel wires to reduce the diameter of each conductor and avoid the skin effect. The proximity effect can be

reduced by using Litz wire [TAN03], which is constructed using hundreds of small-diameter strands divided into many bundles. The strands in each bundle are twisted. [GIL17] measures the no-load power losses of the slotless HSPM machines with and without Litz wires. The results show that under the rated speed (75 krpm), the power loss with Litz wires is lower than 100 W, but the power loss without Litz wires is higher than 400 W. However, the Litz wire also has its own drawback, such as high cost and inferior thermal performance.

In addition, the proximity effect can also be affected by the conductor dispositions. It is found that the proximity effect can be significantly reduced when the conductors are located at the bottom of slots since the additional losses are concentrated at the conductors at the top of the slot due to the influence of the magnetic field caused by the PM [MEL06] [POP13]. However, it is worth noting that for high-speed slotless machines, the magnetic field generated by the PM is much larger than the field caused by the nearby conductor, and thus the proximity effect can be neglected [ZWY05].

### 1.5.3 Rotor Eddy Current Loss

In HSPM machines, although rotor eddy current losses are relatively small, the poor cooling capability may result in overheating in the rotor and demagnetization of magnets. Therefore, rotor losses should be considered and reduced. In general, two factors lead to rotor losses, i.e. one is the space harmonics due to the armature MMF and slot opening, and the other one is the time harmonics of armature current caused by pulse width modulation (PWM). However, in HSPM machines, the large air gap reduces the effect of space harmonics, and the time harmonics play the dominant role in generating the rotor losses [ZHU04] [ZHO06].

As mentioned before, compared with 6s/2p HSPM motors, the 3s/2p HSPM motor has the largest rotor loss due to the space harmonics from the armature MMF, which significantly increases with the increases of speed. In [JUM14], the 2-pole slotless HSPM motors with toroidal, helical, and concentrated windings under square-/sine-waves current waveforms by PWM inverters are compared. The results show that machines fed by square-wave PWM voltage have higher rotor losses than the ones fed by sine-wave PWM voltage due to the larger time harmonics of armature current. In addition, slotless machines with concentrated windings have the largest rotor losses due to the space harmonics from the armature current.

In [JAN04], the 24s/4p HSPM motors with Halbach and parallel magnetized rotors are compared in terms of rotor losses. According to the time and space harmonics analysis, the

motor with a Halbach magnetized rotor has smaller rotor losses than the motor with a parallel magnetized rotor. However, the segmentation of the Halbach magnetized rotor is not mentioned in this paper, which may have a significant effect on the reduction of rotor losses. In [MAJ17], for a 3s/2p PM motor with the constant output torque, the increased magnet thickness decreases the rotor loss due to the reduced phase current and armature reaction. It has been proved that the auxiliary slots can decrease the rotor loss in the 3s/2p PM motors [MAJ19a], which has been mentioned in section 1.3.

Except for reducing the space and time harmonics, splitting the eddy current loop is a direct solution to minimize the magnet and sleeve losses. Although [POL00] believes that segmenting the magnets is better for low speeds and [SHE13] [MAJ19b] consider that PM segmentation will complicate the manufacturing process and is difficult for small size rotors, several large size HSPM motors still employ the rotor magnet segmentation to avoid high rotor loss [GER14] [HUA16]. [ZHA15a] divides the PM into three segments per pole in the circumferential direction, and the axial segmentation of magnets is adopted in [ZHA18b].

#### 1.5.4 Windage Loss

The windage loss results from the aerodynamic loss when the rotor rotates, and it becomes significant with the increase of speed. In general, the rotor will be modelled as a cylinder in the windage loss calculation [MAC67], which is given by

$$P_{windage} = C_f \pi \rho_{air} \omega^3 R_r^4 l_a \quad (1.6)$$

where  $\rho_{air}$  is the air gap density,  $\omega$  is the angular speed,  $R_r$  and  $l_a$  are the rotor radius and length, respectively.  $C_f$  is the friction coefficient and is determined by the air gap structure and rotor surface condition. Compared with the analytical method, fluid field analysis is a more accurate method to calculate the windage loss since the friction coefficient is difficult to determine by theoretical analysis.

[WAN09] studies the windage loss of a 24s/2p HSPM machine with a rated speed of 60 krpm by the 3D FEM of fluid field and experimental study. It shows that the windage loss takes a large part in the total losses and is larger than the core loss at the rated speed. [ZHA17b] and [HUA16] show that the windage losses increase with the increase of rotor speed, rotor roughness height, and ventilation speed (axial cooling air velocity). Therefore, it is advantageous to use a sleeve material with a smooth surface and employ a suitable ventilation speed to balance windage losses and cooling conditions.



### 1.5.5 Rotor Dynamic and Vibration

During high-speed operation, the rotor has a great amount of rotational energy and a small amount of vibration energy. The purpose of rotor dynamics is to make sure the vibration energy is as small as possible. For high-speed machines, it is very important to accurately predict the natural frequency of the rotor to avoid the rated operation frequency close to the natural frequency.

In [EDE02], FE analysis is used to establish the natural frequencies and dynamic models of the rotor. The results show that the shaft extension has a significant influence on the natural frequency, and in order to move rotor bending modes beyond the operating speed range, the shaft should be short and have a large diameter, i.e. small L/D ratio [HON18]. However, in [ZWY05], the length of the shaft is adjusted such that the rated speed (500 krpm, 8.333 kHz) falls between the second and the third bending modes. [FAN12] investigates the influence of rotor static eccentricity on the rotor vibration by UMF and eccentric mass force. The results show that the eccentric mass force leads to fundamental frequency vibration, which is the main source of rotor vibration. In addition, the static/dynamic rotor eccentricities have a significant influence on the back-EMF, cogging torque, and UMF [ZHU13] [ZHU13b] [ZHU14], which will be researched in this thesis.

### 1.5.6 Thermal Aspect

In high-speed machines, thermal analysis is necessary due to large motor loss and low cooling capability of the rotor. The computational fluid dynamics (CFD) method is adopted to calculate the temperature rise distributions, in which the coolant flow rate, the velocity, and the surface heat transfer coefficient should be determined simultaneously.

[DON14a] optimizes the stator structure by the CFD method, and the results show that most axial coolant flows through the inner and outer slots while few enter the air gap. The highest winding temperature is found near the outlet, which is approximately 96.0 °C. The hottest spot occurs in the middle of the rotor, which is 125.5 °C. Since the complex modelling and meshing procedure requires certain skills and is quite time-consuming, a time-saving lumped-parameter thermal network (LPTN) linked with the CFD modelling is employed in [DON14]. In this hybrid method, the fluid and temperature fields are firstly evaluated by the CFD modelling, and then the LPTN model is created.

## 1.6. Scope and Contributions

In this thesis, 2-pole UHSPM (180 krpm) motors with different winding configurations for vacuum cleaner applications are optimally designed and analyzed in terms of electromagnetic performance and mechanical strength. In addition, the influence of rotor eccentricity on the electromagnetic performance is investigated considering the unbalanced phase back-EMF waveforms and circulating current.

This chapter reviews the advantages and disadvantages of various machine types for high-speed applications. For three-phase HSPM machines, the applications and characteristics of different stator structures, winding configurations, and rotor constructions have been summarized. In addition, the parasitic effects caused by the high-speed operation have been discussed. For vacuum cleaner applications, the design requirements include ultra-high-speed, high power density, low noise, small size, and lightweight. Therefore, the 6s/2p number combination is selected due to no UMF, low vibration, and less rotor loss. Further, 2 slot-pitch winding configuration is an attractive solution for 6s/2p HSPM motors. The research scope and outline are shown in Fig. 1. 29, and the outline of this thesis will be presented as follow.

**Chapter 2:** 6s/2p HSPM motors with different winding configurations, i.e. 1, 2, and 3 slot-pitches, respectively, are comparatively studied. The advantages of short stator active length of 2 slot-pitch windings are highlighted.

**Chapter 3:** 6s/2p HSPM motors with two alternate layouts of 2 slot-pitch winding configurations are proposed for vacuum cleaner applications. Firstly, two motors have been optimized considering thermal limit and allowed maximum current density. Secondly, the electromagnetic performances of the two motors have been analyzed. Thirdly, a 3s/2p HSPM motor and the proposed 6s/2p HSPM motor are compared since they have the same winding factor.

**Chapter 4:** The influence of rotor eccentricity on the electromagnetic performances of the 2-pole HSPM motors is investigated. Firstly, the back-EMFs, the cogging torques, the output torques, and the UMFs of the 3s/2p motors with static/dynamic rotor eccentricities are analyzed. Secondly, the 6s/2p motors with static/dynamic rotor eccentricities are analyzed and compared with the 3s/2p motors.

**Chapter 5:** The electromagnetic performances of 6s/2p HSPM motors with circulating currents in parallel-connected windings due to rotor eccentricity are analyzed. Firstly, the principle of circulating current production is presented and the effect of rotor eccentricity ratio is considered.

Secondly, the effect of the no-load and on-load circulating currents in the parallel-connected windings at steady-state operation with rotor eccentricity is investigated. Thirdly, the circulating currents with DC components at the beginning of rotor eccentricity is further analyzed.

**Chapter 6:** General conclusions the future work are described.

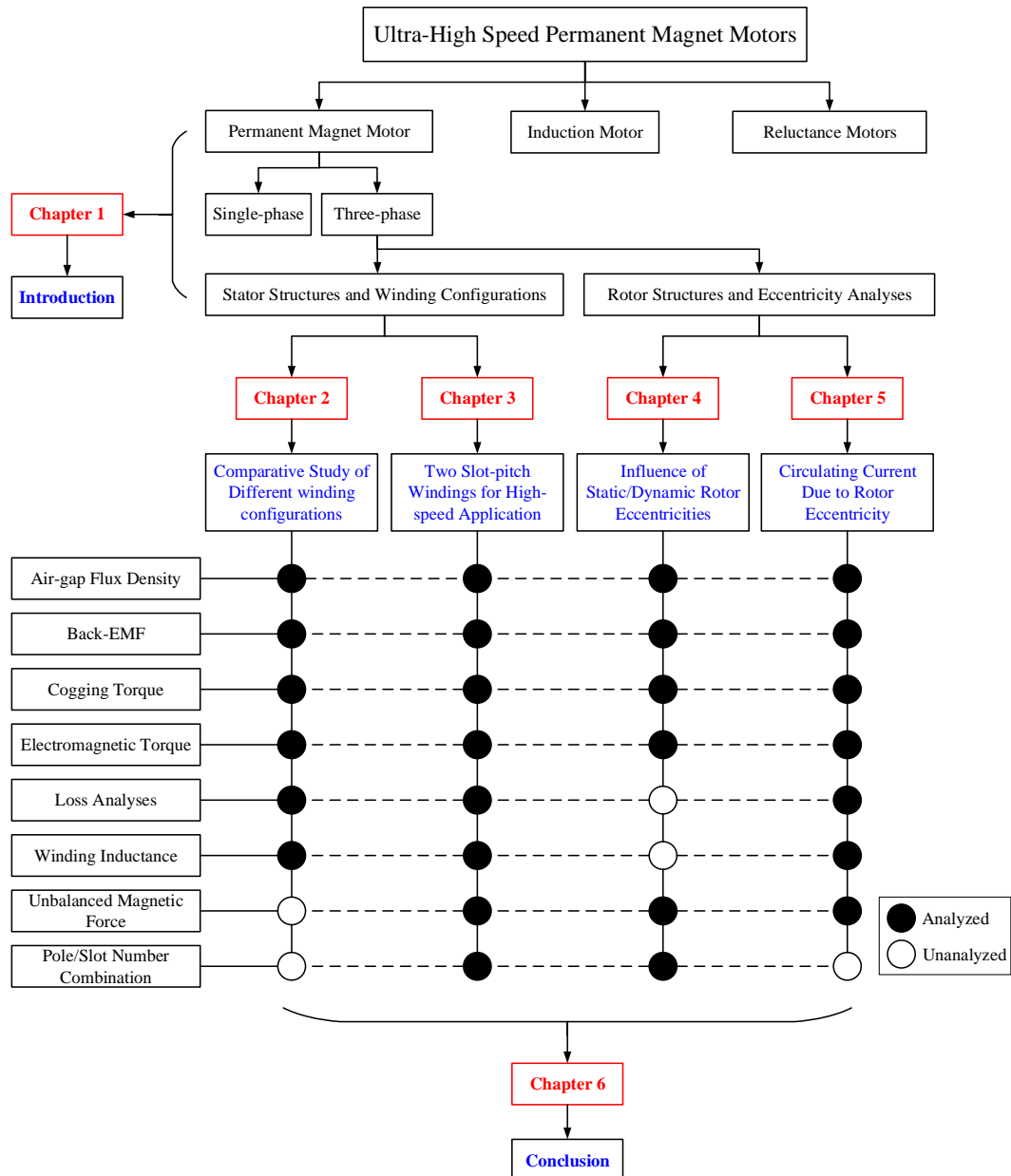


Fig. 1. 29. Research scope and outline.

The major contributions of the thesis include:

1. 2 slot-pitch windings are proposed for high-speed applications in 6s/2p PM motors. Then, two 2 slot-pitch winding configurations with different end-winding structures have been

analyzed. Finally, with the same winding factor, the 3s/2p and 6s/2p HSPM motors are compared, and the advantages of the 2 slot-pitch windings are highlighted.

2. Comparative study of the electromagnetic performances of 6s/2p HSPM motors with 1, 2, and 3 slot-pitch winding configurations, with particular emphasis on the 2 slot-pitch winding having the relatively large winding factor and relatively short end-winding axial length. In addition, the advantages of short stator active length of 2 slot-pitch windings are highlighted.
3. The influence of static/dynamic rotor eccentricities on the amplitudes and phase angles of back-EMF waveforms in the 3s/2p HSPM motor are investigated for the first time. Further, the dynamic rotor eccentricity results in the asymmetric positive and negative half-periods of phase back-EMF waveforms in the 3s/2p HSPM motor. In addition, the influence of the rotor initial position in the dynamic rotor eccentricity is investigated.
4. The electromagnetic performances of the 6s/2p HSPM motor with steady-state circulating currents in parallel-connected windings due to rotor static and dynamic eccentricities are analyzed under no-load and on-load conditions. In addition, the circulating currents with transient direct current (DC) components at the beginning of rotor eccentricity when it occurs are discussed.

## CHAPTER 2

### COMPARATIVE STUDY OF 6-SLOT/2-POLE HIGH-SPEED PERMANENT MAGNET MOTORS WITH DIFFERENT WINDING CONFIGURATIONS

PM motors with 6s/2p number combination and non-overlapping windings have been employed in high-speed applications due to no UMF and short end-winding. However, different winding configurations can be used in 6s/2p PM motors, with different winding factors and output torques. In this chapter, three 6s/2p HSPM motors with 1, 2, and 3 slot-pitch windings are optimized by the analytical method and finite element (FE) method under different conditions, such as a fixed current density, a fixed stator copper loss, and a fixed total stator loss (iron core loss and copper loss). The electromagnetic performances of the optimized designs are analyzed and compared, including air-gap flux density, back electromagnetic force, electromagnetic torque, winding inductances, and various loss components. For high-speed application, compared with 1 and 3 slot-pitch windings, the proposed 2 slot-pitch windings have a good trade-off between winding factor and end-winding axial length which are attractive for improved torque density. Finally, some of predictions by FEM are validated by experimental results.

This chapter was published in IEEE Transactions on Industry Applications

#### 2.1 Introduction

High-speed (HS) motors have been developed for a few decades and used extensively, e.g. centrifuge, air compressor, flywheel, turbo generator, high-speed spindle, vacuum cleaner, and aircraft [SHE18] [BEN18] [GER14] [BEN99]. For household appliances, low power, small size, and lightweight HSPM motors are preferred. In literature, the stator/rotor topologies of these HSPM motors mainly contain 3s/2p, 6s/2p, and 2-pole slotless types. The 3s/2p brushless HSPM motors are designed and analyzed for hand-tool application and a friction welding unit in [HES87] and [ZHU97], respectively. However, the 3s/2p combination exhibits UMF, leading to large vibration and noise. To reduce undesirable UMF, auxiliary slots are introduced to the 3s/2p PM motor in [PAN14] and [MAJ18]. However, the performance is significantly influenced by the load condition. [BIA05] compares 3s/2p motors with slotted and slotless stators. The disadvantages of slotless motors include low torque density and complex winding. Apart from the 3s/2p motor, the 6s/2p motor can also be used for small size and ultra-high-speed motors with tooth-coil windings [SHI04]. In [NOG05], 3s/2p and 6s/2p motors with

tooth-coil windings are compared to illustrate the advantages of the 6-slot stator structure with same overall size. Based on the 6s/2p HSPM motor, there are various research topics, including magnet assembly [WAN10], rotor retaining sleeve design [ZHO06], rotor eddy current loss reduction [NIU12], multidisciplinary design process [UZH16], reduction of noise and vibration [GIL17], etc. However, the influence of winding configurations on high-speed applications of 6s/2p PM motors has not been systematically investigated in literature. In [HE20], a 6s/2p HSPM motor with 2 slot-pitch windings is introduced and compared with different winding configurations. As an extension to [HE20], the 6s/2p HSPM motors are optimized by taking the iron loss into consideration and fixing the stator copper and iron losses. By using 3-D finite element (FE) modeling, the winding inductances of different winding configurations are analyzed accounting for end-windings. Finally, three prototype motors are manufactured and tested to verify some of the FE predicted results.

In section 2. 2, the motor topologies, winding factors, and end-winding models of 6s/2p HSPM motors with 1, 2, and 3 slot-pitch windings are described. In section 2. 3, three motors are optimized by the analytical method and FE method for the maximum torque or torque density under different conditions. Section 2. 4 investigates the electromagnetic performances of three optimized motors with a fixed stator active length. In section 2. 5, the influence of end-winding on the torque and torque density with different stator active lengths is analyzed. Three prototype motors with different slot-pitch windings are tested to validate the FE predicted results in section 2. 6, and section 2. 7 is the conclusion.

## 2.2 Machine Topologies

Fig. 2. 1 (I) shows the machine topologies and winding configurations of three 6s/2p HSPM motors with 1, 2, and 3 slot-pitch windings, designated as M1, M2, and M3, respectively. Their winding configurations are described as:

- M1 has coil pitch = 1 slot pitch ( $y=1$ ) and two conductors in one slot from different phases and the same current polarity, Fig. 2. 1(a);
- M2 has coil pitch = 2 slot pitches ( $y=2$ ) and two conductors in one slot from different phases and opposite current polarity, Fig. 2. 1(b);
- M3 has coil pitch = 3 slot pitches ( $y=3$ ) and two conductors in one slot with the same phase and same current polarity, Fig. 2. 1(c).

Their basic parameters are given in Table 2.1. PMs with parallel magnetization and a magnetic

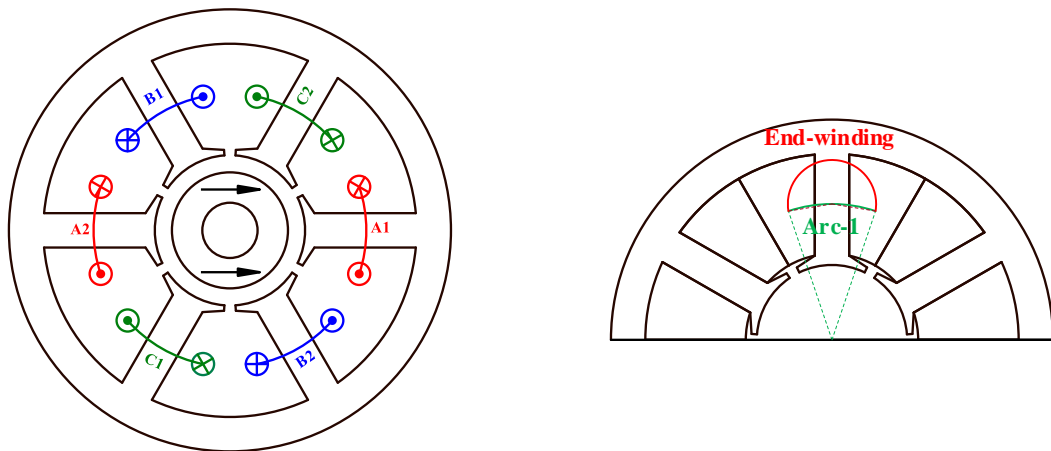
rotor shaft are adopted to produce a sinusoidal air-gap field distribution [NGK96]. A stainless-steel sleeve is employed to retain the PMs from centrifugal force. In general, three phase 120° electric square wave current waveforms are employed for high-speed application. The slot-pitch mainly affects winding factor and end-windings, which will be analyzed in this part.

### 2.2.1 Winding Factor

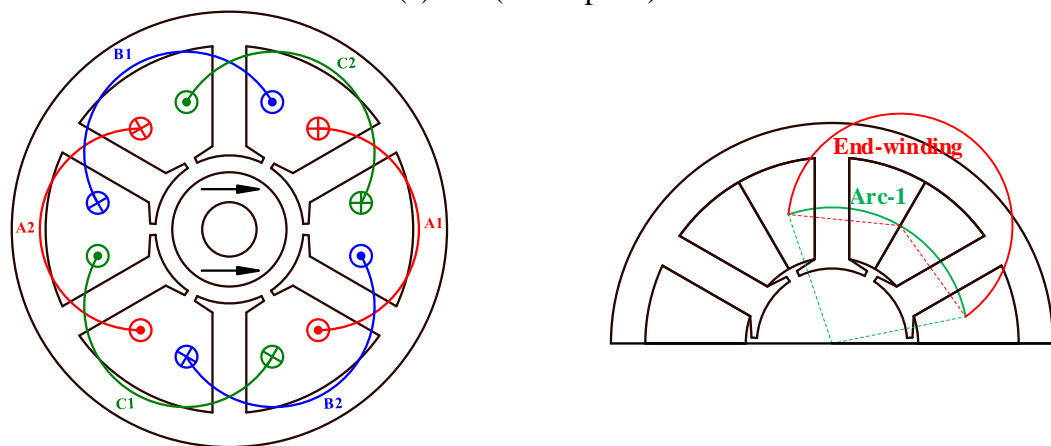
Although with different slot-pitch windings, all of three 6s/2p HSPM motors employ concentrated windings, and thus their distribution factors are 1. Hence, their winding factors ( $k_w$ ) are equal to the pitch factors ( $k_p$ ), which can be calculated by

$$k_p = \cos\left(\frac{\alpha}{2}\right) \quad (2.1)$$

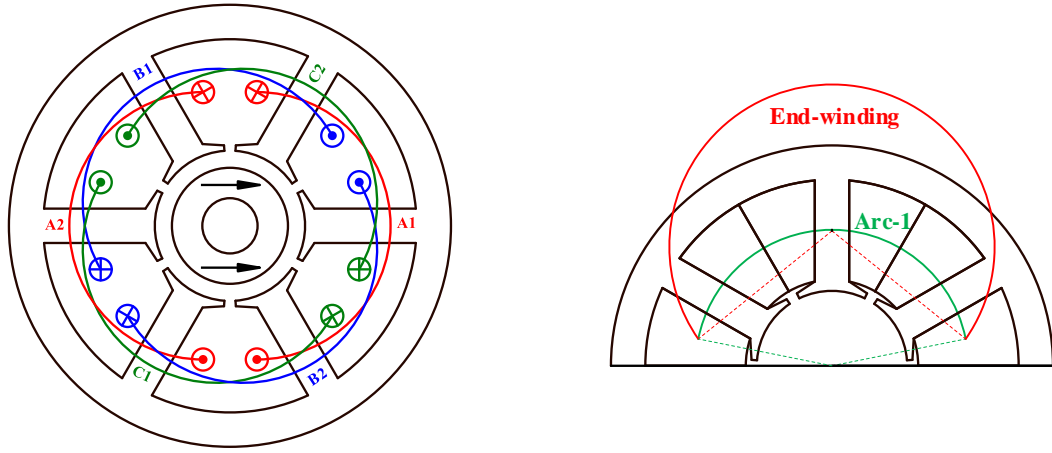
where  $\alpha$  is the electric degree of the shortened coil span angle. For the motor with full-pitch windings, i.e. 3 slot-pitch windings, the shortened coil span angle is 0°, and the pitch factor is 1. For the motors with short-pitch windings, i.e. 1 and 2 slot-pitch windings, the shortened coil span angles are 120° and 60°, and thus their pitch factors are 0.5 and 0.866, respectively.



(a) M1 (1 slot-pitch)



(b) M2 (2 slot-pitch)



(I). Motor topologies (c) M3 (3 slot-pitch) (II). End-winding models

Fig. 2. 1. Motor topologies and end-winding models of three motors with 1, 2, and 3 slot-pitch windings.

Table 2. 1

Main Parameters of Initial Design

Rated speed, krpm	180	Number of turns per phase	20
Stator outer diameter, mm	40	Lamination material	20JNEH1200
Stator active length, mm	9.6	Magnet material	N45SH
Air-gap length, mm	1.55	Magnet remanence, T	1.3
Sleeve thickness, mm	0.3	Sleeve material	Stainless steel
Shaft diameter, mm	5.0	Shaft material	GCr15

### 2.2.2 End-winding Length

In this chapter, for simplicity, the shape of end-winding in motors with 1 slot-pitch windings can be assumed to be semi-circular with the diameter of the length of ‘Arc-1cp’ [PAN06], as shown in Fig. 2. 1 (II) and their end-winding lengths ( $l_e$ ) can be calculated as

$$l_{e(y=1)} = \frac{\pi}{2} \left( \frac{(2y-1) \left( \frac{D_i}{2} + h_t + \frac{D_o}{2} - h_y \right) \pi}{2N_s} + \frac{w_t}{2} \right) \quad (2.2)$$

where  $y$  is the slot-pitch,  $N_s$  is the slot number,  $D_o$ ,  $D_i$ ,  $w_t$ ,  $h_t$ , and  $h_y$  are the stator outer diameter, stator inner diameter, tooth width, tooth-tip height, and yoke thickness, respectively.



For 2 and 3 slot-pitch windings, the end-windings include extend part ( $l_{ex}$ ) and connected part ( $l_{con}$ ), as shown in Fig. 2. 2. The connected part is assumed as the semi-circular with the diameter of the length of ‘Arc-2cp’ or ‘Arc-3cp’, Fig. 2. 1(II). The angle ( $\theta_{end}$ ) between extend and connected parts has a maximum value for ensuring that the connected part will not overlap the outside of the stator. The end-winding lengths of 3 slot-pitch windings can be calculated as

$$l_{e(y=2,3)} = \frac{\pi}{2} \left( \frac{(2y-1) \left( \frac{D_i}{2} + h_t + \frac{D_o}{2} - h_y \right) \pi}{2N_s} + \frac{w_t}{2} \right) + 2l_{ex} \quad (2.3)$$

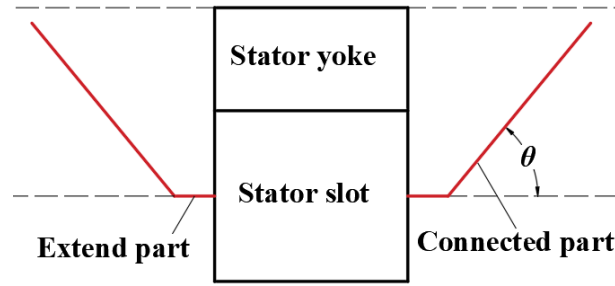


Fig. 2. 2. Side view of stator of 6s/2p HSPM motors with 2 and 3 slot-pitch windings.

### 2.2.3 End-winding Axial Length

The coil pitch also affects the end-winding axial length ( $l_{ea}$ ). With a fixed stator active length, longer end-winding axial length leads to longer motor axial length ( $l_{ma}$ ), which results in low torque density and rotor dynamic issues for high-speed operations. Therefore, for high-speed application, the motor axial length should be designed relatively short, i.e. short end-winding axial length. For 1 slot-pitch windings, the total end-winding axial lengths for both ends are assumed to be the diameter of end-winding length, i.e. the length of ‘Arc-1’, which can be computed by

$$l_{ea(y=1)} = \frac{2}{\pi} l_e \quad (2.4)$$

For 2 and 3 slot-pitch windings, the axial length of the connected part is the half-length of ‘Arc-2cp’ or ‘Arc-3cp’, and thus the total end-winding axial lengths for both ends can be calculated as

$$l_{ea(y=2,3)} = \frac{2}{\pi} (l_e - 2l_{ex}) \cos(\theta_{end}) + 2l_{ex} \quad (2.5)$$

## 2.3 Optimal Designs

In this section, three 6s/2p HSPM motors with different slot-pitch windings are optimized by analytical and FE methods with three different conditions, i.e. a fixed current density, a fixed stator copper loss, and a fixed total stator loss. The optimal goal is the maximum torque or torque density. Several parameters are fixed in the optimization, such as stator outer diameter, stator active length, air-gap length, sleeve thickness, turns number, and shaft diameter, as shown in Table 2. 1.

### 2.3.1 Fixed Current Density

Current density is an essential parameter of motor design, which depends on the current level, the number of conductors in the slot, and the slot area. The large current density will lead to winding overheating and insulation damage, causing short circuit fault etc. In general, according to the experience, the maximum allowed current density under the forced air cooling is 10 A/mm<sup>2</sup> [HAN03]. In this case, the insulation class of ultra-high-speed motors is ‘F’, which is higher than that of conventional low- and medium-speed motors. Thus, the maximum allowable current density is defined as 12 A/mm<sup>2</sup> in this section.

With a fixed current density, two design variables will be focused on: the split ratio ( $\lambda$ ) and the maximum stator iron flux density ( $B_{max}$ ). In this optimization, the shaft diameter is fixed and thus the magnet thickness varies with the split ratio. With three phase 120° electric square wave currents, the average torque can be calculated by

$$T_{ave} = 2l_s (D_i - 2l_g) B_g k_w I_{max} N_{ph} \quad (2.6)$$

With a fixed current density, the torque equation can be rewritten as

$$T_{ave} = 2l_s (D_i - 2l_g) B_g k_w \left(\frac{S_{slot}}{2}\right) k_p J a \quad (2.7)$$

where  $(S_{slot}/2)$  means the half slot area for the double layer winding configuration,  $k_p$  is the slot packing factor, which is 0.27 provided by the company. The small slot packing factor is employed to avoid local overheating since it increases the distances between the conductors and offers forced-air cooling channels, which can reduce the AC loss and improve the winding cooling capability.  $a$  is the number of parallel paths. In addition, the slot area can be calculated by the tooth width ( $w_t$ ), the yoke height ( $h_y$ ), the tooth-tip height ( $h_t$ ), the slot number ( $N_s$ ), and the split ratio due to  $D_i = \lambda D_o$ .

$$S_{slot} = \frac{\pi(D_o^2 - (D_i + 2h_t)^2)}{4N_s} - \frac{\pi(D_o^2 - (D_o - 2h_y)^2)}{4N_s} - w_t(D_o/2 - h_y - D_i/2 - h_t) \quad (2.8)$$

Based on the Gauss' Law, the tooth width and yoke height can be calculated by  $\lambda$ ,  $B_{max}$ , and the average air-gap flux density ( $B_{ave}$ ).

$$B_{ave}A_g = B_{max}A_{iron} \Rightarrow B_{ave}D_g\pi = 2B_{max}h_y \quad (2.9)$$

where  $A_g$ ,  $A_{iron}$ , and  $D_g$  are the air-gap area, stator iron area, and air-gap diameter. Since the air-gap flux density waveform of 2-pole motors with parallel magnetization is sinusoidal,  $B_{ave}=(2/\pi) B_g$ . According to [ZHU97],  $B_g$  can be represented by

$$B_g = B_r \frac{[1 - (\frac{R_{sh}}{R_m})^2][(\frac{R_m}{R_{si}})^2 + (\frac{R_m}{R_g})^2]}{[1 + (\frac{R_m}{R_{si}})^2][1 - (\frac{R_{sh}}{R_m})^2] + \mu_r[1 - (\frac{R_m}{R_{si}})^2][1 + (\frac{R_{sh}}{R_m})^2]} \quad (2.10)$$

where  $B_r$  is the magnet remanence,  $\mu_r$  is the relative permeability of magnet,  $R_{si}$ ,  $R_g$ ,  $R_m$ , and  $R_{sh}$  are the radius of the stator inner, the air-gap, the magnet, and the shaft, respectively.

For the 6s/2p PM motor, the ratio of tooth-pitch to pole-pitch is 1/3, and Fig. 2. 3 shows the idealized open-circuit flux distribution [PAN06]. It indicates that the maximum flux in the stator tooth, i.e. stator tooth '1' or '4', is the same as the maximum flux in the stator yoke. Thus, the tooth width equals the yoke height, which can be calculated by

$$w_t = h_y = (\frac{D_o}{2}\lambda - \frac{l_g}{2})\frac{B_g(\lambda)}{B_{max}} \quad (2.11)$$

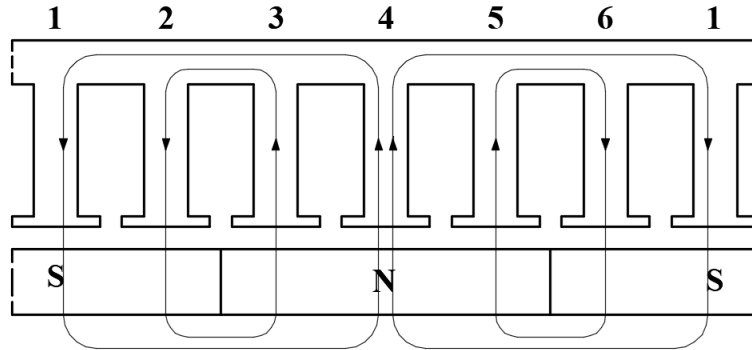


Fig. 2. 3. Idealized open-circuit flux distribution of 6s/2p PM motor.

Consequently, the average torque can be calculated by the function of  $\lambda$  and  $B_{max}$ , i.e.  $f(\lambda, B_{max})$ .

$$T_{ave} = l_s k_w k_p J a f(\lambda, B_{max}) \quad (2.12)$$

$$f(\lambda, B_{max}) = (\lambda D_o - 2l_g) B_g(\lambda) S_{slot}(\lambda, B_{max}, D_o) \quad (2.13)$$

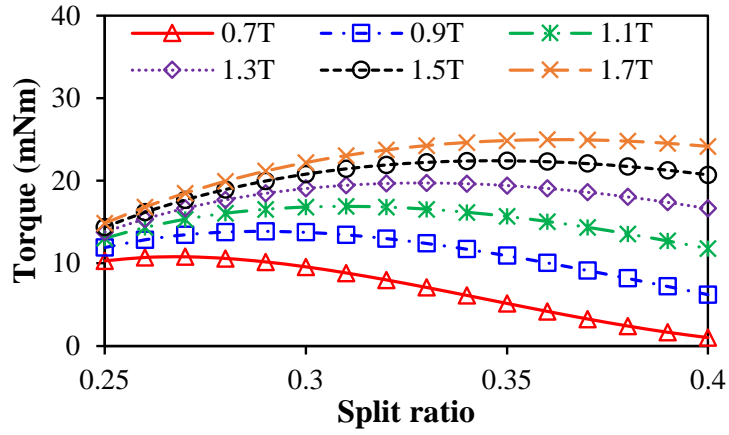
When the optimal goal is the maximum torque, with a given stator outside diameter and a given maximum stator iron flux density, the optimal split ratio can be obtained by

$$\frac{\partial f(\lambda)}{\partial \lambda} = 0 \quad (2.14)$$

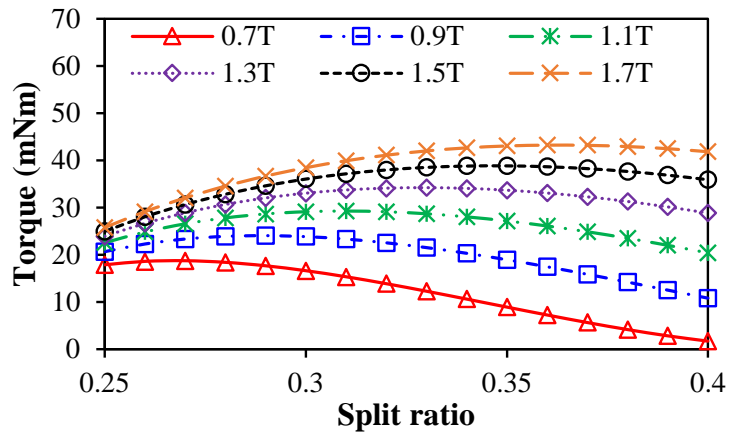
It is worth noting that the winding factor, slot packing factor, and current density are included in (2.12) but not in (2.13), which means those parameters can affect the output torque but do not change the optimal split ratio.

The relationship between torque and split ratio under various maximum stator iron flux densities is shown in Fig. 2. 4. The results show that the torque increases with the increase of split ratio at first and then decreases, and thus the optimal split ratio for maximum torque exists. Meanwhile, with the increase of  $B_{max}$ , the maximum torque and optimal split ratio increase, Fig. 2. 5. Therefore, the maximum stator iron flux density is designed at the knee point of the B-H curve of the stator lamination material, i.e.  $B_{max} = 1.5\text{T}$ , Fig. 2. 6, and thus the optimal split ratios of M1, M2, and M3 are all 0.34. Three motors with different slot-pitch windings have the same optimal split ratio, which has been explained by analytical calculation based on (2.12) and (2.13). The equipotential and flux contour distributions of the optimized design are shown in Fig. 2. 7. The comparison of FE and analytically predicted torques of three motors with 1, 2, and 3 slot-pitch windings indicates that their optimal split ratios have a good agreement, Fig. 2. 8.

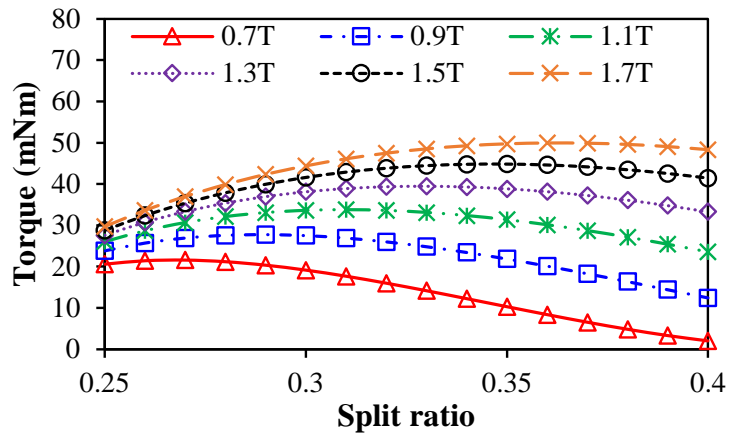
As mentioned in section 2. 2, three 6s/2p HSPM motors with 1, 2, and 3 slot-pitch windings have different end-winding lengths, which is the main difference and should be considered in the optimization. However, with a fixed current density, the influence of end-winding on the optimal design is neglected in theory. Therefore, another optimal condition, i.e. fixed copper loss, is employed and discussed in the next section.



(a) M1

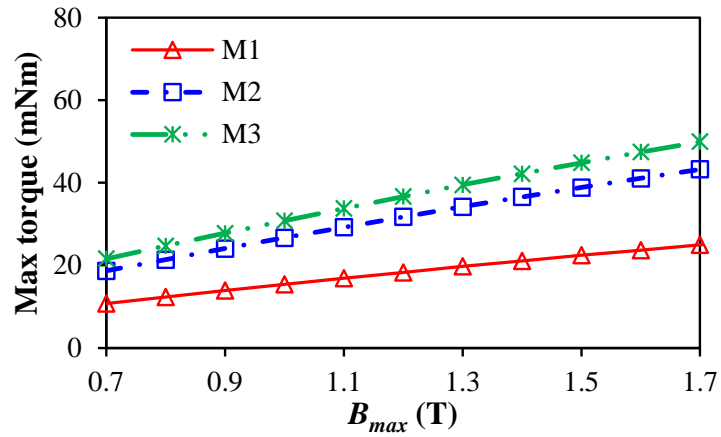


(b) M2

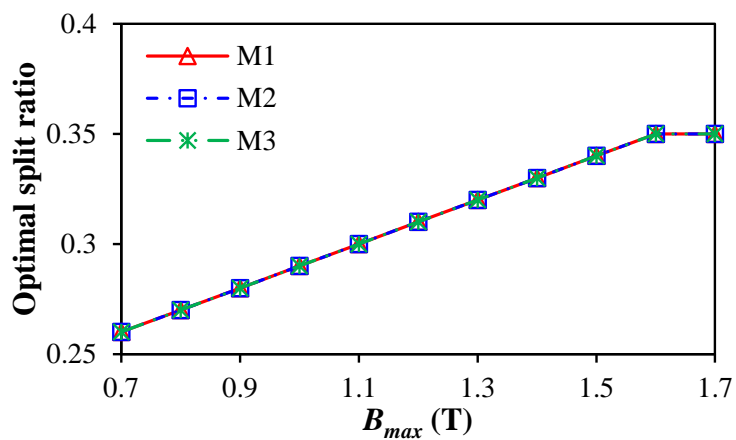


(c) M3

Fig. 2. 4. Relationship between torque and split ratio under various maximum stator iron flux densities.



(a) Maximum torque



(b) Optimal split ratio

Fig. 2. 5. Variation of maximum torque and optimal split ratio with maximum stator iron flux density.

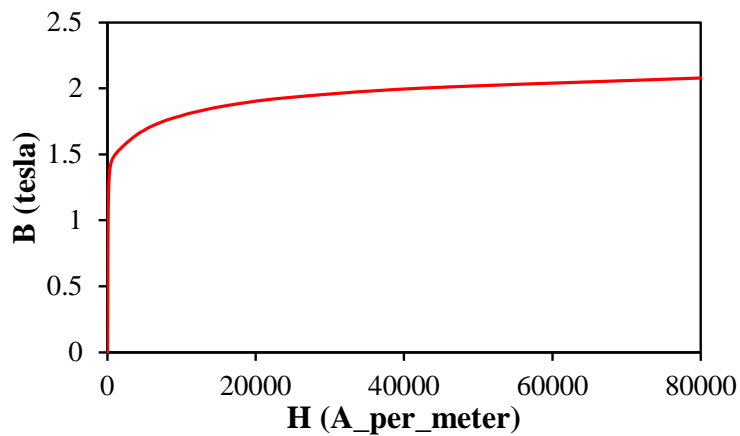


Fig. 2. 6. B-H curve of stator lamination material, 20JNEH1200.

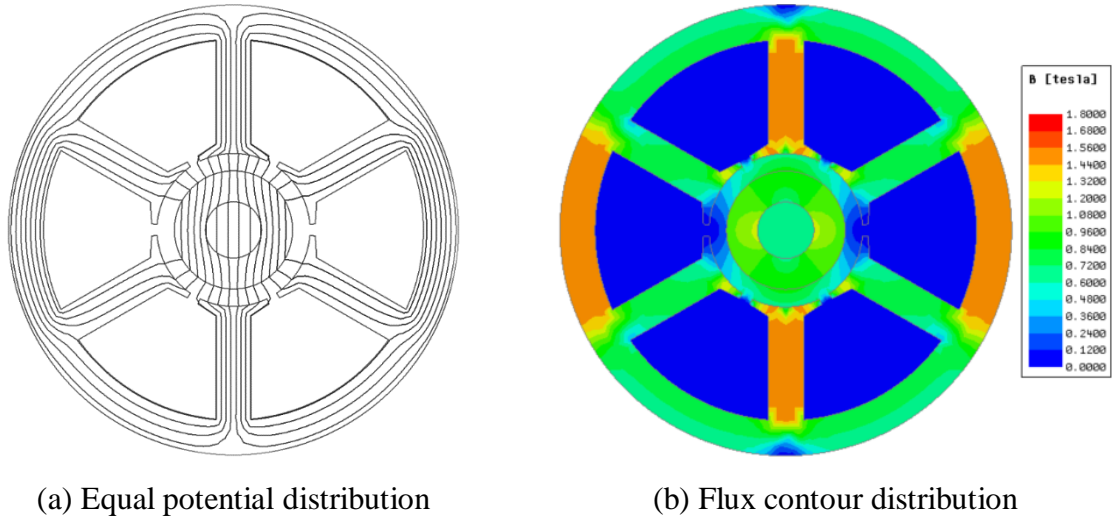


Fig. 2. 7. Equal potential and flux contour distributions of the optimized design ( $\lambda=0.34$ ,  $B_{max}=1.5T$ ) by fixing current density.

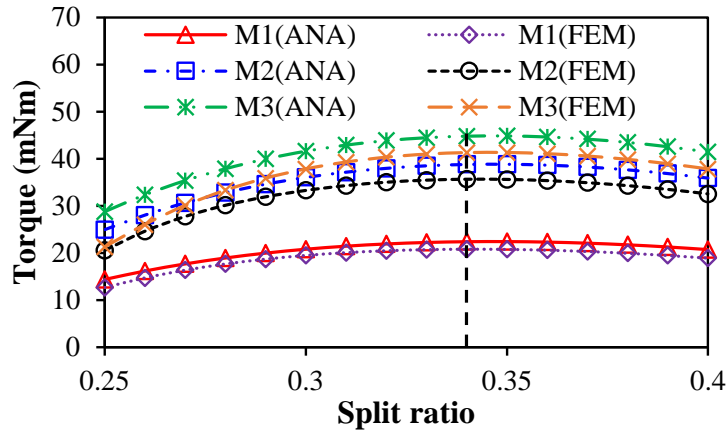


Fig. 2. 8. Comparison of FE and analytically predicted torques when  $B_{max}=1.5T$ .

### 2.3.2 Fixed Copper Loss

In general, if the iron loss is neglected, the copper loss represents the major loss which causes temperature rise of the motor and is limited in optimization. Compared with a fixed current density, the optimization with a fixed copper loss can consider the influence of different end-windings caused by different slot-pitch windings. Therefore, three scenarios for the maximum torque or torque density, i.e. torque per unit volume, are analyzed by analytical and FE methods, which are given as follows.

- Neglecting end-winding copper loss, the optimal goal is maximum torque;
- Accounting for end-winding copper loss, the optimal goal is maximum torque;

- Accounting for end-winding copper loss and axial length, the optimal goal is maximum torque density.

According to literature, the stator thermal limitation ( $P_{limit}$ ) [BIN04] can be introduced to restrict the stator copper loss, which can be calculated by

$$P_{limit} = hV_m\pi D_o l_s \quad (2.15)$$

In this case,  $h=100 \text{ W/}^\circ\text{Cm}^2$  [BIA04], since the small size HSPM motors employ external forced-air cooling.  $V_m$  is the maximum motor operation temperature.

#### A. Neglecting end-winding copper loss

In this scenario, the copper loss is fixed neglecting the end-winding copper loss, and the optimal goal is the maximum torque. As mentioned before, the average torque can be calculated by

$$T_{ave} = 2l_s(D_i - 2l_g)B_g k_w I N_{ph} \quad (2.16)$$

Since the phase current can be replaced by the function of the copper loss ( $P_{cu}$ )

$$P_{cu} = 2I^2 \rho_{cu} \frac{2l_s N_{ph}^2}{(S_{slot}/2)k_p a} \quad (2.17)$$

The torque equation can be rewritten as

$$T_{ave} = 2l_s(\lambda D_o - 2l_g)B_g k_w N_{ph} \sqrt{\frac{P_{cu} S_{slot} k_p a}{8\rho_{cu} N_{ph}^2 l_s}} \quad (2.18)$$

where  $\rho_{cu}$  is the copper resistivity at 20°C, i.e.  $1.68 \times 10^{-8} \text{ } (\Omega \cdot \text{m})$ .

With a fixed copper loss, the split ratio and maximum stator iron flux density are two design variables for the maximum torque, and the average torque can be given by

$$T_{ave} = k_w \sqrt{\frac{P_{cu} k_p l_s a}{2\rho_{cu}}} f(\lambda, B_{max}) \quad (2.19)$$

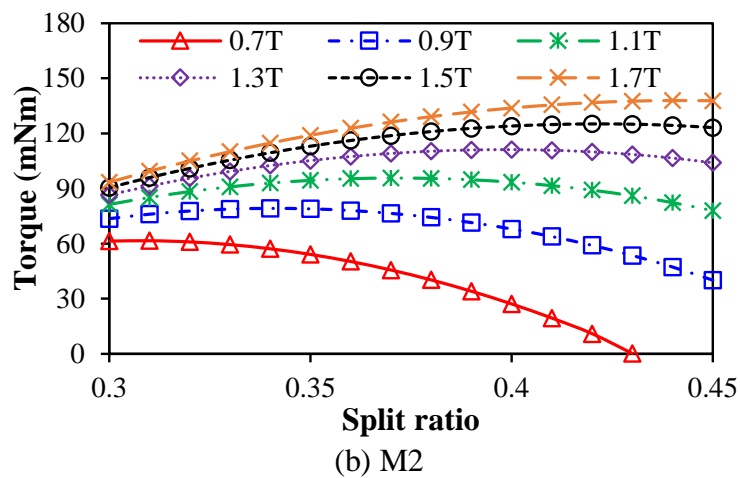
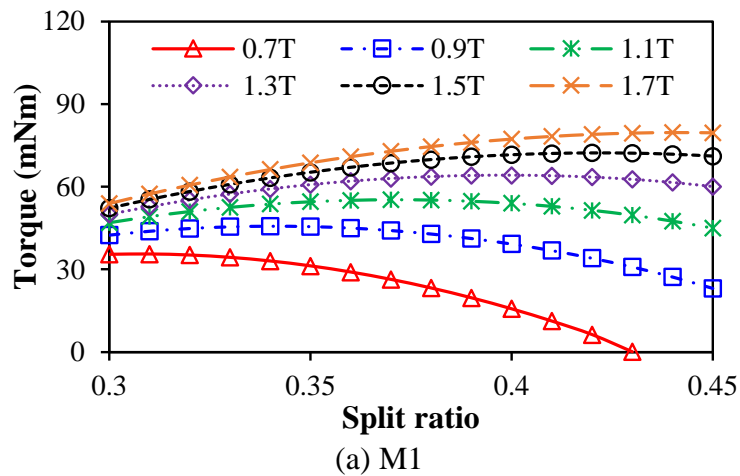
$$f(\lambda, B_{max}) = (\lambda D_o - 2l_g)B_g \sqrt{S_{slot}} \quad (2.20)$$

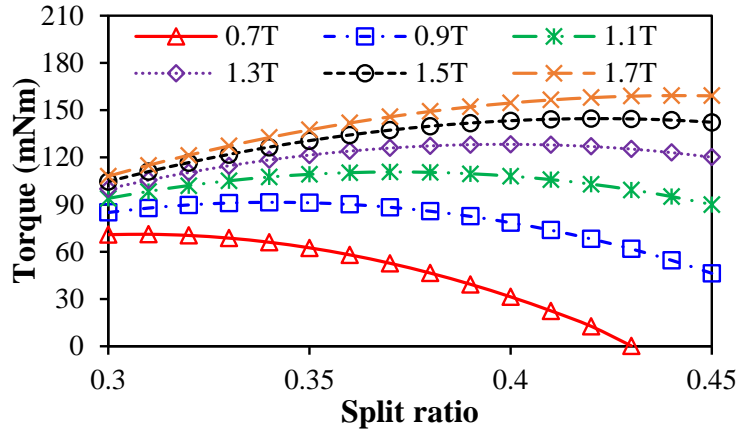
With a given maximum stator iron flux density and a given stator outside diameter, the optimal split ratio for the maximum torque can be obtained by



$$\frac{\partial f(\lambda)}{\partial \lambda} = 0 \quad (2.21)$$

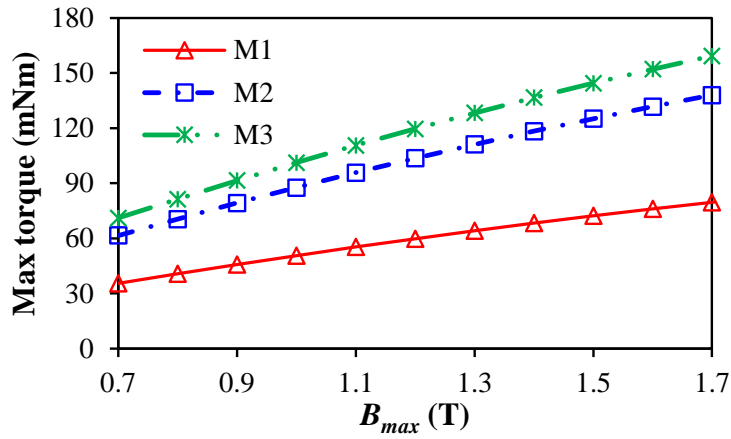
Fig. 2. 9 shows the relationship between torque and split ratio under various maximum stator iron flux densities when the end-winding copper loss is neglected. It shows that for each  $B_{max}$ , the torque climbs up and then decline with the split ratio. In addition, the maximum torque and optimal split ratio increase with  $B_{max}$ , Fig. 2. 10, and the three motors have the same results. When  $B_{max}=1.5\text{T}$ , the optimal split ratios of M1, M2, and M3 are all 0.42, which is larger than that optimized by fixing current density. The reason is that with a fixed copper loss, a balance of the electrical loading and magnetic loading is achieved for the maximum torque. However, a fixed current density restricts the electrical loading and leads to a relatively large slot area and relatively small optimal split ratio. Fig. 2. 11 shows the equipotential and flux contour distributions of the optimized design. Fig. 2. 12 shows the variation of analytically and FE predicted output torques with the split ratio when  $B_{max}=1.5\text{T}$ , and their optimal split ratios have a good agreement.



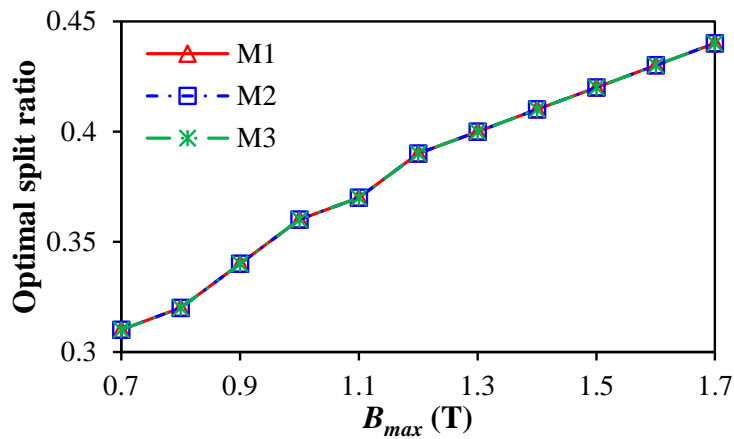


(c) M3

Fig. 2. 9. Relationship between torque and split ratio under various maximum stator iron flux densities, neglecting end-winding copper loss.

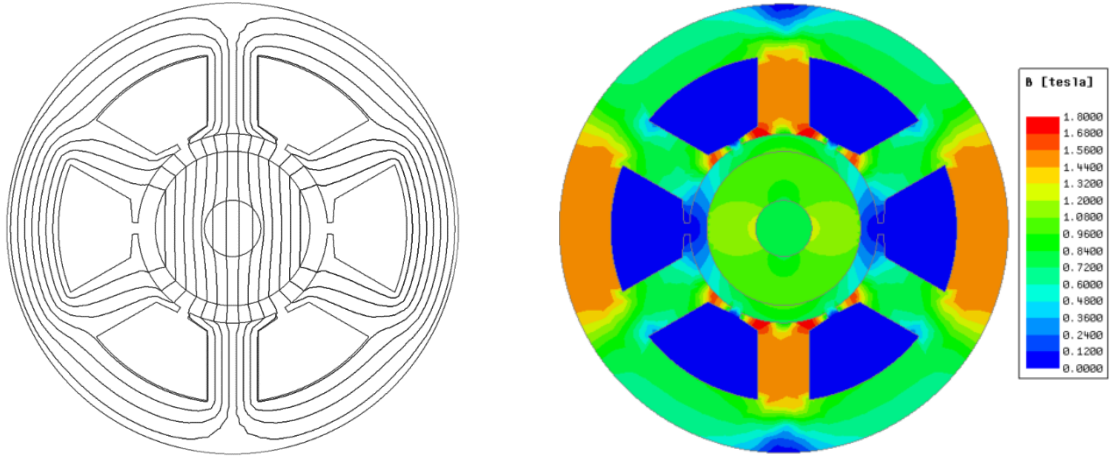


(a) Maximum torque



(b) Optimal split ratio

Fig. 2. 10. Variation of maximum torque and optimal split ratio with maximum stator iron flux density, neglecting end-winding copper loss.



(a) Equal potential distribution

(b) Flux contour distribution

Fig. 2. 11. Equal potential and flux contour distributions of the optimized design ( $\lambda=0.42$ ,  $B_{max}=1.5T$ ) by fixing copper loss, without end-winding.

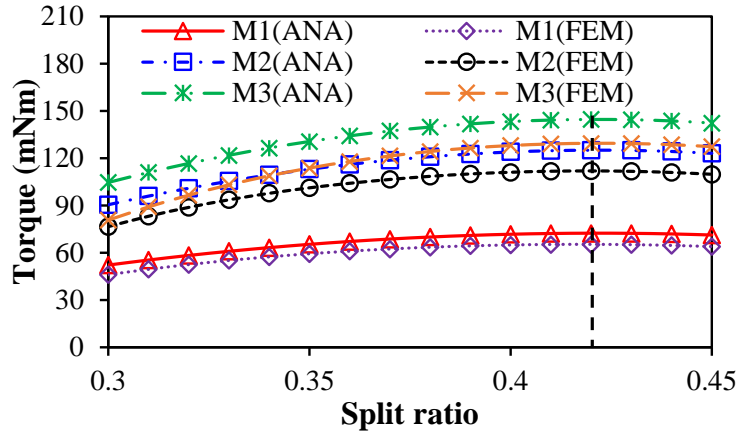


Fig. 2. 12. Comparison of analytical predictions and FE results when  $B_{max}=1.5T$ , without end-winding copper loss.

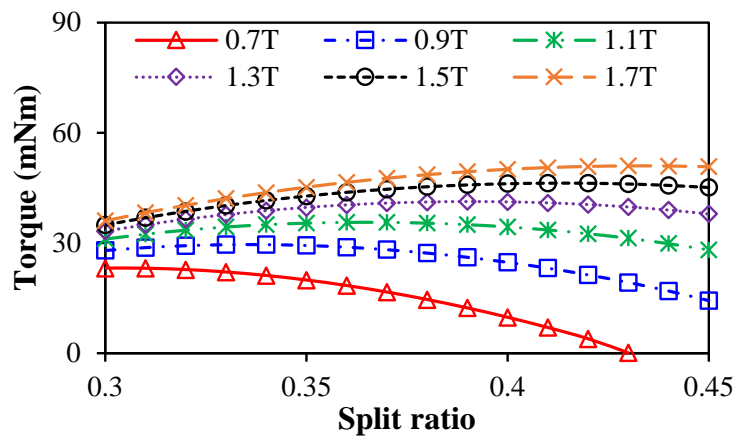
## B. Accounting for end-winding copper loss

In this scenario, the end-winding copper loss is taken into account, and the optimal goal is the maximum torque. Considering end-winding copper loss, (2.18) can be rewritten as

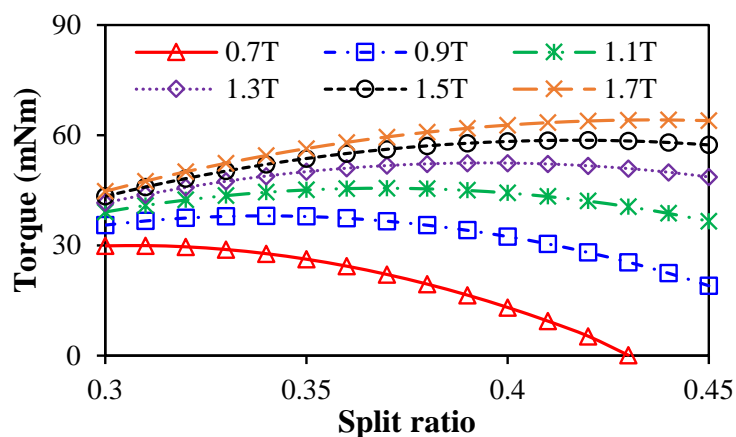
$$T_{ave} = 2l_s(\lambda D_o - 2l_g)B_g k_w N_{ph} \sqrt{\frac{P_{cu} S_{slot} k_p a}{8\rho_{cu} N_{ph}^2 (l_s + l_e)}} \quad (2.22)$$

The relationship between torque and split ratio under various maximum stator iron flux densities is shown in Fig. 2. 13. With a given  $B_{max}$ , the maximum torque can be achieved and the optimal split ratio exists. Compared with the first scenario, the considered end-winding

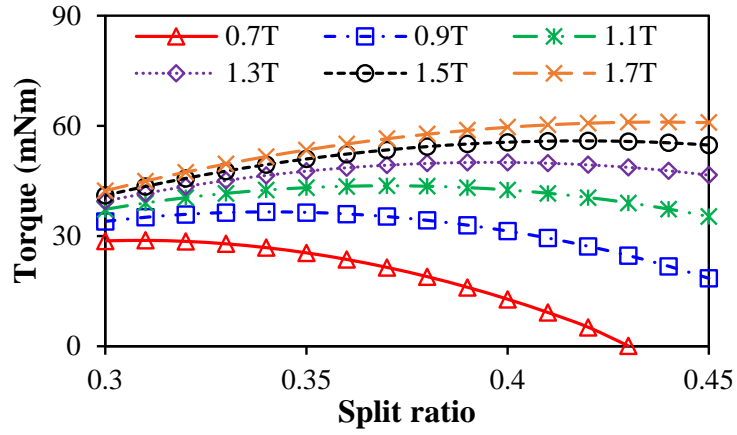
copper losses decrease the maximum torques of three motors. Fig. 2.14 (a) shows that M2 has a larger maximum torque for each  $B_{max}$  than M3 since M3 has the longest end-winding length but M2 has a relatively short end-winding length and relatively large winding factor. In addition, Fig. 2. 14 (b) shows three motors do not have the same optimal split ratio for each maximum stator iron flux density due to accounting for different end-winding copper losses. However, in this case, the difference is slight and can be neglected. Since the maximum torque increases with  $B_{max}$ , the optimal split ratios of three motors are achieved at  $\lambda=0.42$  when  $B_{max}=1.5T$ , which is the same as that in the first scenario, i.e. neglecting end-winding copper loss. Thus, the equipotential and flux contour distributions of the optimized design are the same as those shown in Fig. 2. 11. Fig. 2. 15 shows the variation of analytically and FE calculated output torques with the split ratio when  $B_{max}=1.5T$ . Although the analytically predicted torques are slightly larger than the FE results, their optimal split ratios have a good agreement.



(a) M1

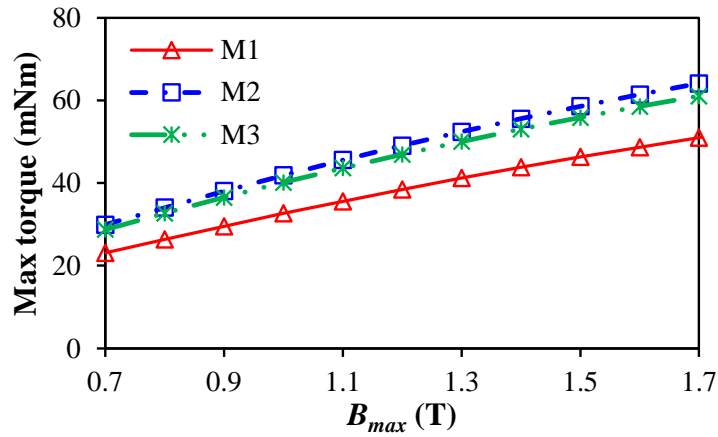


(b) M2

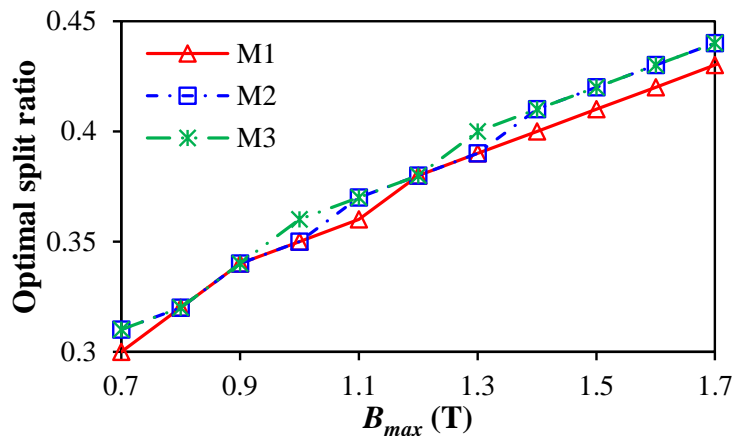


(c) M3

Fig. 2. 13. Relationship between torque and split ratio under various maximum stator iron flux densities, with end-winding copper loss.



(a) Maximum torque



(b) Optimal split ratio

Fig. 2. 14. Relationships between maximum torque and  $B_{max}$ , optimal split ratio and  $B_{max}$ , with end-winding copper loss.

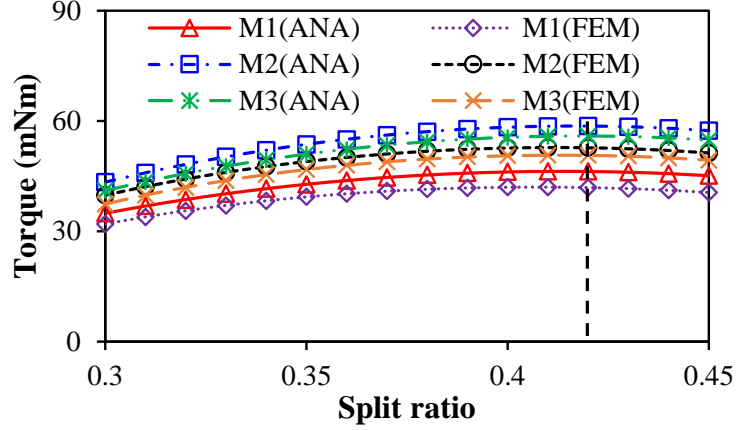


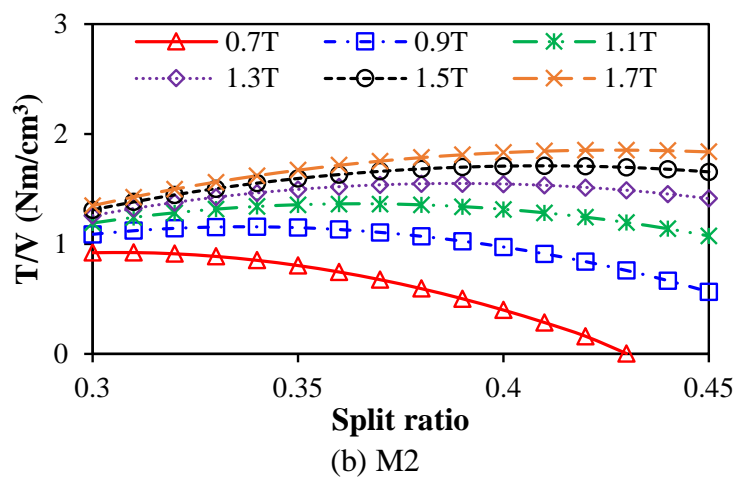
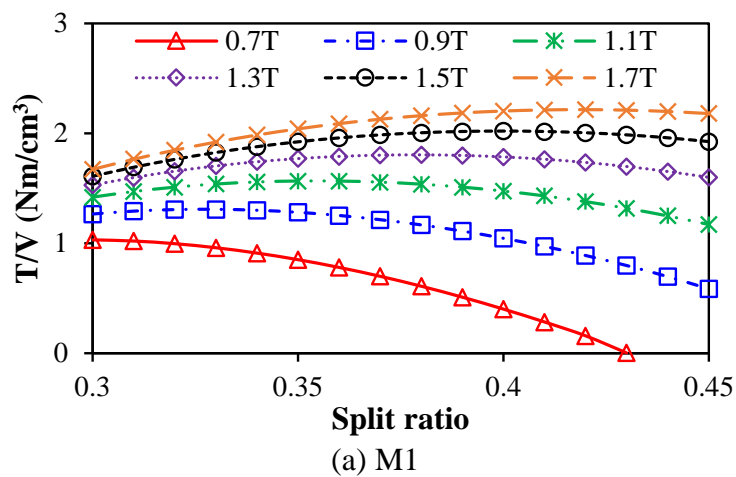
Fig. 2. 15. Comparison of analytical predictions and FE results when  $B_{max}=1.5T$ , with end-winding copper loss.

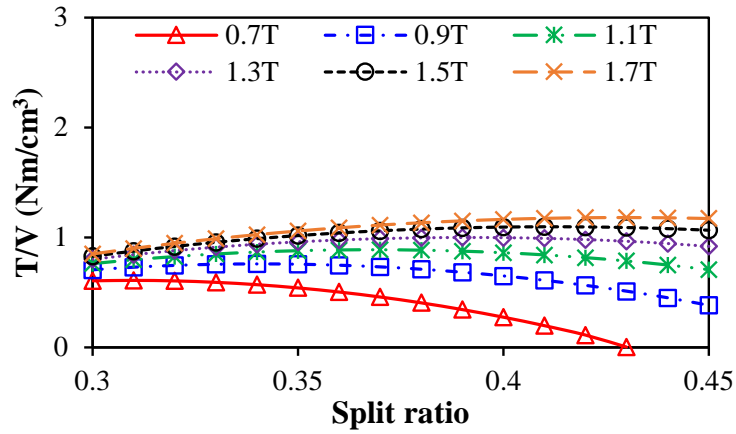
### C. Accounting for end-winding copper loss and axial length

In the second scenario, M2 and M3 have larger torques than M1, but their longer end-winding axial lengths may lead to lower torque densities. Therefore, in this scenario, the end-winding copper loss and axial length are taken into account, and the optimal goal is the maximum torque density rather than the maximum torque as described earlier.

Fig. 2. 16 shows the relationship between torque density and split ratio under various maximum stator iron flux densities. For each  $B_{max}$ , the torque density climbs up and then declines with split ratio, the optimal split ratio for the maximum torque density can be achieved. Fig. 2. 17 shows the maximum torque density and optimal split ratio increase with  $B_{max}$ . In addition, M1 with the shortest end-winding axial length has the highest torque density, but M3 has the lowest torque density due to the longest end-winding axial length. Three motors have almost the same optimal split ratio, which means the coil-pitch has negligible effect. However, compared with the second scenario, i.e. only accounting end-winding copper loss, the considered end-winding axial length decreases the optimal split ratio from 0.42 to 0.41. Take the design with  $B_{max}=1.5T$  as an example, Fig. 2. 18 shows the variation of output torque and end-winding axial length (both sides) with split ratio. It can be seen that the end-winding axial length increases linearly with the split ratio. Therefore, the maximum torque can be achieved when  $\lambda=0.42$ , but the split ratio should be smaller for the maximum torque density, i.e.  $\lambda=0.41$ . Fig. 2. 19 shows the equipotential and flux contour distributions of the optimized design, and the variation of analytically and FE method calculated torque densities with the split ratio when  $B_{max}=1.5T$  is shown in Fig. 2. 20, and their optimal split ratios have a good agreement.

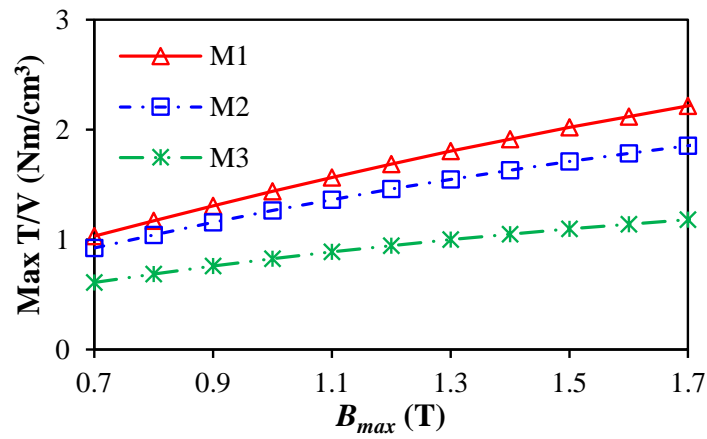
In the foregoing analyses, the optimal goal is the maximum torque, and thus the stator active length is fixed since it cannot change the optimal split ratio. However, in this part, the optimal goal is the maximum torque density, the stator active length has influence on the results of three motors. With the same optimal design for three motors, i.e.  $\lambda=0.41$ ,  $B_{max}=1.5T$ , the variations of torque and torque density with stator active length are shown in Fig. 2. 21. With the increase of stator active length, M2 and M3 have almost the same torque, which is larger than M1, and the difference between M1 and M2 increases. Therefore, with the fixed end-winding axial length, the torque density of M1 is overtaken by M2 at  $l_s=17mm$ , and by M3 at  $l_s=37mm$ . In general, when the stator active length is significantly large, the end-winding axial length can be neglected, and then M3 with the largest winding factor has the highest torque density. In addition, the torque densities of three motors increase firstly and then decrease with the stator active length, and thus different optimal stator active lengths exist for the maximum torque density.



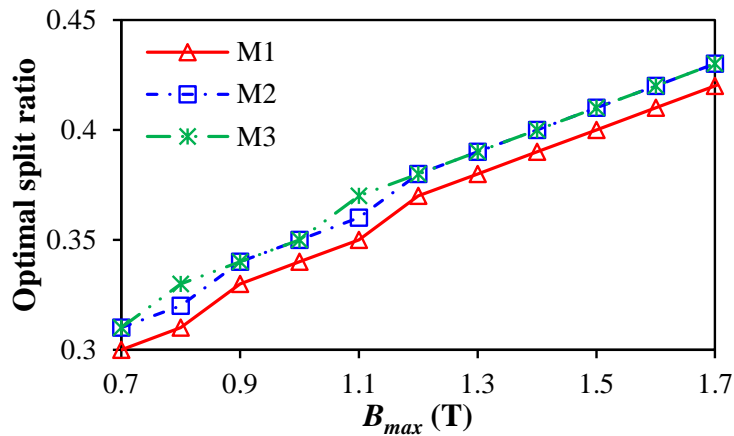


(c) M3

Fig. 2. 16. Relationship between torque density and split ratio under various maximum stator iron flux densities, with end-winding copper loss and axial length.



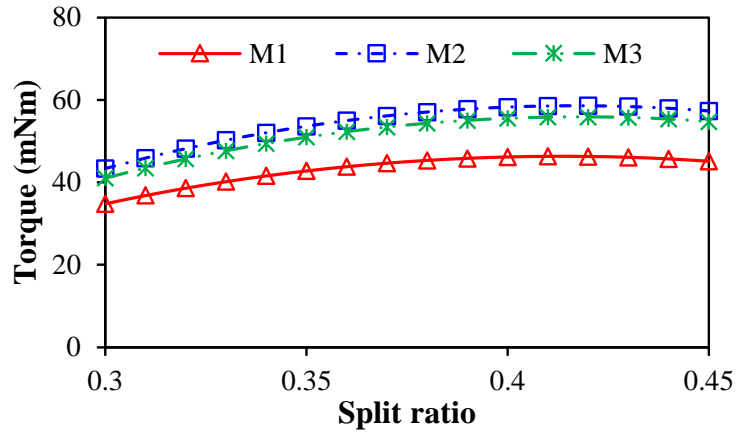
(a) Maximum torque



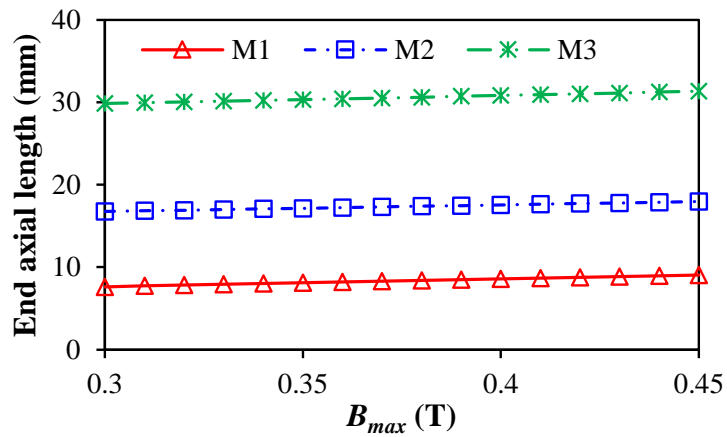
(b) Optimal split ratio

Fig. 2. 17. Variation of maximum torque and optimal split ratio with maximum stator iron flux density, with end-winding copper loss.





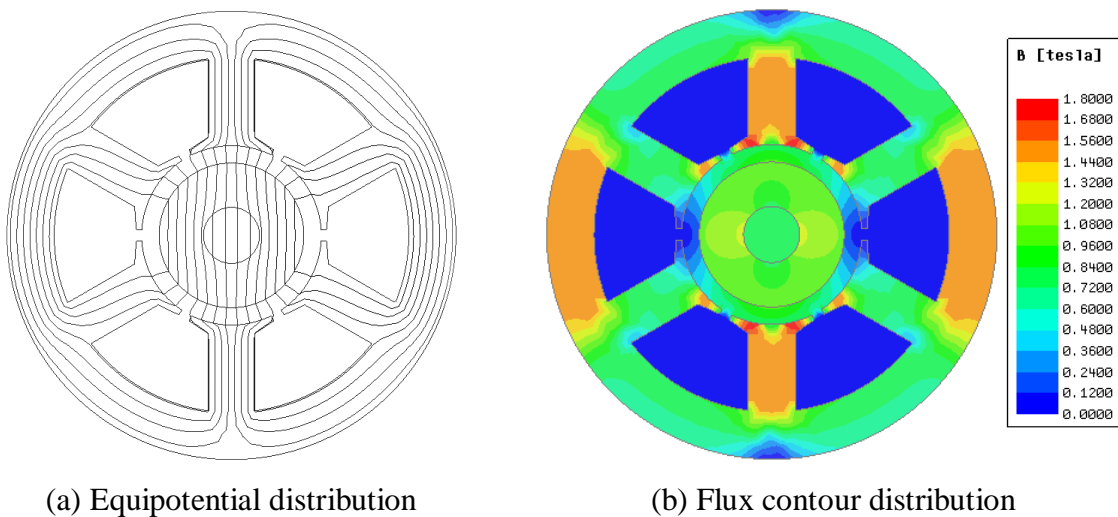
(a) Torque



(b) End-winding axial length (both sides)

Fig. 2. 18. Variation of torque and end-winding axial length (both sides) with split ratio,

$$B_{max}=1.5T.$$



(a) Equipotential distribution

(b) Flux contour distribution

Fig. 2. 19. Equipotential and flux contour distributions of the optimized design by fixing copper loss, with end-winding copper loss and axial length.

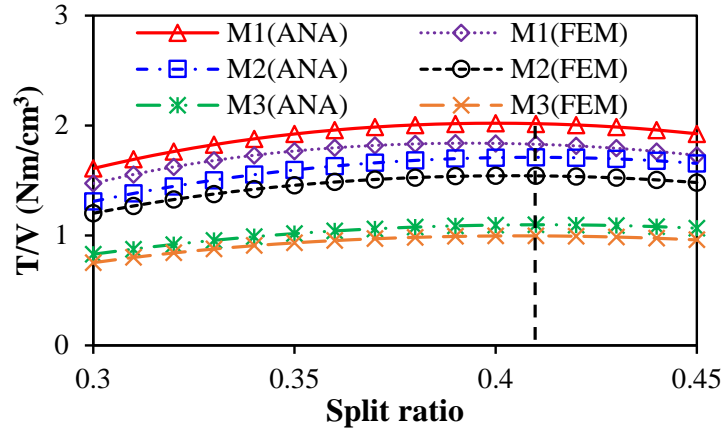
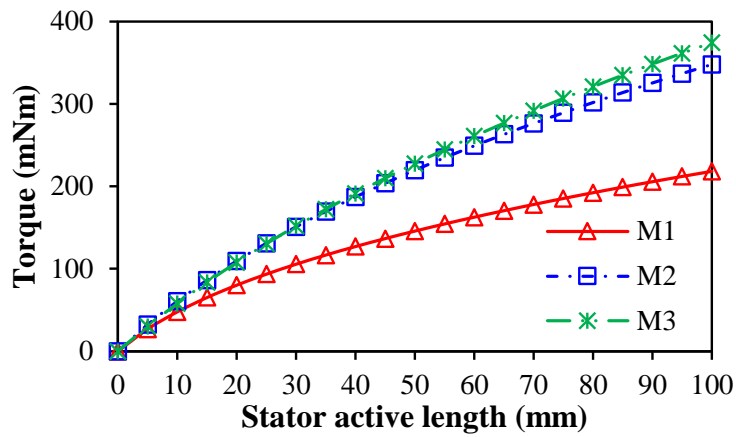
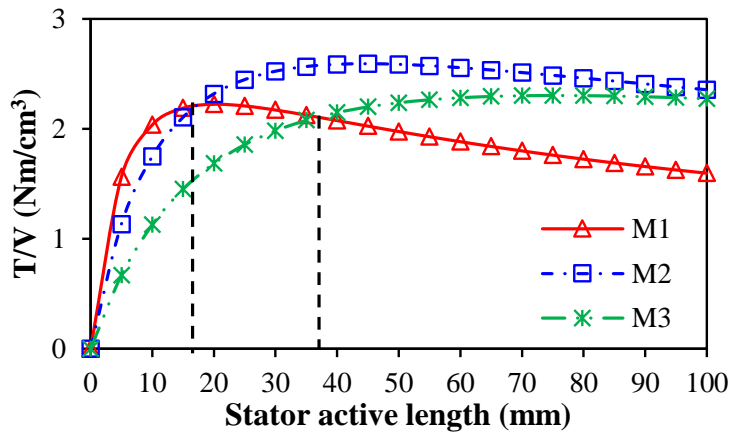


Fig. 2. 20. Comparison of analytically and FE method predicted results when  $B_{max}=1.5T$ , with end-winding copper loss and axial length.



(a) Torque



(b) Torque density

Fig. 2. 21. Variation of torque and torque density with stator active length,  $\lambda=0.41$ ,  $B_{max}=1.5T$ .

#### D. Comparison of fixing current density and copper loss

In this section, the optimized designs by fixing current density and copper loss are compared since their maximum stator iron flux densities are the same, i.e.  $B_{max}=1.5T$ . All the designs are shown in Table 2. 2, and there are several conclusions as follows.

- Different slot-pitch windings have negligible influence on the optimal split ratio no matter fixing current density or copper loss;
- Values of the fixed current density and copper loss do not influence the optimal split ratio for the maximum torque since they only affect the output torque;
- Optimal split ratio under a fixed copper loss is larger than that under a fixed current density due to the limitation of electrical loading with a fixed current density;
- Neglecting the influence of end-winding, the output torques of three motors correspond to their winding factors, which means M3 has the largest torque and M1 has the smallest torque;
- Accounting for end-winding copper loss, the output torques of three motors do not correspond to their winding factors. M2 with a relatively large winding factor and relatively short end-winding length has the largest output torque;
- Accounting for end-winding axial length, the optimal split ratio is smaller than that only considering end-winding copper loss since the increased split ratio leads to the decrease of end-winding length in axial direction.

Table 2. 2

## Three Optimized Motors by Different Optimal Methods

	Fixed current density			Fixed copper loss								
				Without end-winding			With end-winding copper loss			With end-winding copper loss and axial length		
Optimal goal	Max torque									Max torque density		
$B_{max}$ , T	1.5			1.5			1.5			1.5		
Optimal split ratio	0.34			0.42			0.42			0.41		
	M1	M2	M3	M1	M2	M3	M1	M2	M3	M1	M2	M3
Torque, mNm	22.4	38.8	44.8	72.2	125.1	144.5	46.3	58.6	55.9	46.2	58.3	55.5
Torque density, Nm/cm <sup>3</sup>	-						2.00	1.71	1.09	2.01	1.71	1.10

However, in these optimal conditions and scenarios, the maximum stator iron flux density is designed by the B-H curve of stator lamination material, which has a close relationship with stator iron loss. In HSPM motors, stator iron loss leads to temperature rise significantly due to high frequency and should be considered in the optimization [ZHU97] [EDE01]. By considering stator iron loss, the maximum stator iron flux density can be optimized.

### 2.3.3 Fixed Total Stator Loss

In HSPM motors, the large stator iron loss caused by high frequency will result in temperature rise dominantly. In literature [LIQ15], [WAN18] and [MAJ19b], the split ratio is optimized by analytical methods considering open-circuit stator iron loss but neglecting the influence of armature reaction. [ZHU01b] proposes an analytical method for predicting flux density waveforms and stator iron loss densities of several regions of stator iron core accounting for load condition. However, for motor design optimization, this analytical method is complicated since the stator flux density waveforms should be calculated analytically at first, and it is difficult when considering armature reaction. Thus, in [ATA92] and [THO14], although the stator iron losses are calculated by the analytical method, the stator flux density waveforms are computed by FEM. Therefore, by FEM, three 6s/2p HSPM motors with 1, 2, and 3 slot-pitch windings are optimized with a fixed total stator loss, accounting for the on-load stator iron loss. In this part, the stator thermal limitation ( $P_{limit}$ ) [BIN04] can be introduced to restrict the total stator loss ( $P_{stator}$ ) including stator iron loss and copper loss, which can be calculated by

$$P_{limit} = hV_m \pi D_o l_s \quad (2.23)$$

Considering the different end-winding lengths and axial lengths of three motors, three scenarios with two different optimal goals are analyzed, which are given as follows.

- Neglecting end-winding copper loss, the optimal goal is maximum torque;
- Accounting for end-winding copper loss, the optimal goal is maximum torque;
- Accounting for end-winding copper loss and axial length, the optimal goal is maximum torque density;

In the optimization, there are three design variables: split ratio ( $\lambda$ ), maximum stator iron flux density ( $B_{max}$ ), and phase current ( $I_{max}$ ). The split ratio limits the PM thickness due to the fixed shaft diameter, and thus the open-circuit  $B_g$  can be calculated. Based on  $B_{max}$ , tooth width, yoke thickness, and slot area can be computed since the tooth width equals the yoke thickness in

6s/2p PM motors [PAN06]. With various phase currents, the electromagnetic torques, copper losses, and stator iron losses accounting for the influence of armature reaction can be calculated by FEM. Finally, the optimal design with the maximum torque can be selected from the designs with  $P_{stator} \leq P_{limit}$ .

#### A. Neglecting end-winding copper loss

With the fixed stator thermal limitation, the relationship between maximum torque and  $B_{max}$  is shown in Fig. 2. 22. For each slot-pitch, the optimal  $B_{max}$  exists, while for each  $B_{max}$ , the larger the coil-pitch, the higher the maximum torque. In addition, three motors with different slot-pitch windings have almost the same optimal  $B_{max}$ . With the optimal  $B_{max}$ , the average torque climbs up and the decline with the split ratio, Fig. 2. 23, and thus the optimal split ratio exists for each slot-pitch. In addition, the increased coil-pitch increases not only the maximum torque but also the optimal split ratio. Fig. 2. 24 shows that with a fixed phase current, the motor with 3 slot-pitch windings has the highest stator iron loss due to the largest magnitudes of stator magnetomotive force (MMF) spatial harmonics. However, the copper loss remains unchanged for different slot-pitch due to neglecting end-winding copper loss. Therefore, three motors with different slot-pitch windings have the same optimal  $B_{max}$  but different optimal split ratios when neglecting end-winding copper loss but accounting for the on-load stator iron loss.

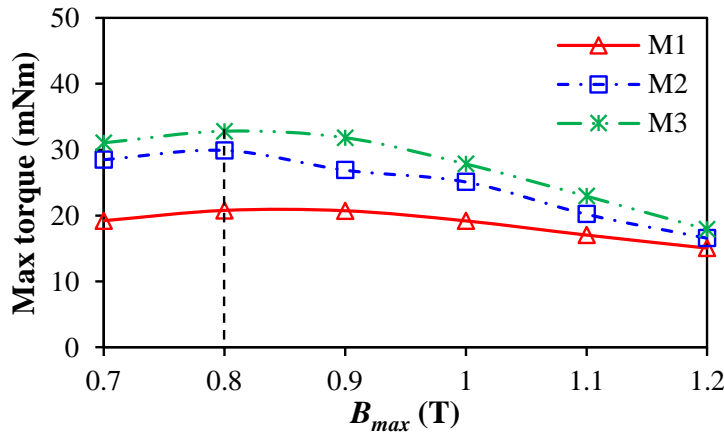


Fig. 2. 22. Relationship between maximum torque and  $B_{max}$  in the motors with different winding configurations neglecting end-windings.

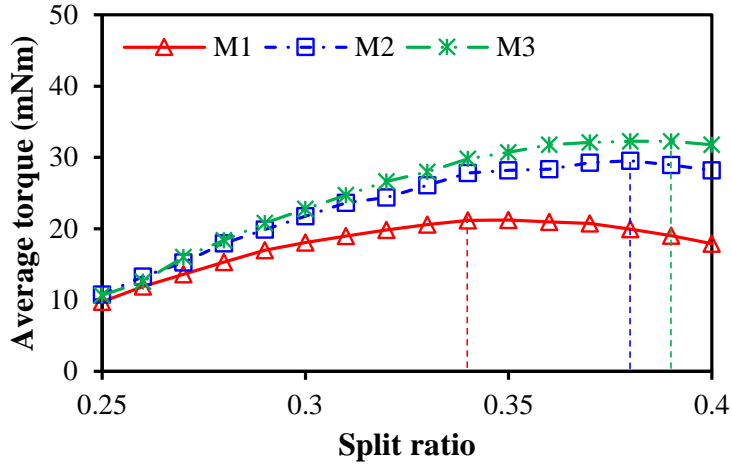


Fig. 2. 23. Relationship between average torque and split ratio in the motors with different winding configurations neglecting end-windings,  $B_{max}=0.8T$ .

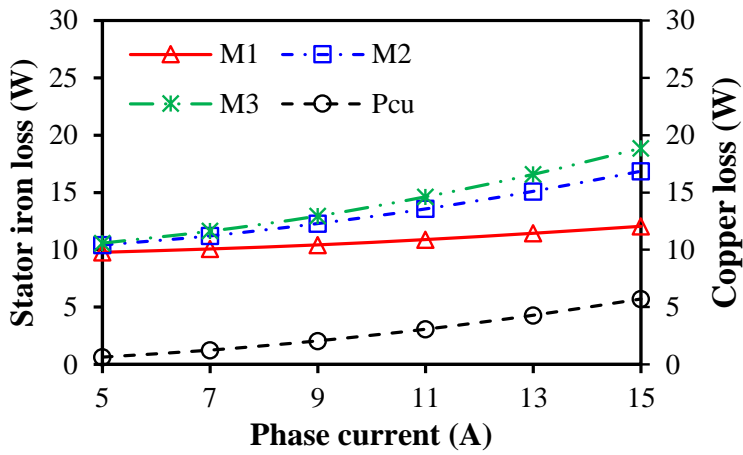


Fig. 2. 24. Relationships between stator iron loss, copper loss, and phase current in the motors with different winding configurations neglecting end-windings,  $B_{max}=0.8T$ ,  $\lambda=0.34$ .

### B. Accounting for end-winding copper loss

Accounting for the end-winding copper loss, the variations of maximum torque with  $B_{max}$  and slot-pitch are shown in Fig. 2. 25. Compared with the first scenario, the end-winding copper loss significantly decreases the maximum torques of three motors, however, the optimal  $B_{max}$  remains unchanged since the stator iron loss is the dominant loss. With the optimal  $B_{max}$ , the average torque climbs up and then decline with the split ratio, and three motors have almost the same optimal split ratio, Fig. 2. 26. Compared with the first scenario, the end-winding copper loss reduces the electrical loading, and thus the optimal split ratio is decreased, especially for the motors with 2 and 3 slot-pitch windings. With the increase of slot-pitch, the stator iron loss and end-winding copper loss increase synchronously, which results in a

canceling effect. Therefore, accounting for the end-winding copper loss, three motors with different slot-pitch windings have almost the same optimal split ratio and  $B_{max}$  for maximum torque. Although the optimal split ratio exists, the average torque increases and decreases slowly before and after reaching the maximum value, respectively. In other words, the average torque is insensitive to the split ratio around the optimal split ratio since the stator iron loss is the dominant loss.

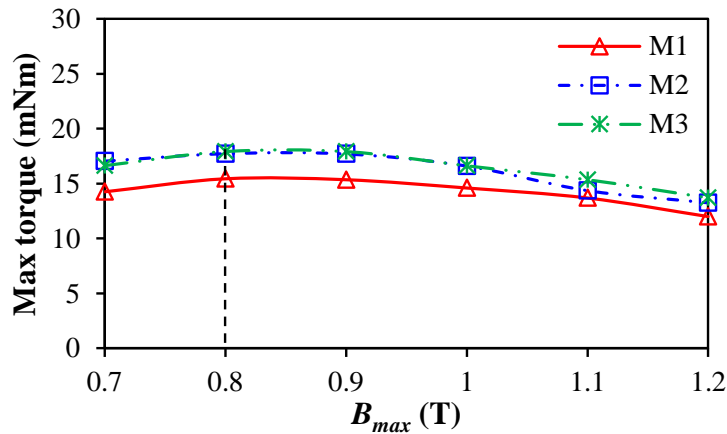


Fig. 2. 25. Relationship between maximum torque and  $B_{max}$  in the motors with different winding configurations considering end-winding copper loss only.

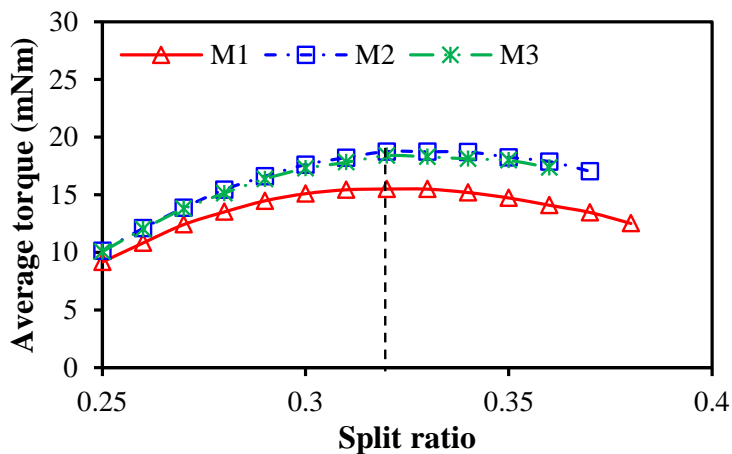


Fig. 2. 26. Relationship between average torque and split ratio in the motors with different winding configurations considering end-winding copper loss only,  $B_{max}=0.8T$ .

### C. Accounting for end-winding copper loss and axial length

As mentioned before, the motors with 2 and 3 slot-pitch windings have large average torques, but they also have relatively long end-winding axial lengths, which may lead to low torque densities. Therefore, accounting for the end-winding copper loss and axial length, three motors



will be optimized for maximum torque density in this section, rather than the maximum torque as described earlier. The relationship between maximum torque density and  $B_{max}$  is shown in Fig. 2. 27, and three motors have the same optimal  $B_{max}$ , which is the same as that in the first and second scenarios. Compared with the second scenario, the optimal split ratio of M1 is slightly smaller, but those of M2 and M3 remain unchanged, Fig. 2. 28, since the motor axial length of M1 increases mildly with the increase of split ratio while those of M2 and M3 almost remain unchanged, Fig. 2. 29. However, the torque density of M1 increases and decreases slowly before and after reaching the maximum value, respectively, and thus for maximum torque density, the optimal split ratios of three motors can be considered almost identical, which is the same as that in the second scenario.

In summary, with a fixed stator thermal limitation, the end-winding copper loss, end-winding axial length, and slot-pitch have negligible influence on the optimal  $B_{max}$  since the stator iron loss is dominant. Compared with the first scenario, the optimal split ratios and average torques of three motors are reduced by accounting for the end-winding copper loss. Compared with the second scenario, the end-winding axial length has almost no influence on the optimal design. Therefore, accounting for end-windings, three 6s/2p HSPM motors with 1, 2, and 3 slot-pitch windings have the same optimal design no matter for maximum torque or maximum torque density, as shown in Table 2. 3.

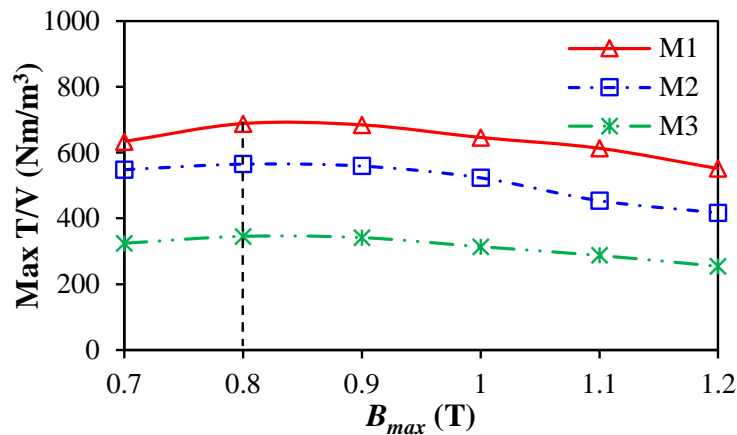


Fig. 2. 27. Relationship between maximum torque density and  $B_{max}$  in three motors considering end-winding copper loss and axial length.

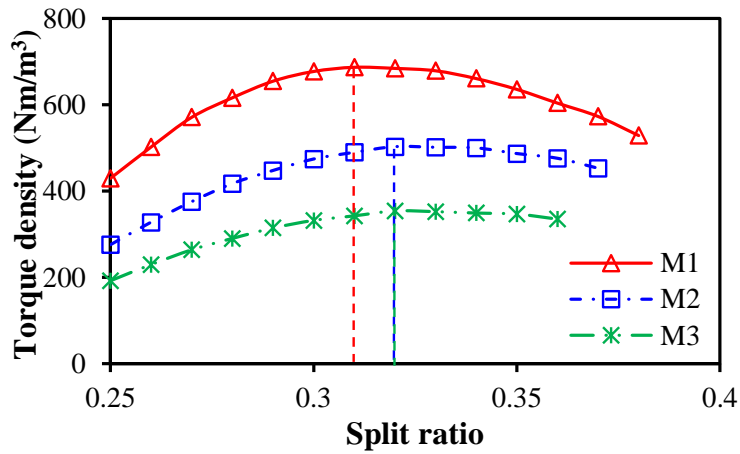


Fig. 2. 28. Relationship between maximum torque density and split ratio in three motors considering end-winding copper loss and axial length,  $B_{max}=0.8T$ .

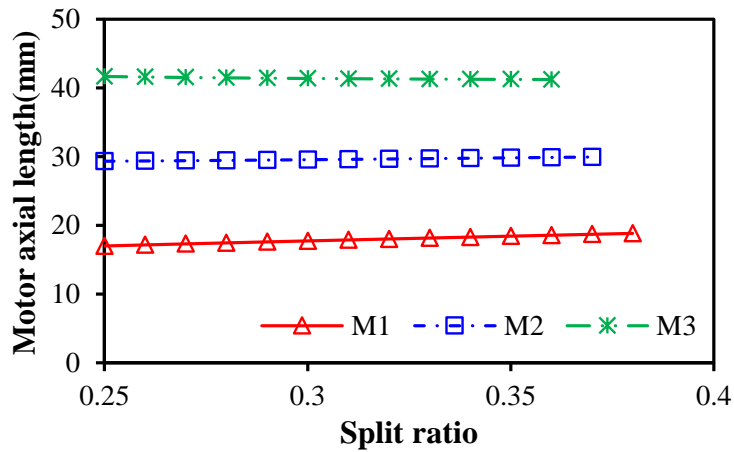


Fig. 2. 29. Relationship between motor axial length and split ratio in three motors considering end-winding copper loss and axial length,  $B_{max}=0.8T$ .

## 2.4 Electromagnetic Performance of Optimized Motors

In this section, with a fixed stator active length, the electromagnetic performances of three 6s/2p HSPM motors with 1, 2, and 3 slot-pitch windings are analyzed and compared, including open-circuit  $B_g$ , back-EMF, electromagnetic torque, winding inductances, and various loss components.

Table 2. 3

## Optimized Design Parameters (180KRPM)

Motor type	M1	M2	M3
Stator outer diameter, mm	40		
Stator active length, mm	9.6		
Thermal limitation, W	18.1		
Optimal split ratio	0.32		
Maximum stator iron flux density, T	0.8		
Phase current, A	12.1	8.4	7.2
Torque, mNm	15.5	18.6	18.4
Torque ripple, %	12.6	12.1	12.4
End-winding axial length (both), mm	8.40	17.36	26.30
Motor axial length, mm	18.00	26.96	35.90
Torque density, Nm/m <sup>3</sup>	680.80	549.01	407.86
Stator iron loss, W	10.6	11.6	11.3
Copper loss, W	7.4	6.4	6.8
Rotor loss, W	3.5	5.1	5.0
Motor total loss, W	21.5	23.1	23.1
Output power, W	292.2	350.6	346.8
Efficiency, %	93.2	93.8	93.8

### 2.4.1 Open-circuit Air-gap Field

Since the coil-pitch does not affect not only the open-circuit air-gap field but also the optimal design for the specific application, as mentioned above, only the optimized motor with 1 slot-pitch windings (M1) is analyzed. Figs. 2. 30 and 31 show the equipotential and flux contour distributions of M1 and the open-circuit air-gap field distribution. Due to 2-pole magnet with parallel magnetization, the open-circuit air-gap flux density waveform is almost sinusoidal, and there are almost no harmonics except those due to slotting.

### 2.4.2 Back-EMF

The back-EMF waveforms of three motors with 1, 2, and 3 slot-pitch windings are sinusoidal and there are almost no harmonics, as shown in Fig. 2. 32. The spectra show that three motors have different fundamental magnitudes, which correspond with their winding factors, i.e., 0.5, 0.866, and 1.

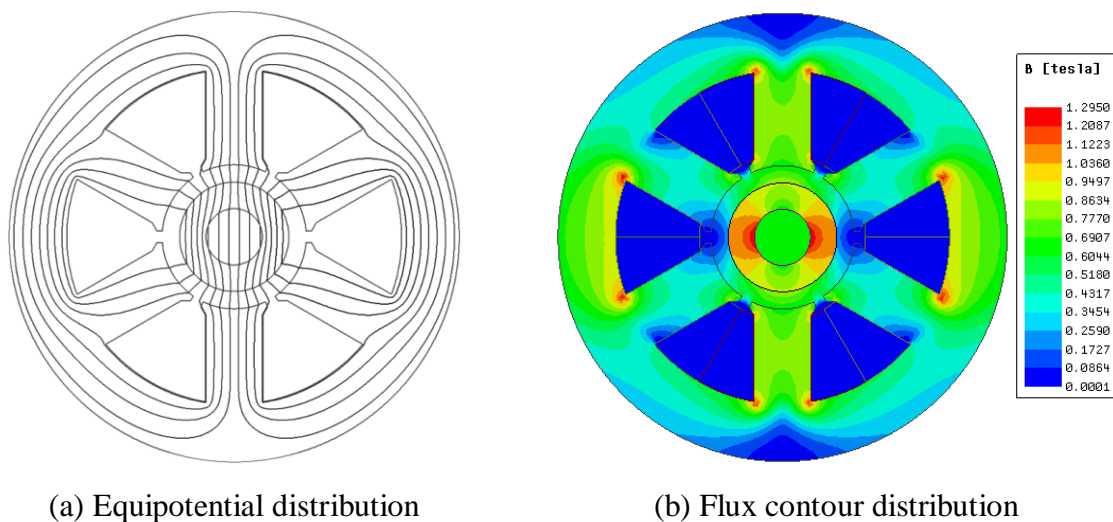
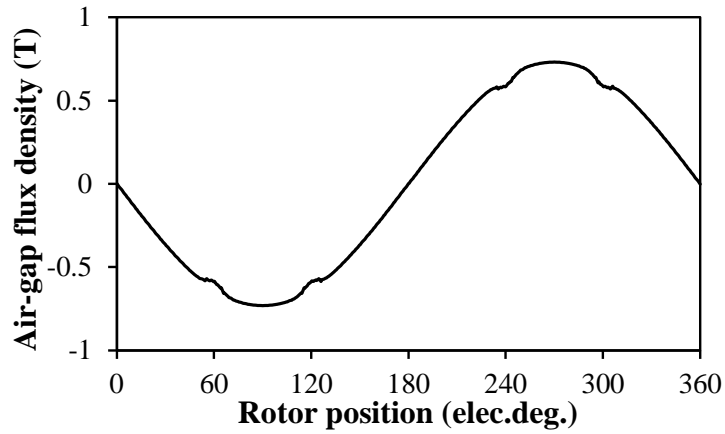
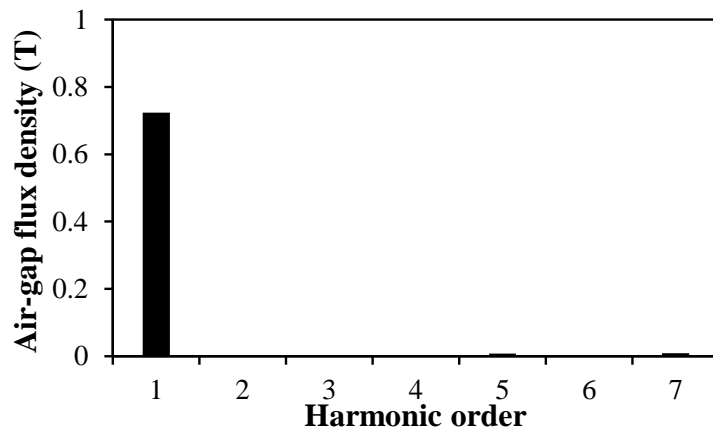


Fig. 2. 30. Equipotential and flux contour distributions of the optimized motor with 1 slot-pitch windings.

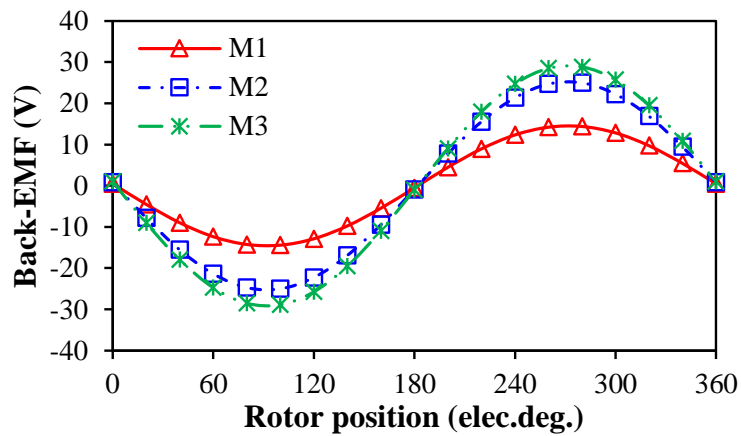


(a) Waveform

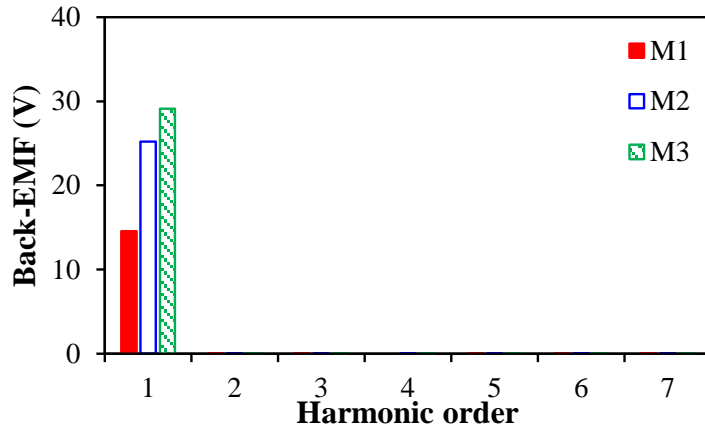


(b) Spectra

Fig. 2. 31. Open-circuit air-gap field distribution of the optimized motor with 1 slot-pitch windings.



(a) Waveforms



(b) Spectra

Fig. 2. 32. Back-EMF waveforms of motors with 1, 2, and 3 slot-pitch windings, 180krpm, phase A.

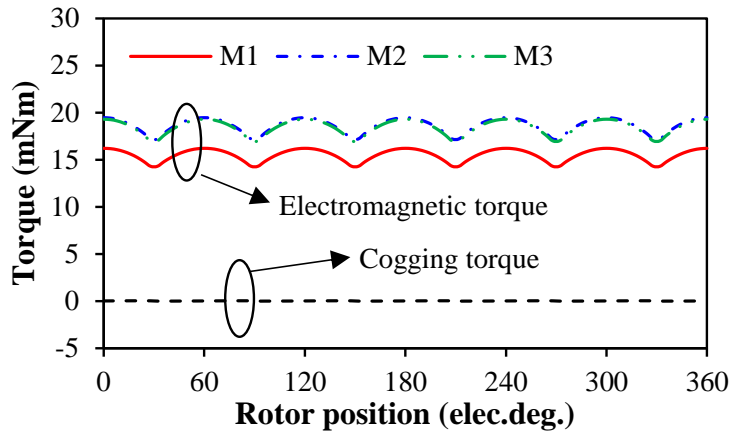
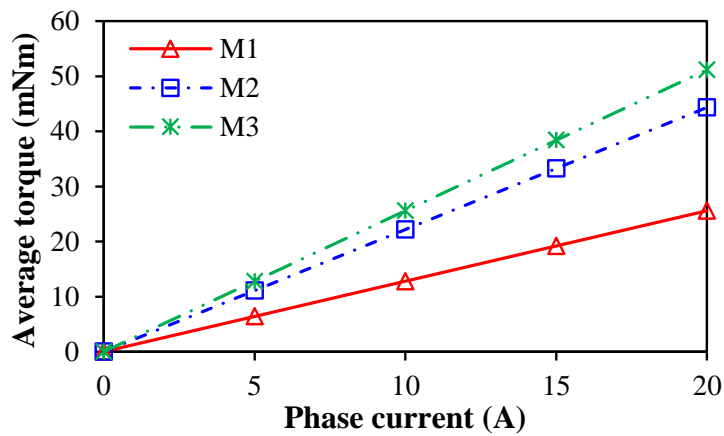
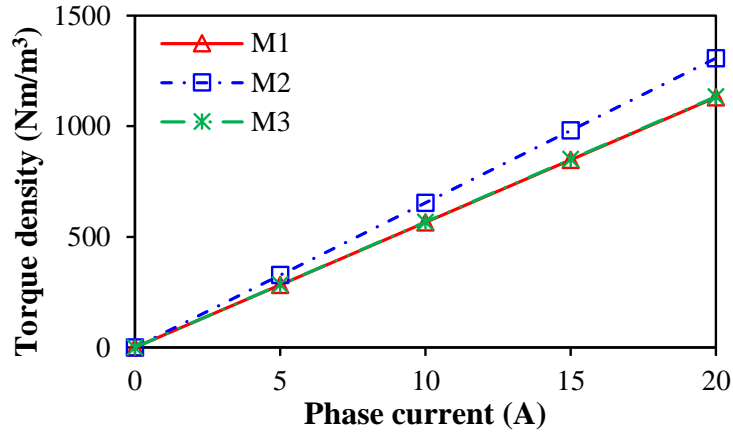


Fig. 2. 33. Rated electromagnetic torque and cogging torque waveforms of three motors with 1, 2, and 3 slot-pitch windings.



(a) Average torque



(b) Torque density

Fig. 2. 34. Variation of average torque and torque density with phase current of three motors with 1, 2, and 3 slot-pitch windings, without stator thermal limitation.

### 2.4.3 Electromagnetic Torque

The rated electromagnetic torque and cogging torque waveforms of three motors with 1, 2, and 3 slot-pitch windings are shown in Fig. 2. 33. With the same maximum stator loss, the motor with 1 slot-pitch windings has the smallest rated torque. M2 and M3 have almost the same rated torque. In addition, three motors have almost the same torque ripple. There is almost no cogging torque in three 6s/2p HSPM motors due to diametrically-magnetized magnet. The average torques and torque densities versus phase currents of three HSPM motors are compared in Fig. 2. 34. The average torques correspond to the winding factors of three motors, and the torque density of the motor with 2 slot-pitch windings is the largest since it has a good trade-off between winding factor and end-winding axial length.

### 2.4.4 Winding Inductances

For the small size HSPM motor, sensorless control is employed widely and the winding inductance is a key parameter. Therefore, the influence of slot-pitch on the self-and mutual-inductances is investigated by 2-D and 3-D FE models.

It is assumed that only phase A is excited, i.e.  $I_A=1A$ ,  $I_B=I_C=0A$ , and two coils from the same phase are connected in parallel. Fig. 2. 35 shows the flux distributions of three 6s/2p HSPM motors when only phase A is excited and Fig. 2. 36 shows the 3-D FE models of three motors. The self- and mutual-inductances of 2-D and 3-D FE models are shown in Table 2. 4. In 2-D FE models without end-windings, the self-inductances increase with the increase of slot-pitch and that of M3 is almost doubled compared with M1. In the slot of M3, two same phase

conductors have the same current polarity, which produces the positive mutual-inductance between two conductors and subsequently doubles the self-inductance, Fig. 2. 35 ©. In M1, two different phase conductors with the same connection polarity are located at the sides of the slot, which leads to the positive mutual-inductance. However, in M2, two different phase conductors with the opposite connection polarities are located at the sides of the slot, which leads to the negative mutual-inductance. In M3, compared with self-inductance, the mutual inductance is small and can be neglected as in one slot there is only one phase winding.

According to 3-D FE models, the end-region components of self-and mutual-inductances can be calculated, Table 2. 4. The motor with 3 coil-pitch windings has the longest end-winding axial length, thus the largest end-winding inductances, while that in the motor with 1 coil-pitch windings is the smallest.

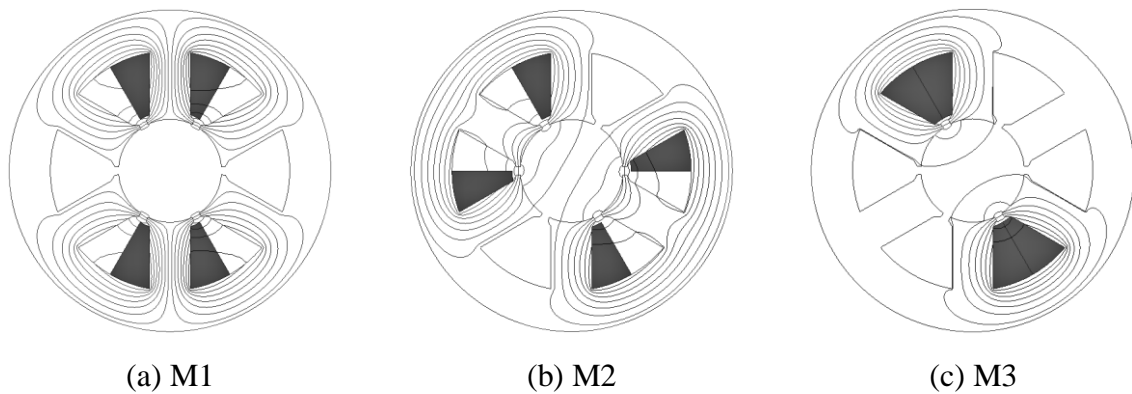


Fig. 2. 35. Flux distributions of 6s/2p motors with 1, 2, and 3 slot-pitch windings when only phase A is excited.

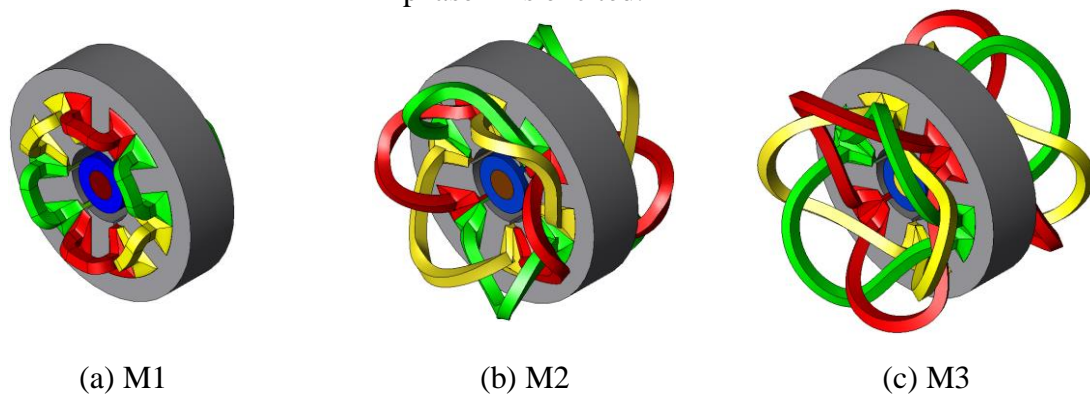


Fig. 2. 36. 3-D FE models of 6s/2p motors with 1, 2, and 3 slot-pitch windings.



Table 2. 4

Winding Inductances of Three Motors ( $\mu\text{H}$ )

		2-D FE	3-D FE	End-windings
M1	Self-	13.85	20.29	6.44
	Mutual-	5.13	6.16	1.03
	Phase-	8.72	14.12	-
M2	Self-	16.60	25.79	11.67
	Mutual-	-7.88	-10.62	-3.76
	Phase -	24.48	36.41	-
M3	Self-	29.76	49.75	20.73
	Mutual-	-2.75	-7.30	-4.60
	Phase-	32.51	57.05	-

#### 2.4.5 Loss Analysis

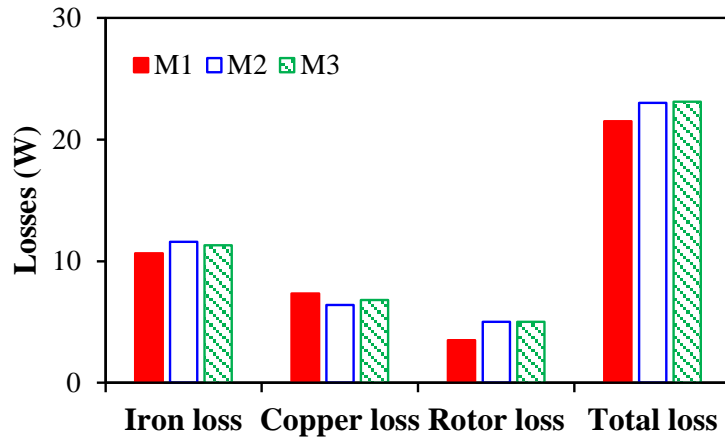
The various loss components of three 6s/2p HSPM motors with 1, 2, and 3 slot-pitch windings are shown in Fig. 2. 37 (a), including stator iron loss ( $P_{iron}$ ), copper loss ( $P_{cu}$ ) including end-winding, and rotor eddy current loss ( $P_{rotor}$ ). Since three optimized motors have different output powers, the losses per output power are also compared, as shown in Fig. 2. 37 (b).

##### A. Stator iron loss

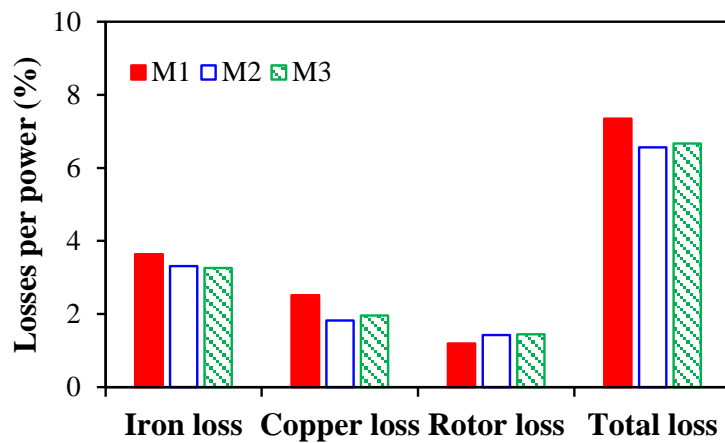
The on-load stator iron loss is calculated by FEM accounting for the space harmonics of stator magnetomotive force (MMF), the space harmonics due to slotting, and time harmonics of 120° electric square wave current waveforms [ATA92]. The stator iron losses increase with the phase current and the coil-pitch, Fig. 2. 38. The reason has been mentioned before, but it can also be explained by on-load stator iron flux density. Since the stator iron loss depends on the frequency and flux density squared, the small difference of stator iron flux density will result in the large difference of stator iron loss. Fig. 2. 39 shows that M1 has the smallest fundamental magnitude of on-load stator iron flux density, which results in the smallest stator iron loss. M3 has larger magnitudes of the 3<sup>rd</sup> and 7<sup>th</sup> order harmonics than M2, thus larger stator iron loss.

Three optimized motors with different slot-pitch windings have different phase currents to meet

the stator thermal limitation and different output powers. Fig. 2. 37 (a) shows that although M1 and M2 have the smallest and largest stator iron losses, respectively, the stator iron loss per power decreases with the slot-pitch, Fig. 2. 37 (b).



(a) Losses



(b) Losses per power

Fig. 2. 37. Comparison of stator iron loss, copper loss, PM loss, and total loss of three motors.

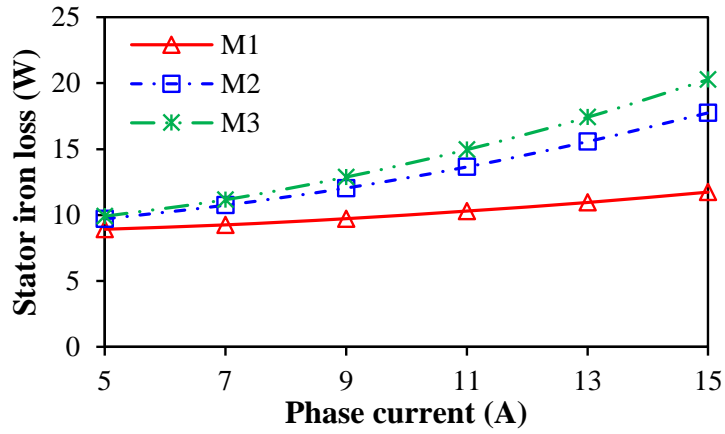
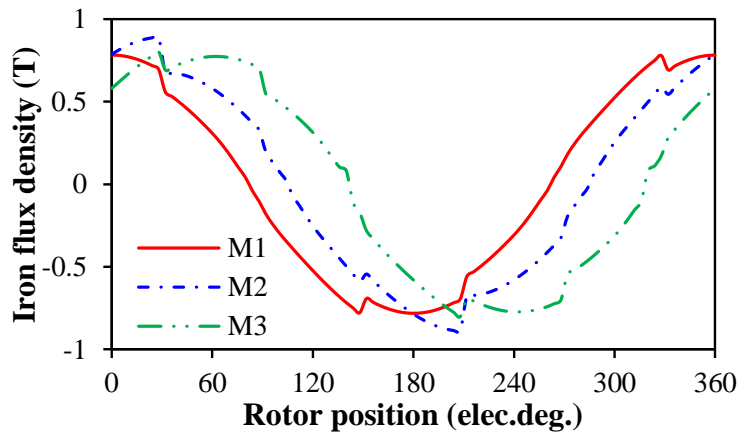
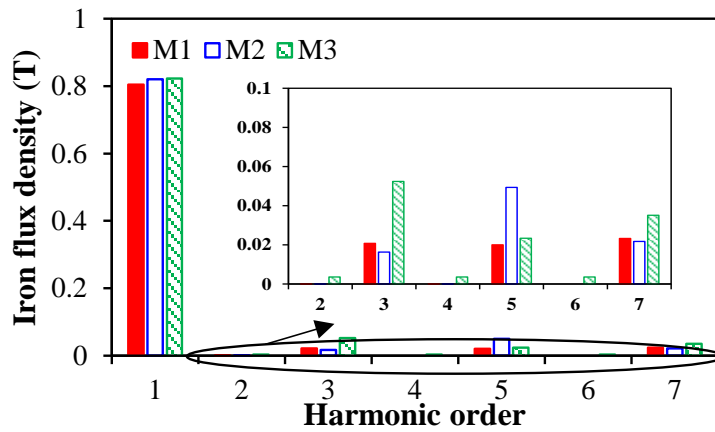


Fig. 2. 38. Variation of stator iron loss with phase current and slot-pitch,  $B_{max}=0.8T$ ,  $\lambda=0.32$ .



(a) Waveforms



(b) Spectra

Fig. 2. 39. Stator tooth iron flux density distributions of three optimized motors with 1, 2, and 3 slot-pitch windings,  $I_{max}=12A$ .

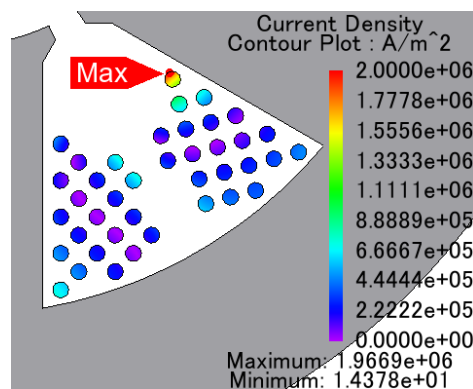
## B. Copper loss

In HSPM motors, the copper loss consists of two parts, DC and AC copper losses. The AC copper losses mainly result from the skin effect and proximity effect. To avoid the skin effect, the diameter of conductors should be less than the skin depth ( $\delta$ ) [UZH14], which can be calculated by

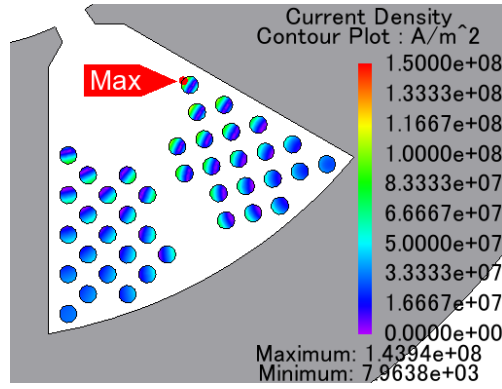
$$\delta = \sqrt{\frac{\rho}{\pi f \mu}} \quad (2.24)$$

In this thesis, the frequency is 3000 Hz and the skin depth is 1.2mm. Hence, the skin effect can be mitigated since the diameter of the conductor is less than the skin depth. In addition, fixing the coils deeper in the slot can reduce proximity losses [MEL06].

Fig. 2. 40 shows the current density distributions of conductors in the slot with and without phase current at 180krpm. When there is no current, the conductors at the top of slot still have the proximity currents. When the phase current is 12A, the conductors have larger current density, which results from high eddy and proximity currents. Fig. 2. 41 shows the ratio of AC resistance ( $R_{AC}$ ) to DC resistance ( $R_{DC}$ ) remains unchanged with the rise of phase current and the results also mean the AC copper loss is small and can be neglected in this chapter. According to the results in [WRO10], the proximity effect in the end-windings is significantly lower compared to those in the active length of the conductors. Therefore, AC copper loss is neglected in this chapter and the motor with larger end-winding length has larger DC copper loss.



(a) Phase current = 0A



(b) Phase current = 12A

Fig. 2. 40. Current density distributions of conductors in the slot with and without phase current at 180 krpm.

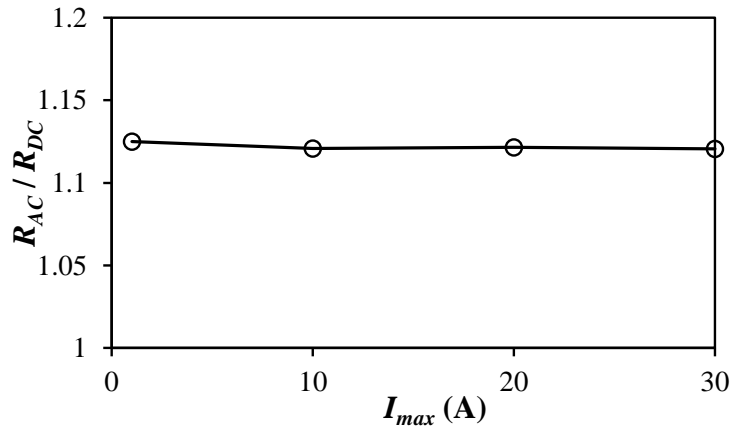


Fig. 2. 41. Variation of the ratio of  $R_{AC}$  to  $R_{DC}$  with phase current at 180krpm, without end-windings.

### C. Rotor loss

In this chapter, the rotor loss includes eddy current losses in the stainless-steel sleeve, magnet, and shaft. Generally, rotor eddy current losses in HSPM BLDC motors results from space harmonics due to stator slotting, space harmonics of MMF, and time harmonics due to armature current. Fig. 2. 42 describes the relationship between rotor loss and phase current with different coil-pitch. Both slot-pitch and phase current affect the rotor loss by the space harmonics of MMF and time harmonics of armature current, respectively. Fig. 2. 43 shows that with a fixed phase current, three motors with 1, 2, and 3 slot-pitch windings have the same fundamental magnitude of on-load  $B_g$ . However, the spectra show that the motor with 3 coil-pitch windings has the largest magnitudes of the 5<sup>th</sup> and 7<sup>th</sup> order harmonics, which will cause the largest 6<sup>th</sup> harmonic in the rotor. In Fig. 2. 44 (I), the maximum rotor loss increases with the coil-pitch,

as well as all rotor loss components, Fig. 2. 44 (II-a), but the ratio of each rotor loss component to total rotor loss remains almost unchanged, Fig. 2. 44 (II-b).

For three optimized motors with the same stator loss limitation, M1 with the largest rated phase current has the smallest magnitudes of the 5<sup>th</sup> and 7<sup>th</sup> order harmonics of on-load  $B_g$  due to the smallest space harmonics of armature MMF, Fig. 2. 45. M2 and M3 have almost the same rotor loss. Table 2. 5 shows different rotor loss components of three optimized motors. With the same stator loss, the motor efficiency depends on the rotor loss and output power. Although M1 has the smallest rotor loss, the smallest output power leads to the largest total motor loss per power and the lowest efficiency. M2 and M3 have the largest total motor loss per power and the highest efficiency due to the largest output power.

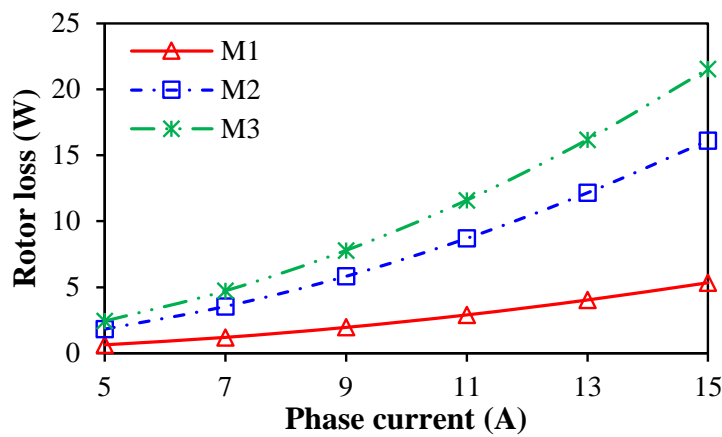
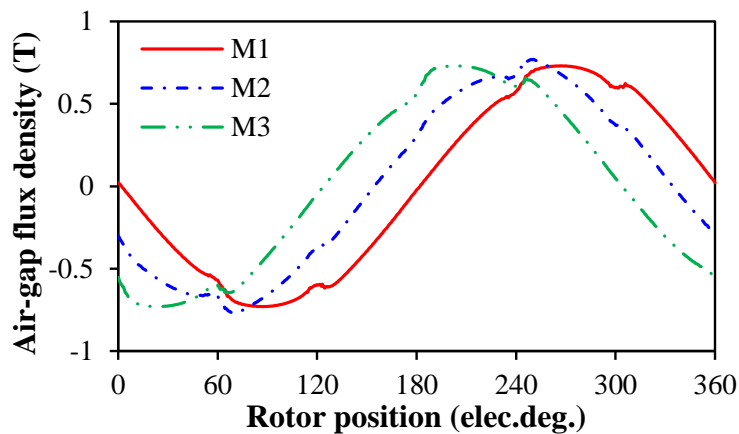
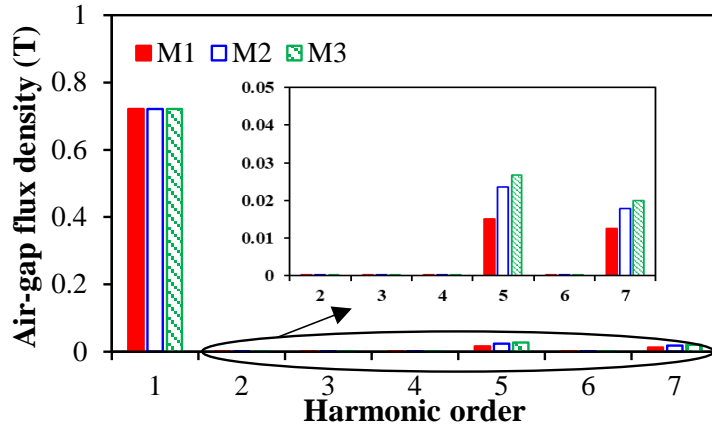


Fig. 2. 42. Variation of rotor PM loss with the phase current and slot-pitch,  $B_{max}=0.8T$ ,  $\lambda=0.32$ .

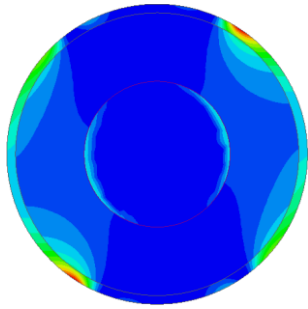


(a) Waveforms



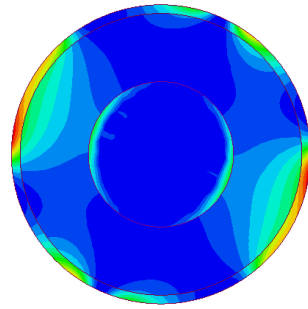
(b) Spectra

Fig. 2. 43. Air-gap field distributions of three optimized motors with 1, 2, and 3 slot-pitch windings,  $I_{max}=12A$ .



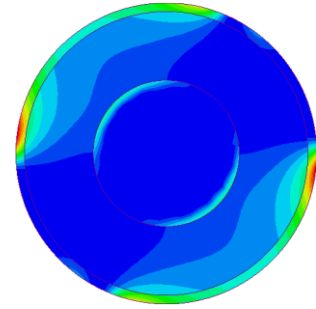
$Loss_{max}=1.30e7W/m^3$

(a) M1



$Loss_{max}=2.68e7W/m^3$

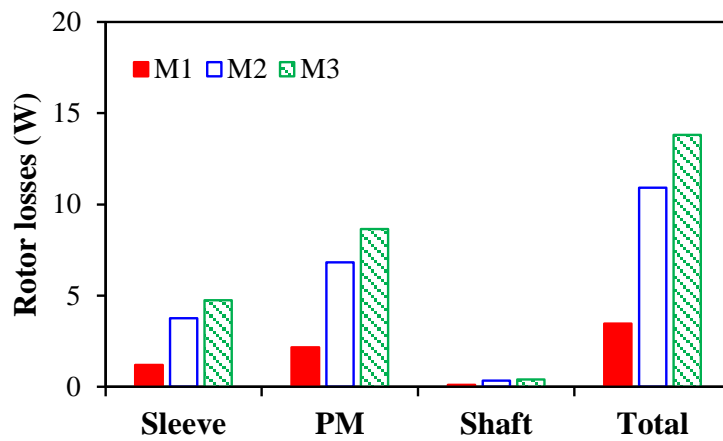
(b) M2



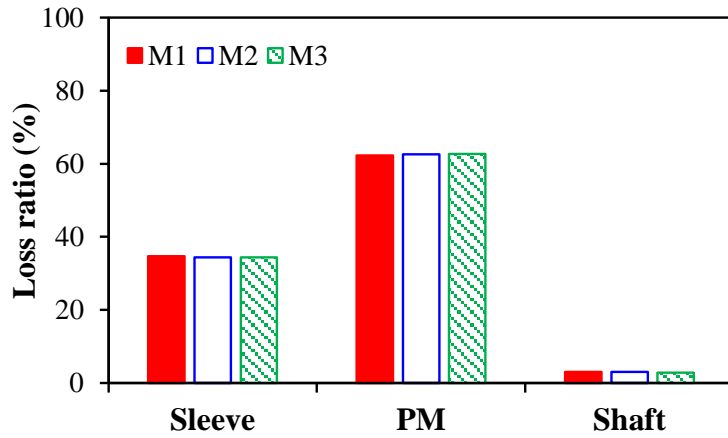
$Loss_{max}=4.20e7W/m^3$

(c) M3

(I) Rotor eddy current loss distributions



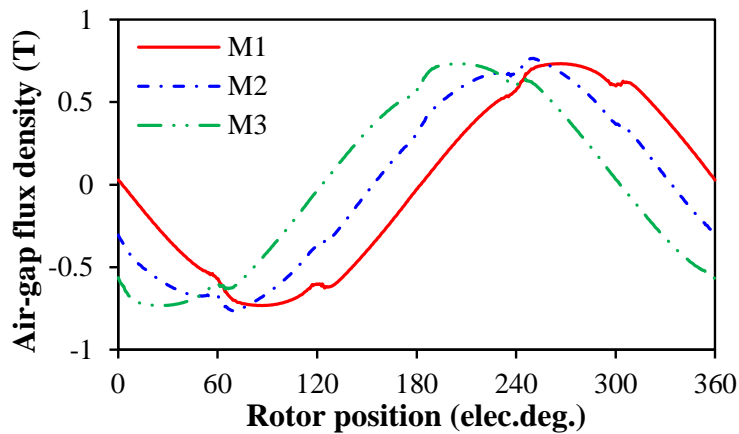
(a) Rotor loss component values



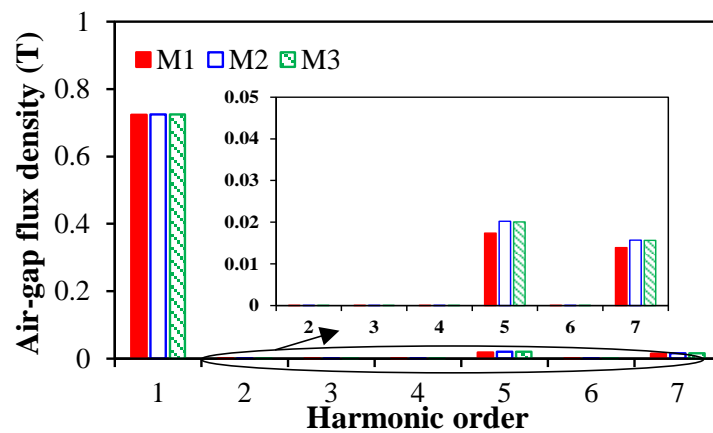
(b) Rotor loss component ratios

(II) Rotor eddy current loss components

Fig. 2. 44. Rotor eddy current loss distributions and components of three optimized motors with 1, 2, and 3 slot-pitch windings,  $I_{max}=12A$ .



(a) Waveforms



(b) Spectra

Fig. 2. 45. Air-gap field distributions of three optimized motors with different phase currents.



Table 2. 5

Rotor Loss Components of Three Optimized Motors (W)

	$I_{max}$ (A)	Sleeve	PM	Shaft	Total
M1	12.1	1.2	2.2	0.1	3.5
M2	8.4	1.8	3.2	0.1	5.1
M3	7.2	1.7	3.1	0.1	5.0

## 2.5 Influence of End-windings

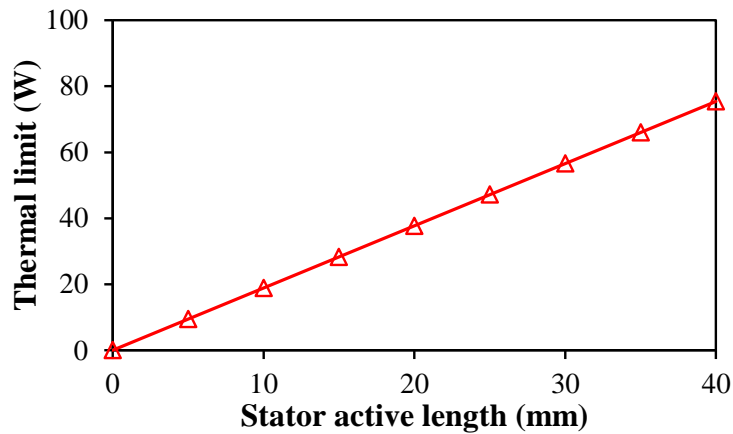
With different stator active lengths, the influence of end-windings is investigated in this section. In theory, when the stator active length is assumed to be infinite, the end-windings can be neglected, which is the same as that of the first scenario in section 2.3.3, and three motors have the same optimal  $B_{max}$  but different optimal split ratios. However, for high-speed applications, the improper design of motor axial length will lead to rotor dynamic issues [EDE02] [LIS16]. In addition, with the increase of stator active length, the average torque becomes less sensitive to the split ratio since the ratio of stator iron loss to stator total loss increases. Therefore, in this section, the maximum allowed stator active length is defined as the same as the stator outer diameter, i.e. 40mm, and the motors with different stator active lengths have the same optimized design. In addition, the end-winding axial lengths of three motors with different slot-pitch windings remain unchanged with the variation of stator active length.

With the increase of stator active length, the stator thermal limitation increases linearly and the average torques of three motors increase, Fig. 2. 46. It shows that M2 and M3 have almost the same average torque, which is larger than that of M1, and the torque difference between M1 and M2 increases with the increase of stator active length, which means M2 has an advantage of large output torque, especially for the relatively large stator active length, so does M3.

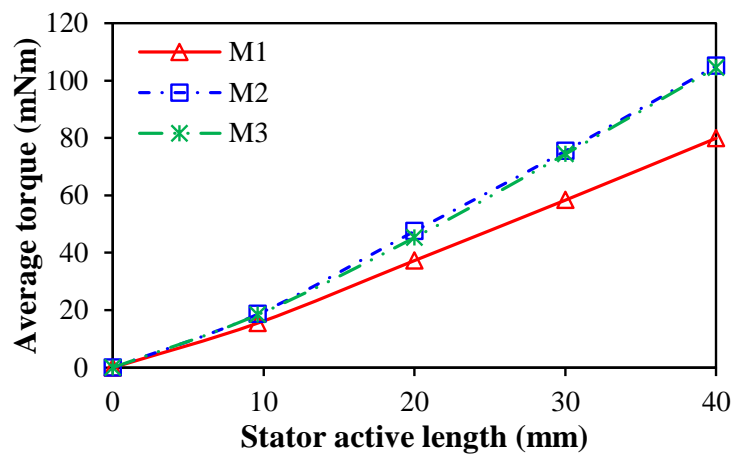
With the increase of stator active length, the ratio of end-winding axial length to motor axial length decreases rapidly at first and then changes mildly, especially for M1, Fig. 2. 47. When  $l_a > 30\text{mm}$ , M2 has the highest torque density due to the largest output torque and relatively short end-winding axial length, Fig. 2. 48. Therefore, the increased stator active length decreases the influence of end-winding axial length on the torque density. It is worth noting that the torque density difference ratio between M1 and M2 is smaller than torque difference

ratio when  $l_a > 14\text{mm}$ , Fig. 2. 49. Therefore, M2 has a better trade-off between torque and torque density when the stator active length is larger than 14mm in this case.

In summary, with the relatively small stator active length, M1 has the highest torque density but the smallest output torque due to the lowest winding factor. With the relatively large stator active length, M2 offers advantages in large output torque and high torque density. M3 with large output torque also could be considered when the stator active length is significantly large.



(a) Stator thermal limit



(b) Average torque

Fig. 2. 46. Variation of stator thermal limit and average torque with stator active length.

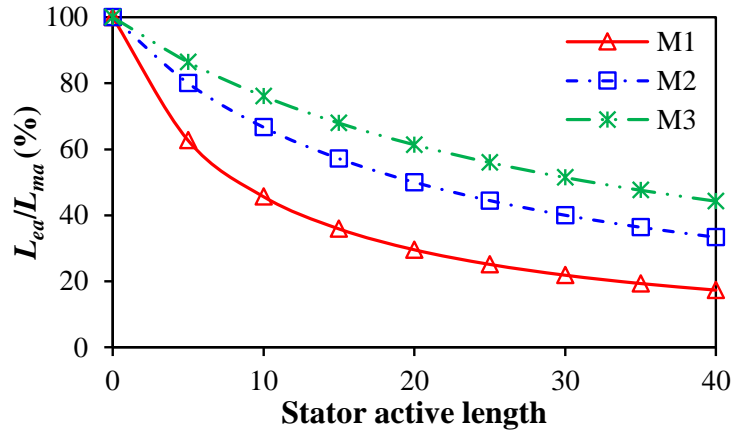


Fig. 2. 47. Variation of the ratio of end-winding axial length to motor axial length with stator active length.

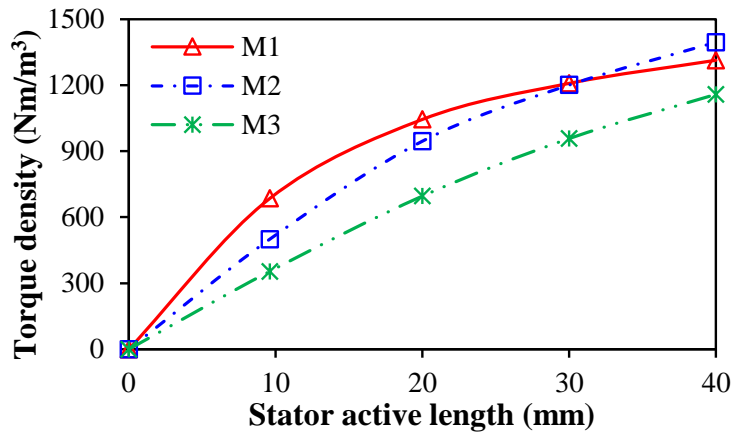


Fig. 2. 48. Variation of torque density with stator active length.

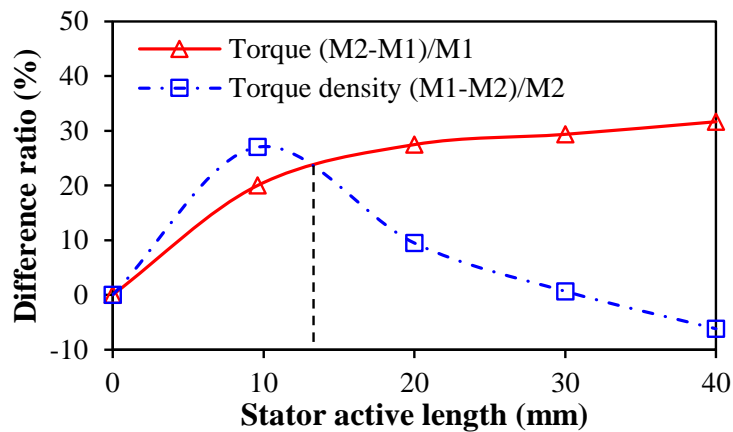


Fig. 2. 49. Variation of torque and torque density difference ratios between M1 and M2 with stator active length.

## 2.6 Experimental Validation

Three optimized motors with 1, 2, and 3 slot-pitch windings are prototyped, Fig. 2. 50. Fig. 2. 51 shows the rotor-bearing system, air duct system, and house of the prototype for high-speed operation. The predictions by FEM and measurement of back-EMFs of phase A in three prototypes are compared in Fig. 2. 52, and have a good agreement. Table 2. 6 shows that the measured motor axial lengths of three prototypes are consistent with those of the FE models. Due to manual winding, the prototypes have larger measured resistances compared with the analytical predictions. In addition, although the measured resistances under high frequency (3kHz) are larger than those DC resistances, the ratio of AC to DC resistances in M1 is around 1.7, but that in M2 and M3 are around 1.3 due to the larger end-winding length. The winding inductances of three motors are measured by an LCR meter (HIOKI IM3533-01). In 3-D FE model, the effect of frequency is neglected, and the predicted winding inductances are ideal. Therefore, the predictions and measurements of winding inductances at 1.0 Hz have a good agreement, Table 2. 7. With high frequency (3000 Hz), the measured inductances become smaller due to the skin effect.



Fig. 2. 50. Three prototypes of 6s/2p HSPM motors with 1, 2, and 3 slot-pitch windings.

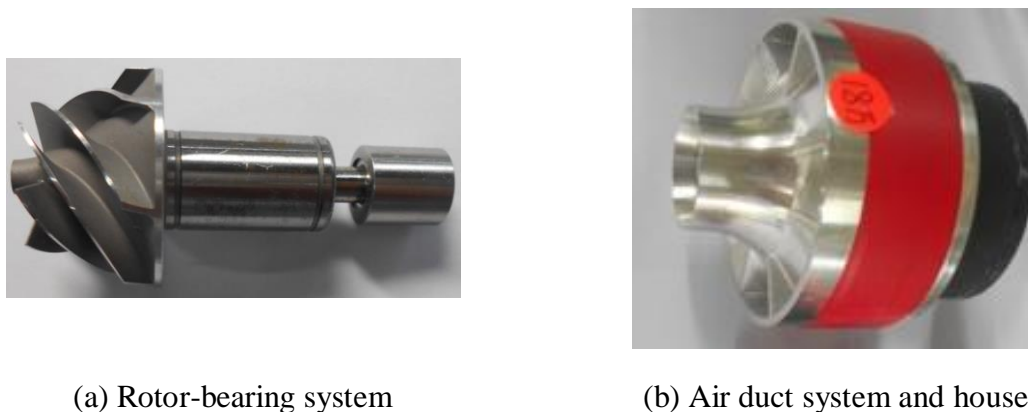
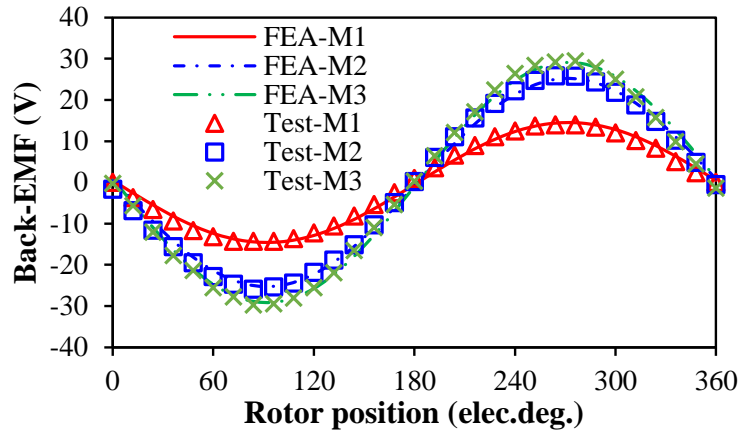
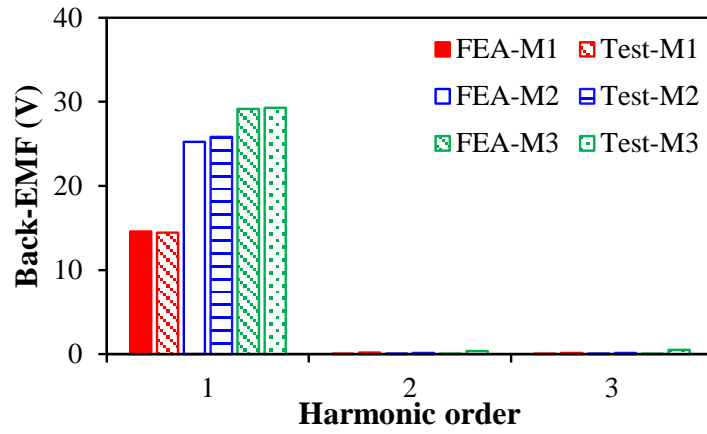


Fig. 2. 51. Rotor-bearing system, air duct system, and house of the prototype.



(a) Waveforms



(b) Spectra

Fig. 2. 52. Predictions and measurements of back-EMFs of phase A in three prototypes.

Table 2. 6

Resistances and Motor Axial Lengths of Motors with 1, 2, and 3 Slot-pitch Windings

	Motor axial length (mm)		Resistance (mΩ)		
	Analytical model *	Measured	Analytical model	Measured (DC)	Measured (3kHz)
M1	18.0	18.0	37.7	48.5	81.3
M2	27.0	27.3	71.3	99.1	133.8
M3	35.9	34.0	101.6	114.0	153.6

\*Note:  $\theta$  (M2) = 40°;  $\theta$  (M3) = 30°;  $l_{ex}$  = 1mm.

Table 2. 7

Inductances of Motors with 1, 2, and 3 Slot-pitch Windings ( $\mu\text{H}$ )

	M1	M2	M3
3-D FE	14.12	36.41	56.70
Measured (1.0Hz)	15.45	37.52	47.05
Measured (3kHz)	14.26	26.18	35.06

The experiment system of static torque measurement is shown in Fig. 2. 53 [ZHU09]. In this test rig, the jaws of lathe are employed to clamp the prototype, and the static torque can be transformed into the force, which can be measured by a digital scale. There is a weight at the end of balance beam to ensure the positive pressure on the digital scale. The phase currents of  $I_A = -I_B = 5 \text{ A}$ ,  $I_C = 0 \text{ A}$  are fed by the DC supply, which corresponds to three phase  $120^\circ$  electric square wave current waveforms. Fig. 2. 54 shows the predictions by FEM and measurements of static torques of three prototypes at different rotor positions and they have a good agreement. The maximum static torque increases with the increase of phase current linearly, and three prototypes have almost the same FE predicted and measured results, Fig. 2. 55. Fig. 2. 56 shows the measured current and voltage waveforms at 180 krpm for the motor with 2 slot-pitch windings.

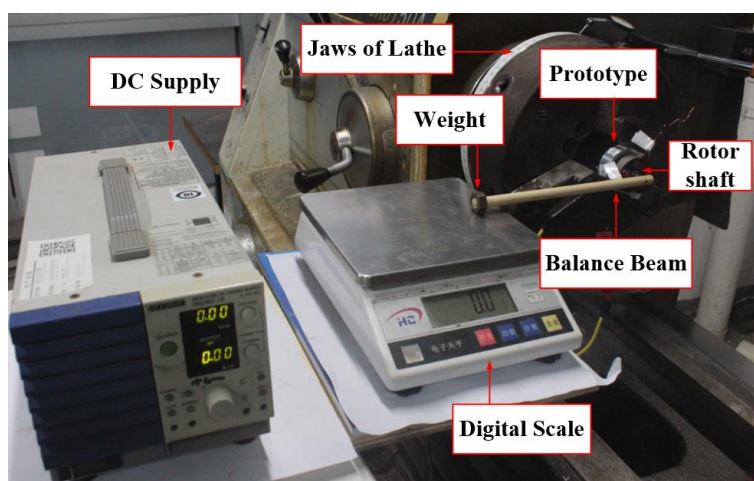


Fig. 2. 53. Experiment system of static torque measurement.

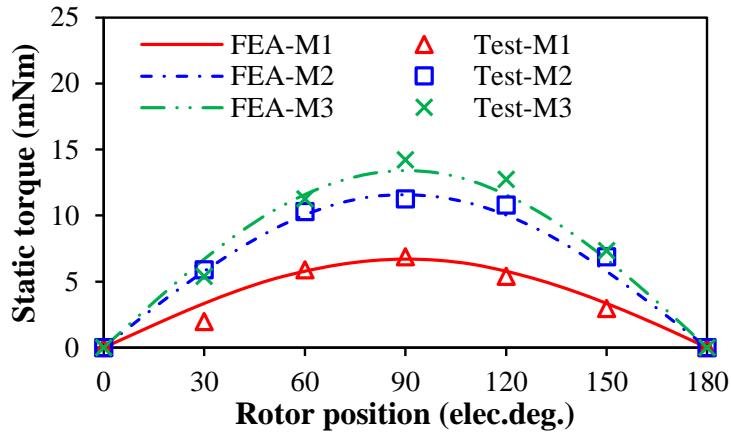


Fig. 2. 54. Predictions and measurements of static torques under the phase currents of  $I_A = -I_B = 5 \text{ A}$ ,  $I_C=0\text{A}$ .

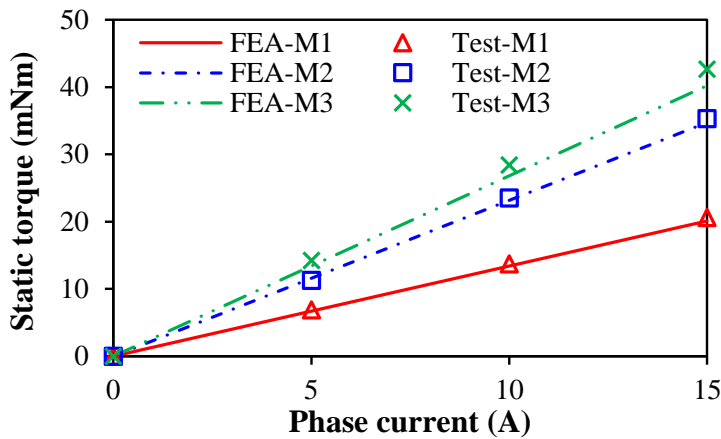


Fig. 2. 55. Predictions and measurements of maximum static torques with various phase currents.

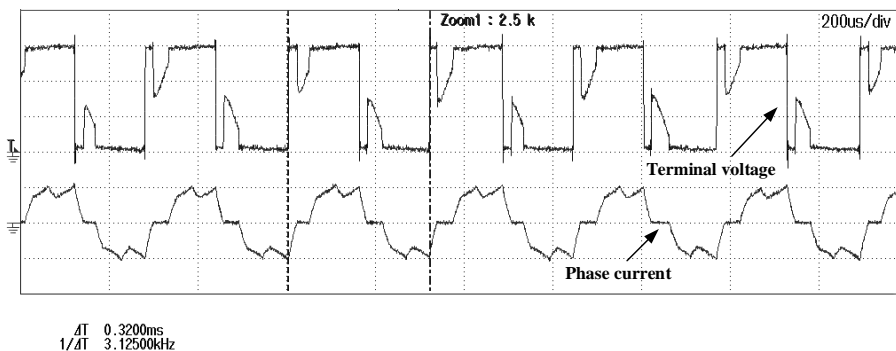


Fig. 2. 56. Measured phase current and terminal voltage waveforms of the motors with 2 slot-pitch windings at the rated speed 180 krpm under speed control (10.0V/div; 20.0A/div).

## 2.7 Conclusion

Three 6s/2p HSPM motors with 1, 2, and 3 slot-pitch windings have been optimized by analytical and FE methods under different optimal conditions and scenarios. It shows that the method by fixing total stator loss, considering the influence of end-winding and the stator iron loss, is suitable for the optimization of the HSPM motors with different slot-pitch windings. When considering the end-windings, the slot-pitch has significant influence on the winding factor, end-winding length, and end-winding axial length, but has negligible influence on the optimal split ratio and  $B_{max}$  due to the canceling effect. With a fixed stator active length, the electromagnetic performances of three optimized motors have been analyzed and compared. The results show that the torques and efficiencies of the motors with 2 and 3 slot-pitch windings are larger than those in the motor with 1 slot-pitch windings. The 3 slot-pitch windings lead to the lowest torque density due to the longest end-winding axial length, but results in the largest phase inductance. However, the influence of end-winding axial length on the torque density decreases with the increase of stator active length. Therefore, for high-speed applications, compared with 1 and 3 slot-pitch windings, the motor with 2 slot-pitch windings has a good trade-off between winding factor and end-winding axial length which are attractive for improved torque density. Three motors have been prototyped and tested. The measured results have a good agreement with that predicted by FEM. The motor with 2 slot-pitch windings has successfully operated up to 180 krpm.



## CHAPTER 3

### ELECTROMAGNETIC PERFORMANCE ANALYSIS OF 6-SLOT/2-POLE HIGH-SPEED PERMANENT MAGNET MOTORS WITH TWO SLOT-PITCH WINDINGS

Compared with 1 and 3 slot-pitch windings, the advantages of 2 slot-pitch windings for 6s/2p HSPM motors have been elaborated in the previous chapter. In this chapter, HSPM motors having 6s/2p number combination and 2 slot-pitch windings are developed for domestic appliance application, such as vacuum cleaners. Two HSPM motors with different layouts of 2 slot-pitch windings are optimized and their electromagnetic performances are evaluated. The best winding configuration is then identified for shorter motor axial length and larger torque density. Since 3s/2p HSPM motors with non-overlapping windings have the same winding factor, a comparison between 3-slot and 6-slot motors is also conducted, particularly for torque density, losses, and UMF. It shows that 6s/2p PM motors with 2 slot-pitch windings are suitable for high-speed application without UMF and less rotor PM loss. Finite element predicted electromagnetic performances are validated by experiments made on two prototype motors.

This chapter was published in IEEE Transactions on Energy Conversion.

#### 3.1 Introduction

HSPM motors have been widely employed for domestic and industrial application, e.g., precision hand tool, gas turbine generator, automotive turbocharger, and vacuum cleaner [HES87] [ZHU97] [ZWY05] [NOG07] [LIM17]. The advantages of high-speed motors include high power density, high efficiency, small size, light weight, and direct-drive for high-speed application. Gearboxes are usually used to connect a conventional speed motor with load to increase the speed, which leads to extra losses, noise issues, high cost, and low reliability. However, high-speed motors can be connected to a load directly, which can improve system mechanical reliability and reduce extra losses, further increasing efficiency [SHE18].

In literature, various HSPM motors have been designed for different applications, and different slot/pole number combinations are employed. Non-overlapping windings, also named as tooth-coil windings, are the most popular one due to several reasons. Firstly, non-overlapping windings reduce the length of end-winding and result in a shorter motor axial length. Therefore, lower copper loss, higher power density, and better rotor dynamic performance can be expected. Secondly, modular design can be achieved by non-overlapping windings, which improves the packing factor and reduces the cost of manufacture [UZH14]. For example, in

[HES87] and [ZHU97], a 3s/2p HSPM motor with non-overlapping windings are adopted. However, the 3s/2p HSPM motor has UMF, which causes vibration issues and results in high noise level [ZHU07]. Meanwhile, significant MMF harmonics and slotting effect lead to rich air gap harmonics and large magnet eddy current losses. [PAN14] proposes to insert an auxiliary slot to reduce the no-load UMF, and [MAJ18] improves this method for eliminating on-load UMF with little sacrifice of flux linkage and output torque. However, the influence of auxiliary slots on UMF highly depends on load condition and the UMF cannot be eliminated completely. Therefore, 6s/2p number combination with non-overlapping windings is preferred due to no UMF. [NOG05] designs and compares 3s/2p and 6s/2p motors with non-overlapping windings for high-speed application. The results show that 6s/2p motors not only have no inherent UMF but also reduce the axial length of end-winding, which reduces the motor total length and improves the rotor mechanical dynamic stability. However, 6s/2p motors with non-overlapping windings have low winding factor (0.5) and thus low torque density. Based on the same slot/pole number combination, full-pitch windings [MER15] [KAB17] can increase the winding factor to 1. However, full-pitch windings result in a long end-winding and subsequently a long motor axial length, which lead to large copper loss and large motor size.

In addition to tooth-coil (1 slot-pitch and short-pitch) windings and full-pitch (3 slot-pitch for a 3-phase motor) windings, 2 slot-pitch windings, which are also a type of short-pitch winding, are also available. In literature, 2 slot-pitch windings are used in PM synchronous machines (PMSM) for hybrid electric vehicles (HEV) to reduce magnet eddy current losses [SPA15]. In addition, 2 slot-pitch windings can also be used in vernier PMSM (VPMSM) to improve the power factor [LIU18a]. The winding pitch can be modified from one slot-pitch to two slot-pitches to reduce the harmonics in fractional-slot non-overlapping winding PM machines [WAN14a] [PAT14] [CHE13] [WAN14b]. [WAN14b] presents a general theory of fractional-slot PM machines with 2 slot-pitch based on several specific slot/pole number combinations. For flux-reversal PM (FRPM) machines, the influence of different slot-pitch on back-EMF has been investigated and for each different slot/pole number combinations, there is an optimal slot-pitch for the maximum fundamental back-EMF [HUA18].

For high-speed application, chapter 2 compares 6s/2p HSPM motors with coil-pitches of 1, 2, and 3 slot-pitches, and the advantages of 2 slot-pitch winding configuration have been proved. However, several special 2 slot-pitch winding configurations and production technologies can be developed to further reduce the end-winding axial length and increase the torque density. In addition, with the same winding factor, the 3s/2p HSPM motors with non-overlapping

windings have not been compared with 6s/2p HSPM motors with 2 slot-pitch windings.

In this chapter, motor topologies and end-winding models of two proposed motors are discussed in section 3. 2. For the maximum torque density, the optimal design by finite element method (FEM) is analyzed in section 3. 3. In section 3. 4, the electromagnetic performances of two optimized motors are analyzed and compared. Section 3. 5 compares the electromagnetic performances of 3s/2p and 6s/2p HSPM motors with the same winding factor. In section 3. 6, two optimized motors with different layouts of 2 slot-pitch windings are prototyped and tested to validate some of the FEM predicted results in section 3. 3, and section 3. 7 is the conclusion.

## 3.2 Motor Topology

This section describes the motor topologies of two 6s/2p HSPM motors with alternate 2 slot-pitch winding configurations. In addition, their different end-winding structures are modelled by 2D- and 3D-models, including end-winding length and axial length.

### 3.2.1 Winding Configuration

Fig. 3. 1 shows two 6s/2p motors with alternate layouts of 2 slot-pitch windings, i.e. Motor A (MA) and Motor B (MB), which have different conductor dispositions. The slot of Motor A is circumferentially divided into two parts, and two coil sides of different phases are accommodated at the left and right sides of the slot. The slot of Motor B is radially divided into two layers, the two sides of one coil are located at the upper and lower layers, respectively. It should be noticed that although both Motor A and Motor B have overlapping end-windings, different winding layouts result in different end-winding structures, which can be discussed in two aspects. One is end-winding length, which affects end-winding copper loss and winding inductance. Since 2 slot-pitch winding configurations have relatively large end-windings, the ratio of end-winding copper loss to total copper loss is relatively large, which cannot be neglected. The winding inductances affect the pulse width modulation and sensorless control [ZHU01], which is not considered in this research but their values will be calculated by FEM and shown in this chapter. The other one is the end-windings axial length, which impacts the motor axial length, rotor mechanical dynamics, and torque density.

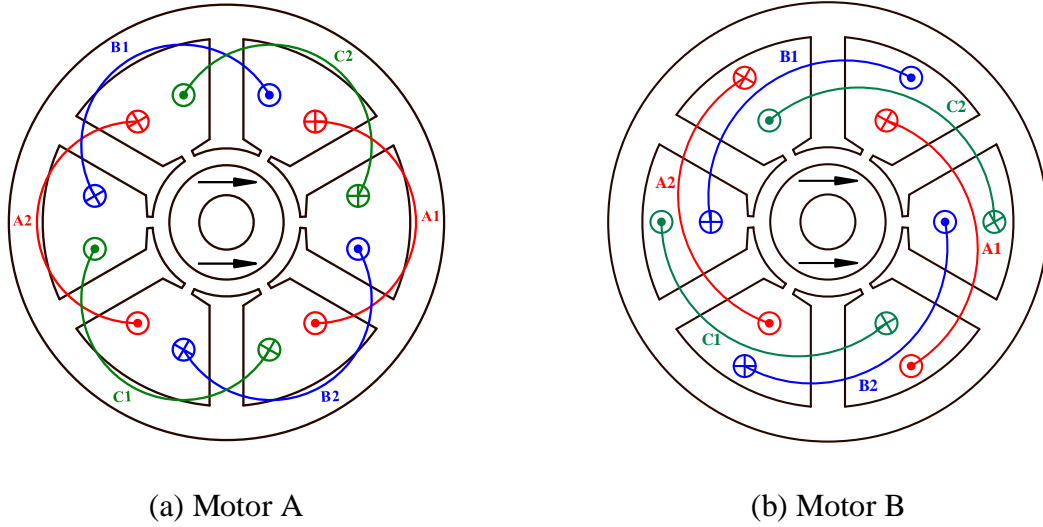


Fig. 3. 1. 6s/2p HSPM motors with alternate layouts of 2 slot-pitch windings.

### 3.2.2 End-winding Length

It is assumed that the end-winding of Motor A is semi-circle [PAN06], Fig. 3. 2I-a, and the length of ‘ArcA’ is assumed as the diameter of end-winding. Since the two sides of one coil are located at the upper and lower layers respectively, the end-winding of Motor B is an arc connected by three points, the center point of the lower layer (point-A), the middle point of layers (point-B), and the center point of the upper layer (point-C), i.e. ‘ArcB’, Fig. 3. 2II-a. In addition, the end-winding of Motor B includes an extra part ( $l_{ex}$ ), i.e. winding overhang region, Fig. 2II-b, which can be changed depending on the winding procedures. In this case, with manual winding, the length of extra part is relatively large, 4mm. If using automatic winding machines, the length of extra part can be reduced.

### 3.2.3 Axial Length of End-winding

The axial length of end-winding in Motor A is assumed to be the length of ‘ArcA’, as shown in Fig. 3. 2I-a. Due to lower and upper layers, Motor B has two end-winding axial lengths, which is assumed as the arc distances between the points-A/B and the adjacent tooth, i.e.  $l_{R1}$  and  $l_{R2}$ , as shown in Fig. 2II-a. Since  $l_{R1}$  is always larger than  $l_{R2}$ ,  $l_{R1}$  is adopted for the calculation of motor axial length, which equals to  $R_{end}$ , Fig. 2II-b. In addition, the axial length of end-winding in Motor B includes an extra part ( $l_{ex}$ ).

The single-side end-winding length ( $l_e$ ) and axial length ( $l_{ea}$ ) of Motor A can be calculated as

$$l_{e(MA)} = \frac{\pi}{2} \left( \frac{(2 \times 2 - 1) \left( \frac{D_i}{2} + h_t + \frac{D_o}{2} - h_y \right) \pi}{2N_s} + \frac{w_l}{2} \right) \quad (3.1)$$

$$l_{ea(MA)} = \frac{2}{\pi} l_e \quad (3.2)$$

The single-side end-winding length and axial length of Motor B can be given by

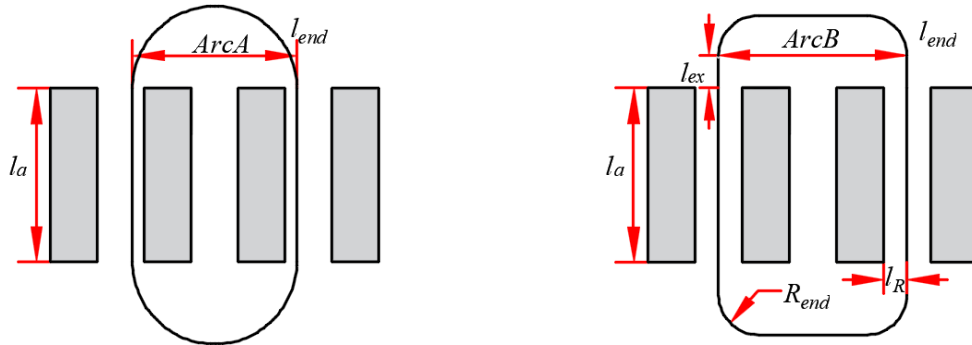
$$l_{e(MB)} = (ArcB - 2l_{R1}) + 2\pi l_{R1} / 2 + 2l_{ex} \quad (3.3)$$

$$l_{ea(MB)} = l_{R1} + l_{ex} \quad (3.4)$$

where ArcB is an arc connected by three points, the center point of the lower layer (point-A), the middle point of layers (point-B), and the center point of the upper layer (point-C), Fig. 3.2II-b, which can be computed by geometric calculation.



(a) 2D-model-1



(b) 2D-model-2

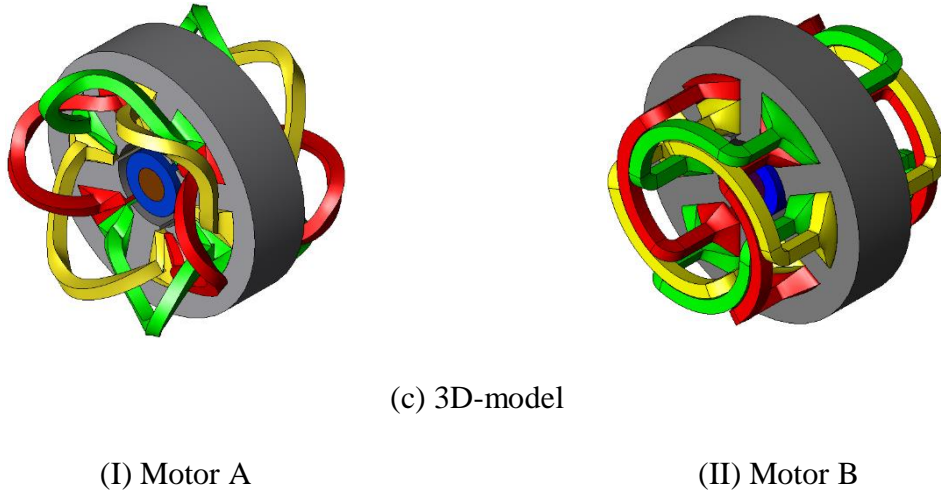


Fig. 3. 2. 2D- and 3D-models of end-windings in 6s/2p motors with alternate layouts of 2 slot-pitch windings.

### 3.3 Design Optimization

Compared with conventional low- and medium-speed PM motors, the stator iron losses of HSPM motors are significant large due to high frequency and cannot be neglected [ZHU97]. Therefore, the stator thermal limitation ( $P_{limit}$ ) including stator iron loss and copper loss is introduced in this optimization. However, the stator thermal limitation only considers the heat caused by stator iron loss and winding copper loss dissipating through the motor external surfaces, but neglects the heat caused by winding copper loss inside the stator (hot spot), especially for on-load operation. Therefore, the maximum allowed current density ( $J_{max}$ ) is also introduced to avoid the thermal issue inside the stator and destruction of winding insulation [REI13]. According to the research experience, the maximum allowed current density is selected as  $12 \text{ A/mm}^2$ . Since two motors with different layouts of 2 slot-pitch windings have different axial lengths of end-windings, the optimal goal is the maximum torque density, accounting for copper loss and axial length of end-windings. Table 3. 1 shows the main designs of Motors A and B.

In literature [BIA04], the stator thermal limitation of the small size HSPM motor is calculated by  $P_{limit}=hV_w\pi D_o l_s$ , where  $h$  is the overall thermal heat transfer coefficient, which is closely related with the type of cooling, and  $h=100 \text{ W/}^\circ\text{Cm}^2$  for the forced air cooling in this case.  $V_m$  is the maximum motor operation temperature.  $D_o$  is the stator outer diameter and  $l_s$  is the stator active length. In this optimization, there are three design variables:  $\lambda$ ,  $B_{max}$ , and  $I_{max}$ . The maximum  $B_g$  is restricted by the split ratio. According to  $B_{max}$ ,  $w_t$  and  $h_y$  can be calculated. With various phase currents, the electromagnetic torques and the total stator losses ( $P_{stator}$ ) can be

obtained, which consists of stator iron loss and copper loss. Only the motor meeting the design requirement, i.e. stator loss limitation and maximum allowed current density, can be selected for the maximum torque or maximum torque density.

With the increase of stator iron flux density, for considering stator loss limitation only, the maximum torque density increases at first and then decreases, but for considering current density limitation only, the maximum torque density increases linearly, Fig. 3. 3. Therefore, the optimal  $B_{max}$  for the maximum torque density occurs at the intersection of two lines, and two motors have the same optimal  $B_{max}$ . This result also shows that when  $B_{max} < 1.0T$ , the current density limitation is a dominant restriction due to the small slot area and large current density, however, when  $B_{max} > 1.0T$ , the stator loss limitation is a dominant restriction due to the large stator iron loss.

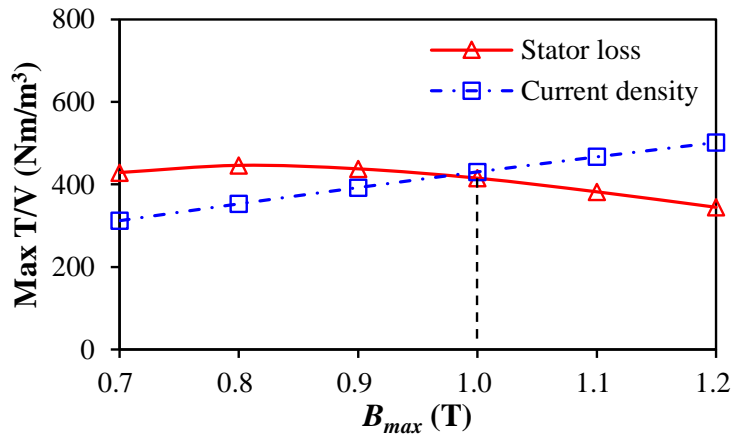
Table 3. 1

Main Designs of 6s/2p HSPM Motors

Stator outer diameter (mm)	40	Stator active length (mm)	9.6
Turns per phase in series	20	Air-gap length (mm)	1.55
Sleeve thickness (mm)	0.5	Shaft diameter (mm)	5
Magnet remanence (T)	1.3	Winding connection	parallel

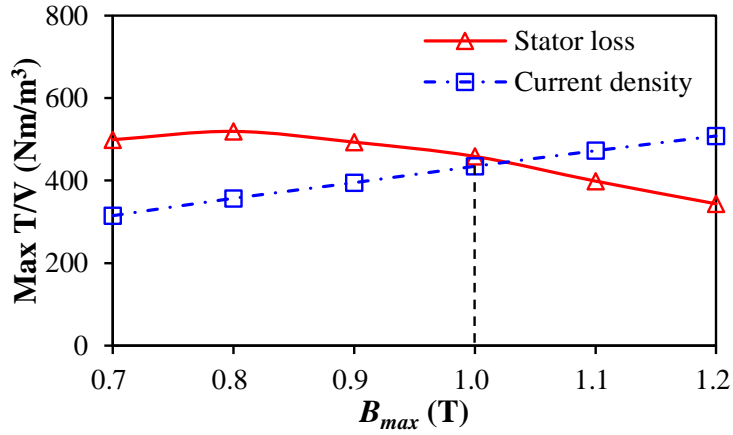
Fig. 3. 4 shows that with the optimal  $B_{max}$ , the maximum torque density increases at first and then decrease with the increase of split ratio when only considering stator loss or current density limitation. However, considering stator loss and current density limitations, the maximum torque density can be achieved at the intersection of two lines, which is the optimal split ratio.

It is worth noting that although two motors have the same optimal  $B_{max}$  and split ratio, MB has slightly larger maximum torque density than MA due to the smaller average torque, Fig. 3. 5, and shorter end-winding axial length, Fig. 3. 6. Table 3. 2 shows the parameters of two optimized motors have the same optimal design.



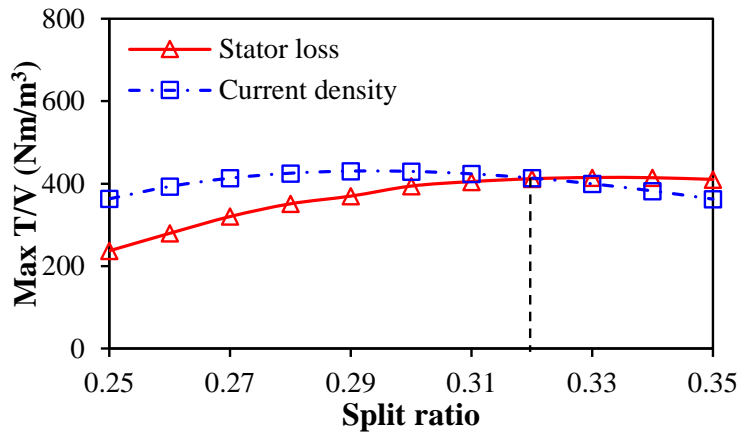
(a) Motor A



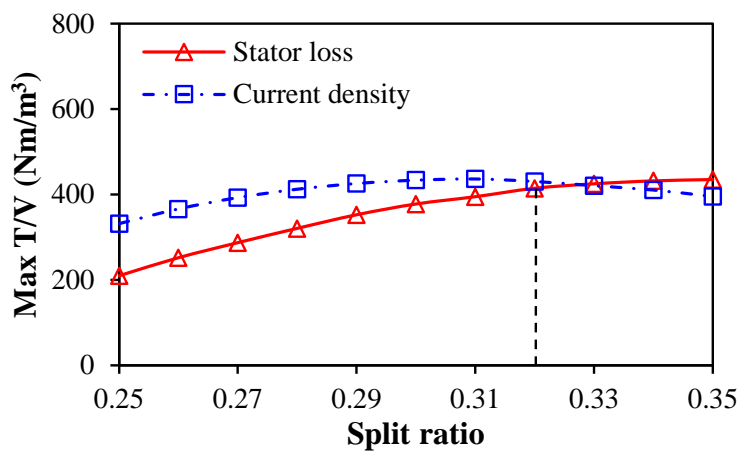


(b) Motor B

Fig. 3. 3. Relationship between maximum torque density and  $B_{max}$  considering stator loss and current density limitations.



(a) Motor A



(b) Motor B

Fig. 3. 4. Relationship between maximum torque density and split ratio considering stator loss and current density limitations,  $B_{max}=1.0T$ .

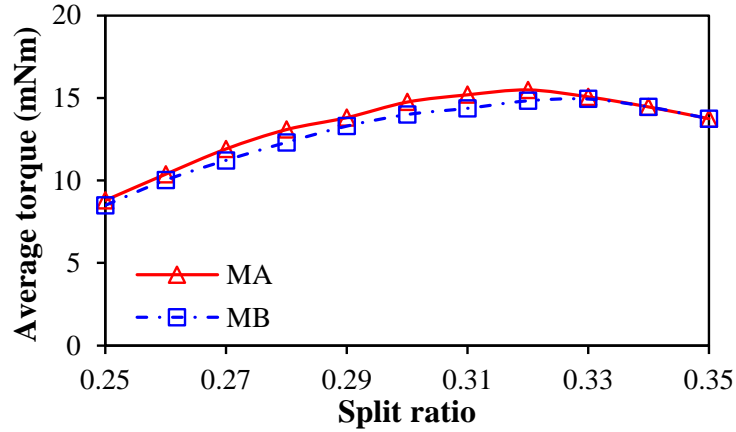


Fig. 3. 5. Relationship between maximum torque and split ratio,  $B_{max}=1.0T$ .

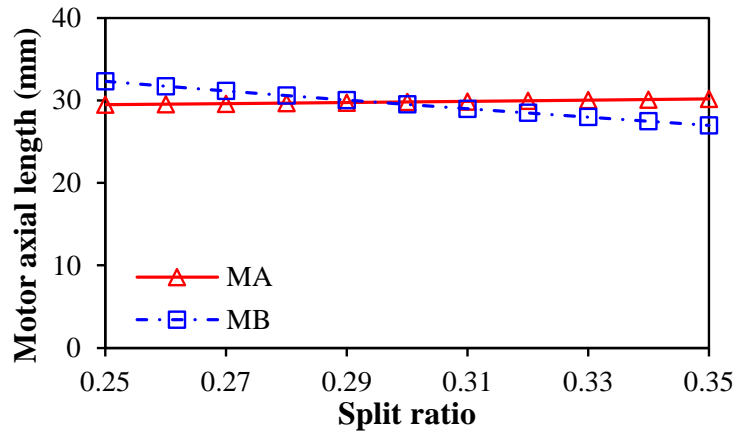


Fig. 3. 6. Relationship between end-winding axial length and split ratio,  $B_{max}=1.0T$ .

### 3.4 Performance Evaluation

The influence of different layouts of 2 slot-pitch windings on the electromagnetic performances of two optimized 6s/2p HSPM motors is investigated, including open-circuit  $B_g$ , back-EMF, electromagnetic torque, cogging torque, winding inductance, various loss components and efficiency.

#### 3.4.1 Open-circuit Analysis

The equipotential distributions of two optimized motors are shown in Fig. 3. 7. Since the HSPM motor requires relatively large air-gap length, the harmonic contents of air-gap field are very small except those due to slotting, Fig. 3. 8. The back-EMF waveforms of phase A in two optimized motors are sinusoidal since the 2-pole magnet is diametrically-magnetized and there are almost no harmonics, Fig. 3. 9. Therefore, with the same motor dimensions, two optimized

motors have the same open-circuit  $B_g$  and back-EMF.

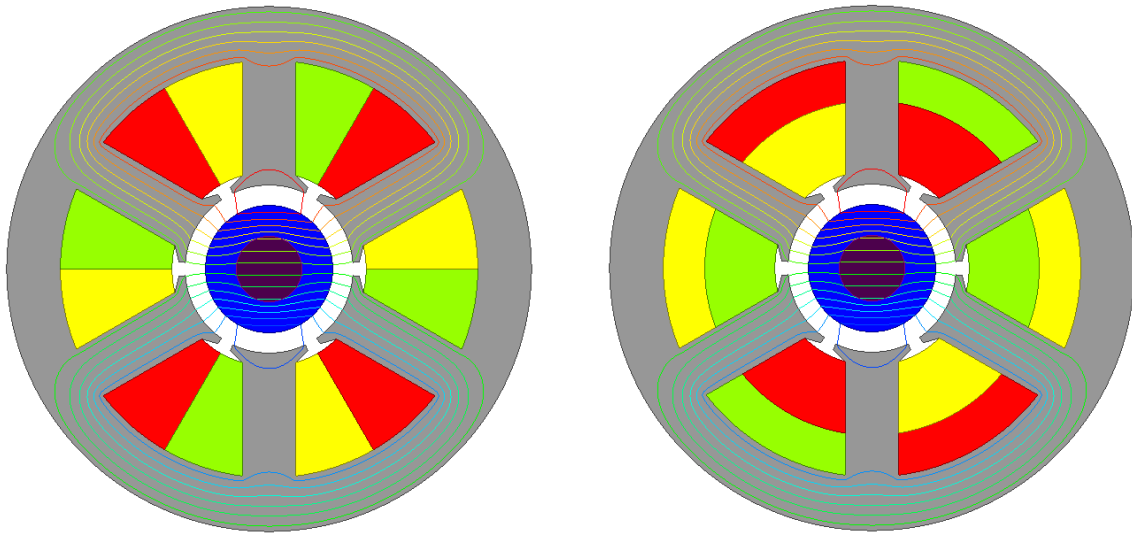
Table 3. 2

Parameters of Optimized Motors with Stator Thermal and Current Density Limitations

	MA	MB	3-slot motor
Stator thermal limitation, W	18.7		
Maximum current density, A/mm <sup>2</sup>	12		
$B_{max}$ , T	1.0		
Optimal split ratio	0.32		
Phase current, A	7.0	6.7	6.5
Current density, A/mm <sup>2</sup>	11.9	11.5	11.8
Torque, mNm	15.5	15.0	14.3
Stator iron loss, W	13.78	13.40	14.78
Copper loss, W	4.78	5.31	3.82
Active stator loss, W	18.56	18.71	18.60
Rotor PM loss, W	3.42	3.13	4.14
Efficiency, %	93.0	92.8	92.2
End-winding length, W	31.97	40.93	26.42
Motor axial length, mm	29.6	28.5	26.4
Torque density, Nm/m <sup>3</sup>	411.7	418.8	430.8

### 3.4.2 Torque Analysis

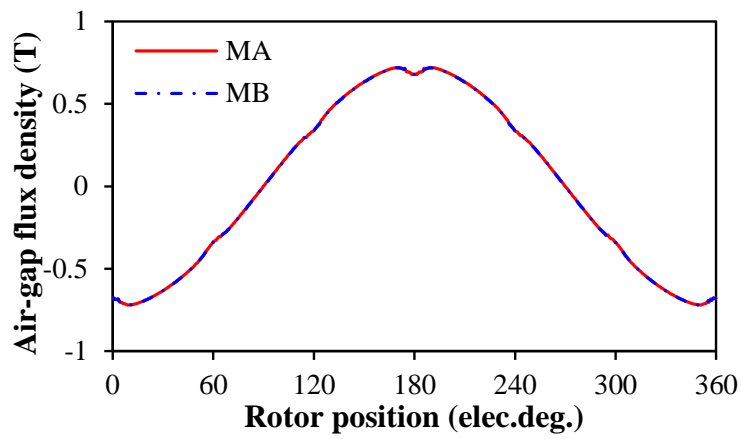
Two 6s/2p HSPM motors have almost zero cogging torques since the 2-pole magnet is diametrically-magnetized, Fig. 3. 10. With thermal limit, MA with larger phase current has larger torque than MB with longer end-winding length, but they have almost the same torque ripple, which results from the sinusoidal back-EMF waveform and 120° electric square wave current waveform, Fig. 3. 11.



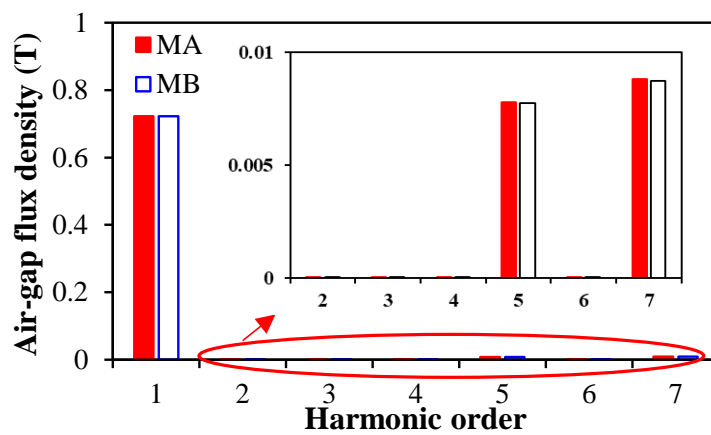
(a) Motor A

(b) Motor B

Fig. 3. 7. Equipotential distributions of two optimized motors.

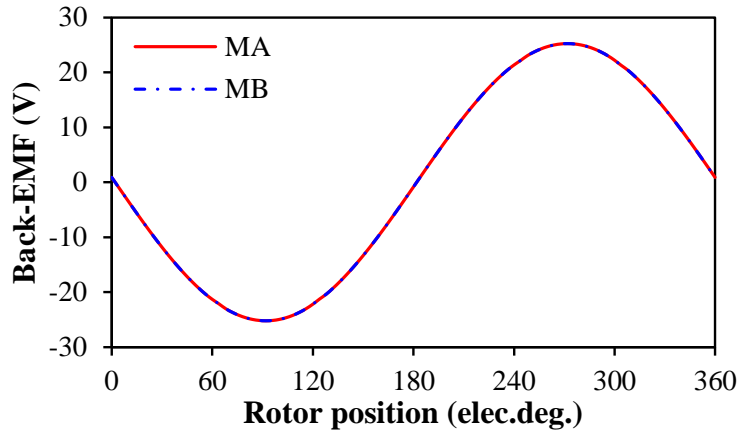


(a) Waveforms

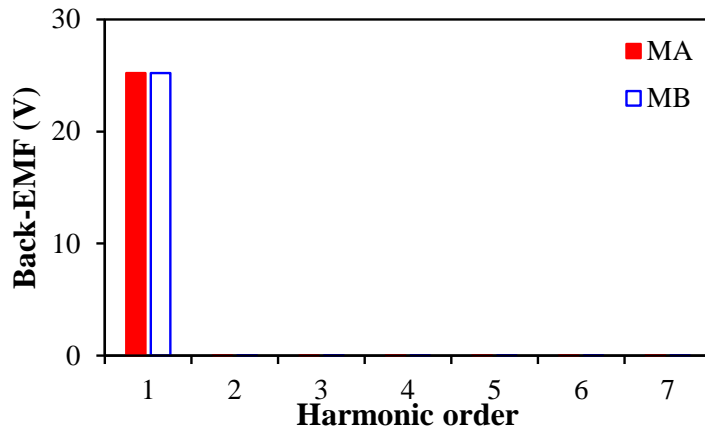


(b) Spectra

Fig. 3. 8. Air-gap field distributions of MA and MB.



(a) Waveforms



(b) Spectra

Fig. 3. 9. Back-EMF waveforms of phase A.

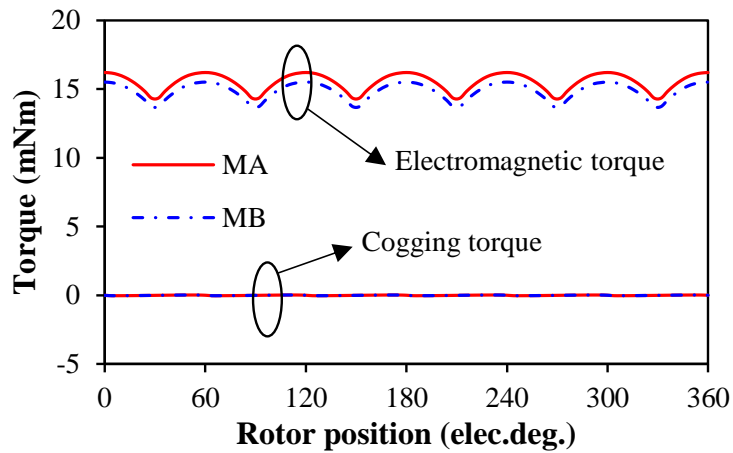


Fig. 3. 10. Cogging torque and electromagnetic torque waveforms.

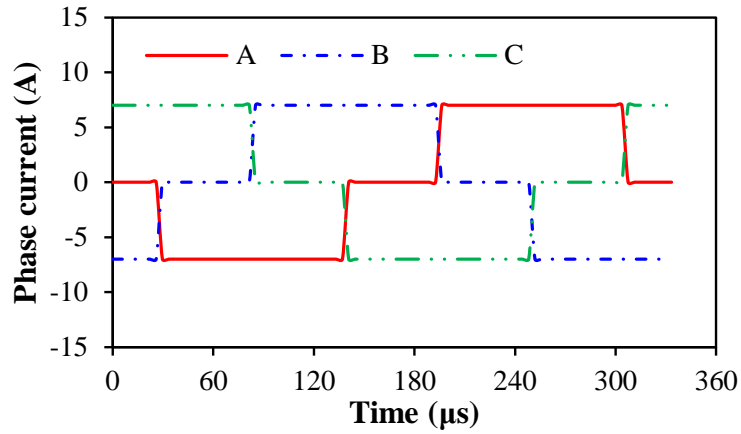
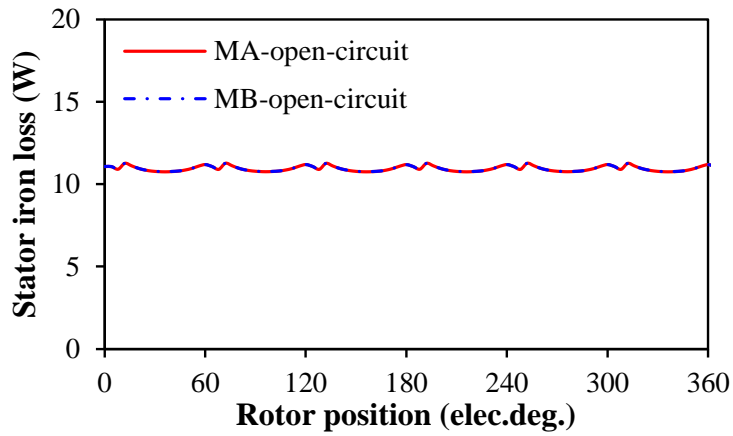
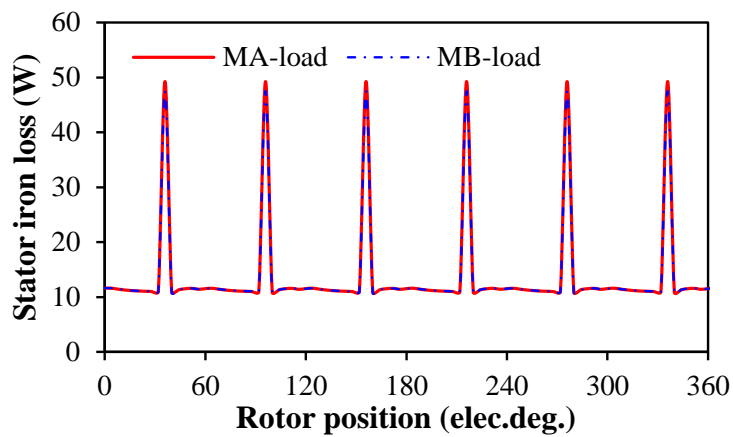


Fig. 3. 11. Square wave current waveforms with 120 ° electric conduction.



(a) Open-circuit



(b) On-load

Fig. 3. 12. Stator iron losses.

### 3.4.3 Loss Analysis

#### A. Stator iron loss

Two 2 slot-pitch winding layouts with the same stator winding MMF distribution and rated phase current have negligible influence on the stator iron loss, Fig. 3. 12. There are six pulsations in Fig. 3. 12 (b), which corresponds to six commutations in the six-step commutation block using a 120 ° electric conduction mode. Due to the increased magnitudes of iron loss pulsations, the average iron loss increases with the rise of phase current, Fig. 3. 13. Therefore, in section 3. 3, the stator iron loss is calculated by FEM considering the influence of armature reaction.

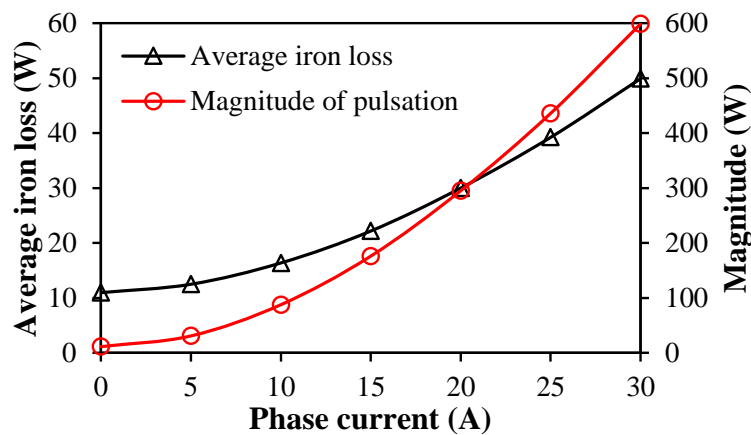


Fig. 3. 13. Variation of average stator iron loss and magnitude of pulsation with phase current.

#### B. Copper loss

In general, the copper loss consists of two parts, DC copper loss and AC copper loss. In HSPM motors, the AC copper losses due to skin effect and proximity effect may increase significantly and should be analysed [LIS16]. To avoid the skin effect, the diameter of conductors should be less than the skin depth ( $\delta$ ) [UZH14], which can be calculated by

$$\delta = \sqrt{\frac{\rho}{\pi f \mu}} \quad (3.5)$$

In this case, the frequency is 3000 Hz, and the skin depth is 1.2mm. Therefore, the skin effect can be neglected when the diameter of conductor is selected as 0.6 mm. It is worth noting that the motor is developed for vacuum cleaners. It employs small conductor diameter and has low slot packing factor for reducing the AC loss. More importantly, the airspaces (between

conductor and stator iron core) in the slot and between conductors are used for the forced-air cooling channels to improve the winding cooling capability and avoid local overheating.

The proximity effect depends on the variation of leakage magnetic field in the slot, e.g. due to the PM rotating and armature reaction magnetic fields [CHA18]. Since MA and MB have small rated phase currents, the PM rotating magnetic field is dominant. Fig. 3. 14 shows that the rotating magnetic field affects the conductors near the slot opening significantly, but has negligible influence for the conductors at the bottom of the slot. Therefore, the coils at the left and right sides of the slot in MA have almost the same maximum flux density, however, the coils at the upper layer of the slot in MB have larger maximum flux density than the coils at the lower layer, Fig. 3. 15. As a result, the coils at the upper layer have larger AC copper loss than the coils at the lower layer. When the frequency is 400Hz, i.e. 24,000 rpm, MA and MB without end-windings have almost the same joule loss and the ratio of AC to DC copper losses, Table 3. 3, which shows that the AC copper losses are small and can be neglected. When the frequency is 3000 Hz, i.e. 180,000 rpm, MB has larger joule loss than MA due to the larger joule losses in the coils at the upper layer.

Since the end-winding region has very small rotating magnetic field, the proximity effect in end-windings depends on the change of magnetic field caused by armature reaction and thus the ratio of AC to DC copper losses in end-windings is the same as that in the coils at the lower layer. Table 3. 4 indicates that considering end-windings decreases the ratio of AC to DC copper losses since only the coils near the slot opening experience proximity effect and produce AC copper loss. Therefore, the AC copper loss can be neglected in this chapter.



Table 3. 3

## Copper Losses without End-windings

Coils		DC loss, W	Joule loss of coils, W		AC/DC copper loss	
			400Hz	3000Hz	400Hz	3000Hz
MA	Left	0.55	0.588	0.72	0.07	0.31
	Right	0.55	0.588	0.72		
	Total	1.100	1.176	1.44		
MB	Lower	0.505	0.534	0.556	0.06	0.10
	Upper	0.505	0.556	0.944	0.10	<b>0.87</b>
	Total	1.01	1.09	1.50	0.08	0.49

Table 3. 4

## Copper Losses with End-windings (3000Hz)

	MA	MB
End-winding length, mm	31.97	40.93
DC loss, W	5.11	5.31
Joule loss of active windings, W	1.44	1.50
Joule loss of end-windings, W	4.50	4.72
Total Joule loss, W	5.94	6.22
AC/DC copper loss	0.16	0.17

## C. Rotor loss

In this chapter, a stainless-steel sleeve is employed to retain the PMs from centrifugal force, and thus the rotor loss includes eddy current losses in sleeve, PMs, and shaft, which not only affects the motor efficiency but also may result in irreversible demagnetization of PMs due to overheating. Due to the same motor dimensions, two motors with the same rated phase current and stator winding MMF distribution have the same rotor loss, Fig. 3. 16. As the same results in the stator iron loss waveforms, there are six pulsations in the rotor loss waveforms, Fig. 3. 16.

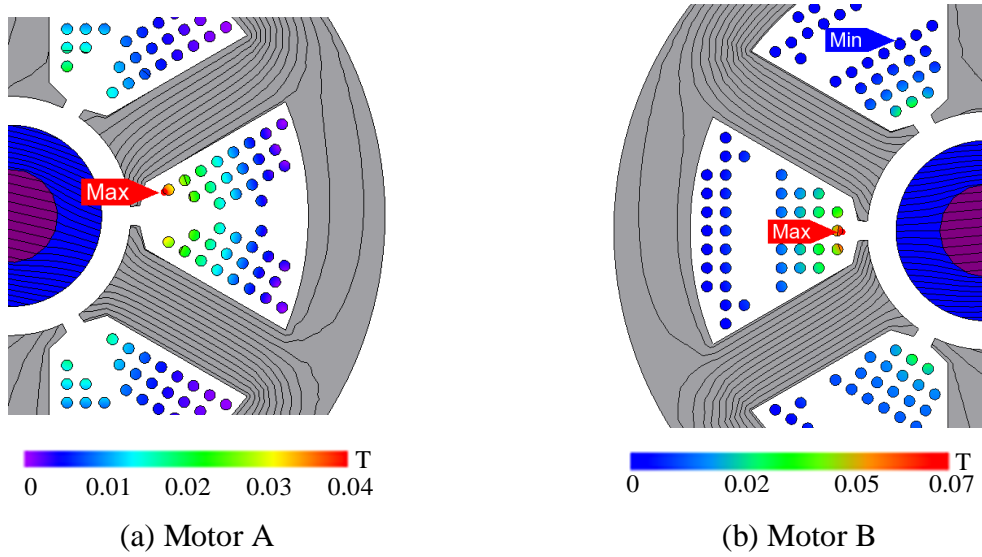


Fig. 3. 14. Flux density of conductors in two motors.

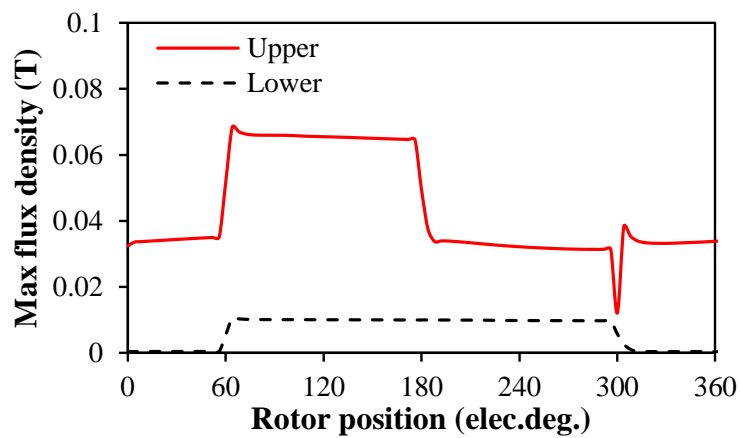
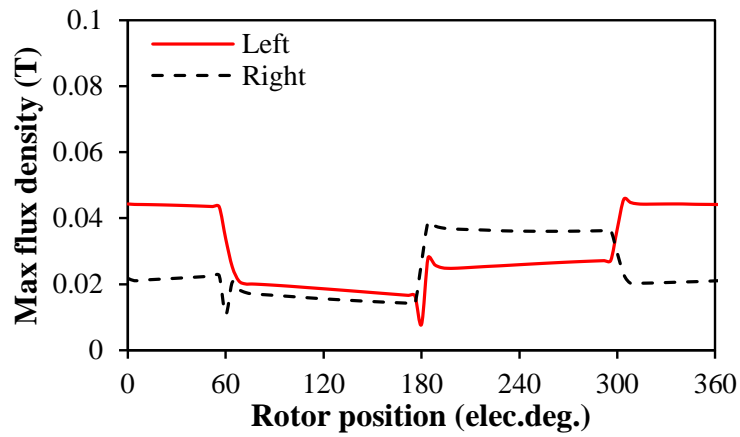


Fig. 3. 15. Maximum flux density of conductors in different positions of the slot.

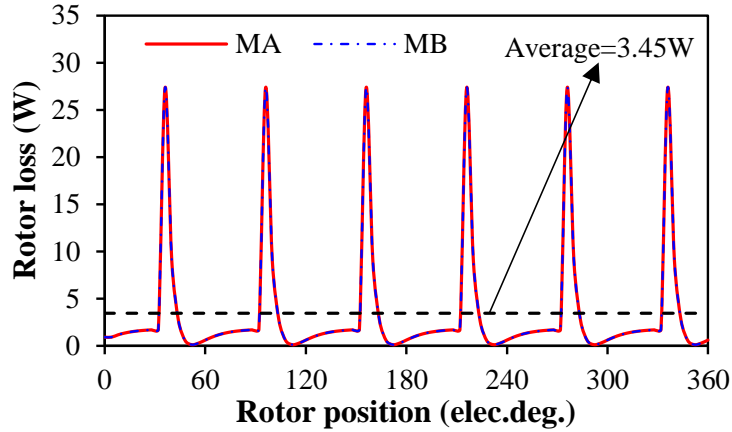
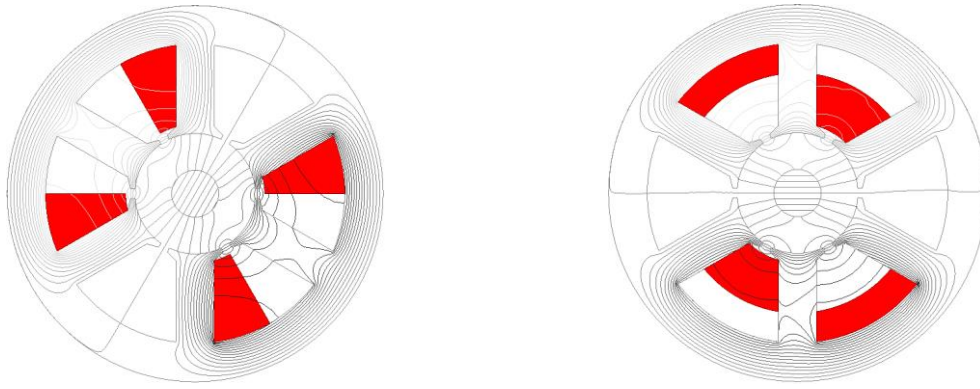


Fig. 3. 16. Rotor eddy current losses of MA and MB under the rated current,  $I_{max}=7A$ .

### 3.4.4 Winding Inductances

The various component inductances of two 6s/2p HSPM motors with different layouts of 2 slot-pitch windings are analyzed in this section. Since the end-winding axial lengths of two optimized motors are larger than the stator active length, the end-region component of inductances should be considered. Fig. 3. 17 shows the flux distributions of two 6s/2p HSPM motors with rotor shaft. In MA, two conductors of one coil, i.e. A+ and A-, have the same flux linkage, Table 3. 5.

In MB, the conductor A+ at the lower layer has larger flux linkage than the conductor A- at the upper layer, however, the flux linkage of coil A is almost the same as that in MA. It is assumed that only phase A is excited, i.e.,  $I_A=1A$ ,  $I_B=I_C=0A$ , and two coils of the same phase are connected in parallel. The slot-region and air-gap region components of inductances are calculated by 2D-FEM, and the end-region component is predicted by 3D-FEM. Table 3. 6 shows that in 2D-FE model, MA and MB have almost the same self-and mutual-inductances since the same motor dimension, but the end-region of MA is larger than that of MB due to the larger end-winding axial length. Therefore, compared with MA, MB has an advantage in smaller inductance, which is beneficial to sensorless operation [TOD05] [LEE17].



(a) Motor A

(b) Motor B

Fig. 3. 17. Flux distributions of MA and MB ( $I_A=1A$ ,  $I_B=I_C=0A$ ).

Table 3. 5

Flux Linkages of Conductors in One Coil ( $\mu Wb$ )

	Motor A	Motor B
Conductor A+	4.77	5.40
Conductor A-	4.77	4.07
Coil A	9.54	9.47

Table 3. 6

Winding Inductances in 2D-and 3D-FE Models ( $\mu H$ )

		2D-FE	End-region	3D-FE	Phase
MA	L	16.1	10.33	26.43	39.20
	M	-7.61	-5.16	-12.77	
MB	L	16	7.4	23.4	34.75
	M	-7.65	-3.7	-11.35	
3-slot	L	24.26	8.43	32.69	47.37
	M	-10.47	-4.21	-14.68	

### 3.5 Comparison of 3s/2p and 6s/2p HSPM Motors

Compared with the non-overlapping windings in 6s/2p HSPM motors, one of the remarkable advantages of the 2 slot-pitch windings is a relatively large winding factor (0.866), which is the same as that of a conventional 3s/2p PM motor with non-overlapping windings. Therefore, in this section, a conventional 3s/2p HSPM motor with non-overlapping windings is optimized and compared with 6s/2p HSPM motors having the same winding factor. Fig. 3. 18 shows the machine topology and end-winding structure of the 3-slot motor. Employing the same optimization method as mentioned before, the 3s/2p HSPM motor is optimized considering the stator loss and current density limitations. According to Fig. 3. 19 and Table 3. 2, for maximum torque density, the 3s/2p motor has the same optimal  $B_{max}$  and optimal split ratio as that of the 6s/2p motor. The motor axial length increases mildly with the increase of split ratio but remains almost the same with the increase of  $B_{max}$ , Fig. 3. 20.

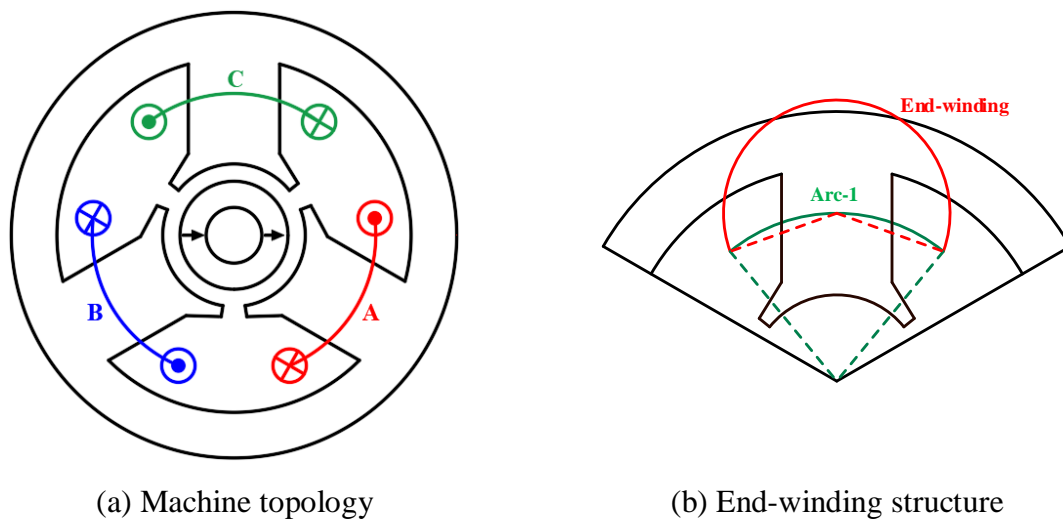
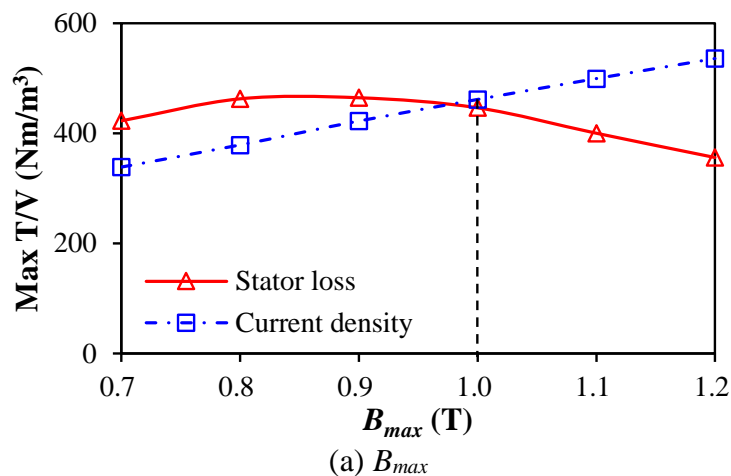
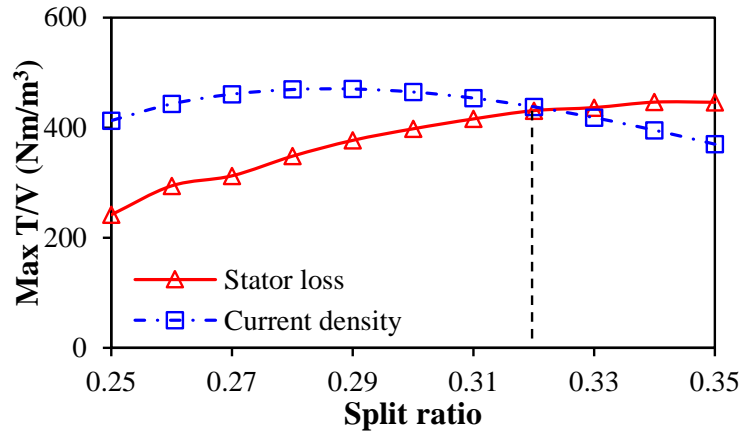


Fig. 3. 18. Machine topology and end-winding structure of the 3-slot motor.





(b) Split ratio

Fig. 3. 19. Relationship between maximum torque density,  $B_{max}$ , and split ratio ( $B_{max}=1.0T$ ) considering stator loss and current density limitations.

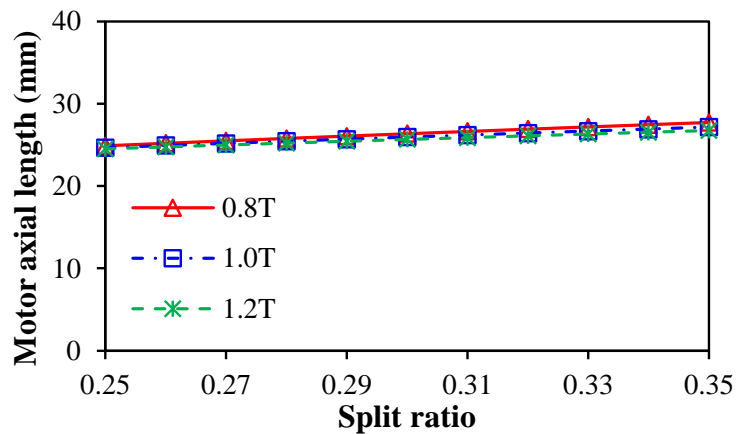


Fig. 3. 20. Relationship between motor axial length and split ratio under different stator iron flux densities.

### 3.5.1 Open-circuit Analysis

Fig. 3. 21 shows the equipotential and flux contour distributions of the 3-slot motor, and the air-gap field distributions of the 3s/2p and 6s/2p motors are shown in Fig. 3. 22. The spectra show that the 3s/2p motor has slightly richer spatial harmonics due to slotting effect, such as the 2<sup>nd</sup> and 4<sup>th</sup> order harmonics.

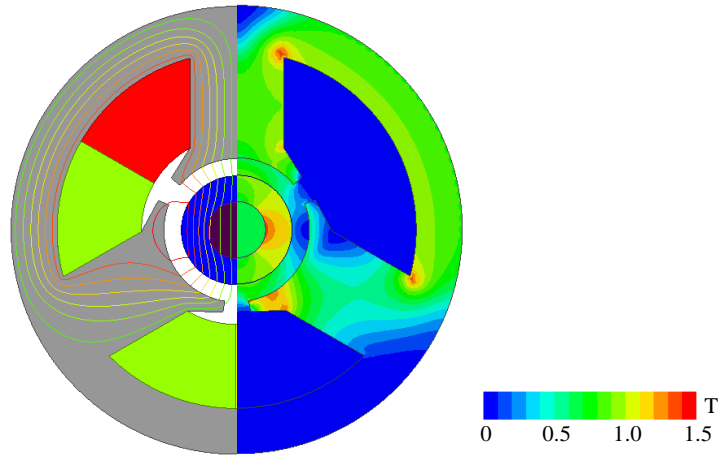
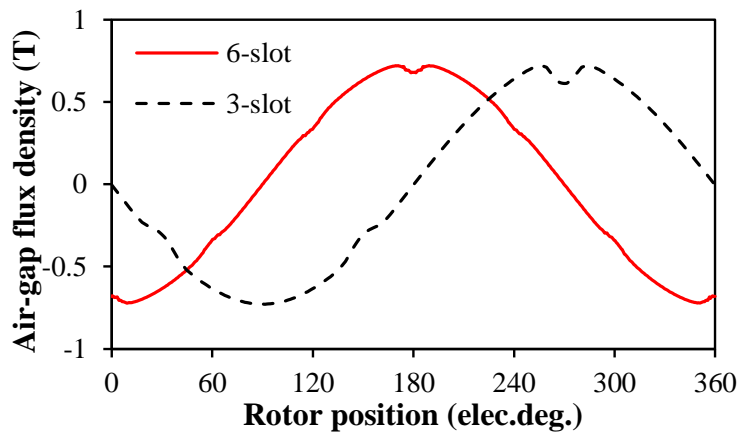
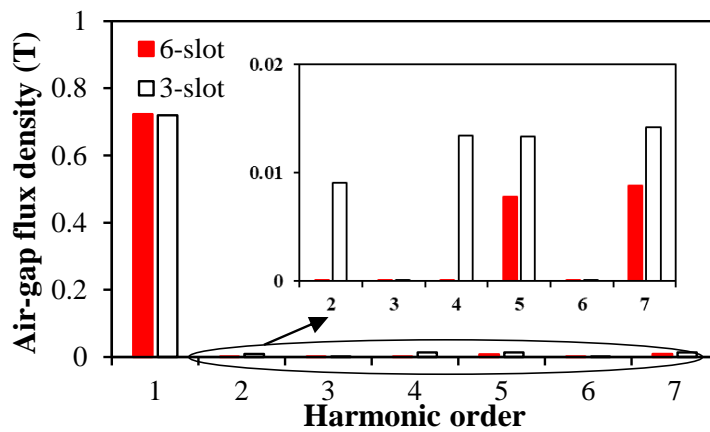


Fig. 3. 21. Equipotential and flux contour distributions of the optimized 3s/2p motor with non-overlapping windings.



(a) Waveforms



(b) Spectra

Fig. 3. 22. Air-gap field distributions of 3s/2p and 6s/2p motors.

### 3.5.2 Torque Analysis

Both the 3s/2p motor and two 6s/2p motors have almost zero cogging torque due to diametrically-magnetized magnet, Fig. 3. 23. Considering stator loss and current density limitation, the 3-slot motor has smaller rated current and subsequently smaller electromagnetic torque.

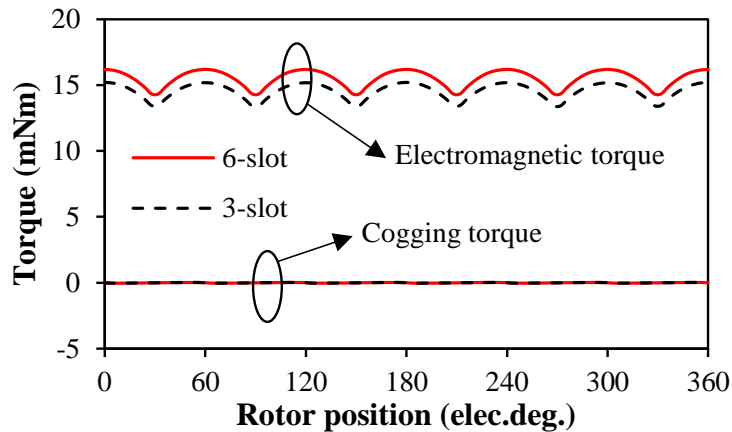


Fig. 3. 23. Electromagnetic and cogging torques of 3s/2p and 6s/2p motors.

### 3.5.3 Unbalanced Magnetic Force

Fig. 3. 24 shows that the 6s/2p motor with symmetrical stator topology has no UMF, while the 3s/2p motor exhibits inherent no-load and on-load UMFs, [ZHU07], which are undesirable in high-speed operation. In addition, with the increase of phase current, the average UMF of the 3s/2p motor increases linearly, but that of the 6s/2p motor remains zero, Fig. 3. 25. Therefore, compared with the 3s/2p motor, the 6s/2p motor offers advantage for no UMF and avoiding high vibration and noise.

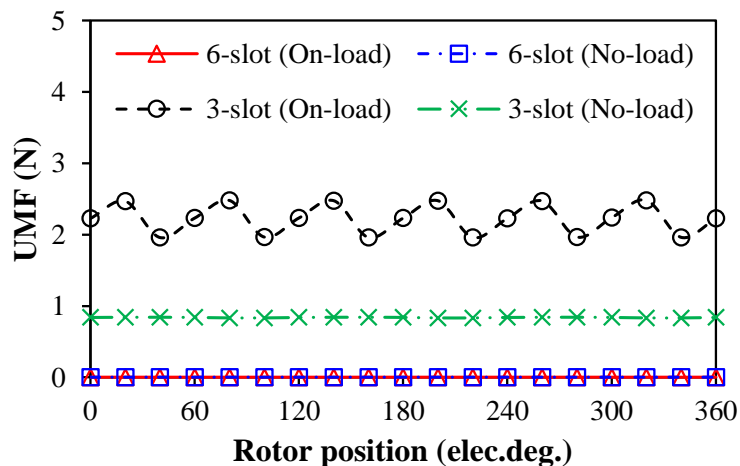


Fig. 3. 24. UMFs of 6-slot ( $I_{max}=7A$ ) and 3-slot motors ( $I_{max}=6.5A$ ).



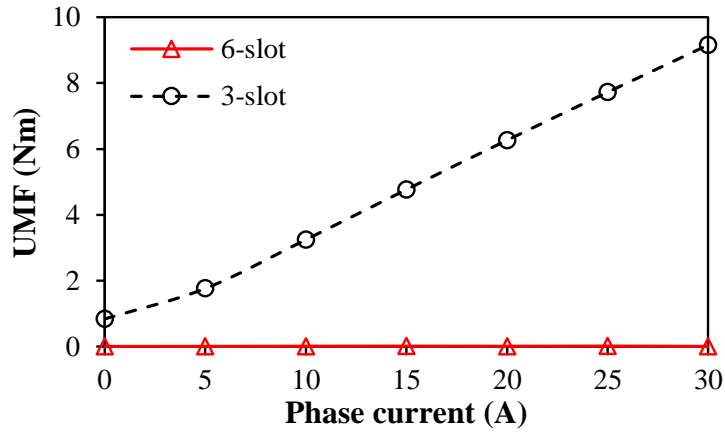


Fig. 3. 25. Relationship between average UMF and phase current in 6-slot and 3-slot motors.

### 3.5.4 Loss Analysis

Fig. 3. 26 shows the comparison of various loss components of the 3s/2p motor and two 6s/2p motors. As mentioned before, the AC copper loss is small and can be neglected. Therefore, with the smallest end-winding length, the 3s/2p motor has the smallest copper loss. In addition, the 3s/2p motor has the largest on-load iron loss due to the local saturation in the tooth tip, Fig. 3. 21. Fig. 3. 27 shows the 3s/2p motor has richer spatial harmonics than the 6s/2p motor, thus the largest rotor loss. Therefore, compared with two 6s/2p motors, the 3s/2p motor exhibits the smallest copper loss, but the largest total loss, Table 3. 2.

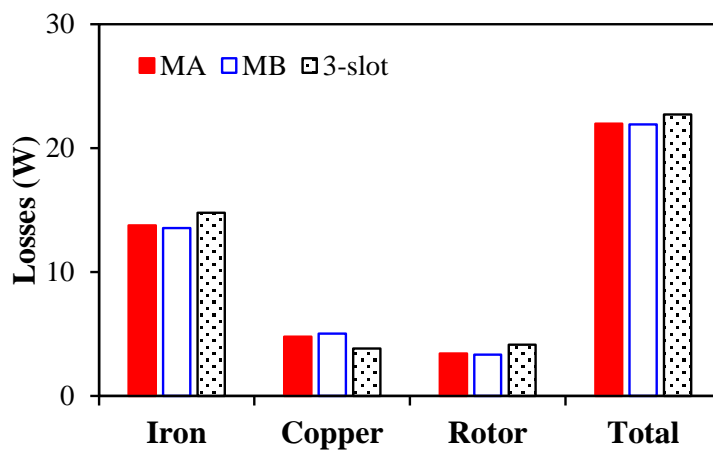
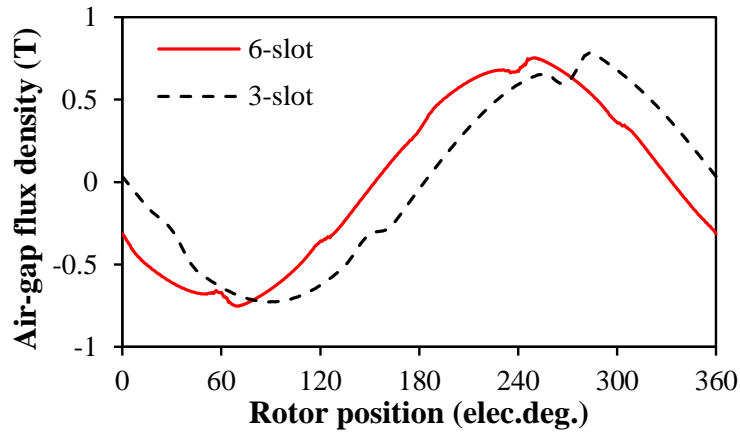
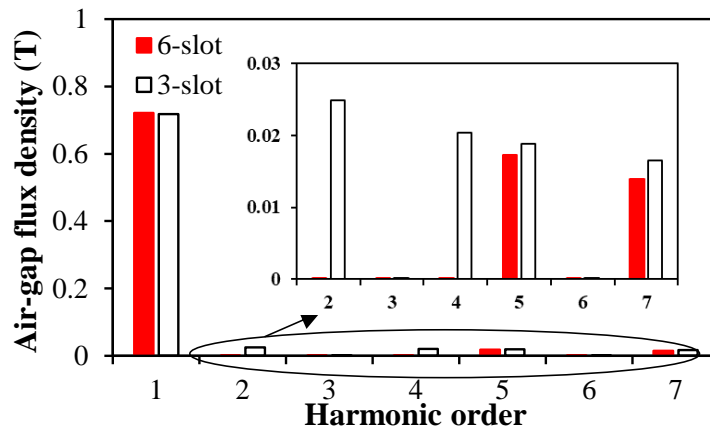


Fig. 3. 26. Losses of MA, MB, and the 3-slot motor under their rated currents.



(a) Waveforms



(b) Spectra

Fig. 3. 27. Air-gap flux density waveforms of 3s/2p and 6s/2p motors at on-load condition.

### 3.5.5 Winding Inductances

The inductances of the 3s/2p motor are shown in Table 3. 6, and the end-region component of inductances is calculated by 3D-FE model. It can be seen that the winding inductance of the 3s/2p motor is larger than that of two 6s/2p motors.

## 3.6 Experimental Validation

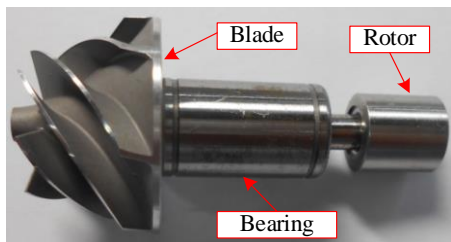
To validate the FE analyses, two 6s/2p HSPM motors with different layouts of 2 slot-pitch windings are prototyped, Fig. 3. 28, together with the rotor-bearing-blade system and the frame with air duct system.



(a) Motor A



(b) Motor B



(c) Rotor-bearing-blade system



(d) Frame with air duct system

Fig. 3. 28. Two prototype motors.

End-winding axial lengths of two prototypes are measured by vernier caliper. The results show the measured end-winding axial lengths of two motors are almost the same as the predicted results, Table 3. 7. Although the measured winding resistances of MA and MB are slightly larger than the analytical predicted results, satisfied agreement is achieved, Table 3. 7.

By an LCR meter, the measured phase inductances are shown in Table 3. 8. In 3-D FE model, the effect of frequency is neglected, and the predicted winding inductances are ideal. Therefore, the predictions and measurements of winding inductances at 1.0 Hz have a good agreement. The measured results also show that the winding inductance increase with the increase of frequency. Fig. 3. 29 compares the back-EMF waveforms of MA and MB by FEM prediction and measurement. It shows that they have a good agreement.

Table 3. 7

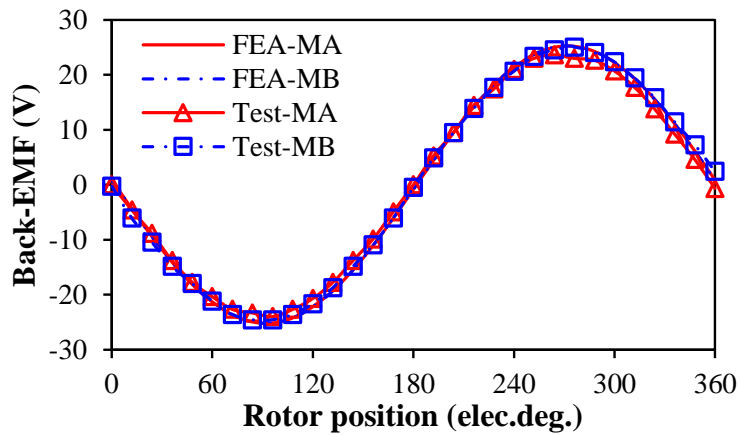
Motor Axial Length and Winding Resistance by Prediction and Measurement

	Motor axial length (mm)		Resistance (mΩ)	
	ANA	Measured	ANA	Measured
MA	29.6	30.2	53.5	64.3
MB	28.5	30.7	59.3	66.5

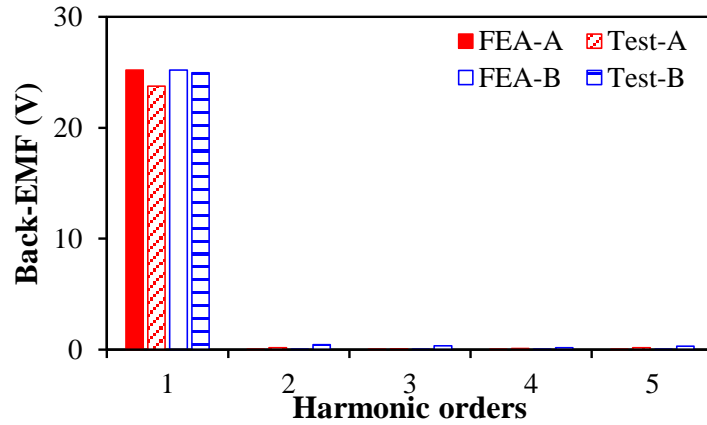
Table 3. 8

Winding Inductances of Two Motors (μH)

	3D-FE	Measured (1Hz)	Measured (3kHz)
MA	40.2	44.05	54.04
MB	42.6	46.02	50.60



(a) Waveforms



(b) Spectra

Fig. 3. 29. Predictions by FEM and measurements of back-EMF waveforms of phase A in MA and MB.

Based on a test rig described in [ZHU09], the on-load static torques can be measured. With the different phase currents of  $I_A = -I_B = 0, 5, 10, \text{ and } 15 \text{ A}$ ,  $I_C = 0 \text{ A}$ , which corresponds to square wave current waveforms with  $120^\circ$  electric condition, the static torques of two prototypes are measured at different rotor positions and they have a good agreement with the FE predicted results, Fig. 3. 30. It also shows that 6s/2p HSPM motors with diametrically-magnetized magnets have negligible cogging torque. The maximum static torque increases with the increase of phase current linearly, and two prototypes have almost the same FE predicted and measured results, Fig. 3. 31.

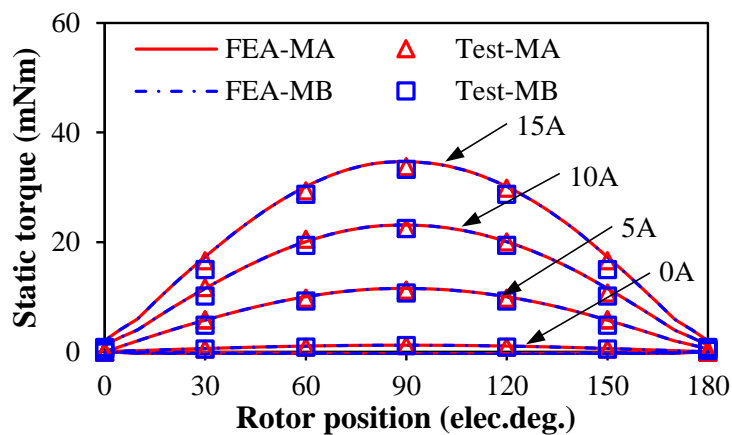


Fig. 3. 30. Predictions and measurements of static torques under different phase currents,  $I_A = -I_B = 0, 5, 10, \text{ and } 15 \text{ A}$ ,  $I_C = 0 \text{ A}$ .

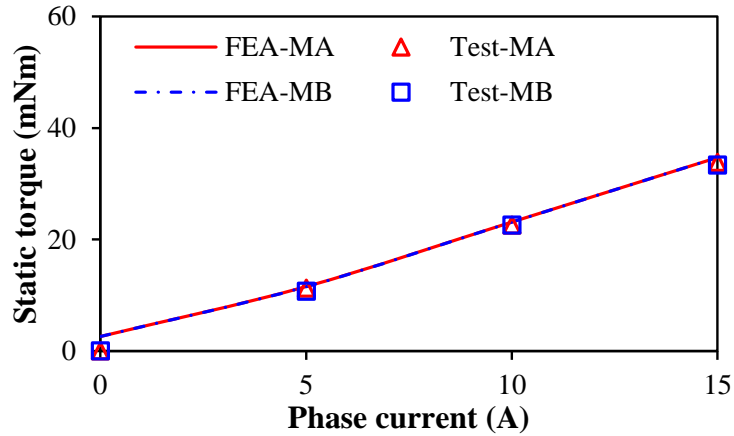
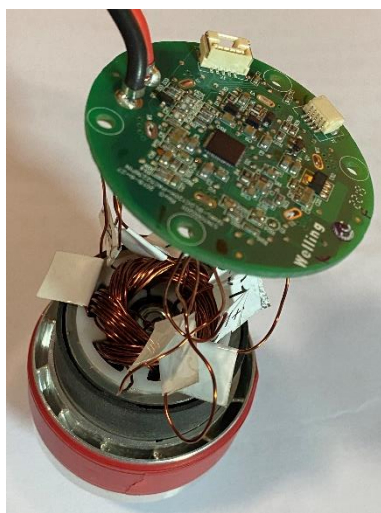
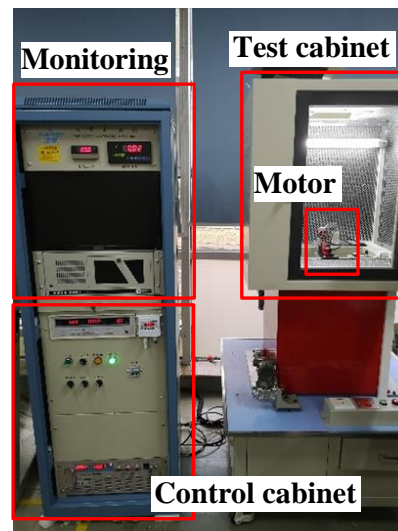


Fig. 3. 31. Maximum measured and FE predicted static torques with various phase currents.

Two motors are tested at the rated speed of 180krpm and Fig. 3. 32 shows the prototypes with drive system and high-speed test platform. The sensorless operation based on the detection of the zero-crossing of the back-EMF waveform is employed. By speed control, two proposed 6s/2p HSPM motors have successfully operated up to 180krpm, Fig. 3. 33. It can be seen that for MA and MB, when the DC link voltage is 30V, both switches are switched on with almost 100% duty cycle. It should be stated that the controller and experimental platform are supplied by the Midea Company.

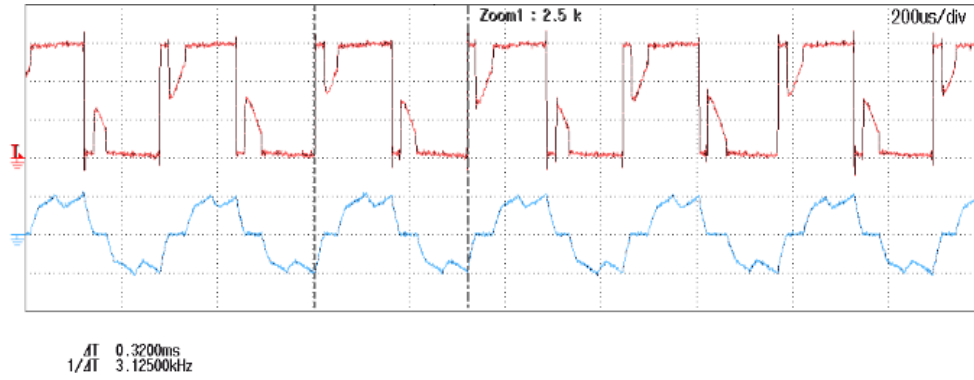


(a) Prototypes

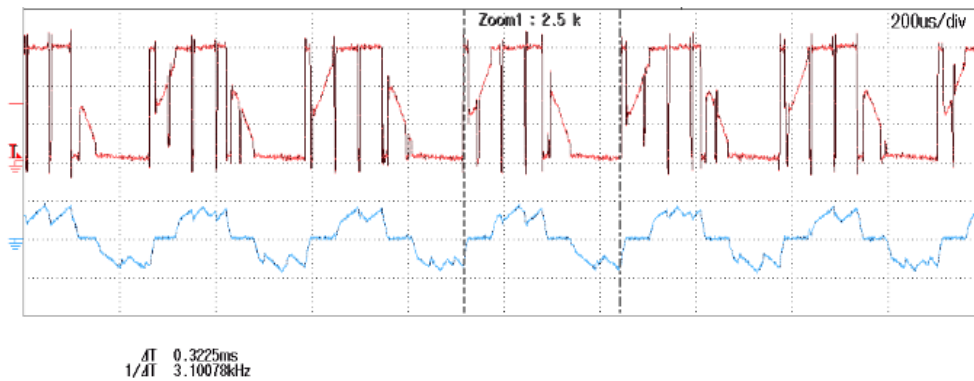


(b) Experimental platform for high-speed operation

Fig. 3. 32. Prototypes and high-speed test platform.



(a) Motor A



(b) Motor B

Fig. 3. 33. Measured terminal voltage and phase current waveforms of two prototypes at the rated speed of 180 krpm under speed control (10.0V/div; 20.0A/div;  $U_{dc} = 30V$ ).

### 3.7 Conclusion

This chapter has proposed two 6s/2p HSPM motors with different layouts of 2 slot-pitch windings. With stator loss and current density limitations, two motors have been optimized for maximum torque density and they have the same optimal design. Then, the electromagnetic performances of two optimized motors have been analyzed and compared. It shows that Motor B is an attractive motor design due to short axial length of end-winding, large torque density, and small phase inductance. Compared with a conventional 3s/2p HSPM motor with non-overlapping windings, the 6s/2p HSPM motor with 2 slot-pitch windings offers advantages in high torque, small phase inductance, low rotor loss and no UMF. Two 6s/2p HSPM motors with alternate layouts of 2 slot-pitch windings have been manufactured and some of the FE analyses have been validated by experiments. By high-speed test, two prototypes have successfully operated up to 180krpm.

### APPENDIX 3. A

In this section, the influence of end-winding models on the end-winding axial lengths of Motors A and B is discussed in detail, and their 2D- and 3D-models are shown in Fig. 3. 2.

From another perspective, the end-winding axial structures of Motors A and B are shown in Fig. 3. 34. For Motor A, Fig. 3. 34 (a), the end-windings of coils B1 and A2 are overlapped totally, Fig. 3. 34 (c). For Motor B, Fig. 3. 34 (b), the coils A1 and B1 are located parallelly and have no intersection, but coil C2 has intersections with half of coil A1 and half of Coil B1, Fig. 3. 34 (d). Therefore, in terms of the overlapping regions of end-windings, Motors A and B have the same overlapped region of end-windings, i.e. two phase windings. However, in Motor A, the width of the overlapped region is twice of that in Motor B, which may result in a longer end-winding axial length.

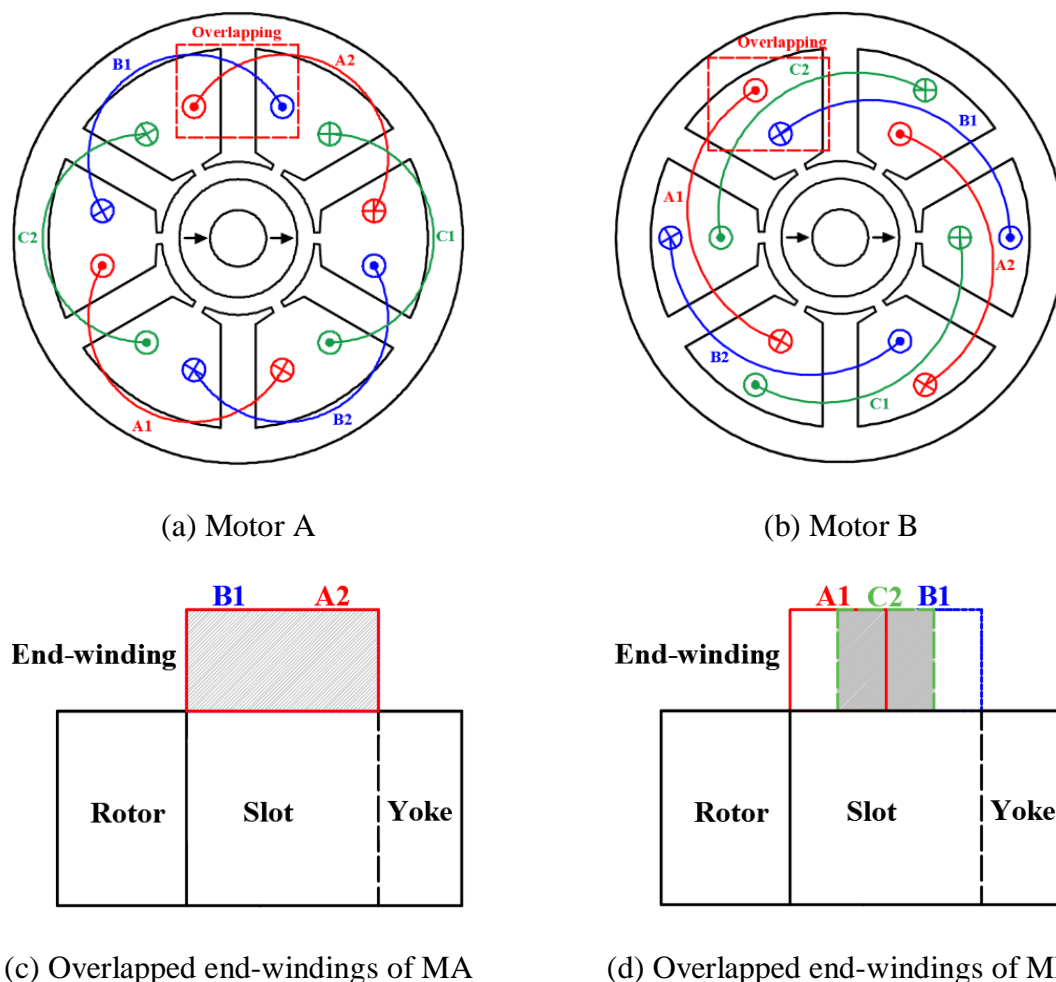


Fig. 3. 34. 6s/2p HSPM motors with alternate layouts of 2 slot-pitch windings.

Although Table 3. 7 shows the end-winding axial length of two prototypes in Fig. 3. 28 are



almost the same, the other prototypes of Motors A and B are manufactured, which are optimized by a fixed current density, Fig. 3. 35. It can be seen that Motor B has a shorter motor axial length. Therefore, in theory, compared with Motor A, Motor B has a smaller width of the overlapped region of end-windings and a shorter axial length of end-windings, which may lead to a higher torque density.



(a) Motor A



(b) Motor B



(c) Motor axial length of MA



(d) Motor axial length of MB

Fig. 3. 35. Two newly wound prototypes and their motor axial lengths.

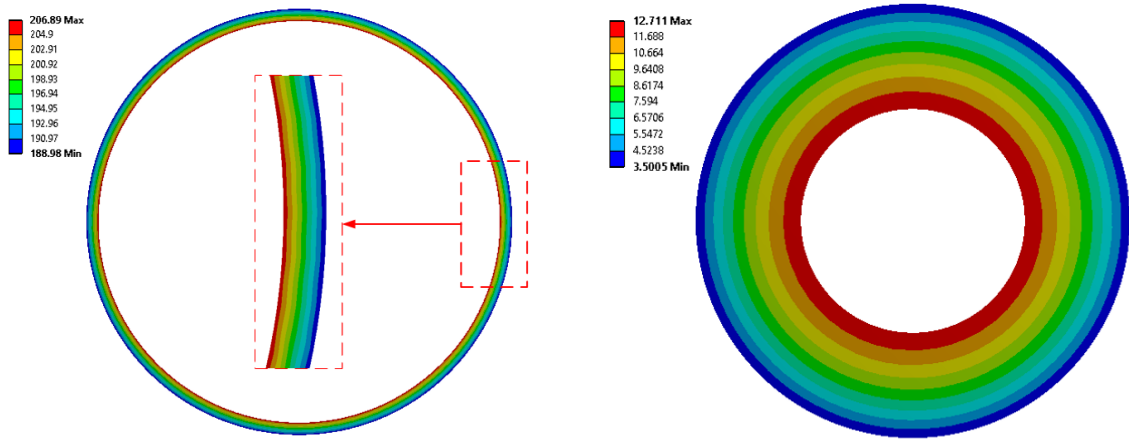
### APPENDIX 3. B

The properties of the magnet and stainless-steel sleeve are listed in Table 3. 9. The thickness of the sleeve is 0.3mm, the interference fit between the sleeve and magnet is 0.005mm. Fig. 3. 36 shows the stress analyses of sleeve and magnet under high-speed operation (180krpm). The maximum Von-Mises stress of the sleeve is 206.89Mpa, Fig. 3.36 (a), which is smaller than its ultimate tensile strength (586Mpa). In addition, the maximum 1<sup>st</sup> principal stress of the magnet, i.e. the maximum tensile stress, is 12.71 MPa, Fig. 3.36 (b), which is smaller than its ultimate tensile strength (80Mpa). Since the magnet is brittle but has high compression strength, the 3<sup>rd</sup> principal stress of the magnet is unnecessary in this thesis. Therefore, the design of sleeve is safe for high-speed operation and no mechanical issues.

Table 3. 9

Mechanical Parameters of Sleeve and Magnet Materials

	N45SH	Stainless steel
Young's modulus, $E$ (Gpa)	160	193
Poisson's ratio, $\nu$	0.24	0.31
Density, $\rho$ (Kg/m <sup>3</sup> )	7400	7750
Ultimate tensile strength, $\sigma_u$ (Mpa)	80	586



(a) Von-Mises stress of sleeve

(b) 1<sup>st</sup> principal stress of magnet

Fig. 3. 36. Stress analyses of sleeve and magnet at 180krpm.

## CHAPTER 4

### INFLUENCE OF ROTOR ECCENTRICITIES ON ELECTROMAGNETIC PERFORMANCE OF 2-POLE PERMANENT MAGNET MOTORS

Rotor eccentricities may exist in PM motors due to manufacturing and mounting tolerances, and bearing wear. This is critical for permanent magnet motors since it will affect the electromagnetic performance and also lead to mechanical issues, noise, and vibration. This chapter analyses the electromagnetic performances of 3s/2p and 6s/2p PM motors with static and dynamic rotor eccentricities considering eccentricity ratio, eccentricity angle, and rotor initial angle. Some of the predictions by FEM are validated by the experimental results.

This chapter was published in IEEE Transactions on Energy Conversion.

#### 4.1. Introduction

There are two types of rotor eccentricity, i.e. static and dynamic rotor eccentricities [DOR97]. In literature, the PM motors with static and dynamic rotor eccentricities have been extensively researched in terms of back-EMF, cogging torque, electromagnetic torque, and UMF, etc. [ZHU13] shows that the rotor eccentricity has a negligible effect on the back-EMF and torque of rotational symmetrical motors, but has significant influence in rotational asymmetric motors, where the rotational symmetrical and asymmetric motors mean that the motor configuration repeats every certain amount of angle or not. [ZHU14] presents that the rotor eccentricity leads to the largest impact on the cogging torque in the motors having  $2p=N_s\pm 1$ , smaller influence in the motors having  $2p=N_s\pm 2$ . In [TON20], a novel analytical model is proposed for predicting the influence of rotor eccentricity and magnet defects on the cogging torque in SPM motors. The effects of rotor eccentricity on the UMFs for 24s/4p IPM and SPM motors are compared in [KIM01]. The comparison shows that the rotor eccentricity has a larger influence on the UMF of the IPM due to a relatively small air gap and severe magnitude saturation. [WUL13] analyses the influence of static/dynamic rotor eccentricities on the UMFs of different pole/slot number combination PM motors with asymmetric windings. [KIM16] investigates the UMF of a slotless 2-pole toroidally wound brushless direct current (BLDC) motor with rotor eccentricity. An improved conformal mapping (ICM) method is presented in [ALA15] for magnetic field analysis in SPM motors with rotor eccentricity, which is employed in [ALA17] for investigating the influence of rotor eccentricity on UMF.

Nowadays, HSPM motors are employed widely for many applications. However, few papers

research the influence of rotor eccentricity on the electromagnetic performance of the HSPM motors. In addition, the 2-pole is popular for high-speed applications due to its limitation of motor size, stator iron loss, and converter loss [ZHU97]. There are different slot and pole number combinations of 2-pole HSPM motors, such as 3s/2p [ZHU97] [HES87] [BIA05] [MAJ17], 6s/2p [SHI04] [NOG05] [UZH14] [LIM17], 12s/2p [WAN03] [XUJ11] [FAN12], and 18s/2p [ZHA19]. Therefore, the influence of static and dynamic eccentricities on the electromagnetic performance of 2-pole rotational asymmetric (3-slot) and symmetrical (6-slot) motors will be investigated in this chapter.

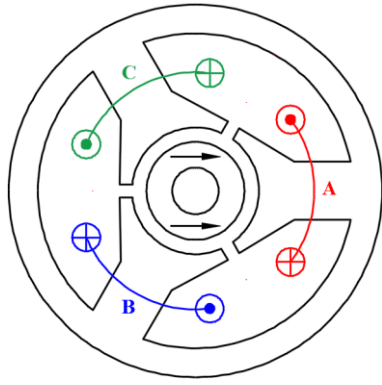
In section 4. 2, motor topologies and rotor eccentricity types are discussed. Section 4. 3 analyses the electromagnetic performance of 3s/2p PM motors with static and dynamic rotor eccentricities accounting for eccentricity ratio, eccentricity angle, and rotor initial angle. In section 4. 4, 6s/2p PM motors with different winding configurations and rotor eccentricity are analyzed. In section 4. 5, 2-pole prototype motors without and with static/dynamic eccentricities are tested to validate the predictions by finite element (FE) method, and section 4. 6 is the conclusion.

## **4.2. Motor Topologies and Rotor Eccentricity Types**

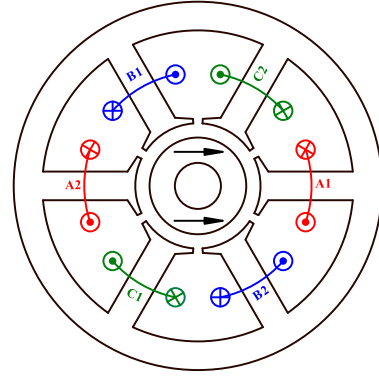
In this section, the topologies of a 3s/2p PM motor and 6s/2p PM motors with 1, 2, and 3 slot-pitch windings will be described, and two rotor eccentricity types will be introduced.

### **4.2.1 Motor Topologies**

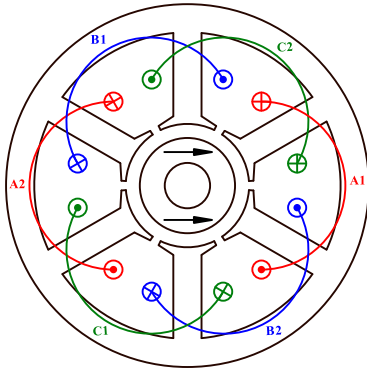
Fig. 4. 1 shows the topologies of 2-pole PM rotational asymmetric and symmetrical motors, i.e. 3s/2p PM motor with tooth-coil windings, 6s/2p PM motors with 1, 2, and 3 slot-pitch windings. They have a rated torque of 27 mNm at the rated current 10 A. The main parameters of 3s/2p and 6-slot PM motors are shown in Table 4.1. Four motors have different numbers of turns per phase due to different winding factors. A 2-pole magnet ring with parallel magnetization and a magnetic shaft are adopted. It is intended for high-speed operation, three phase 120° electric square wave current waveforms are employed.



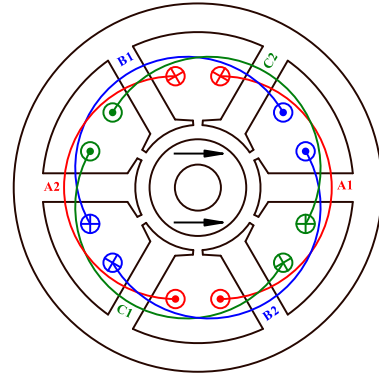
(a) 3s/2p motor



(b) 6s/2p motor with 1 slot-pitch windings



(c) 6s/2p motor with 2 slot-pitch windings



(d) 6s/2p motor with 3 slot-pitch windings

Fig. 4. 1. Topologies of 3s/2p and 6s/2p motors.

#### 4.2.2 Rotor Eccentricity Types

There are two kinds of rotor eccentricity: static eccentricity (SE) and dynamic eccentricity (DE). Their main difference is the position of the center of the rotor ( $O_r$ ).  $O_r$  is fixed for the static eccentricity when the rotor is rotating, while it is rotating around the center of the stator bore ( $O_s$ ) for the dynamic eccentricity, as shown in Fig. 4. 2, where  $g$  is the air-gap length of the motor without eccentricity,  $X$  is the rotor offset distance along the eccentricity direction,  $R_{in}$  is the stator bore radius,  $R_m$  is the magnet radius, i.e. rotor outer radius,  $\alpha$  and  $\beta$  are the eccentricity angle and the rotor initial angle,  $\delta$  is the angle difference between  $\alpha$  and  $\beta$ . When the rotor is offset towards phase A, the eccentricity angle ( $\alpha$ ) is defined as 0 elec. deg. The rotor initial position ( $\beta$ ) is defined as 0 elec. deg. when the back EMF of phase A equals zero. To describe the degree of rotor eccentricity, the eccentricity ratio ( $\varepsilon$ ) is introduced, which is the ratio of rotor offset distance to the air-gap length of the motor without eccentricity, i.e.  $\varepsilon = X/g$ .

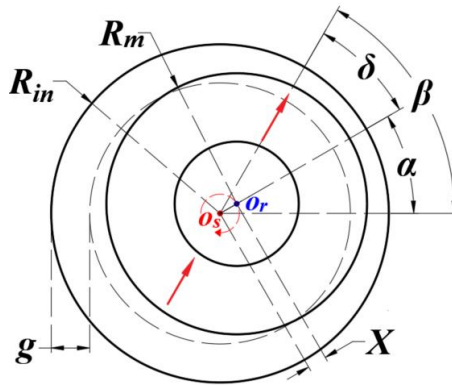


Fig. 4. 2. Illustration of static and dynamic rotor eccentricities.

Table 4.1

Main Parameters of 2-pole PM Motors

Pole / Slot number	2/3	2/6		
Winding configuration	Tooth-coil	1 slot-pitch	2 slot-pitch	2 slot-pitch
Winding factor	0.866	0.5	0.866	1.0
Stator outer diameter, mm	40	40	40	40
Stator bore diameter, mm	13.6	13.6	13.6	13.6
Stator active length, mm	10	10	10	10
Tooth body width, mm	6.22	3.11	3.11	3.11
Stator yoke height, mm	3.11	3.11	3.11	3.11
Air-gap length, mm	1.55	1.55	1.55	1.55
Slot opening, mm	1.5	1.0	1.0	1.0
Magnet thickness, mm	2.75	2.75	2.75	2.75
Magnet remanence, T	1.3	1.3	1.3	1.3
Shaft diameter, mm	5	5	5	5
Number of turns/phase	21	36	21	18

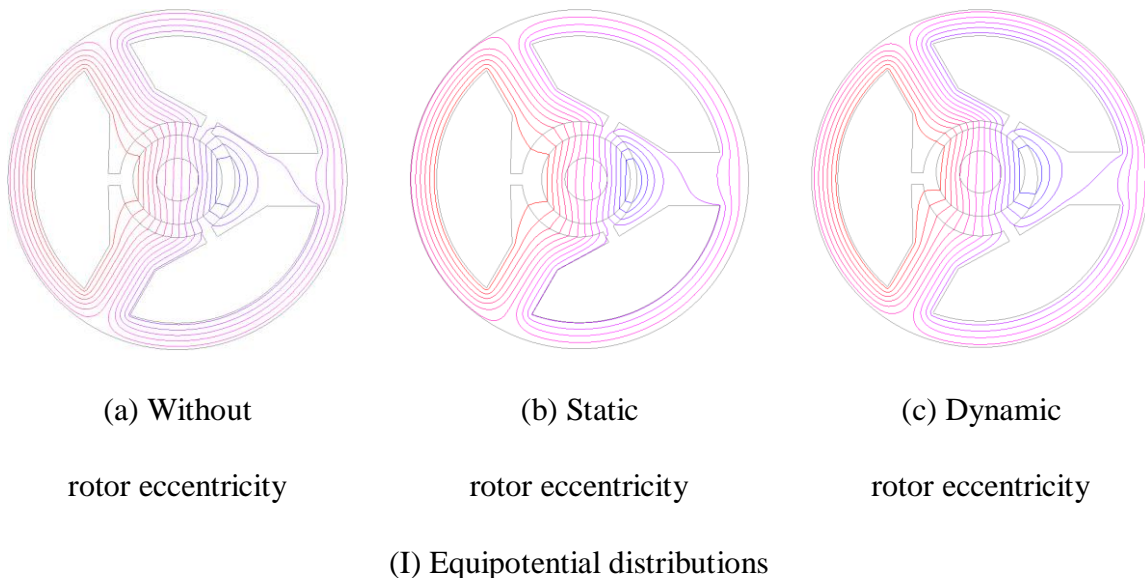
### 4.3. 2-Pole Asymmetric Motor with Rotor Eccentricity

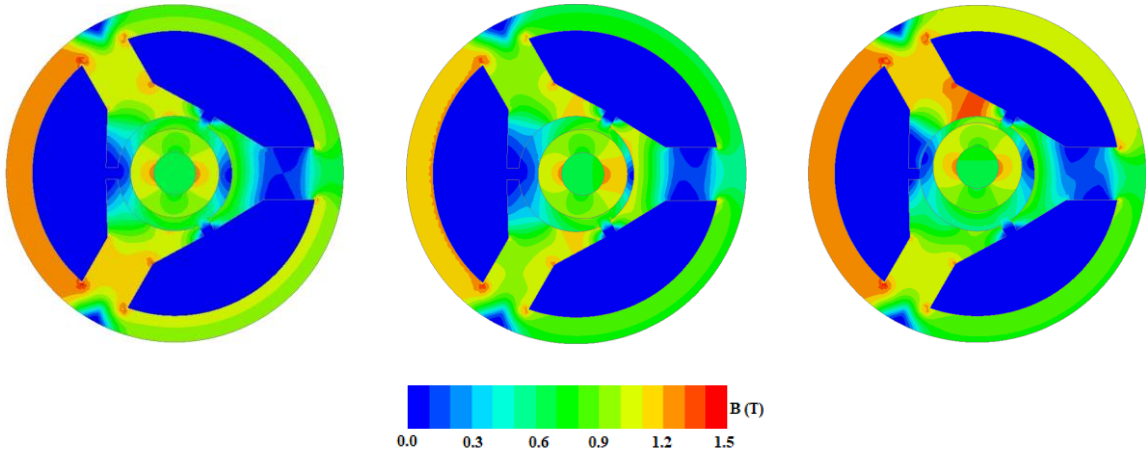
The electromagnetic performances of the 3s/2p PM motor with rotor eccentricity is analyzed in this section.

#### 4.3.1 Open-circuit Air-gap Field

Figs. 4. 3 and 4. 4 show the equipotential, flux contour, and air-gap field distributions of 3s/2p PM motors without/with static/dynamic eccentricities when the eccentricity ratio is 0.5 and the rotor position ( $\theta$ ) is  $90^\circ$ . It is assumed that the eccentricity angle and rotor initial angle are  $0^\circ$ . It can be seen that with static rotor eccentricity, the smallest air-gap is fixed relative to the stator, but with dynamic rotor eccentricity, the smallest air-gap is rotating relative to the stator. The spectra show both static and dynamic rotor eccentricities lead to the 2<sup>nd</sup>, 3<sup>rd</sup>... order harmonics.

In [ZHU14], the air-gap field  $B_g$  of the motor with rotor eccentricity can be computed by a simple analytical method. The air-gap field has the  $(n\pm v)$ th spatial harmonics caused by rotor eccentricity, where  $n$  is the original field harmonics and  $v$  is an integer. For the 3s/2p motor, the spatial harmonic contents of air-gap flux densities with/without eccentricity are shown in Table 4. 2. The motor without eccentricity has the  $(mp\pm jN_s)$ th harmonics, which are the modulated PM harmonics caused by slotting. Since the largest influence caused by the rotor eccentricity occurs when  $v=1$  [ZHU14], only  $n\pm 1$  is given in Table 4. 2 and the harmonic contents are the same as those shown in Fig. 4. 4 (b).

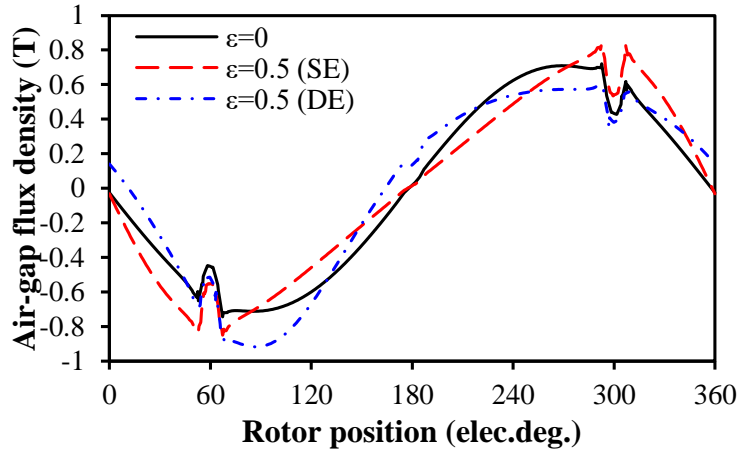




(a) Without rotor eccentricity                      (b) Static rotor eccentricity                      (c) Dynamic rotor eccentricity

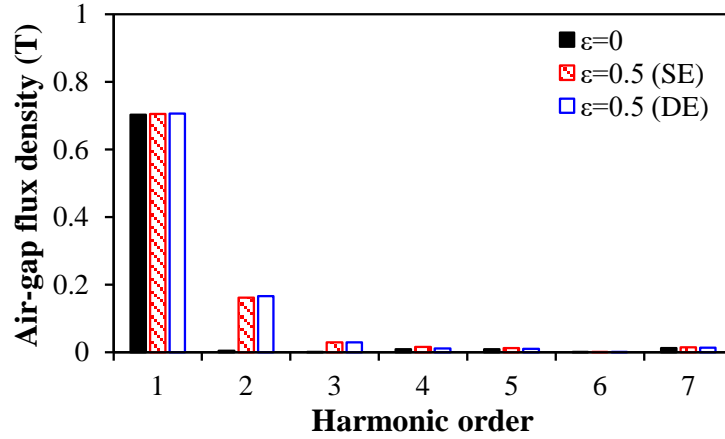
(II) Flux contour distributions

Fig. 4. 3. Equipotential and flux contour distributions of 3s/2p HSPM motors without and with rotor eccentricity,  $\theta=90^\circ$ ,  $\varepsilon=0.5$ .



(a) Waveforms





(b) Spectra

Fig. 4. 4. Air-gap field distributions of 3s/2p motors without/with static/dynamic rotor eccentricities, on the radial position ( $r = R_{si} - 0.25$  mm) and rotor position ( $\theta = 90^\circ$ ).

Table 4.2

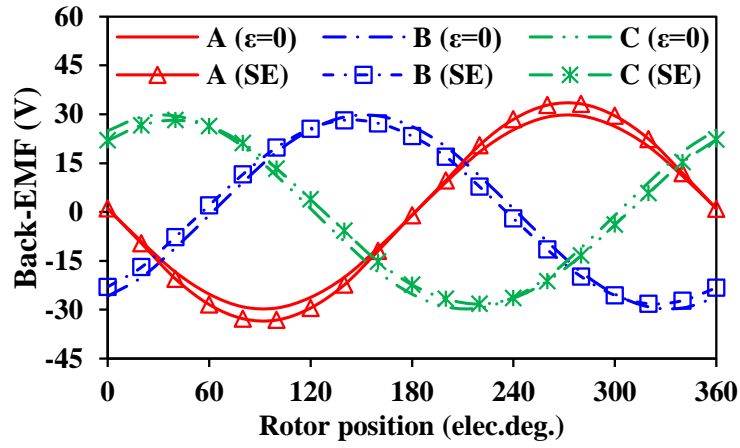
Spatial Harmonic Contents of Air-gap Flux Density

Original PM harmonics	Modulated PM harmonics due to slotting	Additional air-gap field due to rotor eccentricity	
$n = mp$	$n = mp \pm jN_s$	$n \pm v$ ( $v = 1$ )	
1, 3, 5...	1, 2, 3, 4, 5...	$n+1$	$n-1$
		2, 3, 4, ...	1, 2, 3, ...

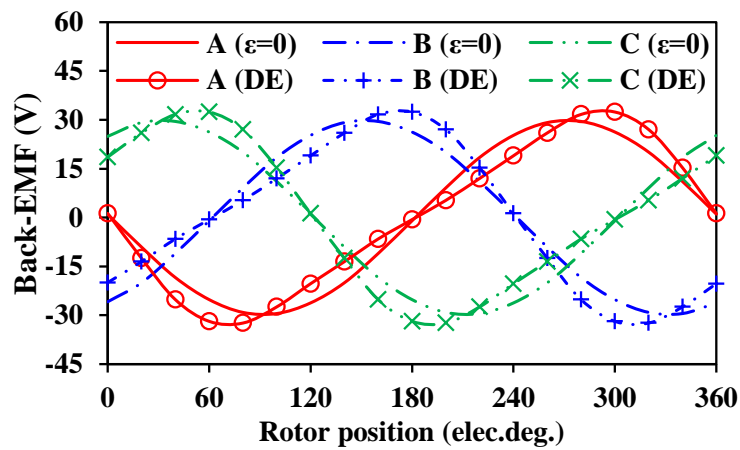
#### 4.3.2 Back-EMF

The back-EMF waveform of the 3s/2p HSPM motor is sinusoidal due to a parallel magnetized magnet rotor. With static rotor eccentricity  $\epsilon=0.5$ , phase A has an increased peak back-EMF while those of phases B and C decrease, which results in the unbalanced back-EMFs of three phase, Fig. 4. 5 (a). The spectra show that phase A has an increased magnitude of fundamental back-EMF, but those of phases B and C decrease. There is no additional harmonic in the three phase back-EMFs caused by static rotor eccentricity. Therefore, the static rotor eccentricity does not change the harmonic contents but affects the fundamental magnitude. With dynamic rotor eccentricity  $\epsilon=0.5$ , the fundamental magnitudes of three phase back-EMFs remain the same, but the 2<sup>nd</sup> order harmonic exists, Fig. 4. 5 (b). Therefore, the dynamic rotor eccentricity does not change the fundamental magnitude but affects the harmonic contents due to the

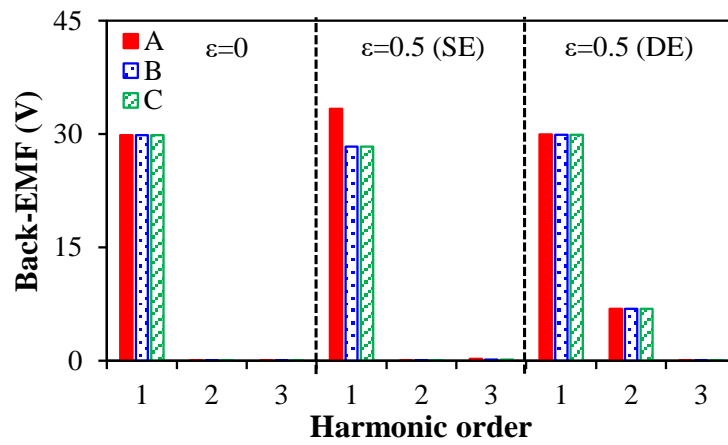
$(n\pm 1)$ th temporal order harmonics [ZHU13]. To investigate the influence of eccentricity ratio, eccentricity angle, and rotor initial angle on the back-EMF, the motors with static and dynamic rotor eccentricities are analyzed separately.



(a) SE



(b) DE



(c) Spectra

Fig. 4. 5. Back-EMFs of 3s/2p motors without/with static/dynamic rotor eccentricities,  $\epsilon=0.5$ .

### A. Static rotor eccentricity

To describe the degree of unbalanced three phase back-EMFs due to static rotor eccentricity, the unbalanced ratio ( $R_u$ ) is employed, which is defined by the National Electrical Manufacturers Association (NEMA) as

$$R_u = \frac{\text{Max}(E_{ph} - E_{ave})}{E_{ave}} \quad (4.1)$$

With the increase of eccentricity ratio, the peak back-EMF of phase A increases linearly while those of phases B and C decrease simultaneously, Fig. 4. 6, which leads to the linear increase of the unbalanced ratio. Due to the rotor eccentricity angle, the increased eccentricity ratio does not change the phase angle of the back-EMF of phase A, but increases or decreases those of phases B and C linearly, Fig. 4. 7. The positive and negative offset phase angles in Fig. 4. 7 (b) indicate the advanced and lagged phase angles, Fig. 4. 8. Therefore, the unbalanced three phase back-EMFs caused by static rotor eccentricity include the unbalanced magnitudes and phase angles of fundamental back-EMF. It is worth noting that with the increase of eccentricity ratio, phase A has the increased peak back-EMF but unchanged phase angle since the eccentricity location is towards phase A, i.e.  $\alpha=0^\circ$ .

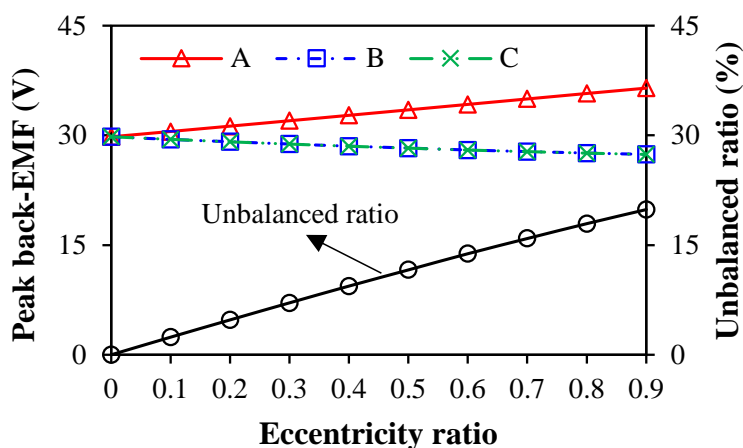
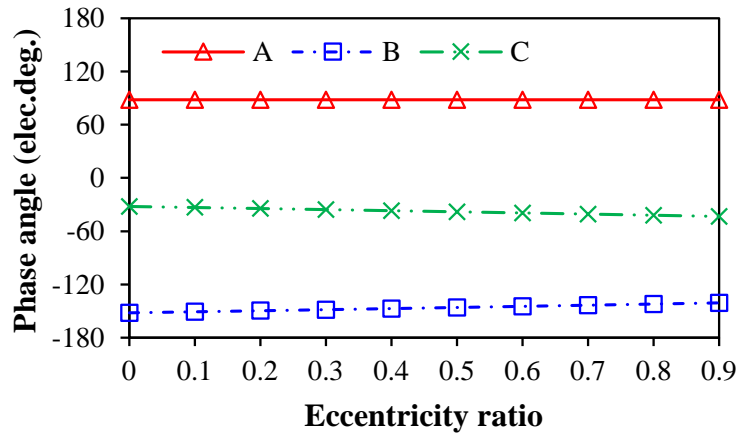
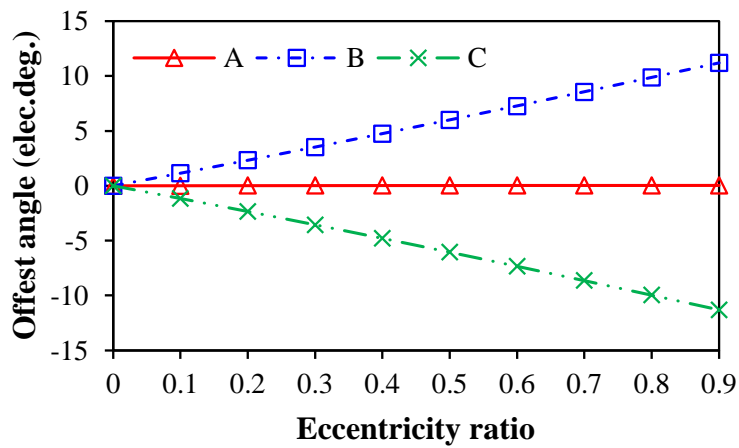


Fig. 4. 6. Variation of peak values and unbalanced ratio of three phase back-EMFs with static rotor eccentricity ratio.



(a) Phase angle



(b) Offset phase angle

Fig. 4. 7. Relationships between phase angles and offset phase angles of back-EMFs of three phases, and eccentricity ratio.

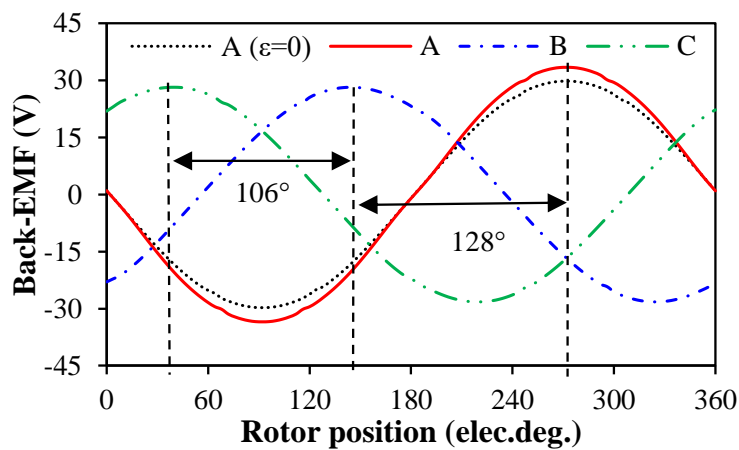


Fig. 4. 8. Unbalanced phase angles with static eccentricity,  $\epsilon=0.5$ .

Considering the eccentricity angle, the rotor can be offset towards any phase winding or angular position. With the increase of eccentricity angle and  $\epsilon=0.5$ , the peak values of back-EMFs of

three phase change periodically, as well as the unbalanced ratio, Fig. 4. 9. When the eccentricity angles are  $60^\circ$  and  $180^\circ$ , the unbalanced three phase back-EMFs have the minimum unbalanced ratio. However, the maximum unbalanced ratio occurs when the eccentricity angles are  $0^\circ$  and  $120^\circ$ , i.e. one phase facing the smallest air-gap. Meanwhile, the changed eccentricity angle leads to the periodic changing of the phase angles of back-EMFs, Fig. 4. 10.

Therefore, for the static rotor eccentricity, the eccentricity ratio affects the maximum value of peak back-EMF, unbalanced ratio, and offset phase angle. However, the eccentricity angle changes the peak value and phase angle of the back-EMF of each phase periodically, so does the unbalanced ratio.

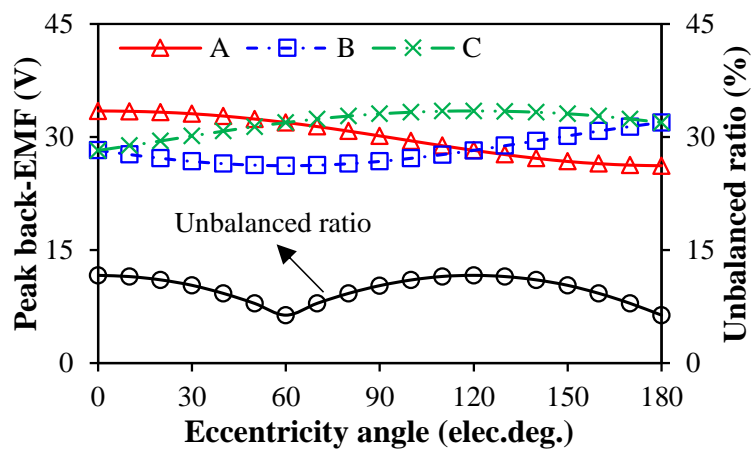
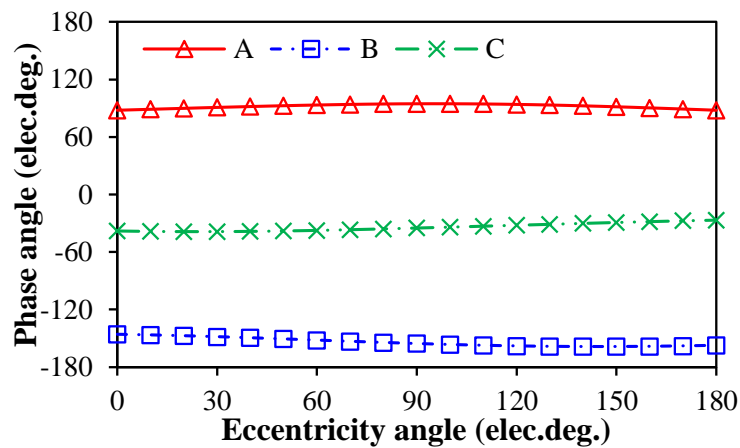
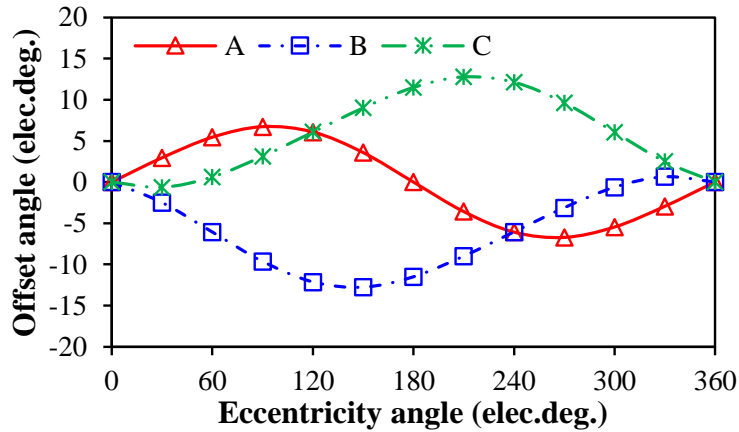


Fig. 4. 9. Variation of peak values and unbalanced ratio of three phase back-EMFs with static eccentricity angle,  $\varepsilon=0.5$ .



(a) Phase angle



(b) Offset phase angle

Fig. 4. 10. Influence of static eccentricity angle on the phase angles of back-EMFs of three phases,  $\varepsilon=0.5$ ,  $\beta=0^\circ$ .

### B. Dynamic rotor eccentricity

The dynamic rotor eccentricity mainly affects the harmonic contents due to the  $(n\pm 1)$ th temporal order harmonics, but does not change the fundamental magnitude and remains balanced in three phase back-EMFs. With the increase of the eccentricity ratio, the positive and negative peak values of three phase back-EMFs increase simultaneously, Fig. 4. 11. The increased eccentricity ratio does not change the fundamental magnitude, but increases the magnitude of the 2<sup>nd</sup> order harmonic, Fig. 4. 12, which leads to the increase of positive and negative peak back-EMFs.

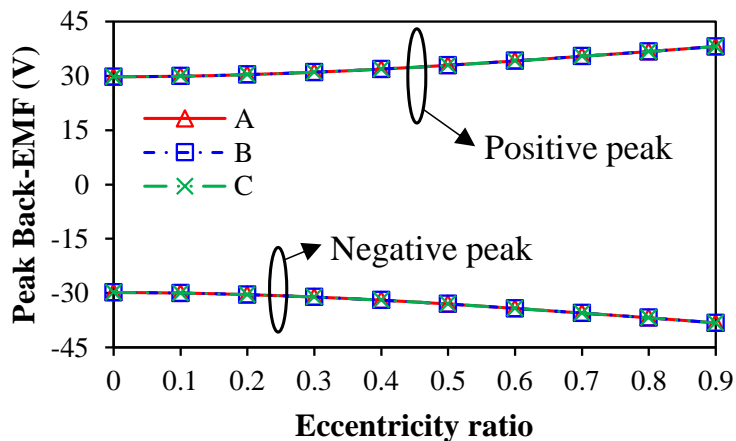


Fig. 4. 11. Influence of dynamic rotor eccentricity ratio on the positive and negative peak values of three phase back-EMFs.

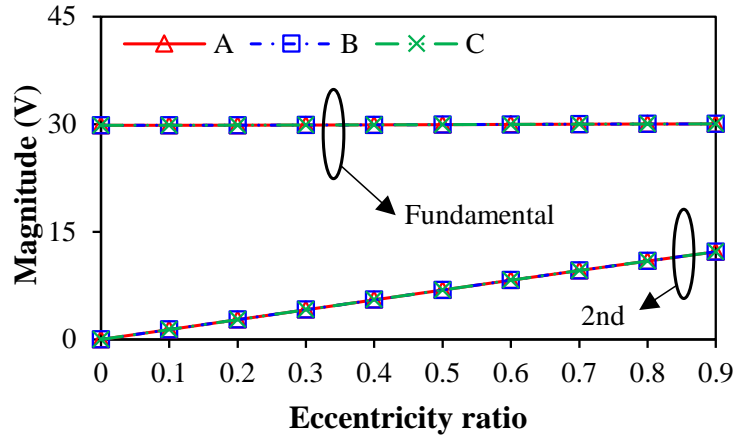
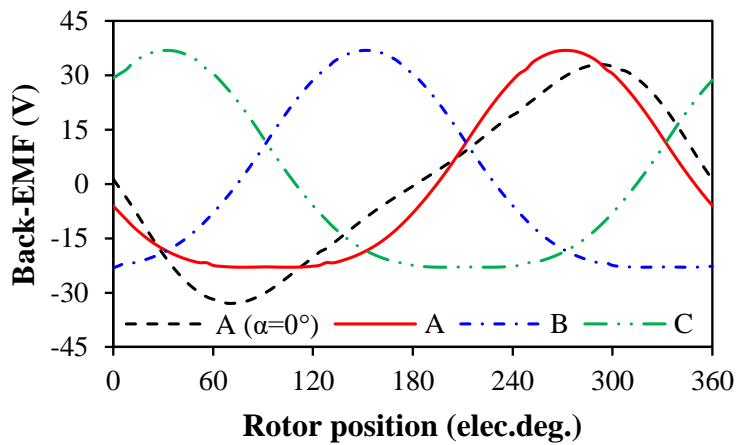
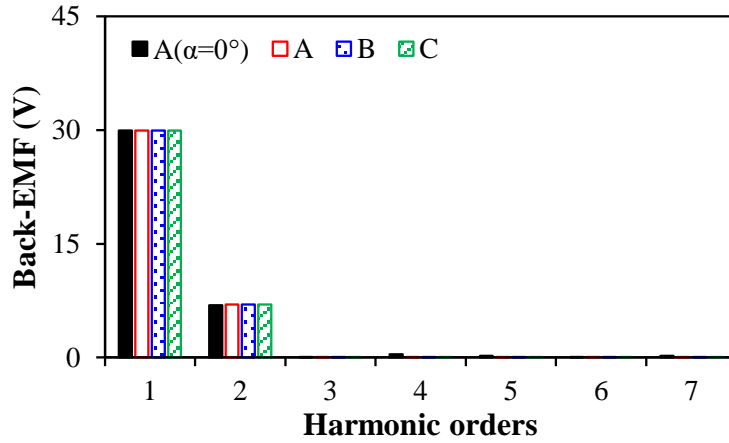


Fig. 4. 12. Influence of dynamic rotor eccentricity ratio on the magnitudes of the fundamental and 2<sup>nd</sup> order harmonic of back-EMFs of three phase.

Considering the eccentricity angle ( $\alpha$ ), when  $\alpha=90^\circ$ ,  $\beta=0^\circ$ , and  $\varepsilon=0.5$ , asymmetric positive and negative half-periods of back-EMF waveforms exist in each phase of the motor with dynamic rotor eccentricity, Fig. 4. 13. The spectra show that the motors with  $\alpha=90^\circ$  and  $\alpha=0^\circ$  have the same harmonic contents and magnitudes. With the increase of the eccentricity angle, the positive peak values of three phase back-EMFs increase slightly at first and then decrease while the negative peak values decrease sharply and then increase, which results in minimum peak-to-peak values of three phase back-EMFs when  $\alpha=90^\circ$ , Fig. 4. 14. Therefore, the largest asymmetric back-EMF waveform occurs when the eccentricity angle is  $90^\circ$ .



(a) Waveforms



(b) Spectra

Fig. 4. 13. Three phase back-EMFs of the motor with dynamic rotor eccentricity,  $\alpha=90^\circ$ ,  $\varepsilon=0.5$ .

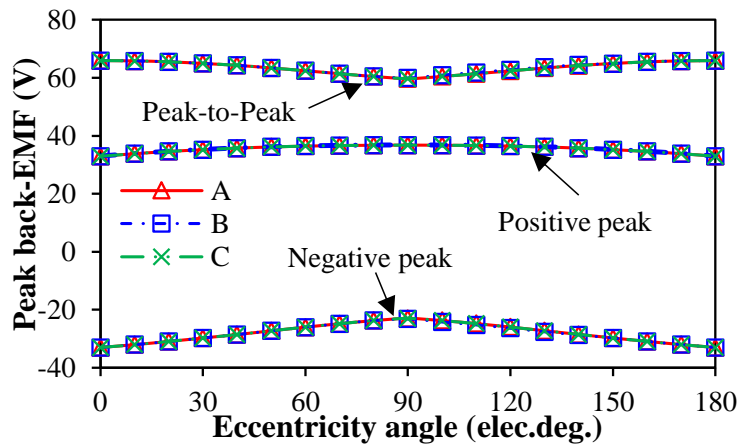


Fig. 4. 14. Variation of positive and negative peak values of three phase back-EMFs with eccentricity angle,  $\varepsilon=0.5$ .

Fig. 4. 15 shows the magnitudes of the fundamental and 2<sup>nd</sup> order harmonic of back-EMFs of three phase remain unchanged with the eccentricity angle. Although the eccentricity angle does not change the phase angle of the fundamental back-EMF, Fig. 4. 16 (a), the changed eccentricity angle affects the phase angle of the 2<sup>nd</sup> order harmonic, Fig. 4. 16 (b), which can be explained by a simple analytical method in the Appendix. When the eccentricity angle is  $0^\circ$ , the fundamentals and 2<sup>nd</sup> order harmonic of back-EMF waveforms of phase A equal to zero at the same rotor position, i.e.  $\theta=0^\circ$  and  $\theta=180^\circ$ , Fig. 4. 17 (a), which results in the symmetrical back-EMF waveform of phase A. When the eccentricity angle is  $90^\circ$ , the fundamental and 2<sup>nd</sup> order harmonic of back-EMF waveforms of phase A have a canceling effect at  $\theta=90^\circ$  but have an additive effect at  $\theta=270^\circ$ , Fig. 4. 17 (b), which results in the largest asymmetric back-EMF



waveform of phase A. Therefore, when the eccentricity angle is  $90^\circ$ , the 2<sup>nd</sup> order harmonic has the largest influence on the asymmetric positive and negative half-periods of phase back-EMF. However, this result depends on the rotor initial angle, which will be discussed in the next part.

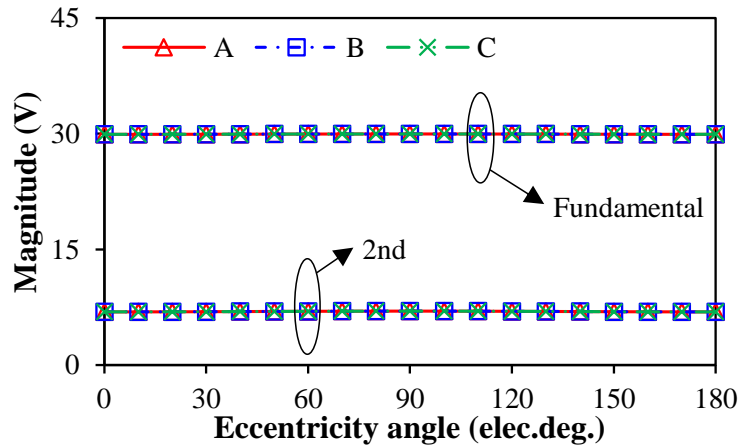
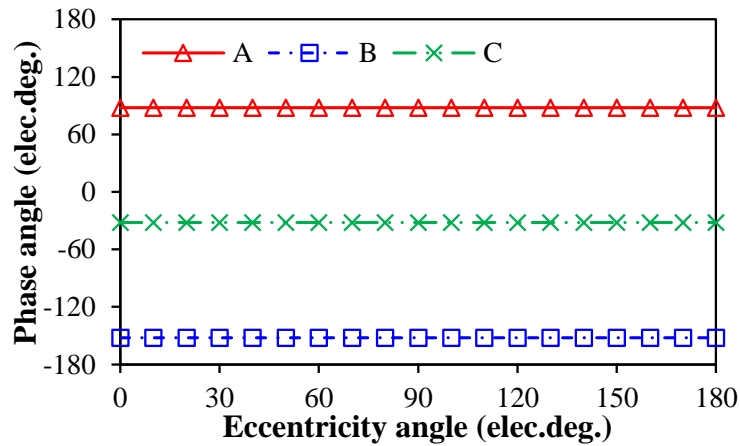
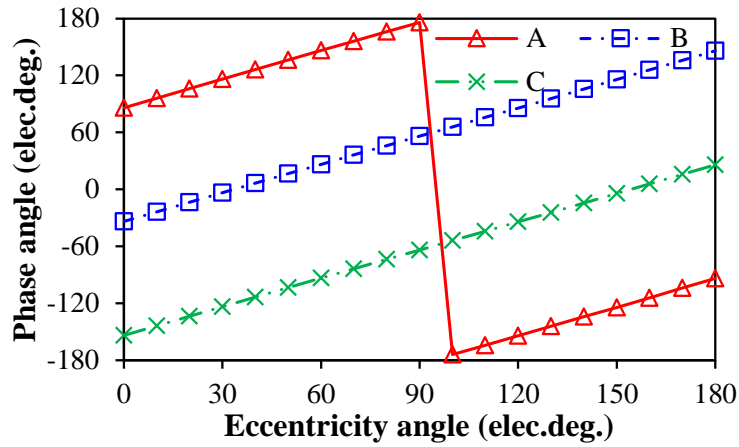


Fig. 4. 15. Variation of magnitudes of the fundamental and 2<sup>nd</sup> order harmonic of three phase back-EMFs with eccentricity angle,  $\varepsilon=0.5$ .

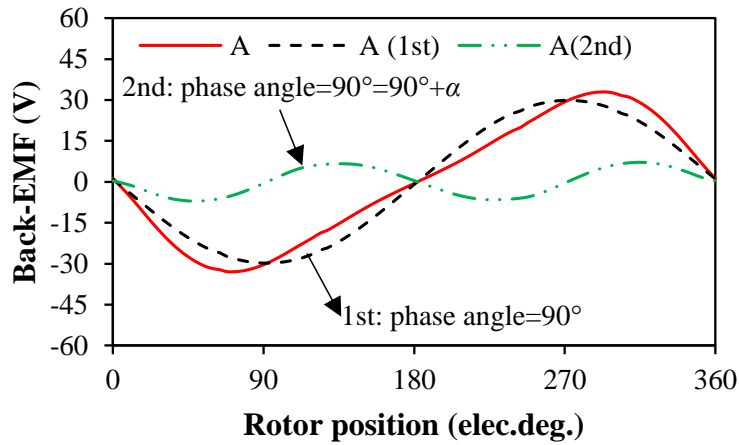


(a) Fundamental

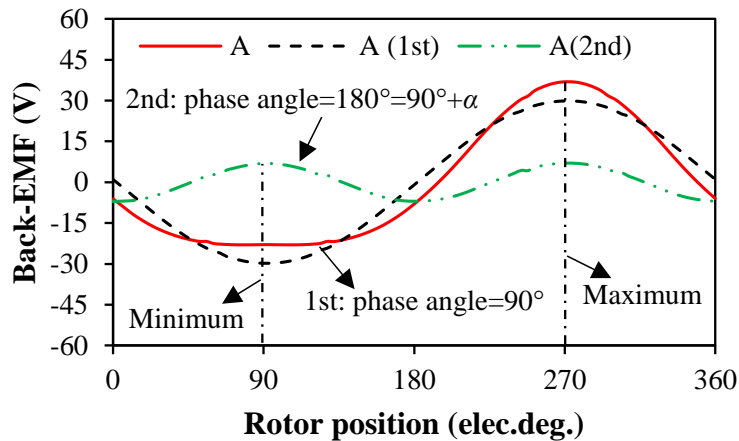


(b) 2<sup>nd</sup> order harmonic

Fig. 4. 16. Variation of phase angles of the fundamental and 2<sup>nd</sup> order harmonic of three phase back-EMFs with eccentricity angle,  $\epsilon=0.5$ .



(a)  $\alpha=0^\circ$



(b)  $\alpha=90^\circ$

Fig. 4. 17. Fundamental and 2<sup>nd</sup> order harmonic of phase A back-EMF waveforms with different eccentricity angles.

Considering the rotor initial angle ( $\beta$ ), the phase angles of the fundamental and 2<sup>nd</sup> order harmonic of back-EMF of phase A are equal to  $90^\circ + \beta$  and  $90^\circ + \beta + \alpha$ , respectively, Fig. 4. 18, since the phase A has a ‘90°’ phase angle of the fundamental back-EMF without rotor eccentricity, Fig. 4. 16 (a). Therefore, the rotor initial angle affects the phase angles of the fundamental and harmonics of back-EMF. However, the eccentricity angle only affects the phase angles of the  $(n \pm 1)$ th temporal order harmonics caused by dynamic rotor eccentricity. For the largest asymmetric back-EMF waveform, the phase angles of the fundamental and 2<sup>nd</sup> order harmonic of back-EMF of phase A should be satisfied as

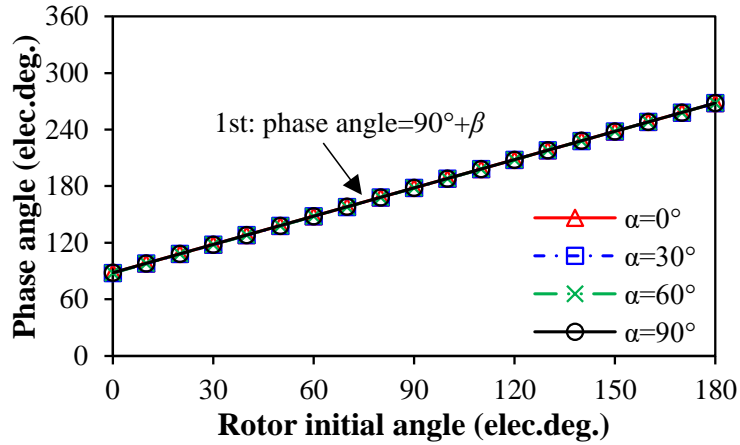
$$90^\circ + \beta = \frac{90^\circ + \alpha + \beta}{2} \Rightarrow \alpha - \beta = \delta = 90^\circ \quad (4. 2)$$

where the phase angle of the 2<sup>nd</sup> order back-EMF harmonic is divided by 2 due to the one cycle of fundamental back-EMF, Fig. 4. 17 (b). For the symmetrical back-EMF waveform, the phase angles of the fundamental and 2<sup>nd</sup> order harmonic of back-EMF of phase A should satisfy

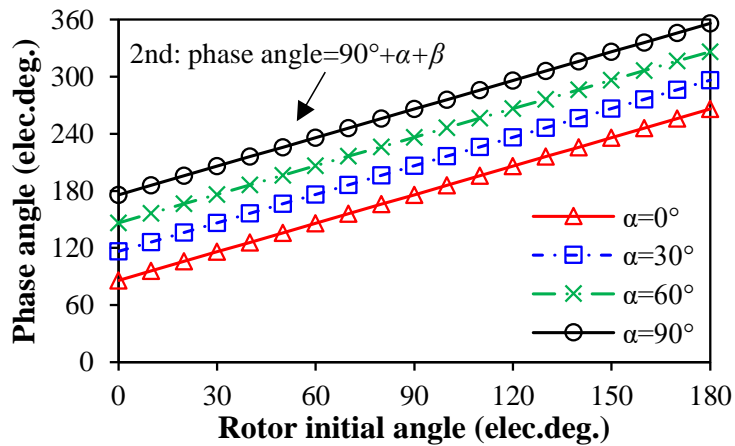
$$90^\circ + \beta - \frac{90^\circ + \alpha + \beta}{2} = \frac{90^\circ}{2} \Rightarrow \alpha = \beta, \delta = 0 \quad (4. 3)$$

where ‘90°/2’ means two sinusoidal back-EMF waveforms equal to zero at the same rotor position, Fig. 4. 17 (a). Fig. 4. 19 shows the variation of peak back-EMF of phase A with the angle difference ( $\delta$ ) between the eccentricity angle and the rotor initial angle. It shows that the maximum and minimum peak-to-peak back-EMFs occur when the angle difference is equal to 0° and 90°, respectively.

Therefore, for a 3s/2p PM motor, the dynamic eccentricity will not cause unbalance in the three phase back-EMFs, but affects the peak value and harmonic contents of phase back-EMFs. Considering the eccentricity angle and the rotor initial angle, the dynamic rotor eccentricity results in the asymmetric positive and negative half-periods of phase back-EMF waveforms and the smallest and largest influences occur when  $\delta=0^\circ$  and  $90^\circ$ , respectively.



(a) Fundamental



(b) 2<sup>nd</sup> order harmonic

Fig. 4. 18. Variation of phase angles of the fundamental and 2<sup>nd</sup> order harmonic of phase A back-EMF with rotor initial angle.

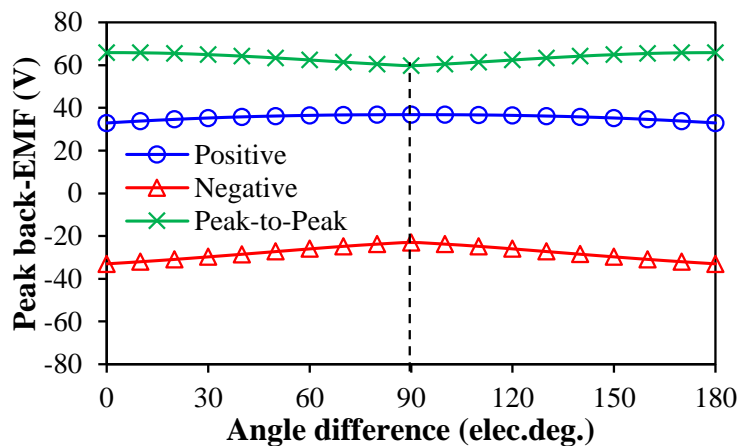


Fig. 4. 19. Influence of angle difference ( $\delta$ ) on the positive/negative peak values and peak-to-peak value of phase A back-EMF in the motor with dynamic rotor eccentricity.

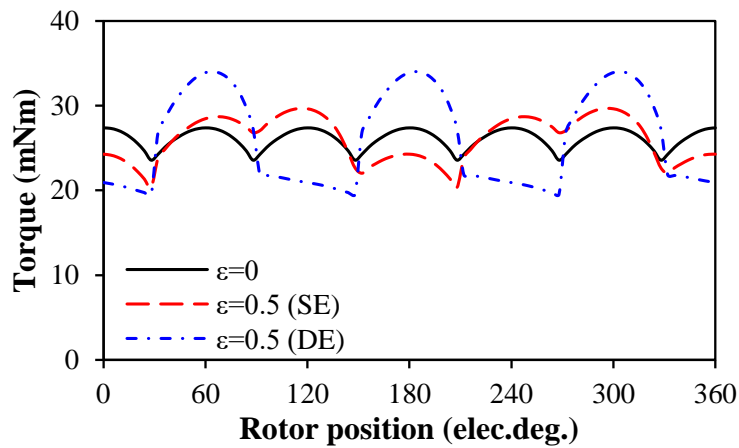
### 4.3.3 Electromagnetic Torque

As mentioned before, the static and dynamic rotor eccentricities have a significant influence on three phase back-EMFs, and hence, the influence on electromagnetic torque and torque ripple should be analyzed, since the electromagnetic torque ( $T_{em}$ ) can be given by

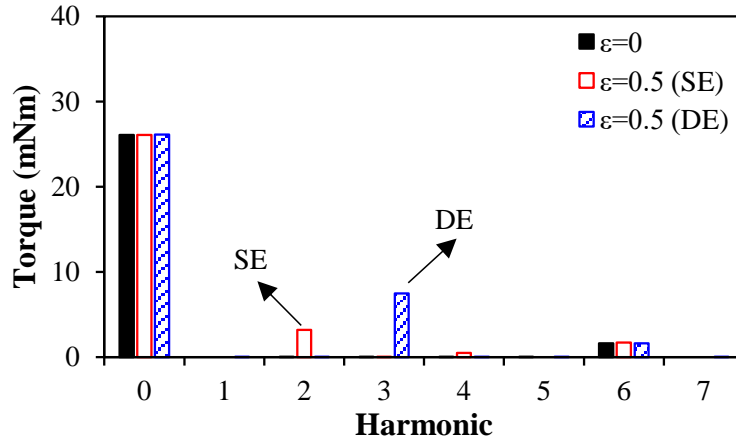
$$T_{em} = \frac{(e_a i_a + e_b i_b + e_c i_c)}{\omega} \quad (4.4)$$

where  $e_a$ ,  $e_b$ , and  $e_c$  are the back-EMFs of phases A, B, and C, respectively.  $i_a$ ,  $i_b$ , and  $i_c$  are the phase currents of phases A, B, and C, respectively, Fig. 4. 20 (c).  $\omega$  is the rotor mechanical speed.

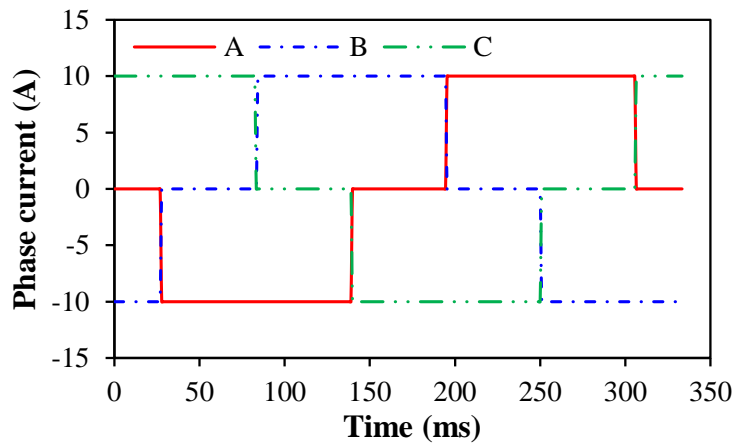
Fig. 4. 20 indicates that the static rotor eccentricity mainly leads to the 2<sup>nd</sup> order harmonic of electromagnetic torque, but the dynamic rotor eccentricity leads to the 3<sup>rd</sup> order harmonic. As mentioned in [ZHU13], the static rotor eccentricity results in the  $(2p)$ th order harmonics of torque, but the dynamic rotor eccentricity results in the triplen order harmonics, which are closest to the pole number. It is worth noting that the magnitude of the 3<sup>rd</sup> order harmonic due to dynamic rotor eccentricity is larger than that of the 2<sup>nd</sup> order harmonic caused by static rotor eccentricity.



(a) Waveforms



(b) Spectra



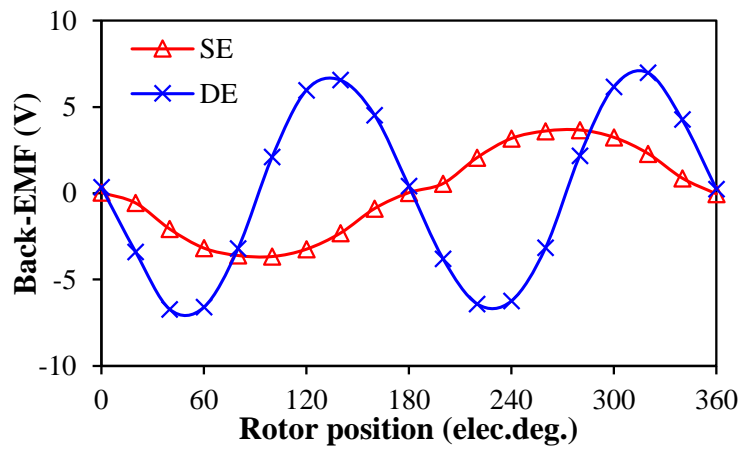
(c) Three phase 120° electric square wave current waveforms

Fig. 4. 20. Electromagnetic torque of 3s/2p HSPM motors with/without eccentricities under three phase 120° electric square wave current waveforms,  $\epsilon=0.5$ ,  $\alpha=\beta=0^\circ$ ,  $I_{max}=10A$ .

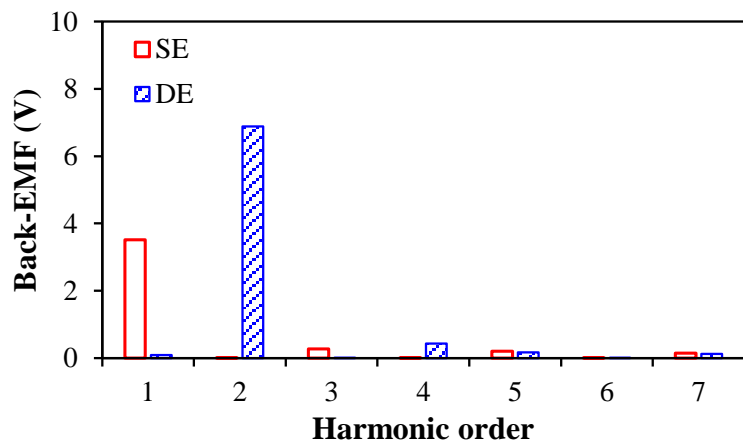
The peak value of additional back-EMF of phase A due to dynamic rotor eccentricity is larger than that due to static rotor eccentricity, Fig. 4. 21, since the smallest air-gap is rotating relative to the stator for dynamic rotor eccentricity. According to the torque calculation formula (4.4), the magnitude of the 2<sup>nd</sup> order harmonic of torque due to static rotor eccentricity is less than that of the 3<sup>rd</sup> order harmonic of torque due to dynamic rotor eccentricity, as shown in Fig. 4. 22. The spectra show the sources of the 2<sup>nd</sup> and 3<sup>rd</sup> order harmonics of torque.

With the increase of the eccentricity ratio, the average torques of the motors with static and dynamic rotor eccentricities remain almost the same, but the torque ripples increase linearly, Fig. 4. 23 (a). The dynamic rotor eccentricity has a larger torque ripple than the static rotor eccentricity due to the larger peak values of additional back-EMF. With the increase of the eccentricity angle, the static and dynamic rotor eccentricities also have negligible influence on

the average torque, but change the torque ripple periodically, Fig. 4. 23 (b).

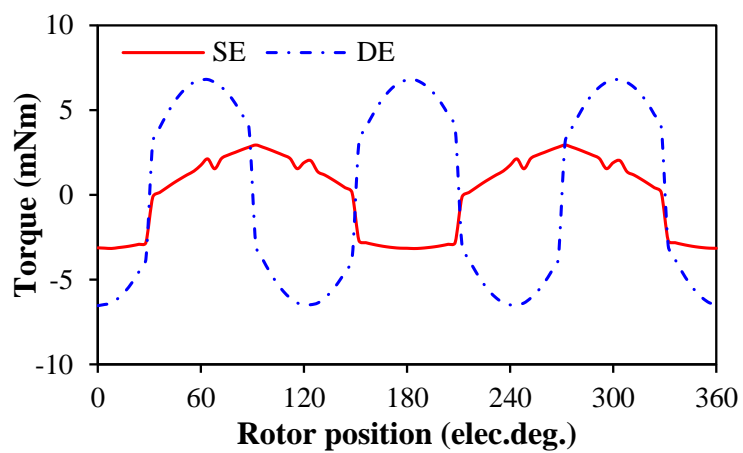


(a) Waveforms

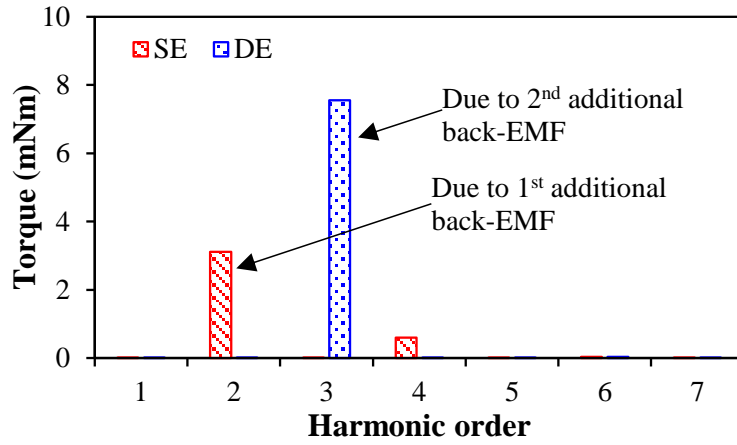


(b) Spectra

Fig. 4. 21. Additional back-EMFs of phase A due to static/dynamic rotor eccentricities.

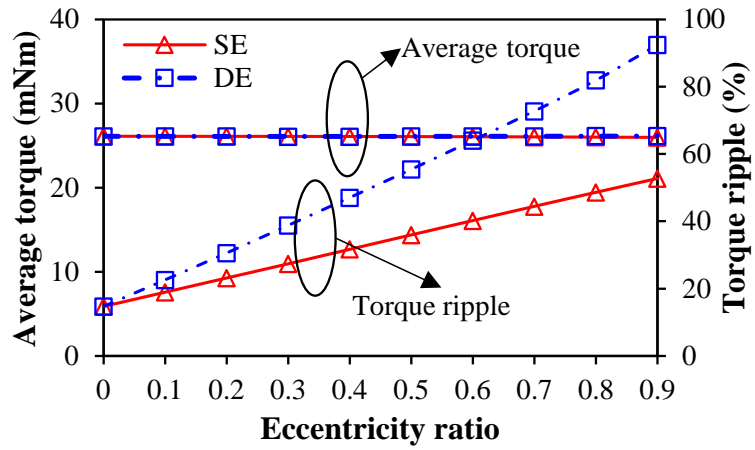


(a) Waveforms

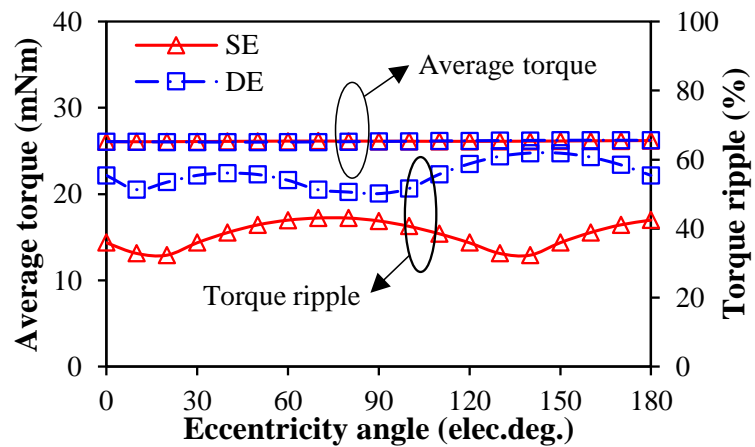


(b) Spectra

Fig. 4. 22. Additional torque due to static/dynamic rotor eccentricities.



(a) Eccentricity ratio,  $\alpha=0^\circ$



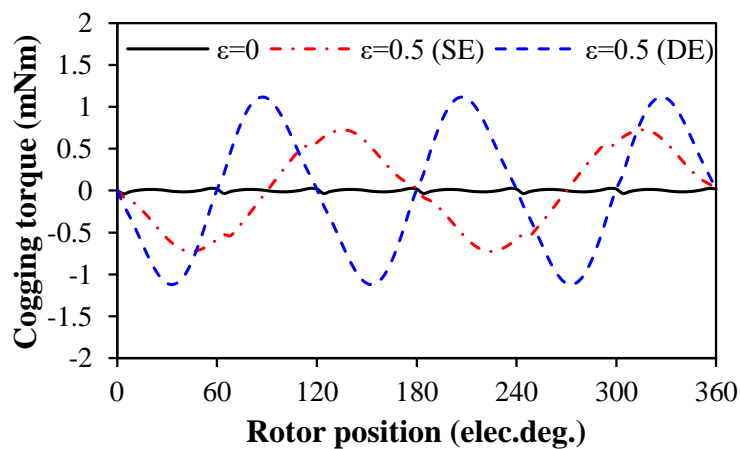
(b) Eccentricity angle,  $\epsilon=0.5$

Fig. 4. 23. Variation of average torque and torque ripple with eccentricity ratio and eccentricity angle.

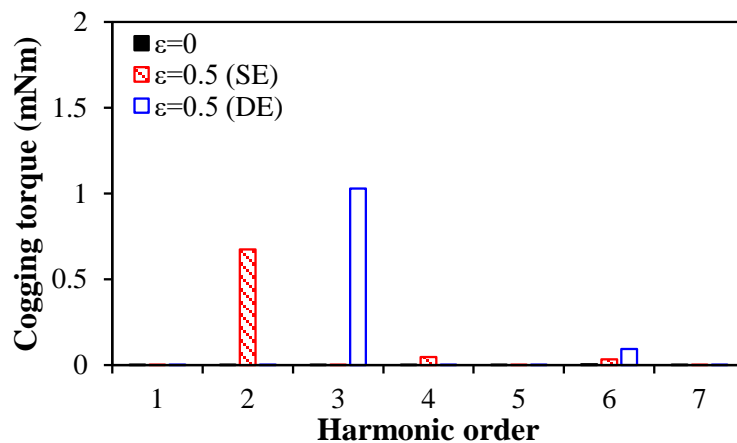


#### 4.3.4 Cogging Torque

As mentioned in Chapter 3, the cogging torque of the 3s/2p PM motor without eccentricity is inherently very small and negligible, while it can be affected by static and dynamic rotor eccentricities [ZHU14]. The static rotor eccentricity leads to the multiples of  $(2p)$ th order harmonics of cogging torque, i.e. 2<sup>nd</sup>, 4<sup>th</sup>, 6<sup>th</sup>,..., and the dynamic rotor eccentricity leads to multiples of  $(N_s)$ th order harmonics of cogging torque, i.e. 3<sup>rd</sup>, 6<sup>th</sup>,..., Fig. 4. 24. It is worth noting that the motor with static rotor eccentricity has less peak cogging torque than the motor with dynamic rotor eccentricity, which will be explained in the next section.



(a) Waveforms



(b) Spectra

Fig. 4. 24. Cogging torques of 3s/2p motors with and without rotor eccentricity,

$$r = R_m + 0.25 \text{ mm (SE)}, r = R_{si} - 0.25 \text{ mm (DE)}, \varepsilon=0.5.$$

To analyze how the rotor eccentricity affects the cogging torque by distorting the air-gap flux density and explain the difference between static and dynamic rotor eccentricities, a hybrid FE

and analytical method [ZHU14] is adopted to show the contribution of each field harmonic to the cogging torque ( $T_c$ ).

$$T_c = \left( l_a r^2 / \mu_0 \right) \int_0^{2\pi} B_{ra} B_{ia} d\alpha_a = \sum_k T_{ck} \quad (4.5)$$

$$T_{ck} = \left( 1 / \mu_0 \right) \pi l_a r^2 B_{rk} B_{tk} \cos(\alpha_{rk} - \alpha_{tk}) \quad (4.6)$$

where  $B_{ra}$  and  $B_{ia}$  are calculated by FE method,  $B_{rk}$  and  $B_{tk}$  are obtained by Fourier analysis. With static and dynamic rotor eccentricities, the predictions by the hybrid method have a good agreement with the direct FE results, Fig. 4. 25. It shows that the maximum cogging torques occur at  $\theta=45^\circ$  and  $30^\circ$  for the static and dynamic rotor eccentricities, respectively. The contribution of air-gap flux density harmonics to cogging torques of the motors with static and dynamic rotor eccentricities are different, Fig. 4. 26. With static rotor eccentricity, only fundamental component contributes to the cogging torque. With dynamic rotor eccentricity, the fundamental, 2<sup>nd</sup>, and 4<sup>th</sup> order harmonics contribute to the cogging torque.

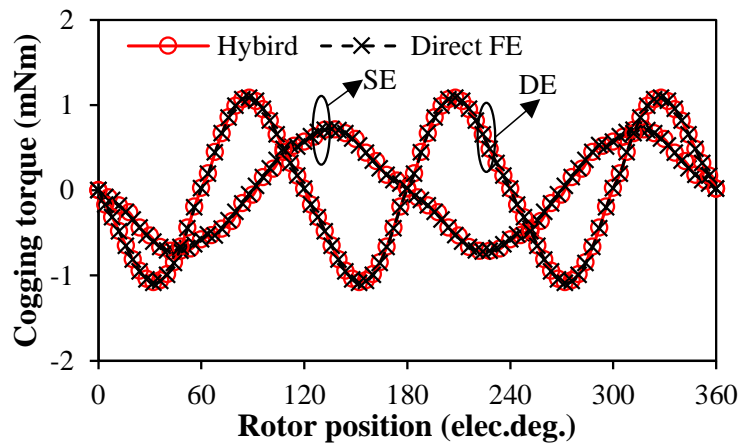


Fig. 4. 25. Cogging torques of motors with static/dynamic rotor eccentricities by direct FE and hybrid FE and analytical method,  $r = R_m + 0.25$  mm (SE),  $r = R_{si} - 0.25$  mm (DE),  $\varepsilon=0.5$ .

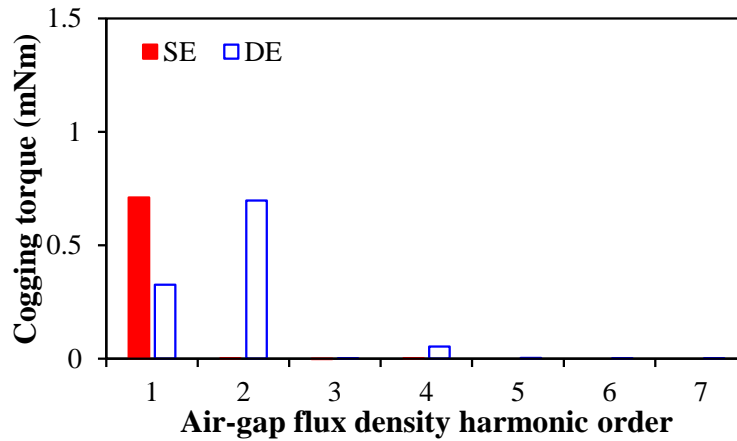
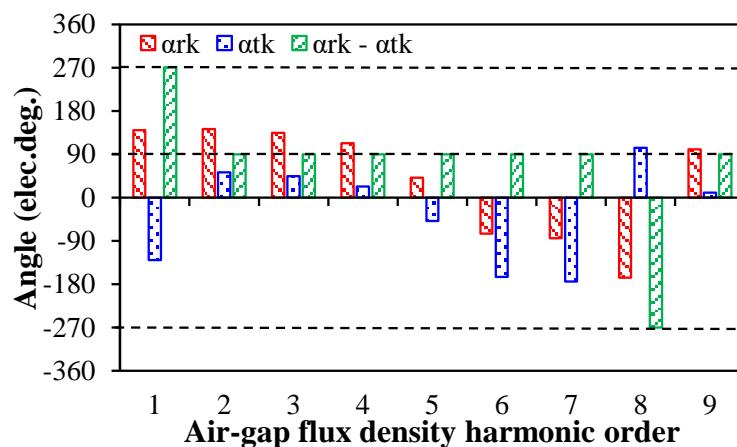
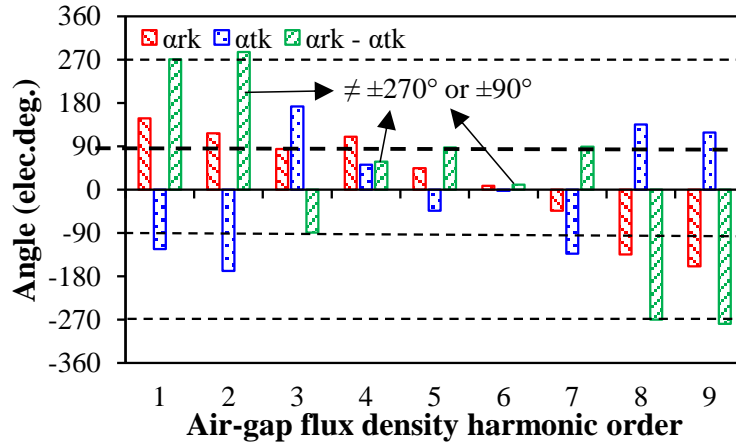


Fig. 4. 26. Contribution of air-gap flux density harmonics to cogging torques of motors with static/dynamic rotor eccentricities,  $\varepsilon=0.5$ .

With static rotor eccentricity, the values of  $(\alpha_{rk} - \alpha_{tk})$  are almost equal to  $\pm 90^\circ$  or  $\pm 270^\circ$ , which means their cosine values are almost equal to zero, Figs. 4. 27 (a) and 4. 28 (a). With dynamic rotor eccentricity, the values of  $(\alpha_{rk} - \alpha_{tk})$  for the 2<sup>nd</sup>, 4<sup>th</sup>, and 6<sup>th</sup> order harmonics do not equal to  $\pm 90^\circ$  or  $\pm 270^\circ$ , Fig. 4. 27 (b), which results in a large cosine of the angle difference, Fig. 4. 28 (a). According to the cogging torque calculation formula (4.6), although the product of fundamental magnitudes of radial and tangential air-gap flux densities in the motor with static rotor eccentricity is large, Fig. 4. 28 (b), the contribution to cogging torque is small due to small cosine of angle difference. It also explains why the dynamic rotor eccentricity results in larger peak cogging torque since more air-gap flux density harmonics have contributed to the cogging torque.

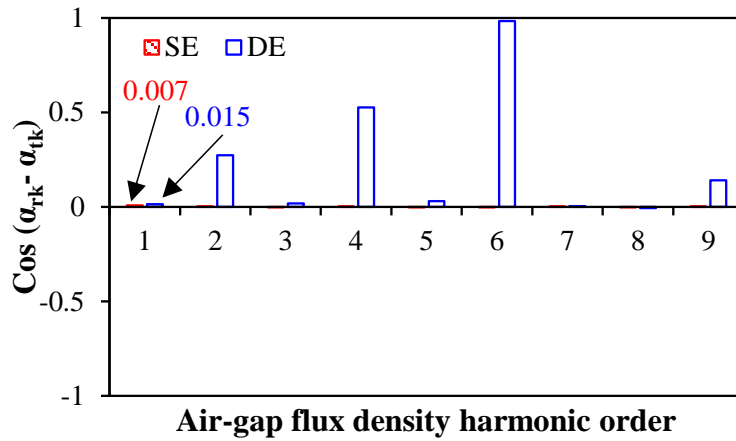


(a) Static rotor eccentricity,  $\theta=45^\circ$

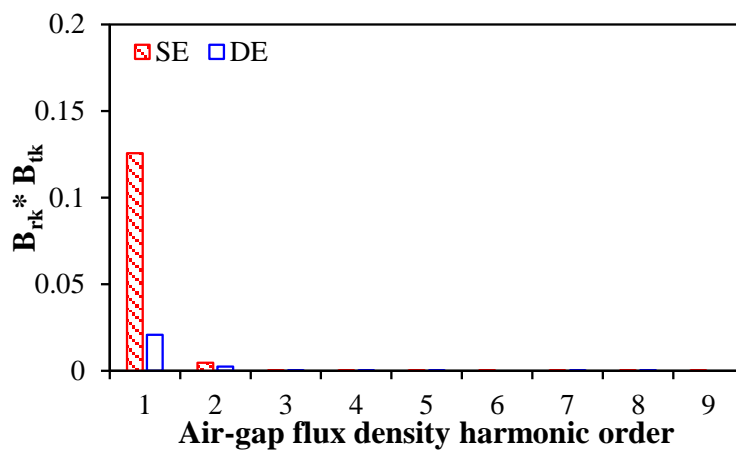


(b) Dynamic rotor eccentricity,  $\theta=30^\circ$

Fig. 4. 27. Angle differences between  $\alpha_{rk}$  and  $\alpha_{tk}$ .



(a) Cosine of angle difference

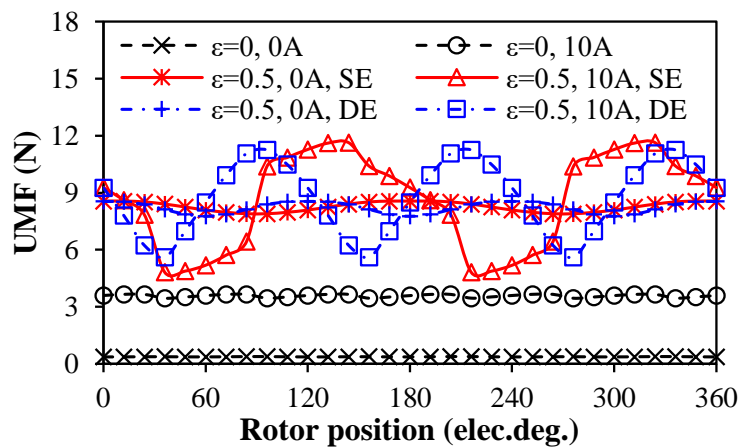


(b) Product of magnitudes

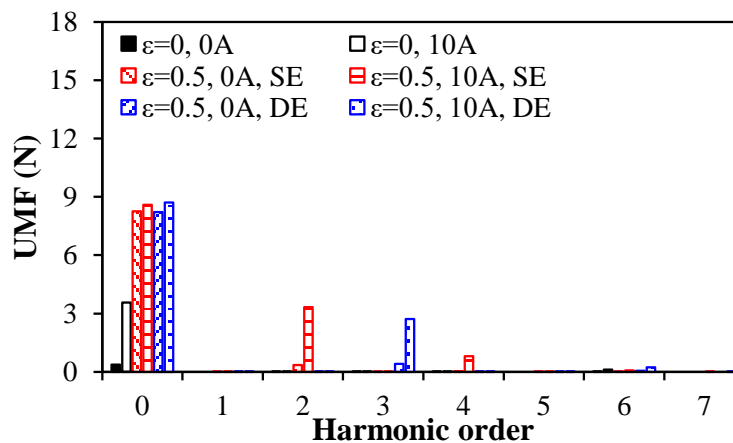
Fig. 4. 28. Relationship between cogging torque and harmonic components.

### 4.3.5 Unbalanced Magnetic Force

The 3s/2p PM motor with rotor eccentricity has larger average open-circuit and on-load UMFs than the motor without rotor eccentricity, Fig. 4. 29. Static and dynamic rotor eccentricities have almost the same average open-circuit and on-load UMFs, but different harmonic contents. The spectra show that the static rotor eccentricity results in multiples of  $(2p)$ th order UMF harmonics, i.e. the 2<sup>nd</sup>, 4<sup>th</sup>,..., and the dynamic rotor eccentricity results in multiples of  $(N_s)$ th order UMF harmonics, i.e. the 3<sup>rd</sup>, 6<sup>th</sup>,...



(a) Waveforms



(b) Spectra

Fig. 4. 29. UMFs of 3s/2p HSPM motors without/with static/dynamic rotor eccentricities, rated current=10A.

With the increase of phase current, the average UMF of the motor without eccentricity increases significantly, but the influence of static and dynamic rotor eccentricities on the average on-load UMF decreases. When the phase current is 50A, the motors with and without

rotor eccentricity have almost the same average UMF, Fig. 4. 30. With the increase of eccentricity ratio, the average open-circuit and on-load UMFs increase significantly, Fig. 4. 31. However, when the eccentricity ratio is 0.9, all the average UMFs with different phase currents are almost the same. Therefore, with the small eccentricity ratio and large phase current, the rotor eccentricity has negligible influence on average UMF and the phase current dominates the resultant UMF. However, with the large eccentricity ratio and small phase current, the rotor eccentricity dominates the resultant UMF and the phase current has negligible influence.

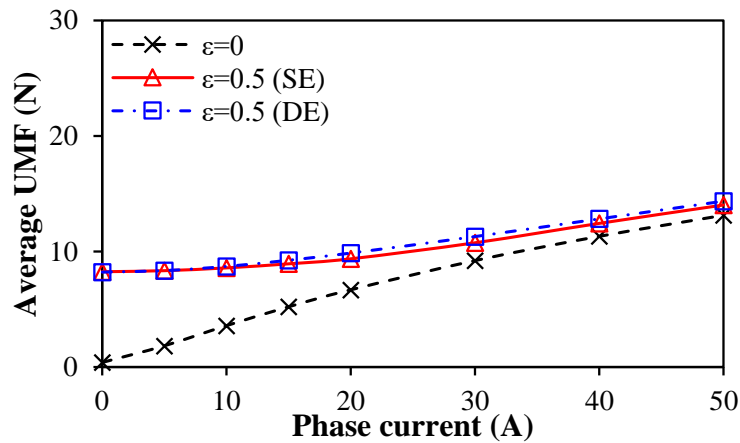


Fig. 4. 30. Average UMFs of the motors with/without static/dynamic rotor eccentricities under different phase currents,  $\epsilon=0.5$ .

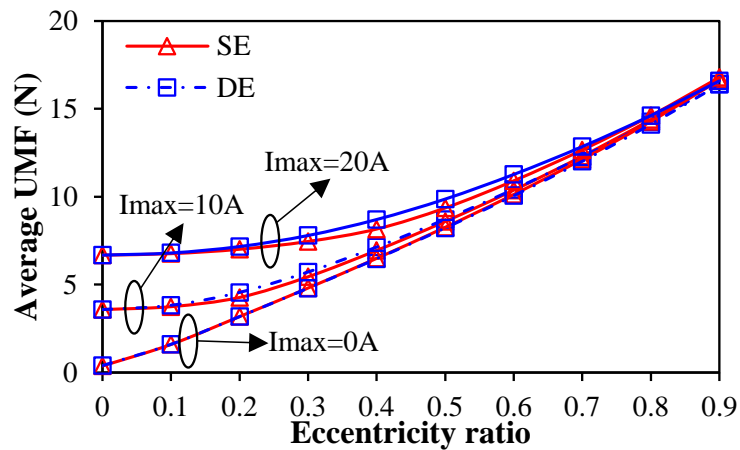


Fig. 4. 31. Variation of average UMFs with eccentricity ratio under different phase currents.

#### 4.4. 2-Pole Symmetrical Motor with Rotor Eccentricity

The 6s/2p PM motors with 1, 2, and 3 slot-pitch windings and rotor eccentricity are analyzed, and the series-connected windings is employed in this section.

#### 4.4.1 Open-circuit Air-gap Field

Since the coil-pitch does not change the open-circuit air-gap field, only 1 slot-pitch winding configuration is analyzed. Figs. 4. 32 and 4. 33 show the equipotential, flux contour, and air-gap field distributions of 6s/2p PM motors with/without static/dynamic rotor eccentricities when the eccentricity ratio is 0.5 and the rotor position is  $90^\circ$ . It can be seen that both static and dynamic rotor eccentricities mainly lead to the 2<sup>nd</sup> order harmonics, and the spatial harmonic contents of air-gap flux densities with and without eccentricity are shown in Table 4. 3.

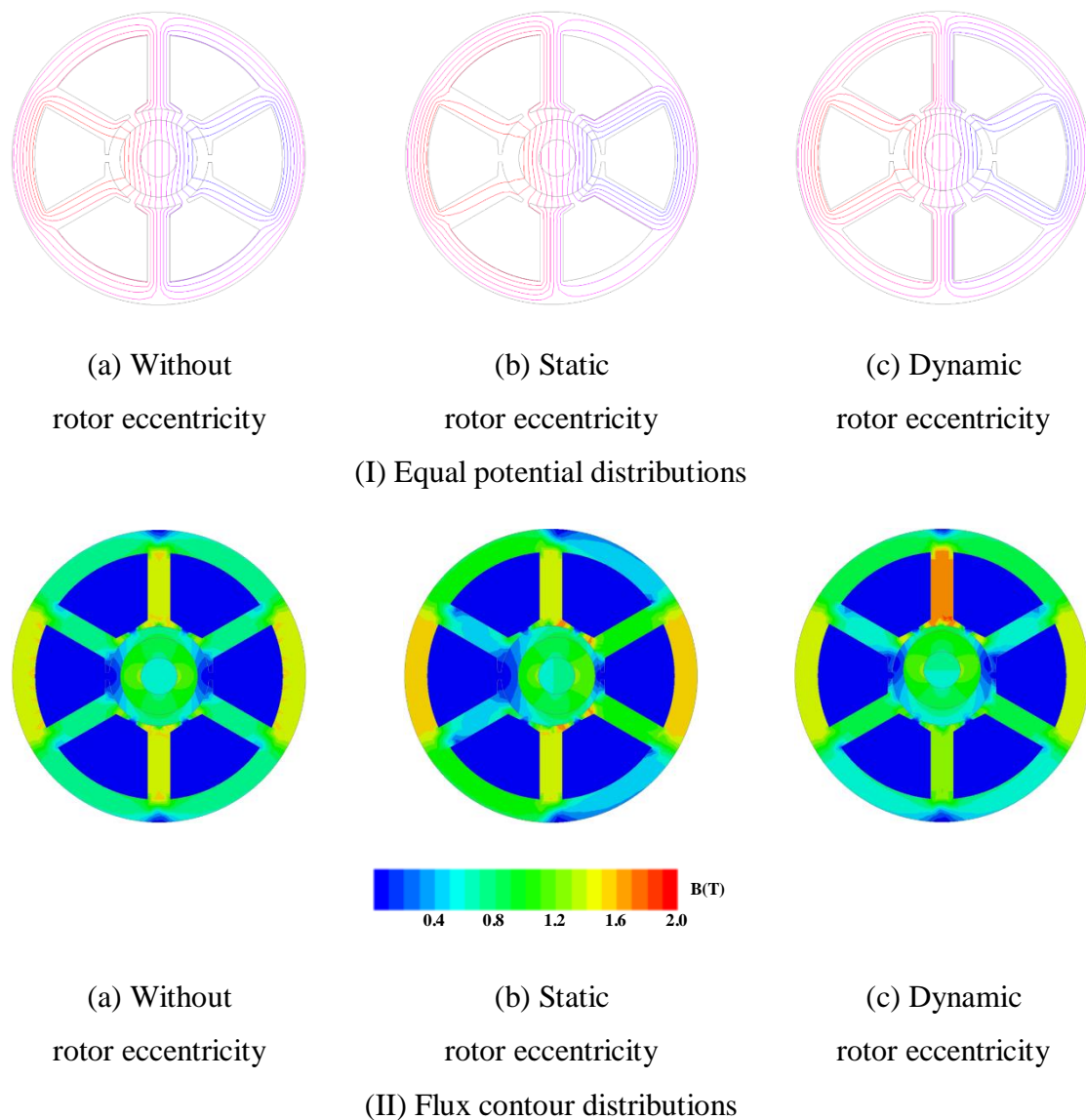
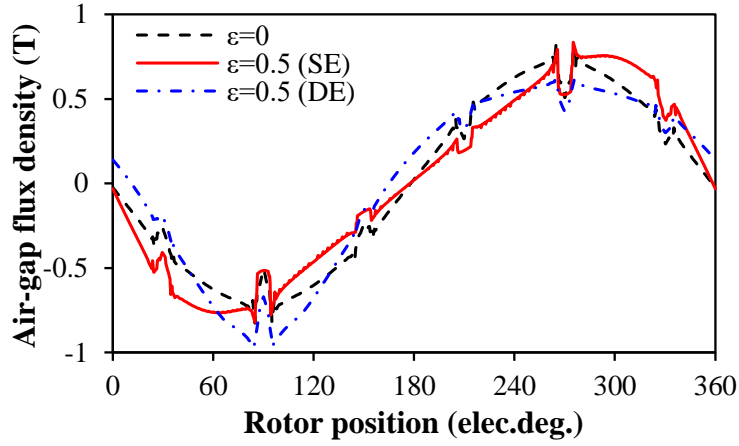
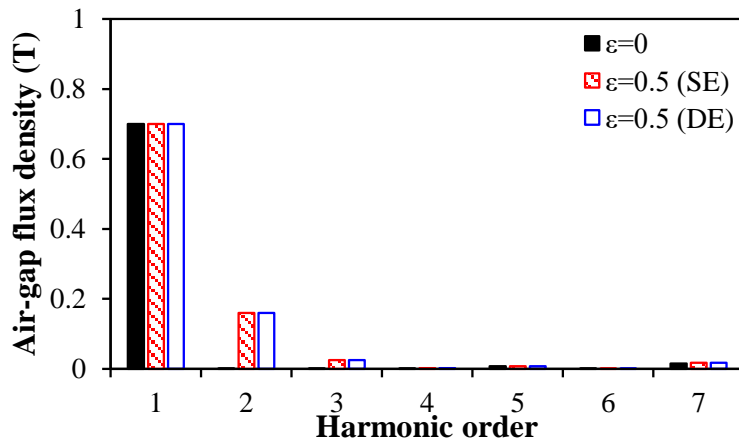


Fig. 4. 32. Equipotential and flux contour distributions of the 6s/2p PM motors without/with rotor eccentricity,  $\theta= 90^\circ$ ,  $\varepsilon=0.5$ .



(a) Waveforms



(b) Spectra

Fig. 4. 33. Air-gap field distributions of the 6s/2p PM motors with/without static/dynamic rotor eccentricities,  $r = R_{si} - 0.25$  mm,  $\theta = 90^\circ$ ,  $\varepsilon = 0.5$ .

Table 4.3

Spatial Harmonic Contents of Air-gap Field

Original PM harmonics	Modulated PM harmonics due to slotting	Additional air-gap field due to rotor eccentricity	
$n = mp$	$n = mp \pm \mu N_s$	$n \pm \nu$ ( $\nu = 1$ )	
1, 3, 5, ...	1, 3, 5, 7, 9, ...	$n+1$	$n-1$
		2, 4, 6, ...	2, 4, 6, ...

#### 4.4.2 Back-EMF

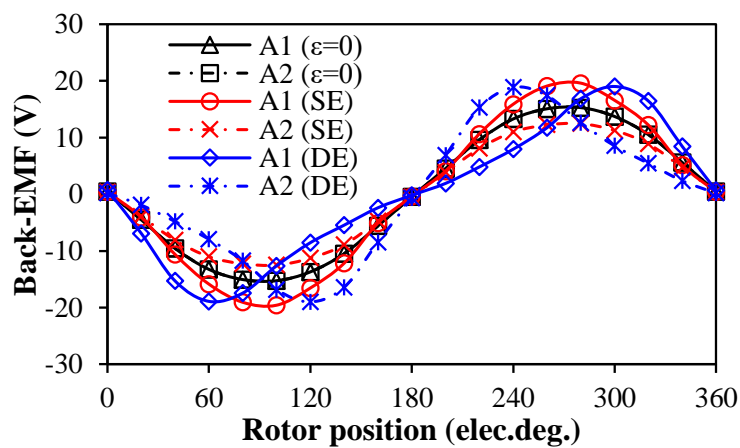
##### A. 6s/2p PM motor with 1 slot-pitch windings

With static rotor eccentricity  $\varepsilon = 0.5$ , the magnitude of fundamental back-EMF of coil 'A1'

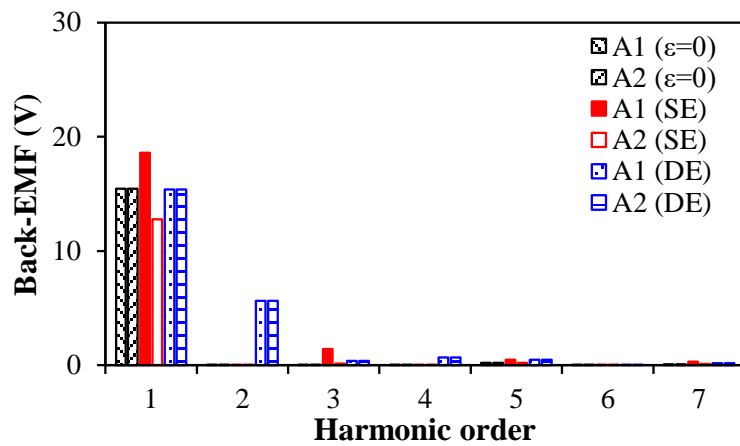


increases but that of coil ‘A2’ decreases, Fig. 4. 34 (b), since the coil ‘A1’ faces the smallest air-gap but the coil ‘A2’ faces the largest air-gap. However, the magnitude of fundamental back-EMF of phase A remains unchanged, Fig. 4. 34 (c), since the decrease of the magnitude of fundamental back-EMF in coil ‘A2’ is compensated completely by the increase in coil ‘A1’ due to the symmetrical distribution and opposite connection polarity of coils ‘A1’ and ‘A2’.

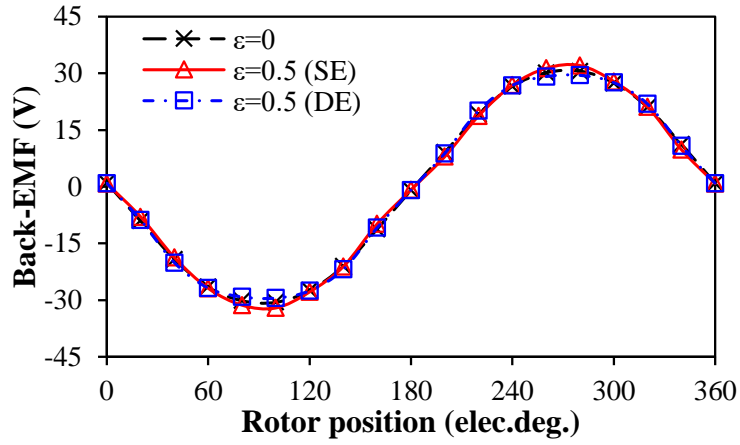
The dynamic rotor eccentricity does not change the magnitudes of fundamental back-EMFs in coils A1 and A2, but leads to the 2<sup>nd</sup> order back-EMF harmonics, Fig. 4. 34 (b). However, the 2<sup>nd</sup> order back-EMF harmonic disappears in the phase back-EMF, Fig. 4. 34 (d), due to the opposite phase angles of coils ‘A1’ and ‘A2’, Fig. 4. 35 (b), and the same magnitude.



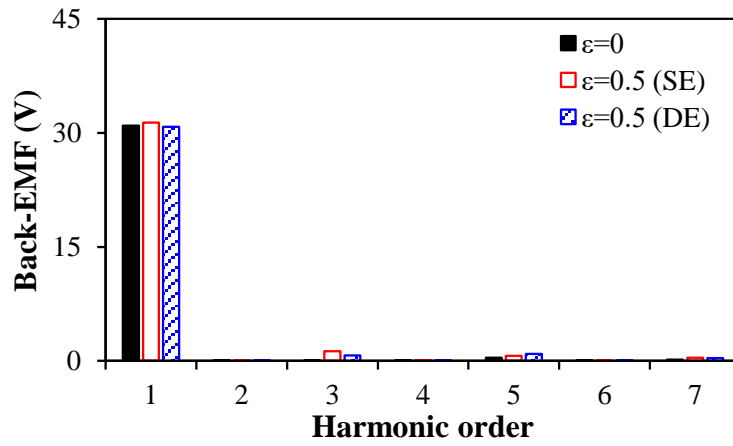
(a) Coils ‘A1’ and ‘A2’, waveforms



(b) Coils ‘A1’ and ‘A2’, Spectra

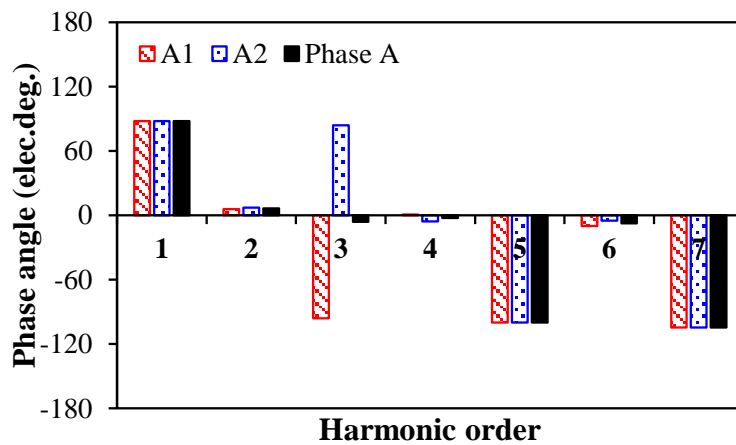


(c) Phase A, waveforms

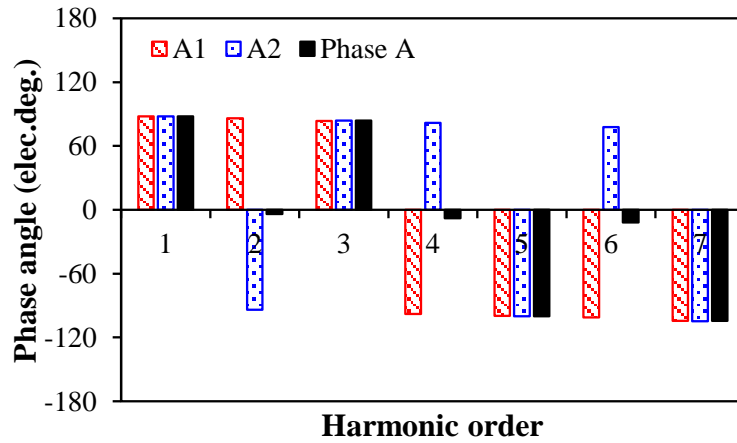


(d) Phase A, Spectra

Fig. 4. 34. Influence of rotor eccentricity on the back-EMFs of coil and phase.



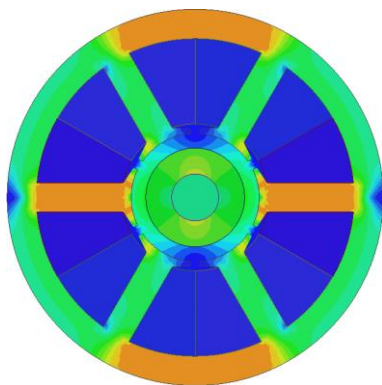
(a) Static rotor eccentricity



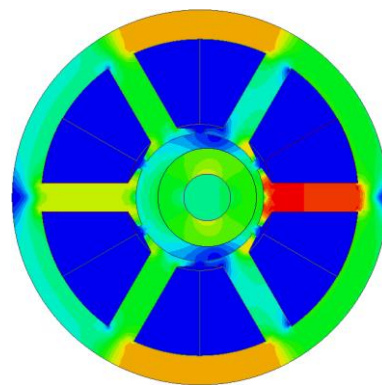
(b) Dynamic rotor eccentricity

Fig. 4. 35. Phase angles of the fundamental and harmonics of back-EMFs in coils and phase with static/dynamic rotor eccentricities.

It is worth noting that the static and dynamic rotor eccentricities also lead to the 3<sup>rd</sup> order harmonics in the back-EMFs of coil ‘A1’, coil ‘A2’, and phase A, which is caused by the saturation effect. Fig. 4. 36 shows that with static rotor eccentricity  $\varepsilon=0.5$ , the maximum stator iron flux density is 1.8T, which leads to the local saturation in the stator tooth facing the smallest air-gap. With static rotor eccentricity, although the 3<sup>rd</sup> order back-EMF harmonics in coils ‘A1’ and ‘A2’ have opposite phase angles, Fig. 4. 35 (a), their different magnitudes result in the existence of 3<sup>rd</sup> order harmonic. With dynamic rotor eccentricity, the 3<sup>rd</sup> order back-EMF harmonics in coils ‘A1’ and ‘A2’ have the same magnitude and phase angle, and hence, it exists in the back-EMF of phase A. When employing linear material for the stator, the 3<sup>rd</sup> order back-EMF harmonic due to saturation effect in the coils ‘A1’ and ‘A2’ are removed, but that due to dynamic rotor eccentricity still exists, Fig. 4. 37, which results from the 2<sup>nd</sup> and 4<sup>th</sup> order spatial harmonics of air-gap field.



(a) Without eccentricity



(b) With eccentricity

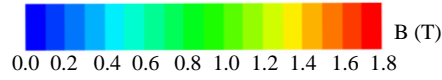
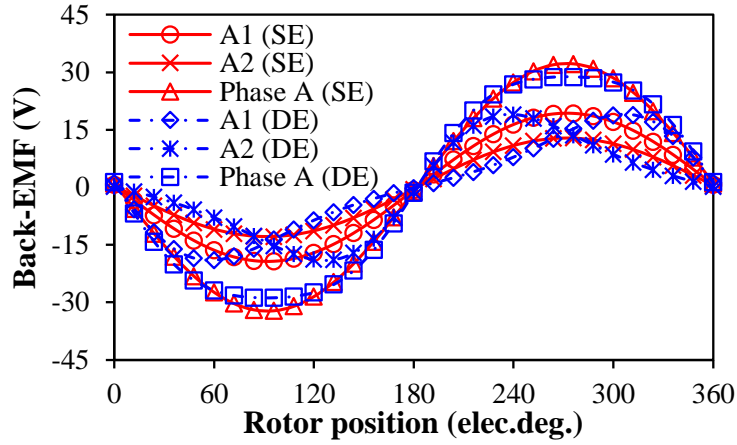
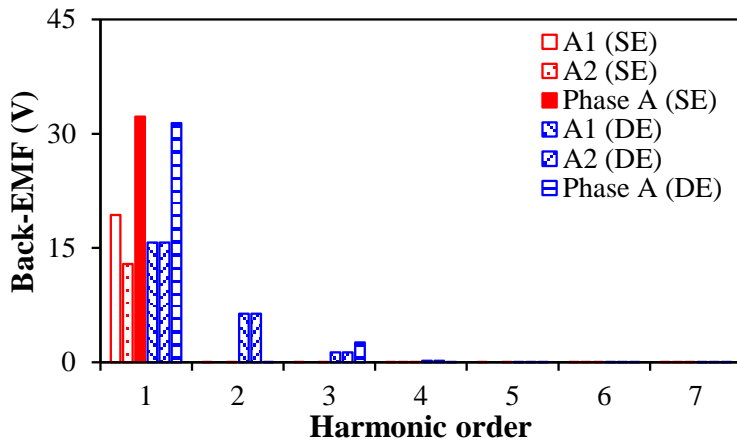


Fig. 4. 36. Flux contour distribution of 6s/2p motors without and with rotor eccentricity,

$$\theta = 0^\circ, \varepsilon = 0.5.$$



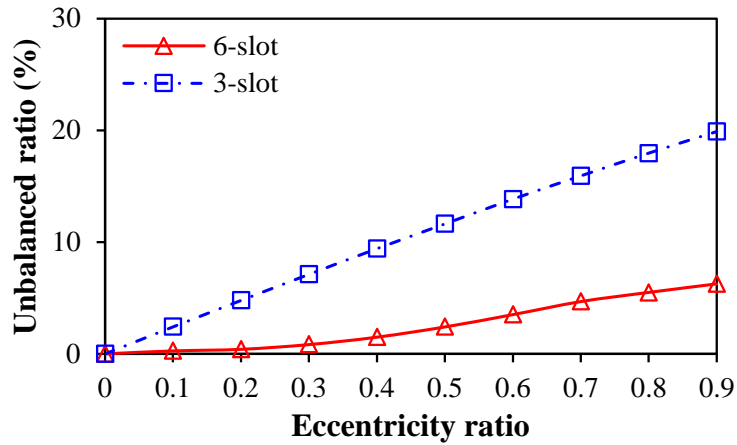
(a) Waveforms



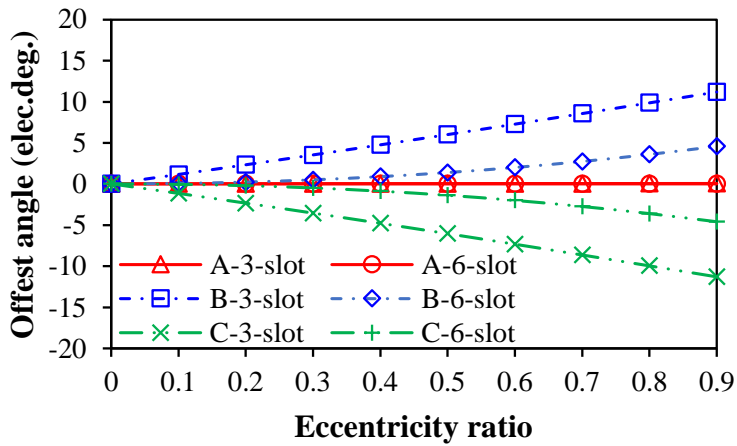
(b) Spectra

Fig. 4. 37. Back-EMFs of coil ‘A1’, coil ‘A2’, and phase A in the motor with rotor eccentricity, linear material of stator lamination.

With the increase of static eccentricity ratio, although the unbalanced ratio of back-EMFs of three phases in the 6s/2p motor with 1 slot-pitch windings increases due to saturation effect, it is significantly smaller compared with the 3s/2p motor, Fig. 4. 38 (a). Meanwhile, the offset phase angles of back-EMF of phases B and C in the 6s/2p motor are smaller than those in the 3s/2p motor, Fig. 4. 38 (b). Therefore, the static rotor eccentricity has a relatively small influence, and hence, the effect of static rotor eccentricity angle and rotor initial angle will not be discussed.



(a) Unbalanced ratio



(b) Offset phase angle

Fig. 4. 38. Variation of unbalanced ratios and offset phase angles with static rotor eccentricity ratio in 3s/2p and 6s/2p motors.

With the increase of dynamic eccentricity ratio, the magnitude of fundamental back-EMF remains unchanged but that of the 3<sup>rd</sup> order harmonic increases, which results in the decrease of the positive and negative peak values, Figs. 4. 39 and 4. 40. Compared with the 3s/2p motor, the influence of dynamic eccentricity ratio on the peak back-EMF is small. With the increase of dynamic eccentricity angle, the peak-to-peak back-EMF of phase A increases at first and then decrease due to the changing magnitude of the 3<sup>rd</sup> order harmonic, Figs. 4. 41 and 4. 42. Therefore, in the 6s/2p PM motor with 1 slot-pitch windings, the dynamic rotor eccentricity with various eccentricity angles has a relatively large influence on the phase back-EMF.

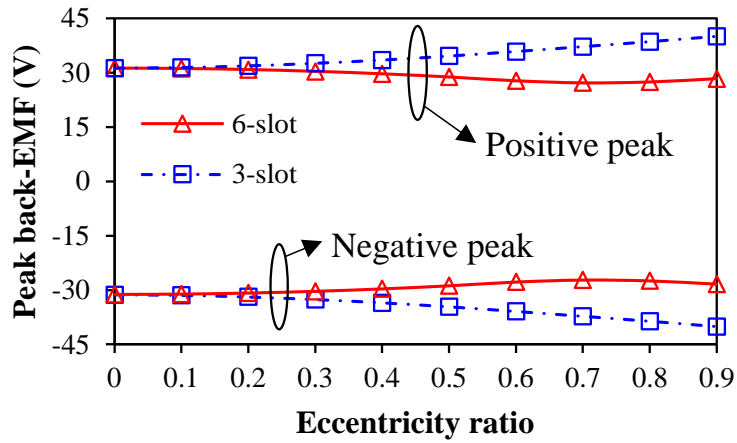


Fig. 4. 39. Influence of dynamic eccentricity ratio on positive and negative peak values of back-EMF of phase A in 3s/2p and 6s/2p motors.

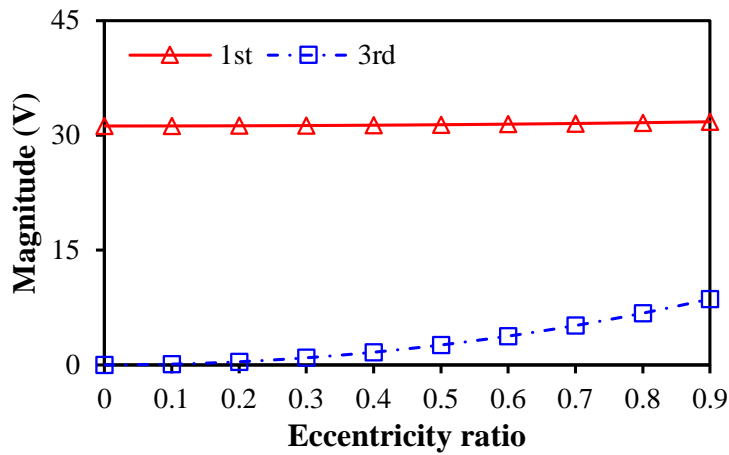


Fig. 4. 40. Influence of dynamic eccentricity ratio on magnitudes of fundamental and 3<sup>rd</sup> order harmonic of back-EMF of phase A in the 6s/2p motor.

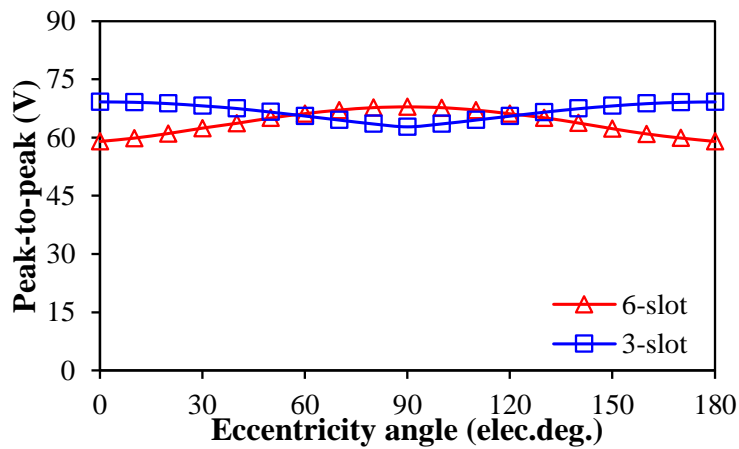


Fig. 4. 41. Influence of dynamic eccentricity angle on peak-to-peak back-EMF of phase A in 3s/2p and 6s/2p motors,  $\epsilon=0.5$ .

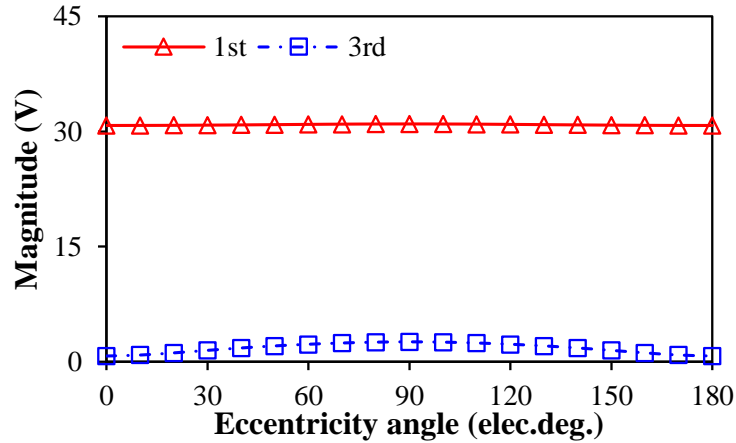
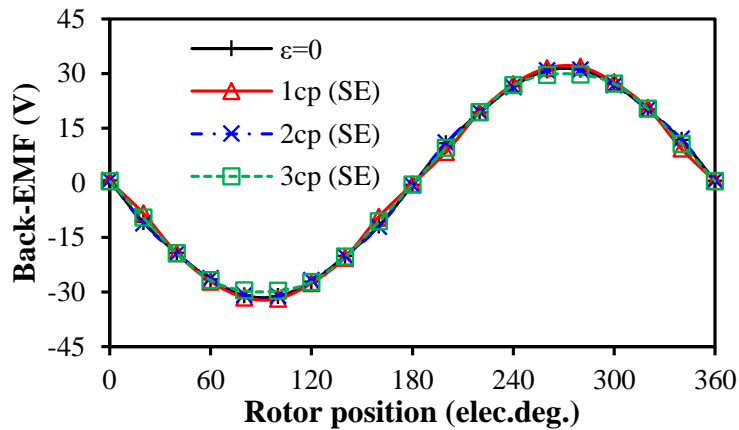


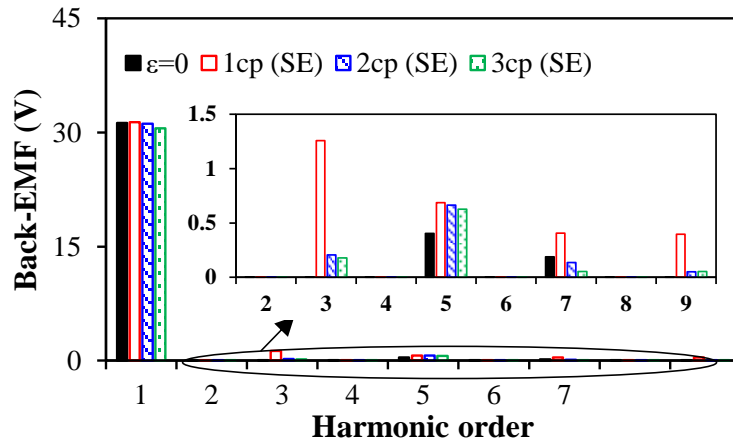
Fig. 4. 42. Influence of dynamic eccentricity angle on magnitudes of fundamental and 3<sup>rd</sup> order harmonic of back-EMF of phase A in the 6s/2p motor,  $\epsilon=0.5$ .

#### B. Influence of slot-pitch on the back-EMF with rotor eccentricity

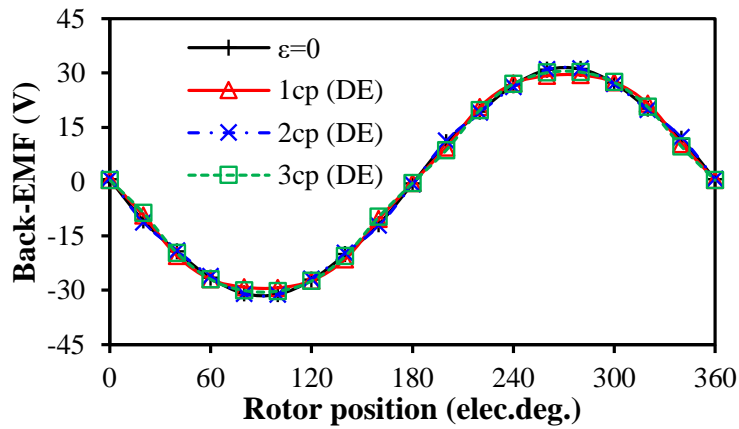
In the 6s/2p PM motor with 1 slot-pitch windings, neglecting saturation effect, both the unbalanced magnitudes of fundamental back-EMFs in coils of the same phase caused by static rotor eccentricity and the additional 2<sup>nd</sup> order harmonic of phase back-EMF caused by dynamic rotor eccentricity are eliminated due to rotational symmetrical windings. The 6s/2p PM motors with 2 and 3 slot-pitch rotational symmetrical windings have the same conclusion. Considering saturation effect, for rotor static eccentricity, the magnitudes of the 3<sup>rd</sup> and 9<sup>th</sup> order phase back-EMF harmonics in the motors with 2 and 3 slot-pitch windings are significantly smaller than that in the motor with 1 slot-pitch windings, Fig. 4. 43. For dynamic rotor eccentricity, there is no 3<sup>rd</sup> and 9<sup>th</sup> order phase back-EMF harmonics in the motor with 2 slot-pitch windings although they will disappear in the line back-EMF waveform and do not contribute to the torque. In addition, in static/dynamic rotor eccentricities, the magnitudes of the 5<sup>th</sup> and 7<sup>th</sup> order phase back-EMF harmonics decrease with the increase of slot-pitch.



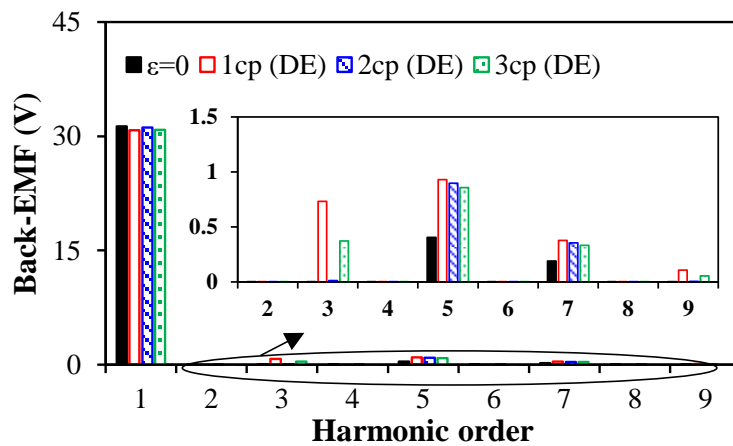
(a) Waveforms (SE)



(b) Spectra (SE)



(c) Waveforms (DE)

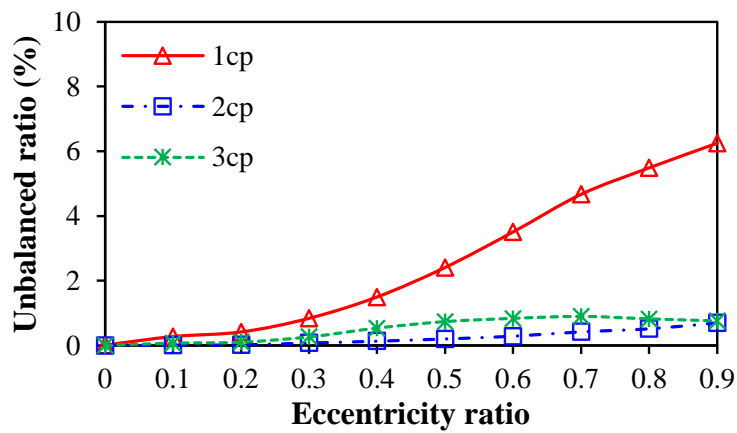


(d) Spectra (DE)

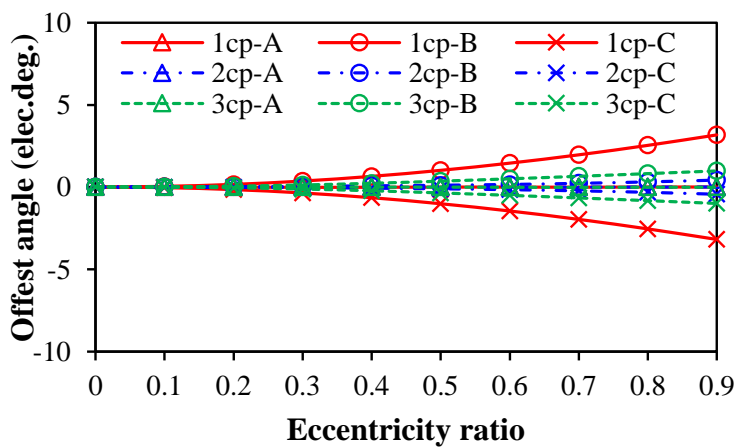
Fig. 4. 43. Influence of winding configuration on the back-EMFs of phase A in the 6s/2p PM motors with rotor static/dynamic eccentricities,  $\epsilon=0.5$ .



With the increase of static eccentricity (SE) ratio, although the unbalanced ratio and offset phase angles of back-EMFs of three phase in the 6s/2p motor with 1 slot-pitch windings is significantly smaller than those in the 3s/2p motor, they remain almost zero in the 6s/2p motors with 2 and 3 slot-pitch windings, Fig. 4. 44 (a), since the magnitude of the 3<sup>rd</sup> order back-EMF harmonic is almost zero, Fig. 4. 45. It is worth noting that the offset phase angles of phases B and C increase with static eccentricity ratio in the motor with 1 slot-pitch windings, but those remain almost unchanged in the motors with 2 and 3 slot-pitch windings, Fig. 4. 44 (b). Therefore, the influence of saturation effect due to static rotor eccentricity on three phase back-EMFs can be eliminated in the motors with 2 and 3 slot-pitch windings.



(a) Unbalanced ratio



(b) Offset phase angle

Fig. 4. 44. Variation of unbalanced ratios and offset phase angles with static rotor eccentricity ratio in 6s/2p PM motors with 1, 2 and 3 slot-pitch windings.

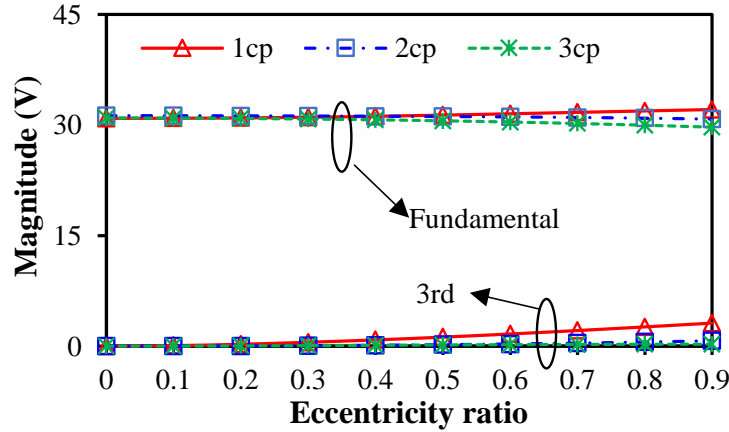


Fig. 4. 45. Influence of static eccentricity ratio on magnitudes of fundamental and 3<sup>rd</sup> order harmonic of back-EMF of phase A in 6s/2p PM motors with 1, 2, and 3 slot-pitch windings.

With the increase of dynamic eccentricity (DE) ratio, the magnitudes of the fundamental back-EMF in the motor with 2 and 3 slot-pitch windings remain unchanged and the magnitude of the 3<sup>rd</sup> order harmonic remains almost zero, which results in the unchanged positive and negative peak values, Figs. 4. 46 and 4. 47. With the increase of dynamic eccentricity (DE) angle,  $\varepsilon=0.5$ , the peak-to-peak value of phase A back-EMF in the motor with 1 slot-pitch windings increases at first and then decreases, which is opposite to the result in the motor with 3 slot-pitch windings, Fig. 4. 48, however, that in 2 slot-pitch windings remains almost unchanged since there is no 3<sup>rd</sup> order back-EMF harmonic, Figs. 4. 43 (d) and 4. 49 (a). Although the fundamental magnitudes remain unchanged and the variation trends of the magnitudes of the 3<sup>rd</sup> order harmonics are the same in the motors with 1 and 3 slot-pitch windings, Fig. 4. 49 (a), the phase angle difference between the 3<sup>rd</sup> order harmonics of 1 and 3 slot-pitch windings is always 180°, Fig. 4. 49 (b). When the dynamic eccentricity angle is 90°, the phase angles of the fundamental and 3<sup>rd</sup> order harmonic are the same in the motor with 3 slot-pitch windings, which leads to a canceling effect, but they differ by 180° in the motor with 1 slot-pitch windings, which results in an additive effect. Therefore, considering dynamic eccentricity angle, the winding configuration has influence on the magnitude and phase angle of the 3<sup>rd</sup> order back-EMF harmonic, which results in different maximum values and the opposite variation trends of peak-to-peak phase back-EMFs.

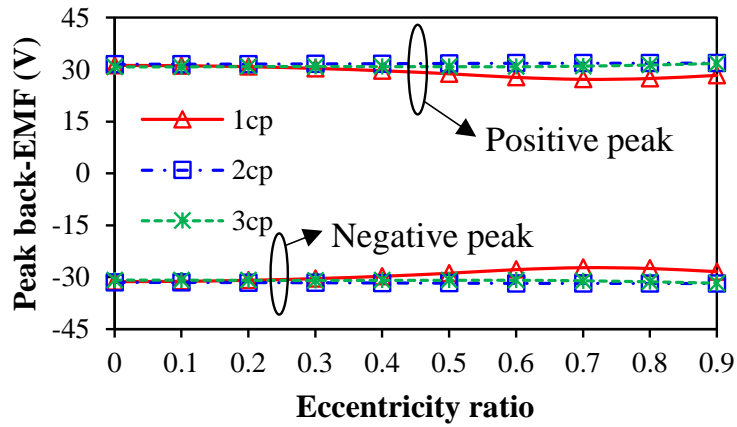


Fig. 4. 46. Influence of dynamic eccentricity ratio on positive and negative peak values of back-EMF of phase A in 6s/2p PM motors with 1, 2 and 3 slot-pitch windings.

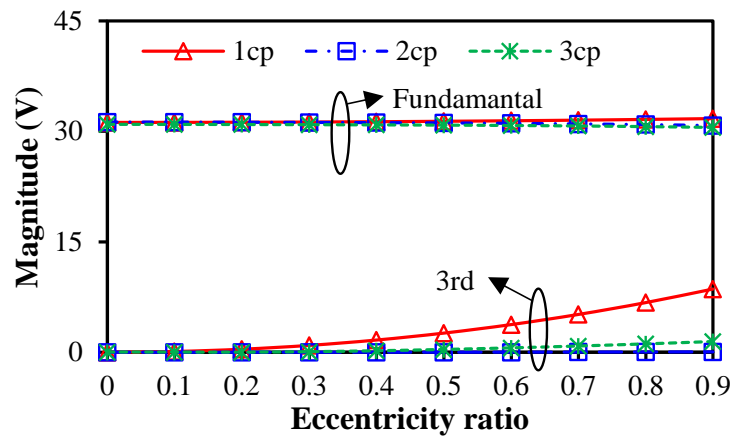


Fig. 4. 47. Influence of dynamic eccentricity ratio on magnitudes of fundamental and 3<sup>rd</sup> harmonic of back-EMF of phase A in the 6s/2p motor with 1, 2, and 3 slot-pitch windings.

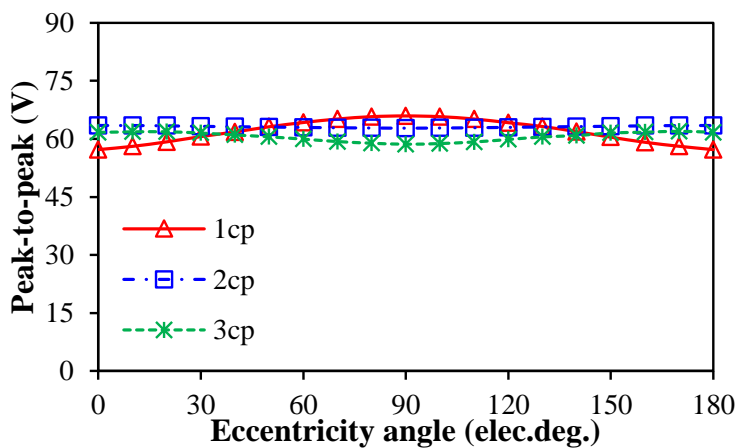
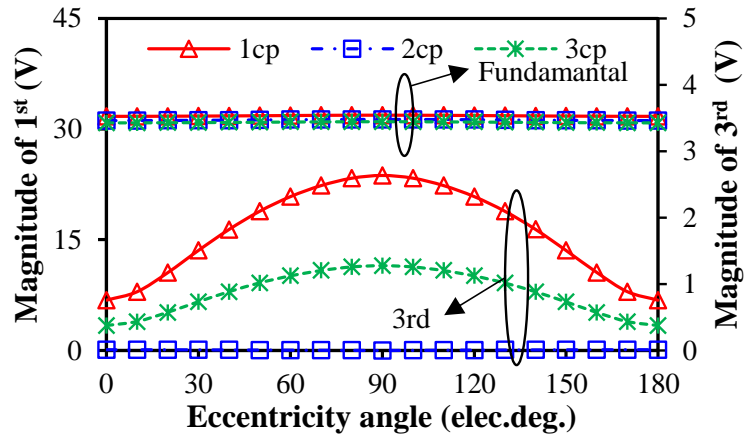
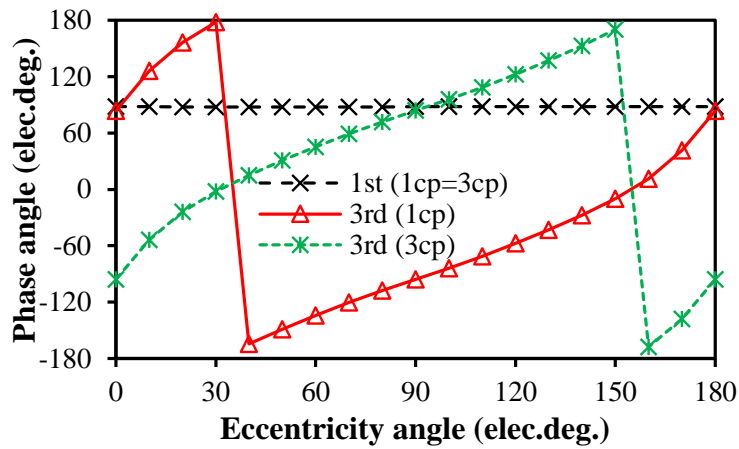


Fig. 4. 48. Influence of dynamic eccentricity angle on peak-to-peak back-EMF of phase A in 6s/2p motors with 1, 2, and 3 slot-pitch windings,  $\epsilon=0.5$ .



(a) Magnitude

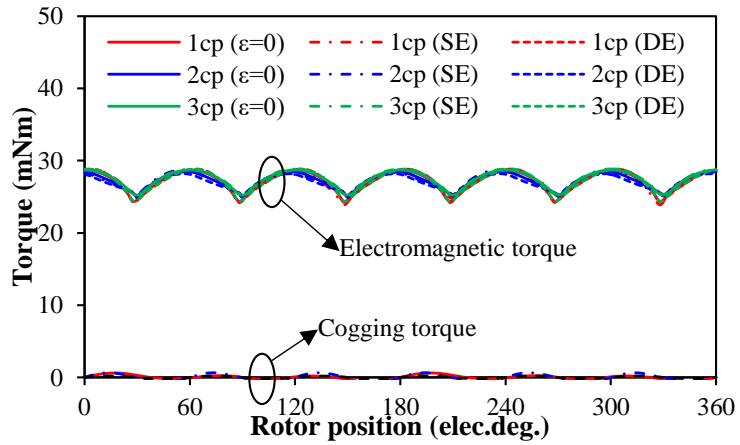


(b) Phase angle (No 3<sup>rd</sup> harmonic in 2 cp)

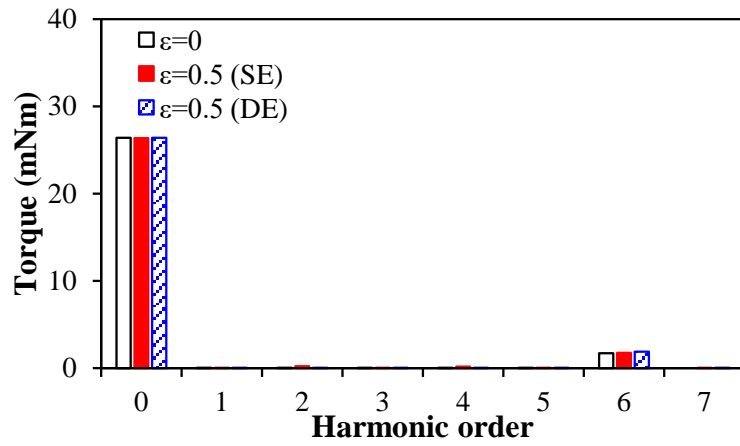
Fig. 4. 49. Influence of dynamic eccentricity angle on magnitudes of fundamental and 3<sup>rd</sup> order harmonic of back-EMF of phase A in the 6s/2p motor with 1, 2, and 3 slot-pitch windings,  $\varepsilon=0.5$ .

#### 4.4.3 Electromagnetic Torque and Cogging Torque

Fig. 4. 50 shows the static and dynamic rotor eccentricities have almost no influence on the electromagnetic torque and cogging torque of 6s/2p PM motors with 1, 2, and 3 slot-pitch windings. The 6<sup>th</sup> order harmonic results from ideal square BLDC current waveforms and sinusoidal back-EMF waveforms. The cogging torque is very small due to parallel magnetization and can be neglected. With the increase of phase current, the influence of saturation effect on the average torque increases, especially for the motor with 1 slot-pitch windings under dynamic rotor eccentricity, Fig. 4. 51.



(a) Waveforms



(b) Spectra of electromagnetic torques, 1 slot-pitch windings

Fig. 4. 50. Electromagnetic torques and cogging torques of 6s/2p motors with/without rotor eccentricity.

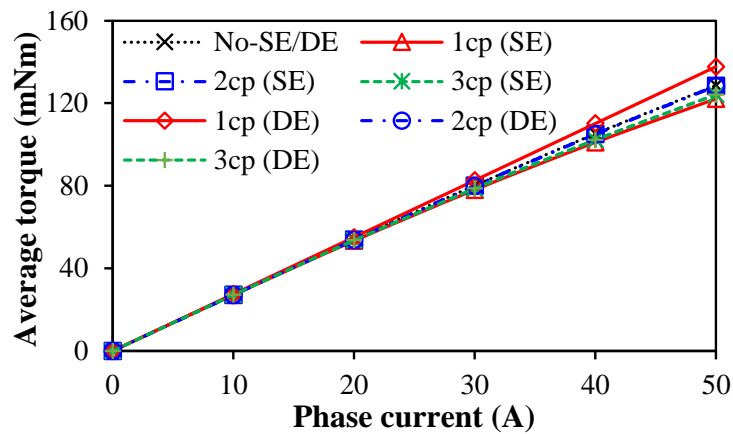
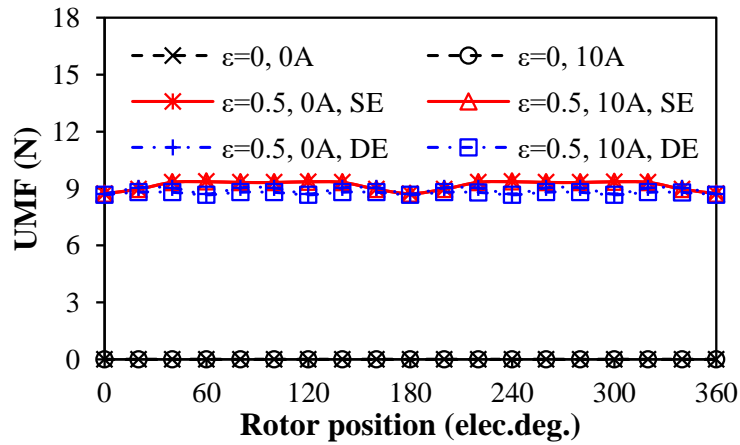


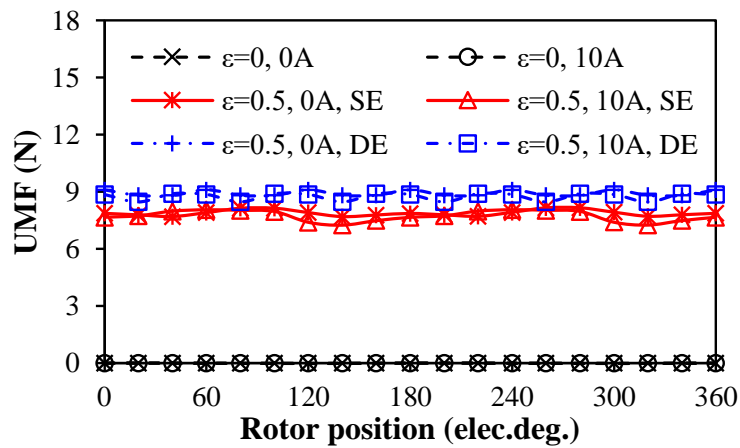
Fig. 4. 51. Relationship between average torque and phase current,  $\epsilon=0.5$ .

#### 4.4.4 Unbalanced Magnetic Force

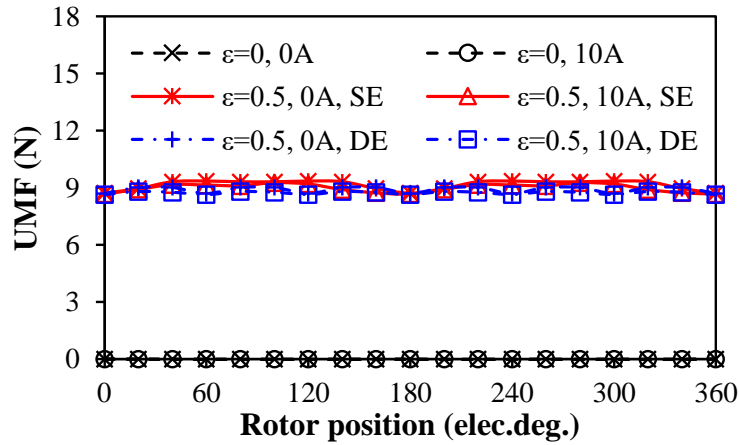
The 6s/2p PM motor has no inherent UMF due to symmetrical stator topology and balanced winding distribution. However, rotor eccentricity leads to large open-circuit and on-load UMFs due to unbalanced air-gap distribution, and both static and dynamic rotor eccentricities have almost the same average UMFs, Fig. 4. 52. In addition, 6s/2p motors with 1, 2, and 3 slot-pitch windings have almost the same average UMFs due to rotational symmetrical windings.



(a) 1 slot-pitch windings



(b) 2 slot-pitch windings



(c) 3 slot-pitch windings

Fig. 4. 52. Open-circuit and on-load UMFs of 6s/2p motors with static/dynamic rotor eccentricities,  $\epsilon=0.5$ , rated current=10A.

With the increase of eccentricity ratio, the average UMF increases linearly no matter what phase current is, Fig. 4. 53, which means the rotor eccentricity dominates the resultant UMF in the 6s/2p PM motor with rotational symmetrical windings. In addition, due to magnetic saturation effect, the average UMF caused by rotor eccentricity decreases with the phase current, Fig. 4. 54. Employing linear material in the stator, the average UMF remains unchanged with the increase of phase current.

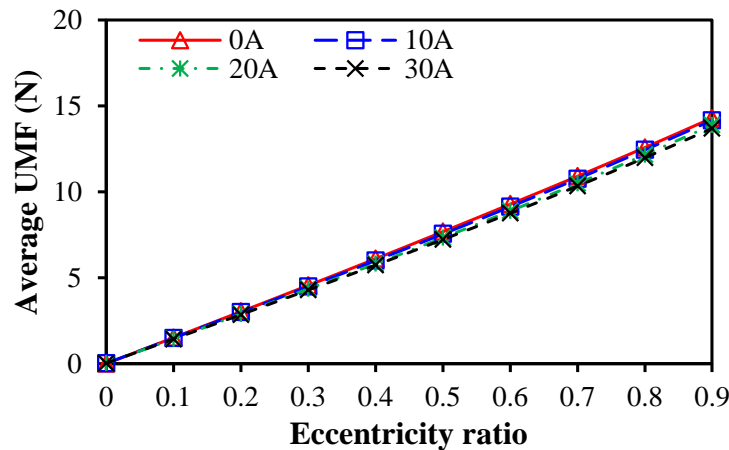


Fig. 4. 53. Variation of average UMFs with static rotor eccentricity ratio in the 6s/2p motors with 1 slot-pitch windings and having different phase currents.

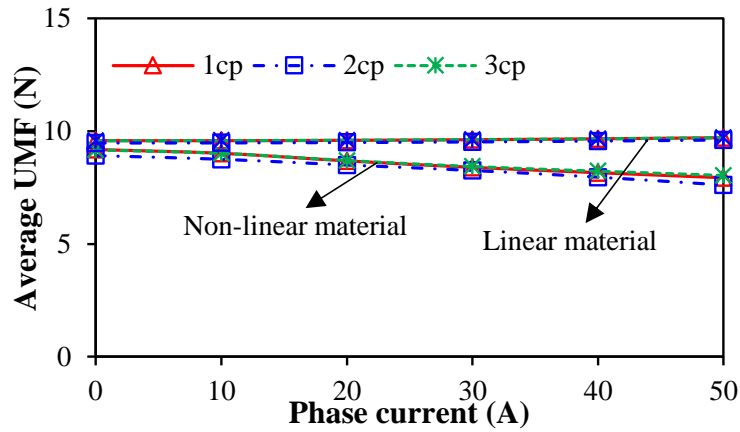


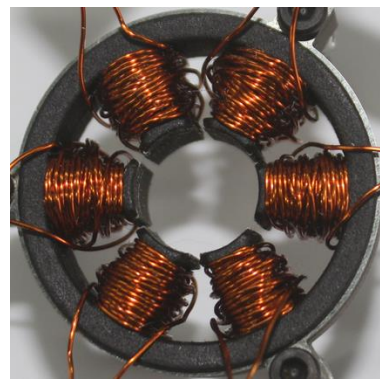
Fig. 4. 54. Relationship between average UMFs and phase current under non-linear and linear materials, static rotor eccentricity,  $\varepsilon=0.5$ .

#### 4.5. Prototyping and Experimental Validation

For validating the predictions by FEM of back-EMF and static torque, three endplates without/with static and dynamic rotor eccentricities ( $\varepsilon=0.5$ ) are manufactured [ZHU13], Fig. 4. 56, and two 3s/2p and 6s/2p PM motors with non-overlapping windings are prototyped, Fig. 4. 55. For static rotor eccentricity, both the bearing and inner sleeve are offset toward the same direction, while for dynamic rotor eccentricity, the bearing is concentric but the inner sleeve is eccentric. In addition, the holes in two endplates are designed for changing the eccentricity angle.



(a) 3-slot



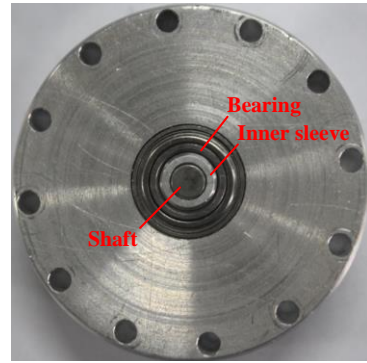
(b) 6-slot

Fig. 4. 55. 3s/2p and 6s/2p prototype motors with tooth-coil windings.

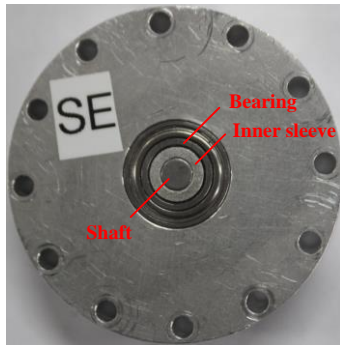




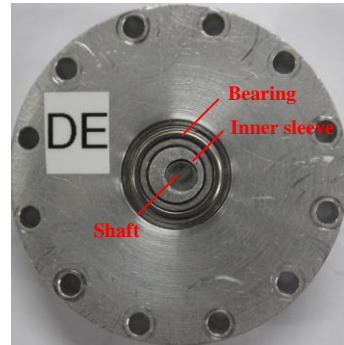
(a) Rotor and bearing



(b) Without rotor eccentricity



(c) Static rotor eccentricity

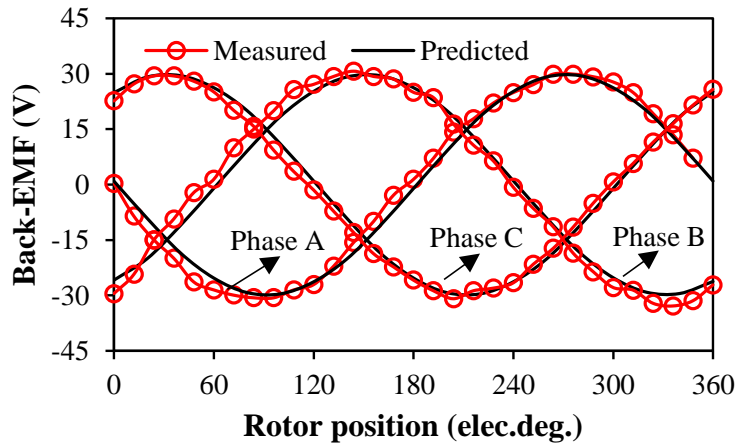


(d) Dynamic rotor eccentricity

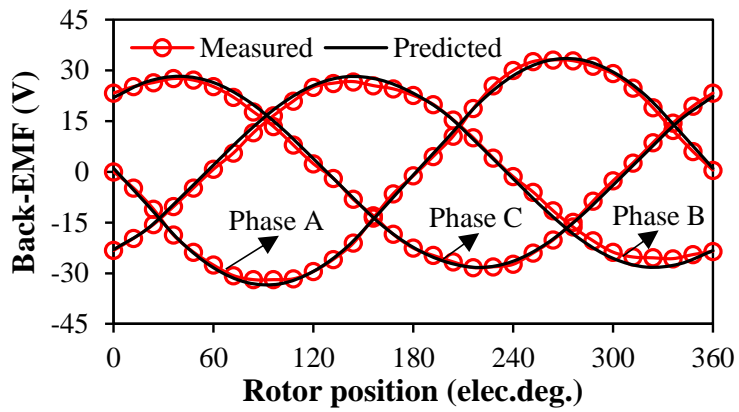
Fig. 4. 56. Endplates with static and dynamic rotor eccentricities.

#### 4.5.1 Back-EMF

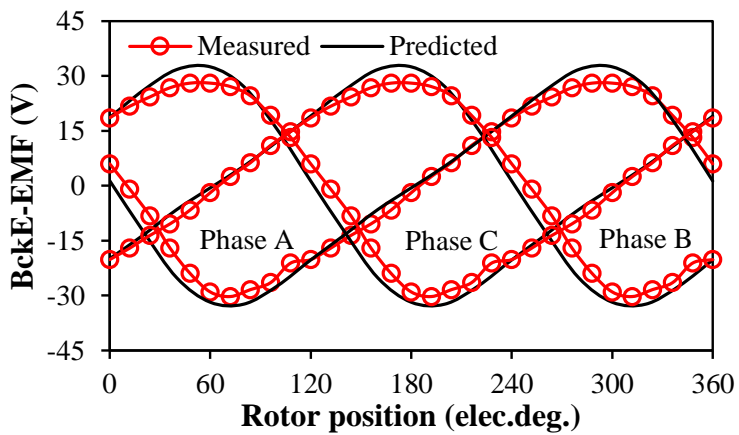
Fig. 4. 57 shows the predictions by FEM and experimental results of back-EMFs of three phases in  $3s/2p$  motors without/with static/dynamic rotor eccentricities, and they have a good agreement. For different static rotor eccentricity angles, the measured back-EMFs of three phase and the FE predicted results have a good agreement, Fig. 4. 58. Fig. 4. 59 shows the phase A back-EMF waveform of the  $3s/2p$  motor with dynamic rotor eccentricity and different eccentricity angles. The FE predicted and measured back-EMFs have a good agreement, indicating the asymmetric back-EMF waveform exists when the eccentricity angle is not equal to the rotor initial angle. Fig. 4. 60 shows the predictions by FEM and measurements of three phase back-EMFs of  $6s/2p$  motors having tooth-coil windings without and with static/dynamic rotor eccentricities. Although the measured back-EMF is slightly different from the FE prediction due to the saturation, the satisfied agreement is achieved.



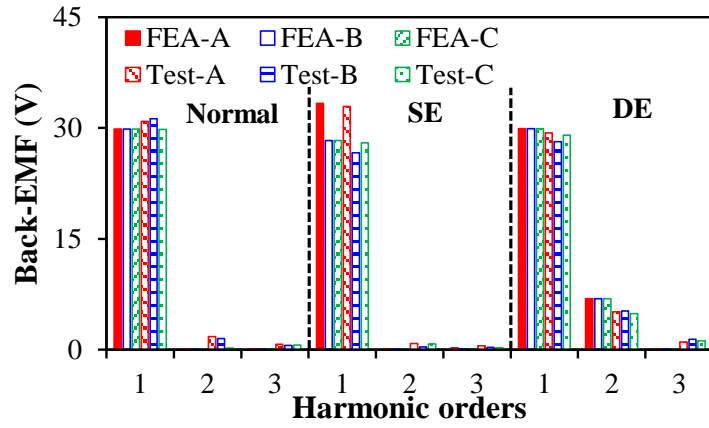
(a) Without rotor eccentricity



(b) Static rotor eccentricity

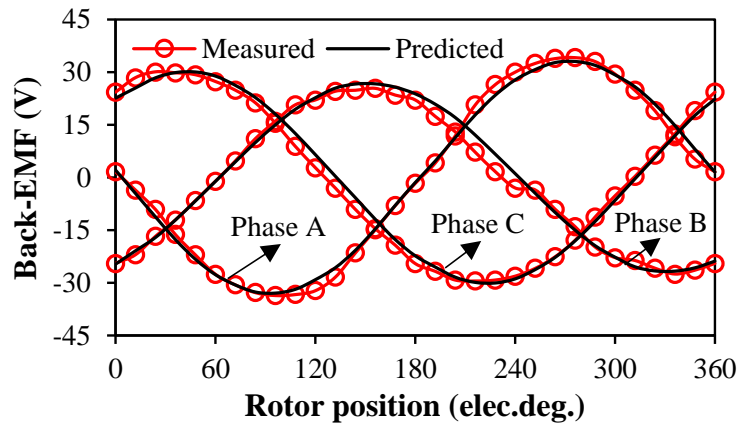


(c) Dynamic rotor eccentricity

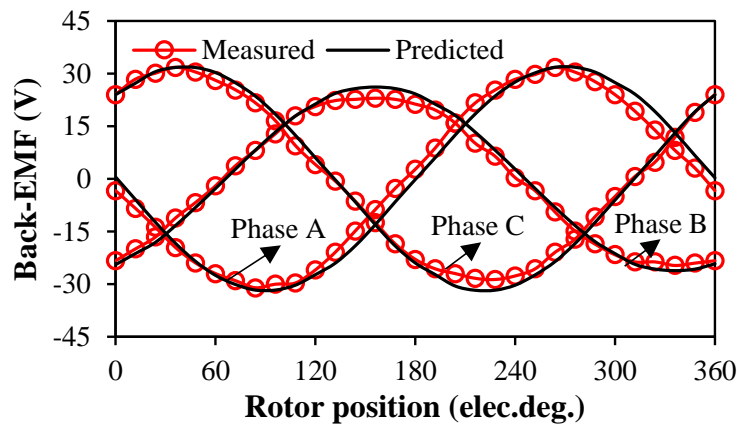


(d) Spectra

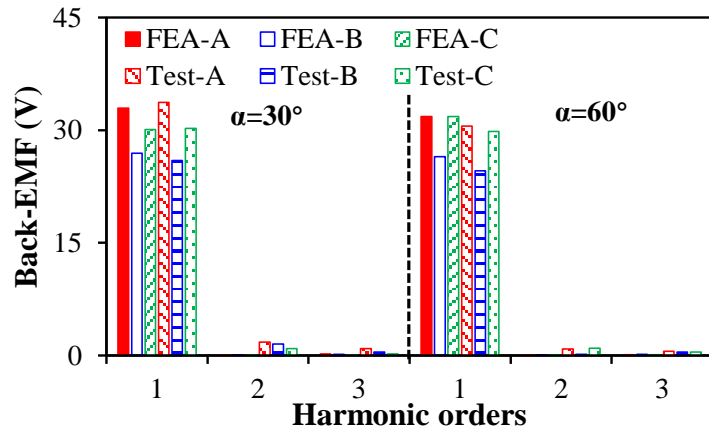
Fig. 4. 57. Predictions by FEM and measurements of three phase back-EMFs of 3s/2p motors with static/dynamic rotor eccentricities,  $\alpha=0^\circ$ ,  $\varepsilon=0.5$ .



(a)  $\alpha=30^\circ$

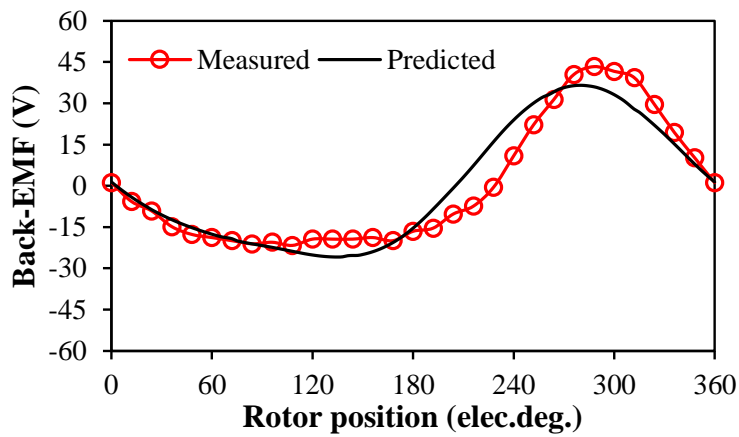


(b)  $\alpha=60^\circ$

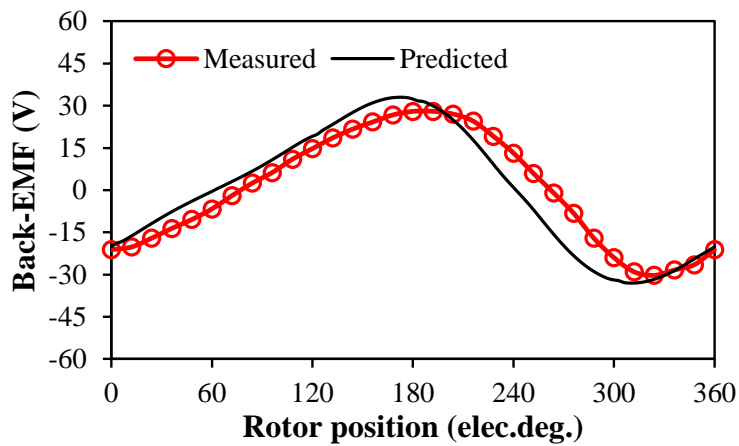


(c) Spectra

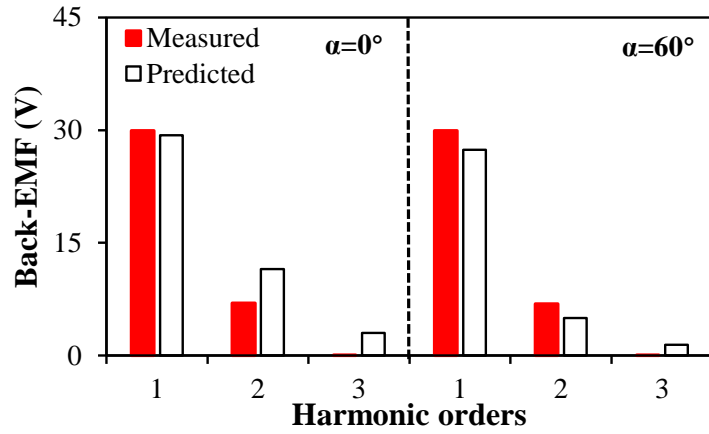
Fig. 4. 58. Predictions by FEM and measurements of three phase back-EMFs of 3s/2p motors with static rotor eccentricity and different eccentricity angles,  $\varepsilon=0.5$ .



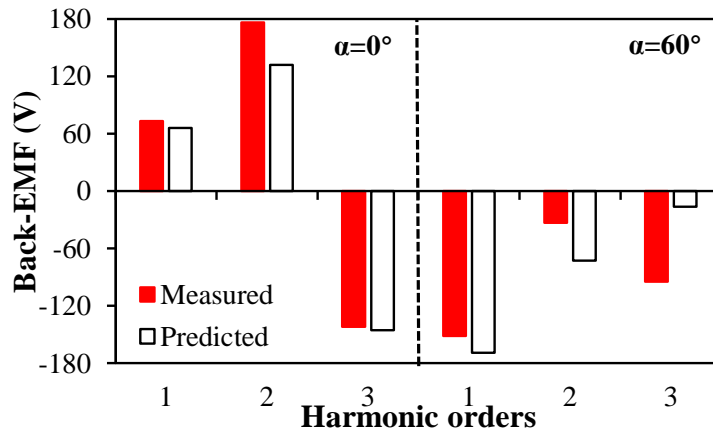
(a)  $\alpha=0^\circ$



(b)  $\alpha=60^\circ$

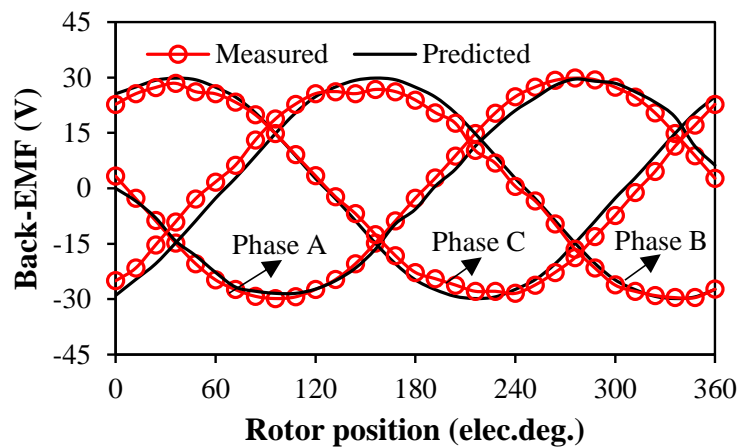


(c) Spectra

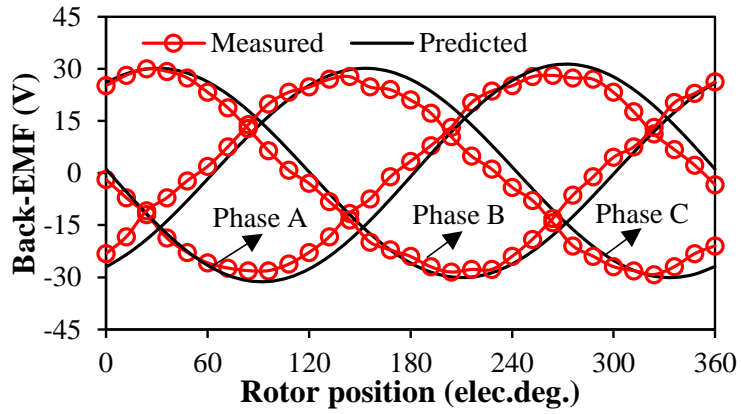


(d) Phase angle of harmonics

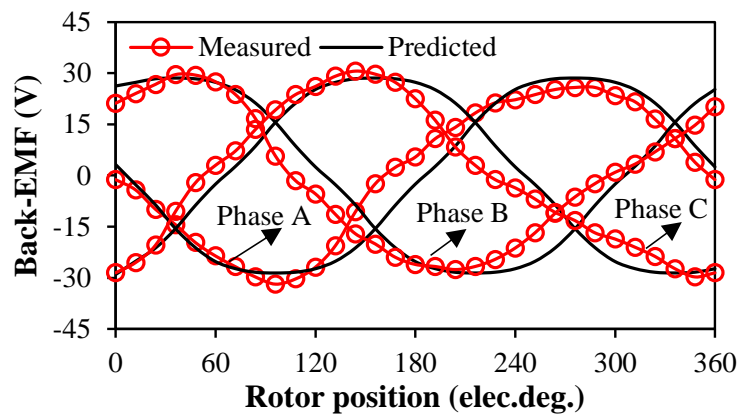
Fig. 4. 59. Predictions by FEM and measurements of phase A back-EMFs of 3s/2p motor with dynamic rotor eccentricity,  $\varepsilon=0.5$ ,  $\beta=60^\circ$ .



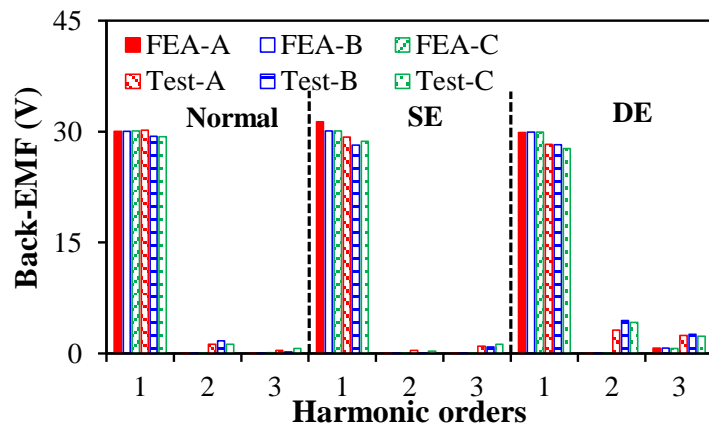
(a) Without rotor eccentricity



(b) Static rotor eccentricity



(c) Dynamic rotor eccentricity



(d) Spectra

Fig. 4. 60. Predictions by FEM and measurements of back-EMFs of three phases in 6s/2p motor with 1 slot-pitch windings having static/dynamic rotor eccentricities,  $\varepsilon=0.5$ ,  $\alpha=0^\circ$ .

#### 4.5.2 Static Torque

According to [ZHU09], the on-load static torque can be measured by a test rig, Fig. 4. 61. The motor with rotor eccentricity is clamped by the jaws of a lathe. The balance beam connects the motor and the digital scale, which transforms the static torque into force. To avoid the balance beam off the digital scale, the weight is employed on the balance beam. The armature winding is fed by the DC supply. Since three phase 120° electric square wave current waveforms are employed, the static torques are measured when only two phases are excited, i.e.  $I_A = -I_B = 5A$ ,  $I_C = 0A$ . For the 3s/2p motor without/with rotor eccentricity,  $\varepsilon=0.5$ , the predictions by FEM of on-load static torques are validated by the experimental results, Fig. 4. 62, and the on-load static torques remains unchanged no matter with/without rotor eccentricity, which verifies that the rotor eccentricity barely changes the average electromagnetic torque. In addition, good agreement between measured and FE predicted on-load static torques also exists under different phase currents, Fig. 4. 63.

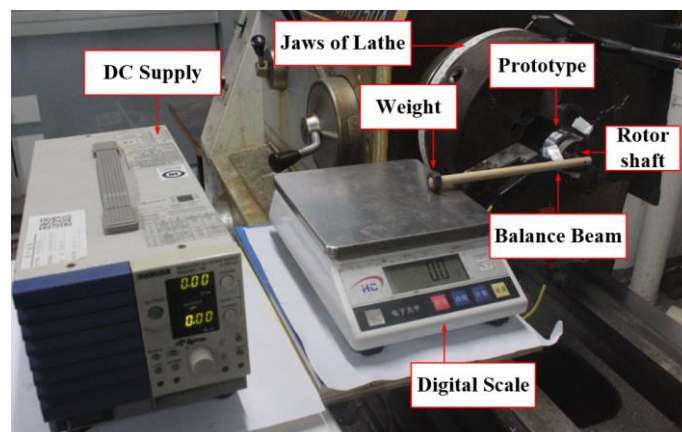
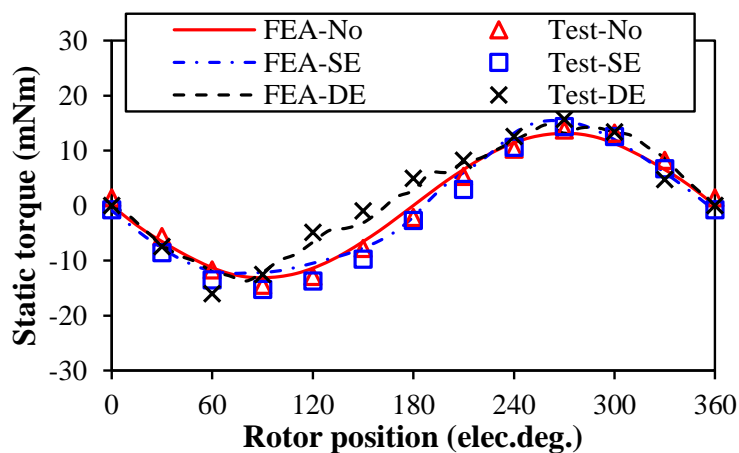
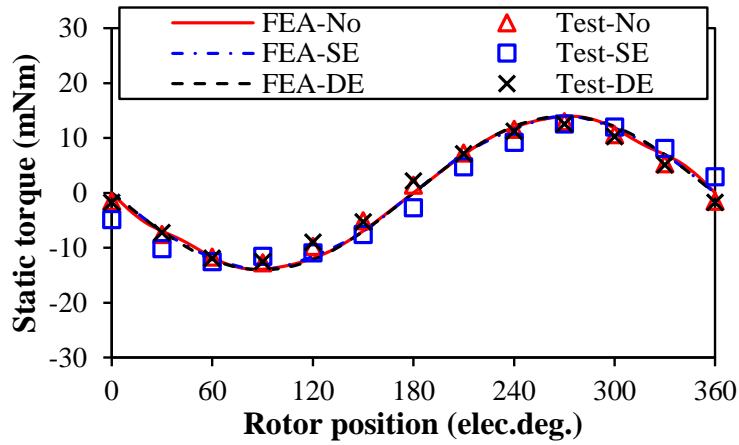


Fig. 4. 61. Experiment system of static torque.

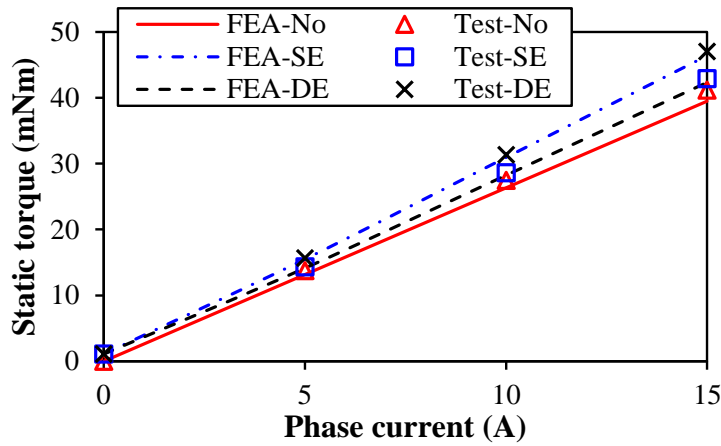


(a) 3s/2p

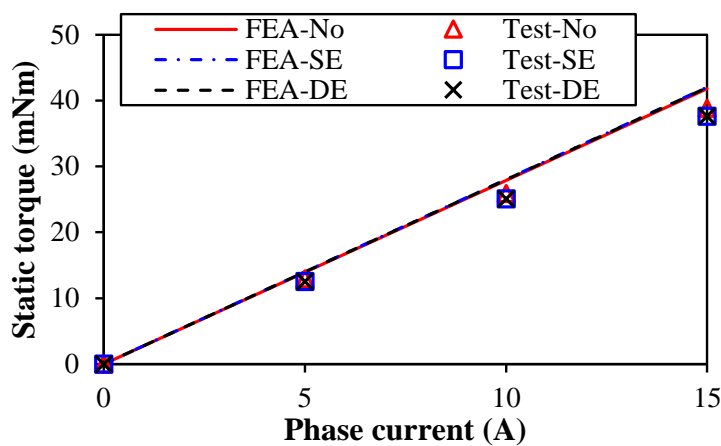


(b) 6s/2p

Fig. 4. 62. Predictions by FEM and measurements of on-load static torques at different rotor positions without and with static/dynamic rotor eccentricities,  $\epsilon=0.5$ ,  $I_A=-I_B=5A$ ,  $I_C=0A$ .



(a) 3s/2p



(b) 6s/2p

Fig. 4. 63. Predictions by FEM and measurements of on-load static torque at different phase currents without and with static/dynamic rotor eccentricities,  $\epsilon=0.5$ ,  $I_A=-I_B=I_{max}$ ,  $I_C=0A$ .



## 4.6. Conclusion

This chapter mainly focuses on the analysis of electromagnetic performances of the 3s/2p and 6s/2p PM motors with static and dynamic rotor eccentricities, accounting for eccentricity ratio, eccentricity angle, and the rotor initial angle. For the 3s/2p motor, the static rotor eccentricity only affects the fundamental back-EMFs of three phases in terms of magnitudes and phase angles. In addition, the eccentricity angle can change the unbalanced ratio and phase angles of back-EMFs of three phases periodically. For the dynamic rotor eccentricity, the three phase back-EMFs remain balanced, but exhibit asymmetric positive and negative half-periods in the phase back-EMF waveform depending on the eccentricity angle and the rotor initial angle. The largest asymmetric back-EMF waveform occurs when the angle difference between the eccentricity angle and the rotor initial angle is equal to 90 elec. deg. Compared with static rotor eccentricity, the dynamic rotor eccentricity has almost the same average torque and UMF but larger torque ripple and peak cogging torque. For 6s/2p motors, when strong magnetic saturation exists, the static rotor eccentricity also leads to unbalanced back-EMFs of three phases, but the 2 and 3 slot-pitch windings can decrease this influence. Without saturation effect, the rotor eccentricity has negligible influence on the phase back-EMF, electromagnetic torque, and cogging torque. However, both static and dynamic rotor eccentricities have a significant influence on the average UMF.

### APPENDIX 4. A

#### Simple Relative Permeance Model

In this chapter, a simple relative permeance model [ZHU13] is used to explain the FE predicted results. To simplify the model, the slotting effect is neglected. The relative air-gap permeances ( $\lambda$ ) for static/ dynamic rotor eccentricities considering eccentricity angle ( $\alpha$ ) are introduced as

$$\lambda_g = 1 + \lambda_{g1} \cos(\theta - \chi\omega t + \alpha) \quad (4.A.1)$$

where  $\theta$  is the angular position,  $\chi$  equals to 1 and 0 for the dynamic and static rotor eccentricities, respectively,  $\omega$  is the rotor speed,  $\lambda_1$  is the 1<sup>st</sup> harmonic magnitude.

Considering the rotor initial angle ( $\beta$ ), the radial component ( $B_{r\_slotless}$ ) can be given by

$$B_{r\_slotless} = \sum_{n=1,3,\dots} B_m \cos[np(\theta - \omega t) + \beta] \quad (4.A.2)$$

where  $B_m$  is the  $n$  th harmonic magnitude [XUJ11]. Considering the rotor eccentricity, the

additional components should be added in  $B_{r\_slotless}$

$$\begin{aligned}
B_{r\_slotted} &= B_{r\_slotless} \lambda_1 \cos(\theta - \chi \omega t + \alpha) \\
&= (1/2) \sum_{n=1,3,\dots} B_m \lambda_1 \left\{ \begin{aligned} &\cos[(np+1)\theta - (np+\chi)\omega t + \alpha + \beta] \\ &+ \cos[(np-1)\theta - (np-\chi)\omega t - \alpha + \beta] \end{aligned} \right\} \quad (4.A.3)
\end{aligned}$$

Thus, the additional flux of the  $n$  th coil can be given by

$$\begin{aligned}
\psi_i &= R_{sl} l_a \int_{\theta_i - \theta_y/2}^{\theta_i + \theta_y/2} B_{r\_slotted} d\theta \\
&= R_s l_a \sum_{n=1,3,\dots} B_m \lambda_1 \times \\
&\quad \left\{ \begin{aligned} &\frac{1}{np+1} \cos[(np+1)\theta_i - (np+\chi)\omega t + \alpha + \beta] k_{pk} \Big|_{k=np+1} \\ &+ \frac{1}{np-1} \cos[(np-1)\theta_i - (np-\chi)\omega t - \alpha + \beta] k_{pk} \Big|_{k=np-1} \end{aligned} \right\} \quad (4.A.4)
\end{aligned}$$

The flux of one phase of the 3s/2p motor with dynamic rotor eccentricity ( $\chi = 1$ ) can be calculated by

$$\begin{aligned}
\psi &= R_s l_a \sum_{n=1,3,\dots} \frac{B_m}{np} \cos[(np)\omega t + \theta_0 + \beta] k_{dk} k_{pk} \Big|_{k=np} \\
&+ R_s l_a \sum_{n=1,3,\dots} \frac{B_m \lambda_1}{np+1} \cos[(np+1)\omega t + \theta_1 + \alpha + \beta] k_{dk} k_{pk} \Big|_{k=np+1} \\
&+ R_s l_a \sum_{n=1,3,\dots} \frac{B_m \lambda_1}{np-1} \cos[(np-1)\omega t + \theta_2 - \alpha + \beta] k_{dk} k_{pk} \Big|_{k=np-1} \quad (4.A.5)
\end{aligned}$$

where  $\theta_0$ ,  $\theta_1$ , and  $\theta_2$  are the phase angles depending on the positions of the coils and the harmonic order, and  $k_{dk}$  is the distribution factor. When  $n=1$  and  $\theta_0=\theta_1=\theta_2=90^\circ$ , the phase angle of the fundamental is  $90^\circ+\beta$ , and the phase angle of the 2<sup>nd</sup> order harmonic is  $90^\circ+\alpha+\beta$ , as shown in (4.A.6). Therefore, the eccentricity angle only affects the phase angle of the 2<sup>nd</sup> order back-EMF harmonic due to dynamic rotor eccentricity, but the rotor initial angle affects the phase angles of the fundamental and 2<sup>nd</sup> order back-EMF harmonic.

$$\begin{aligned}
\psi &= R_s l_a \sum_{n=1,3,\dots} \frac{B_m}{np} \cos[\omega t + \theta_0 + \beta] k_{dk} k_{pk} \Big|_{k=np} \\
&+ R_s l_a \sum_{n=1,3,\dots} \frac{B_m \lambda_1}{np+1} \cos[2\omega t + \theta_1 + \alpha + \beta] k_{dk} k_{pk} \Big|_{k=np+1} \\
&+ R_s l_a \sum_{n=1,3,\dots} \frac{B_m \lambda_1}{np-1} \cos[\theta_2 - \alpha + \beta] k_{dk} k_{pk} \Big|_{k=np-1}
\end{aligned} \tag{4.A.6}$$

## CHAPTER 5

### INFLUENCE OF ROTOR ECCENTRICITIES ON ELECTROMAGNETIC PERFORMANCE OF 6-SLOT/2-POLE PERMANENT MAGNET MOTORS

This chapter investigates the influence of circulating currents in parallel-connected windings due to static and dynamic rotor eccentricities on electromagnetic performance, including back-EMF, various loss components, UMF, cogging torque, and torque, of a 6s/2p HSPM motor on both open-circuit/on-load conditions. The increased rotor eccentricity ratio leads to the increased circulating currents. Compared with no circulating currents, i.e. without rotor eccentricities or series-connected windings, the induced circulating currents in parallel-connected windings result in increased various loss components, as well as decreased average UMF and cogging torque, while the average torque and torque ripple remain almost unchanged.

#### 5.1 Introduction

Circulating currents may exist in the parallel-connected windings due to rotor or stator winding inter-turn short circuit fault, rotor eccentricity, and rotor vibration [WAN05] [KIM11]. The induced circulating current increases the copper loss and decreases the UMF caused by rotor eccentricity [YAN81] [DEB93]. In literature, there are several papers focusing on the circulating current in parallel-connected windings, including analysis and reduction methods for induction machines [DEB93] [TEN03] [MOI17], synchronous machines [WAN05] [ARK10] [WAL11] [SCH20], electrical machines under fault condition [CAN07] [KIM11] [ROD13] [MAF19], as well as permanent magnet machines with/without neutral point connection [TAK10] [MAR13].

For a large synchronous generator [FOG99], the circulating currents caused by short-circuit and rotor eccentricity in the parallel-connected windings are computed, respectively. [WAN05] develops a method for fault detection in the generator by monitoring the circulating currents in parallel-connected stator windings. The machine faults include rotor winding inter-turn short circuit, stator winding inter-turn short circuit, rotor eccentricity, and rotor vibration. [CAN07] presents three methods for static rotor eccentricity detection in a non-salient two-pole synchronous generator. Those methods include axial shaft voltage, vibration, and circulating current monitoring. [ROD13] adopts circulating currents for fault detection in synchronous machines since the specific frequency components of the circulating currents react to the specific fault types. For a 126 MW salient pole synchronous generator, [MAF19] determines the rotor eccentricity position by measuring the values of the circulating currents in parallel

branches. However, those researches mainly employ circulating currents to detect faults, but the influence of circulating currents is not investigated.

[DEB93] investigates the influence of rotor eccentricity and parallel windings in induction motors. It shows that the static and dynamic eccentricities result in the circulating currents in the parallel-connected windings, which can reduce the average UMF caused by rotor eccentricity. [TEN03] analyses the influence of circulating currents due to dynamic rotor eccentricity in the rotor cage and parallel-connected stator windings on the UMF in induction motors. It can be seen that the circulating currents affect the magnitude and direction of UMF. [ARK10] investigates the influence of magnetic forces on the rotor dynamic characteristic for a high-speed synchronous reluctance machine with dynamic rotor eccentricity. The results show when the stator windings are connected in parallel, the magnetic force with the induced circulating current has a large influence on the rotor dynamic characteristic, especially for four parallel branches. In [WAL11], the UMFs due to static rotor eccentricity in the 12-pole salient pole synchronous machine with the parallel-connected windings are calculated. The results show that the circulating current can reduce the UMF, but the reduction effect depends on the winding distribution and rotor offset direction. [TAK10] analyses the influence of rotor eccentricity on a 6s/4p IPM synchronous machine with parallel 2Y connection of windings, i.e. the neutral points are connected. It shows that rotor eccentricity leads to UMF and circulating current, which increases the mechanical loss and magnetic loss, respectively. [MOI17] presents an analytical method to calculate the UMF of doubly-fed induction machines (DFIM) with rotor eccentricity under open-circuit condition. It also shows that the circulating current reduces the UMF.

To reduce the circulating currents, losses, and UMFs, a flux barrier rotor is employed in [TAK10]. [MAR13] compares the circulating currents in the 6s/4p IPM motors with connected and unconnected neutral points. It is found that the connected neutral points can reduce the circulating currents due to static rotor eccentricity. In addition, a theoretical expression for the circulating current is developed. [PER19] segments the rotor pole and actively controls the rotor magnetization to cancel the UMF and circulating currents caused by rotor eccentricity, which can improve the electromagnetic efficiency of the synchronous machines with static rotor eccentricity. [SCH20] proposes a method to calculate the circulating current in parallel-connected windings caused by rotor eccentricity in twelve-pole six-phase salient pole synchronous machines under transient operation and no-load condition. The iron saturation is considered in this calculation method since it can reduce the induced circulating current.

Overall, most researches on circulating current due to rotor eccentricity focus on the large generator, induction motor, and salient pole synchronous machines. However, brushless direct current (BLDC) high-speed permanent magnet (HSPM) motors are widely employed for many applications [BIA04] [GER14] [SHE18], but there is rare research focusing on the influence of circulating current on the electromagnetic performance of the BLDC HSPM motors with rotor eccentricity. In general, the 2-pole rotor is employed to reduce the fundamental frequency and minimize the stator iron loss and converter loss [HES82] [ZHU97], and thus typical small-size HSPM motors include 6s/2p [SHI04] [NOG05] and 3s/2p motors [HES87] [ZHU97]. [ZHU13] presents that the rotor eccentricity does not change the back-EMFs of 6s/2p HSPM motors due to the symmetrical distribution of the coils in each phase. However, in small-size HSPM motors, the parallel winding connection is usually employed to reduce the back-EMF and meet the requirement of terminal voltage limitation. Therefore, the influence of circulating currents caused by rotor eccentricity in the parallel-connected windings on the electromagnetic performance of the 6s/2p HSPM motor will be investigated in this chapter.

In section 5. 2, the machine topology of the 6s/2p HSPM motor and rotor eccentricity types are discussed. Section 5. 3 investigates the influence of rotor eccentricity on the back-EMFs of individual coils in the same phase and presents the production principle of circulating currents. Meanwhile, the effect of the rotor eccentricity ratio on the circulating currents is studied. In section 5. 4, the influence of circulating currents at the steady-state operation is investigated under open-circuit and on-load conditions. Section 5. 5 is the conclusion. In the appendix, the circulating currents with transient direct current (DC) components at the beginning of rotor eccentricity when it occurs are discussed under open-circuit and on-load conditions.

## 5.2 Machine Topologies and Rotor Eccentricity Types

### 5.2.1 Machine Topology and Winding Connection

Fig. 5. 1 (a) shows the machine topology and the main parameters are shown in Table 5. 1. A 2-pole parallel magnetized magnet ring with a magnetic shaft is adopted. It is intended for high-speed operation in handheld vacuum cleaners, and three phase 120° electric square wave current waveforms are employed for excitation. It requires light weight, long run time, and low noise. Therefore, the number of batteries is limited to minimize the weight, which restricts the terminal voltage and back-EMF of the HSPM motor. Therefore, the parallel star connection for two diametrically located phase coils is employed to reduce the back-EMF in the 6s/2p HSPM motor, Fig. 5 1 (b).

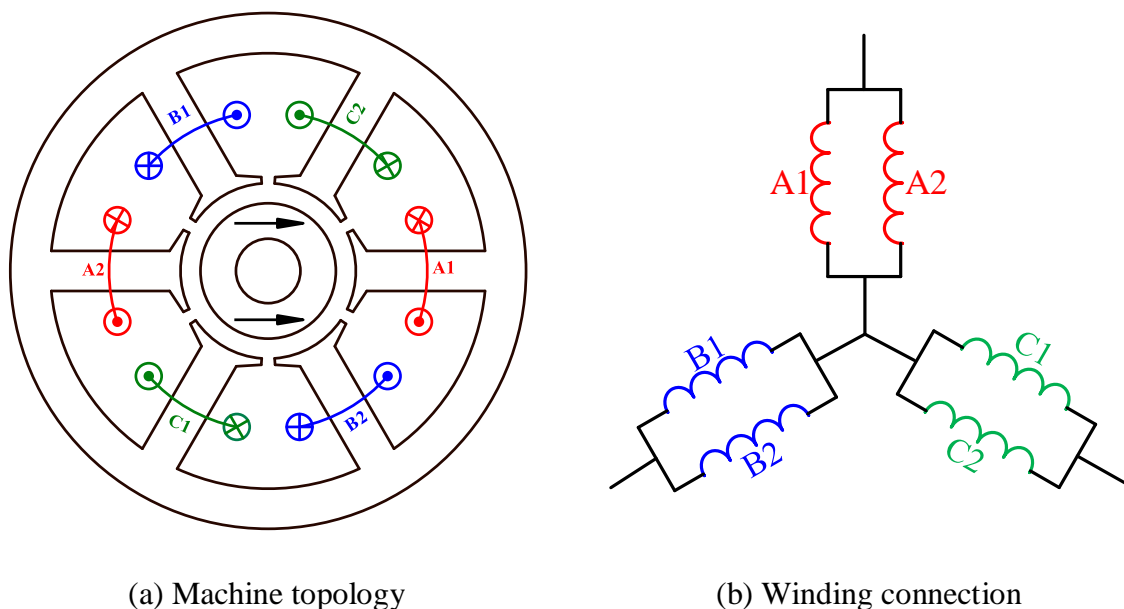


Fig. 5. 1. Machine topology and winding connection of 6s/2p PM motor.

### 5.2.2 Rotor Eccentricity Types

Two kinds of rotor eccentricity are studied in this chapter, i.e. static rotor eccentricity (SE) and dynamic rotor eccentricity (DE). Fig. 5. 2 illustrates the difference between SE and DE, where  $g$  is the air-gap length of the motor without eccentricity,  $X$  is the rotor offset distance along the eccentricity direction,  $R_{in}$  is the stator bore radius,  $R_m$  is the magnet radius, i.e. rotor outer radius,  $O_r$  is the centre of rotor, and  $O_s$  is the centre of stator bore. When the rotor is rotating, the position of the centre of rotor ( $O_r$ ) is fixed for SE, while it is rotating around the centre of stator bore ( $O_s$ ) with a radius of the rotor offset distance for DE. It is assumed that the rotor eccentricity angle is zero when the rotor is offset towards phase A. To describe the degree of

rotor eccentricity, the eccentricity ratio ( $\varepsilon$ ) is introduced, which is the ratio of rotor offset distance to the air-gap length of the motor without rotor eccentricity, i.e.  $\varepsilon = X/g$ .

Table 5.1

Main Parameters of 6S/2P PM Motor

Stator outer diameter, mm	40	Magnet thickness, mm	2.75
Stator bore diameter, mm	13.6	Magnet remanence, T	1.3
Stator active length, mm	10	Shaft diameter, mm	5
Tooth body width, mm	3.11	Winding factor	0.866
Stator yoke height, mm	6.22	Magnet material	N33SH
Air-gap length, mm	1.55	Shaft material	SUS430
Slot opening, mm	1.5	Lamination material	20JNEH1200
Number of turns/phase	20	Magnetization	Parallel

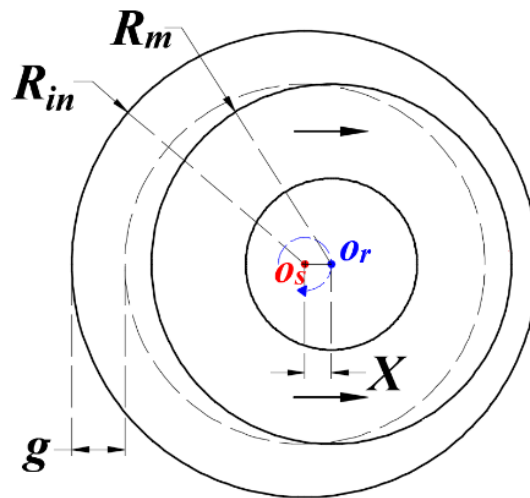


Fig. 5. 2. Illustration of static and dynamic rotor eccentricities.

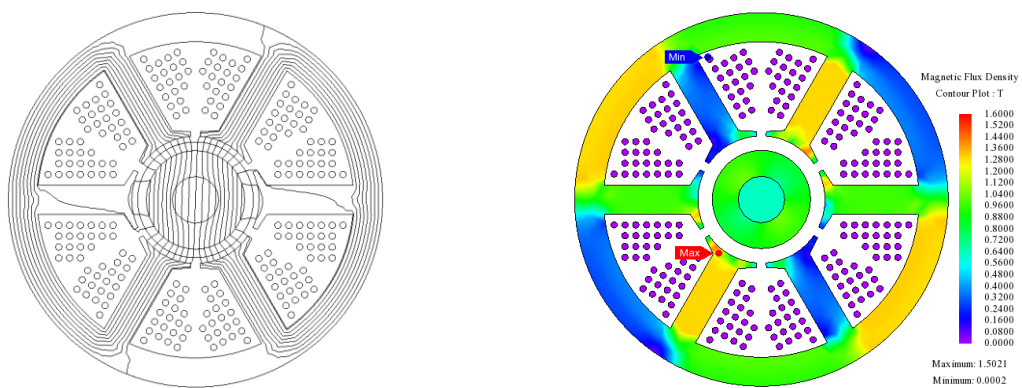
### 5.3 Effect of Rotor Eccentricity on Back-EMF and Circulating Current

In this section, the circulating currents caused by static/dynamic rotor eccentricities in the parallel-connected windings are studied in detail, together with the influence of rotor eccentricity ratio.

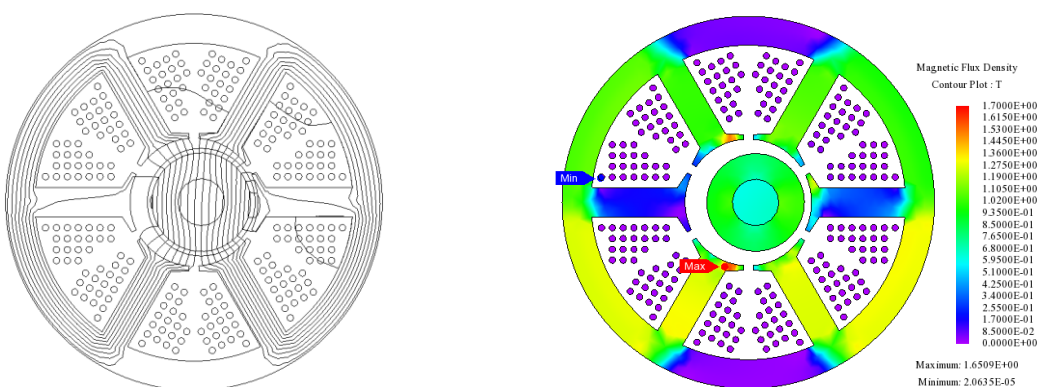


### 5.3.1 Influence of Rotor Eccentricity

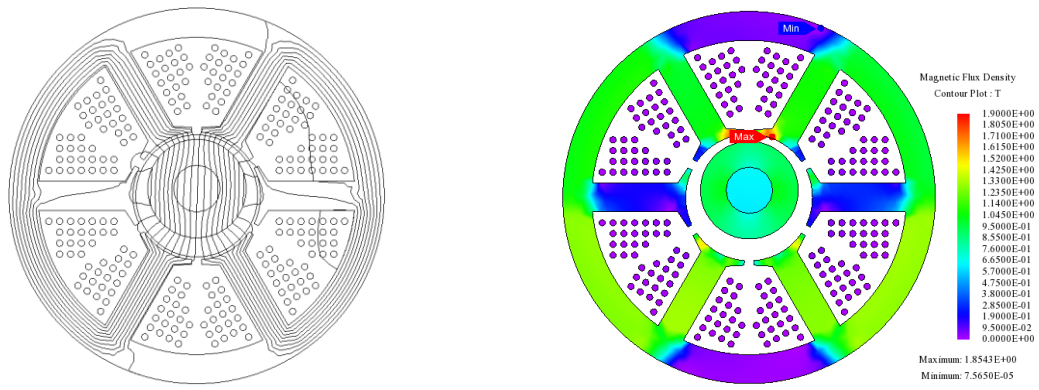
Figs. 5. 3 and 5. 4 show the equipotential, flux contour, and air-gap field distributions of the motor without/with static/dynamic rotor eccentricities when the eccentricity ratio is 0.5 and the rotor position ( $\theta$ ) is  $90^\circ$  (when the rotor position is  $0^\circ$ , the results of static and dynamic rotor eccentricities are the same). It can be seen that with static rotor eccentricity, the non-uniform air-gap distribution is fixed relative to the stator, and coils A1 and A2 face the smallest and largest air-gap, respectively. With dynamic rotor eccentricity, the non-uniform air-gap distribution is rotating relative to the stator, and each coil faces the smallest and largest air-gap once in each rotor mechanical period. The spectra in Fig. 5. 4 show that both static and dynamic rotor eccentricities result in the 2<sup>nd</sup>, 3<sup>rd</sup>... order harmonics, and the fundamental magnitudes of air-gap flux densities with static/dynamic rotor eccentricities are larger than that without rotor eccentricity.



(a) Without rotor eccentricity



(b) Static rotor eccentricity

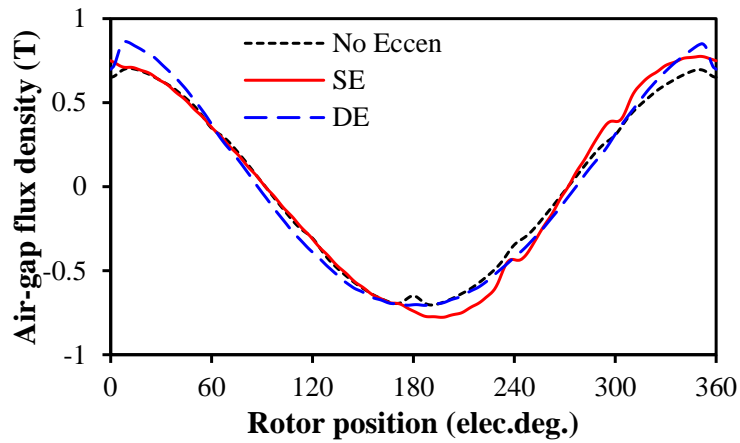


(c) Dynamic rotor eccentricity

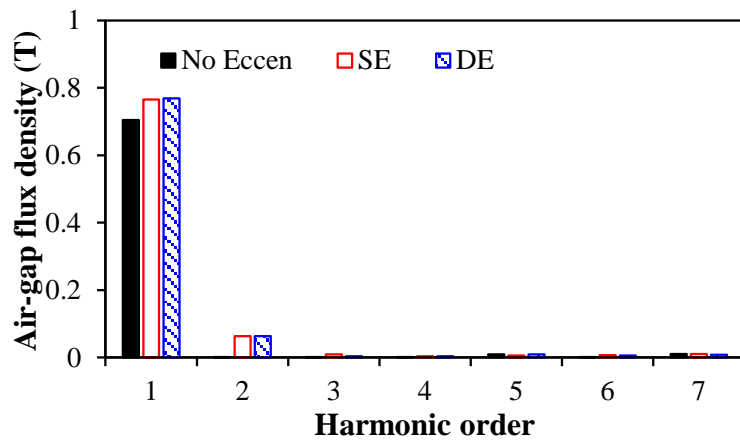
(I) Equipotential

(II) Flux contour

Fig. 5. 3. Equipotential and flux contour distributions of motors without/with rotor eccentricity,  $\theta=90^\circ$ ,  $\varepsilon=0.5$ .



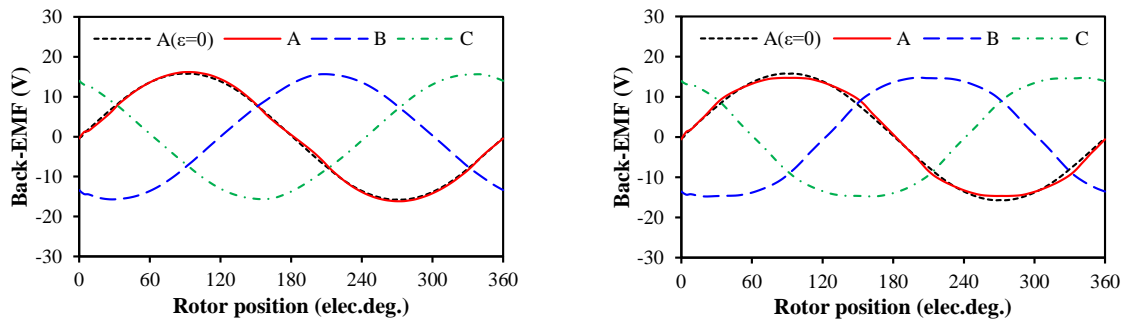
(a) Waveforms



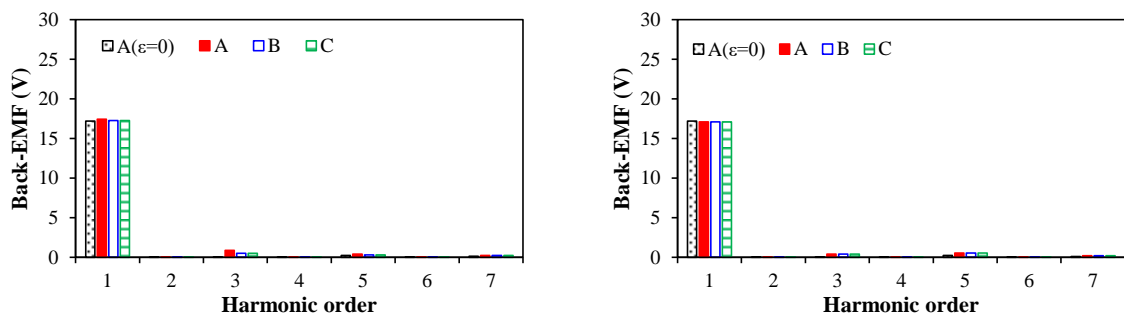
(b) Spectra

Fig. 5. 4. Air-gap field distributions of 6s/2p HSPM motors with/without static/dynamic rotor eccentricities on the radial position ( $r = R_m + 0.3875$  mm) and rotor position ( $\theta=90^\circ$ ),  $\varepsilon=0.5$ , under open-circuit condition.

Both static and dynamic rotor eccentricities have negligible influence on phase back-EMF waveforms, Fig. 5. 5, due to the symmetrical distribution of the coils in each phase winding. However, the static and dynamic rotor eccentricities have a significant influence on the back-EMF waveforms of the individual coils in the same phase, Fig. 5. 6. The static rotor eccentricity not only changes the fundamental magnitudes of the back-EMFs of the coils in the same phase but also affects the phase angles of the back-EMFs of the coils in phases B and C, Fig. 5. 6 (I). It is worth noting that the back-EMF difference between two coils of phase A is the largest compared with phases B and C since the rotor is offset towards phase A. For the same reason, only in phases B and C, two coils have different phase angles of back-EMF. The dynamic rotor eccentricity does not change the magnitude and phase angle of the fundamental back-EMF of the coils in the same phase but leads to the 2<sup>nd</sup> order harmonics, and their phase angles are different, Fig. 5. 6 (II).



(a) Waveforms

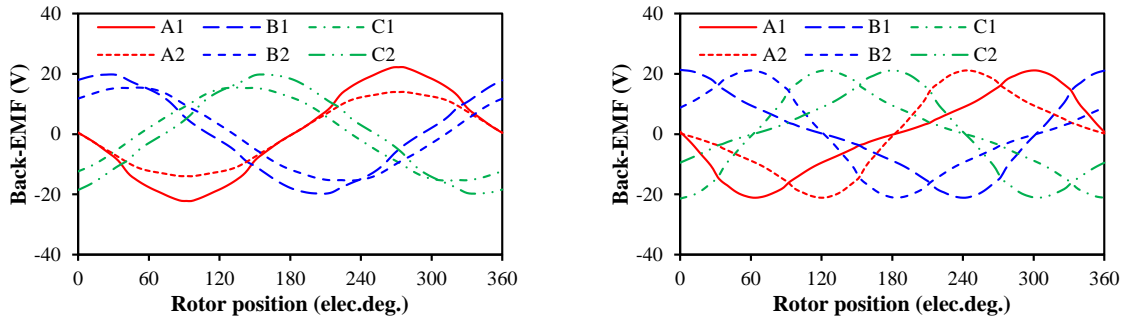


(b) Spectra

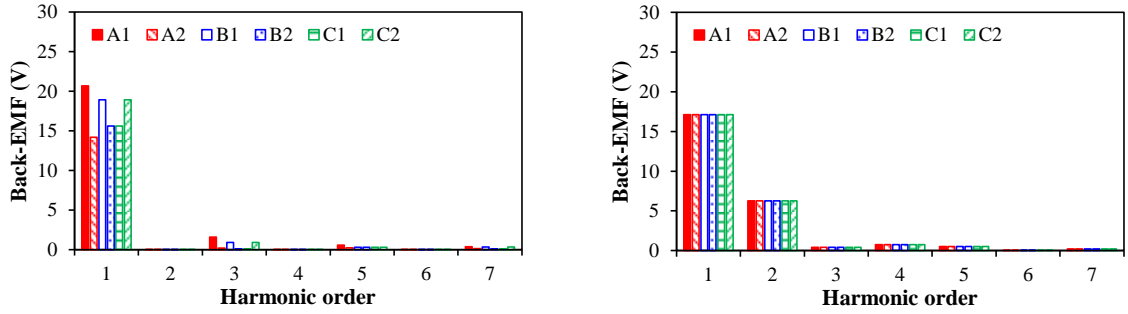
(I) Static rotor eccentricity

(II) Dynamic rotor eccentricity

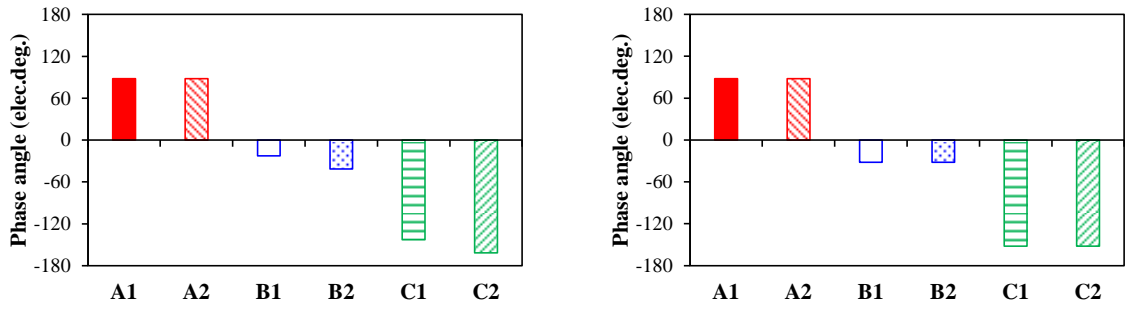
Fig. 5. 5. Back-EMFs of 6s/2p HSPM motors with static/dynamic eccentricities,  $\varepsilon=0.5$ .



(a) Waveforms

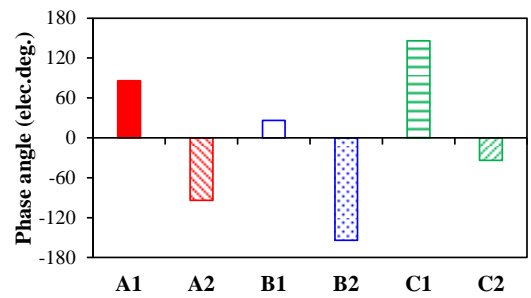


(b) Spectra



(c) Phase angles of fundamental

No 2<sup>nd</sup> order harmonic

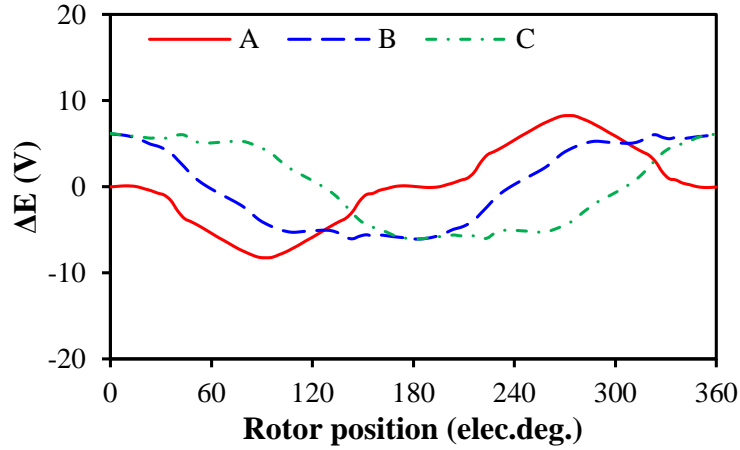


(d) Phase angles of the 2<sup>nd</sup> order harmonic

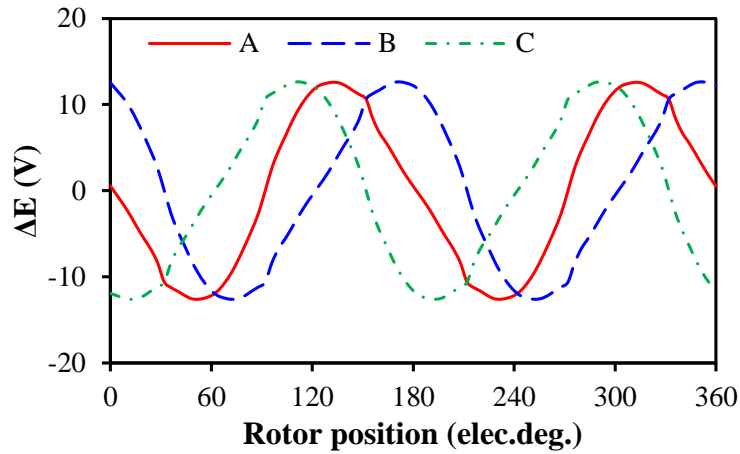
(I) Static rotor eccentricity

(II) Dynamic rotor eccentricity

Fig. 5. 6. Six-coil back-EMFs of 6s/2p HSPM motors with static/dynamic eccentricities,  $\varepsilon=0.5$ .



(a) Static rotor eccentricity



(b) Dynamic rotor eccentricity

Fig. 5. 7. Back-EMF difference between two coils in parallel of three phases,  $\varepsilon=0.5$ .

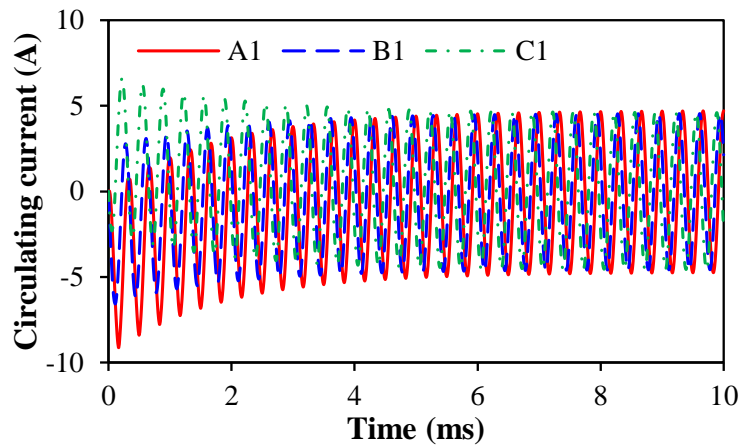
When the unbalanced back-EMFs of the parallel-connected coils in the same phase exists due to rotor eccentricity, the circulating current ( $I_{CIR}$ ) is produced and can be calculated by

$$I_{CIR} = \frac{E_1 - E_2}{2R + 2j\omega L} = \frac{\Delta E}{2Z} \quad (5.1)$$

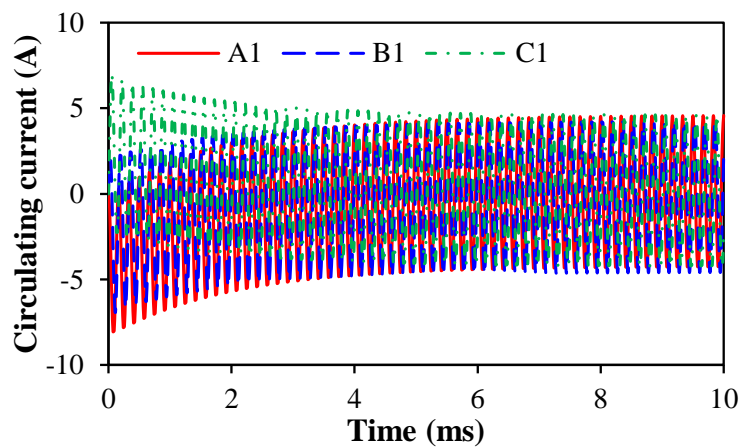
where  $E_1$  and  $E_2$  are the back-EMFs of two coils in the same phase.  $\Delta E$  is the back-EMF difference between two coils, Fig. 5. 7.  $R_{coil}$  and  $L_{coil}$  are the resistance and inductance of one coil.  $Z_{coil}$  is the coil impedance, i.e.  $Z_{coil} = R_{coil} + j\omega L_{coil}$ .  $\omega$  is the angular frequency, i.e.  $\omega=2\pi f$ . In this 2-pole motor, the rated speed is 180 krpm, and the frequency is 3,000 Hz.

Since the circulating currents in two coils of the same phase have the same magnitude but the opposite directions, only the circulating currents of coils A1, B1, and C1 are shown in Fig. 5.

8 which shows the circulating current waveforms due to static and dynamic rotor eccentricities in 10 ms, i.e. 30 electric cycles. The positive and negative circulating currents mean the current directions in the coils. It can be seen that although the direct current (DC) components exist in the circulating currents at the beginning, they disappear after several electric cycles, Fig. 5. 9. Therefore, the effect of circulating currents in the 30<sup>th</sup> electric cycle without DC components is more important and will be investigated in the next section. The transient circulating currents with DC components will be discussed in the appendix since it only lasts a short time.

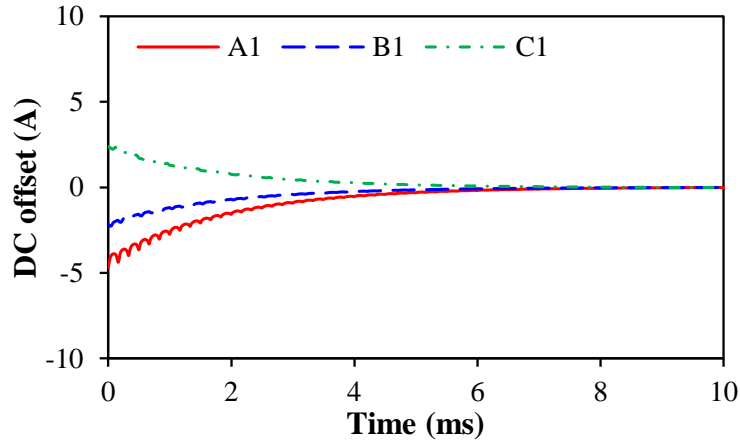


(a) Static rotor eccentricity

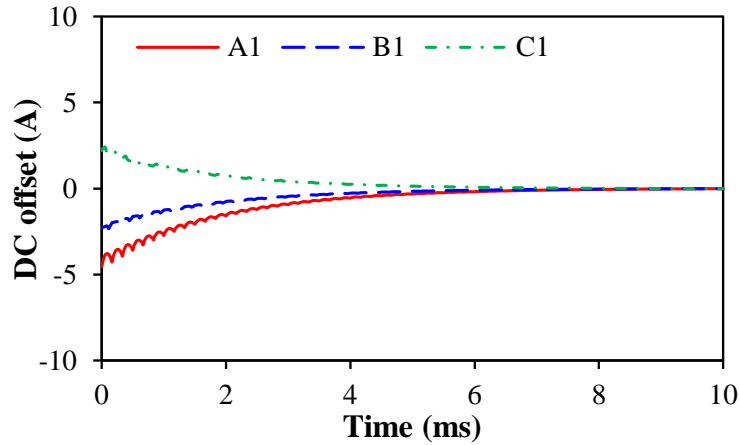


(b) Dynamic rotor eccentricity

Fig. 5. 8. Relationship between circulating currents and time under static/dynamic rotor eccentricities.



(a) Static rotor eccentricity



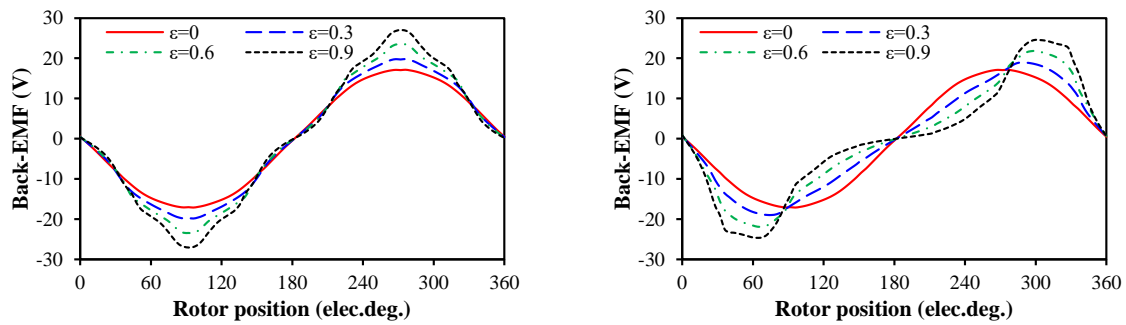
(b) Dynamic rotor eccentricity

Fig. 5. 9. Relationship between DC components and time under static/dynamic rotor eccentricities.

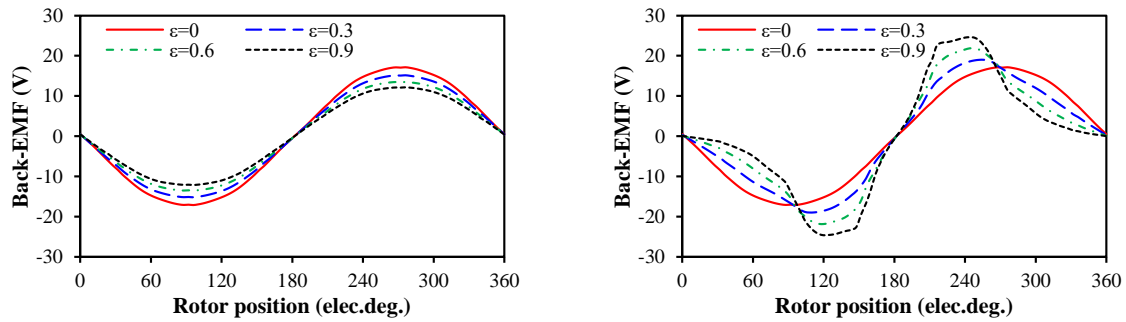
### 5.3.2 Influence of Rotor Eccentricity Ratio

The influence of rotor eccentricity ratio on back-EMF and circulating current in the 6s/2p HSPM motor with parallel-connected windings is investigated. Since the same principle of the influence of rotor eccentricity ratio on the three phase windings, only phase A is presented in this section. Figs. 5. 10 and 5. 11 show the influence of rotor eccentricity ratio on the back-EMF waveforms of coils A1 and A2, and the back-EMF difference between two coils. The results show that the increased static rotor eccentricity ratio results in an increase of magnitudes of the fundamental and the 3<sup>rd</sup> order harmonic of back-EMF in coil A1 due to it facing the shortest air-gap length and the local saturation exists. However, facing the longest air-gap length, coil A2 has a decreased magnitude of the fundamental back-EMF. Therefore, the back-

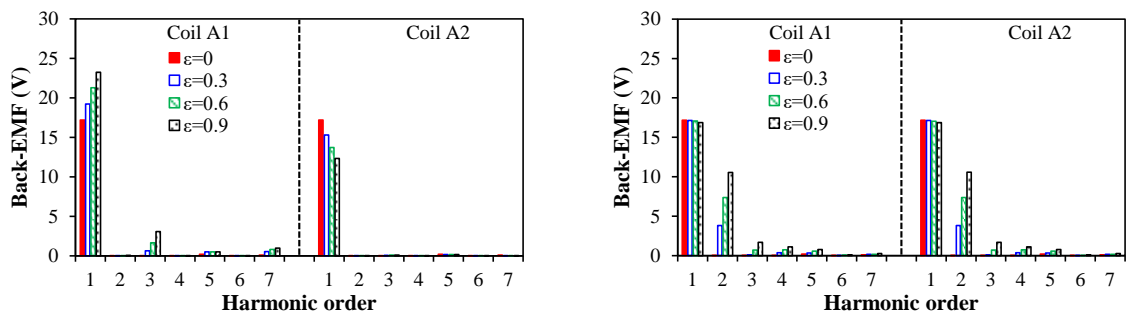
EMF difference between coils A1 and A2 increases with static rotor eccentricity ratio. With the increase of dynamic rotor eccentricity ratio, the fundamental magnitudes of the back-EMFs of coils A1 and A2 remain almost unchanged, while the magnitudes of the 2<sup>nd</sup> order back-EMF harmonic of coils A1 and A2 increase. Therefore, the back-EMF difference between coils A1 and A2 increases with dynamic rotor eccentricity ratio since the phase angles of the 2<sup>nd</sup> order back-EMF harmonics of coils A1 and A2 are opposite.



(a) Waveforms of Coil A1



(b) Waveforms of Coil A2



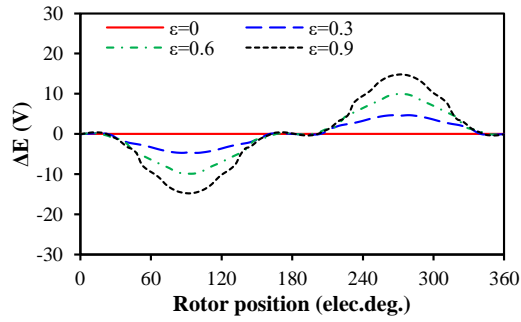
(c) Spectra

(I) Static rotor eccentricity

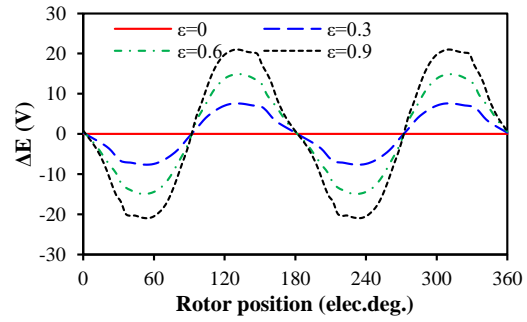
(II) Dynamic rotor eccentricity

Fig. 5. 10. Influence of rotor eccentricity ratio on the back-EMFs of coils A1 and A2.





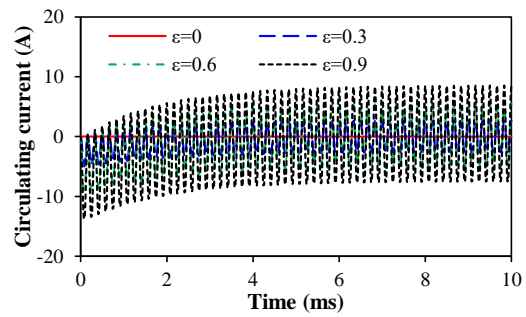
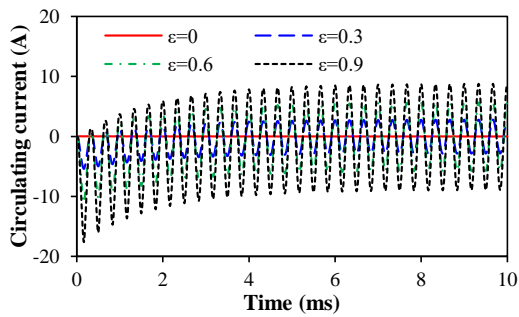
(a) Static rotor eccentricity



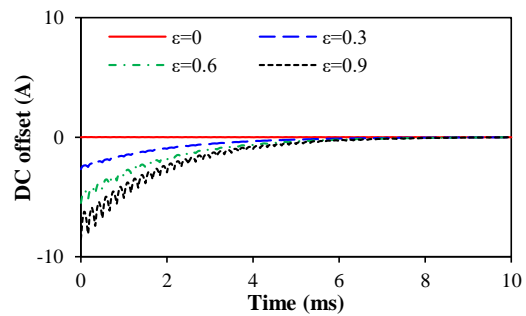
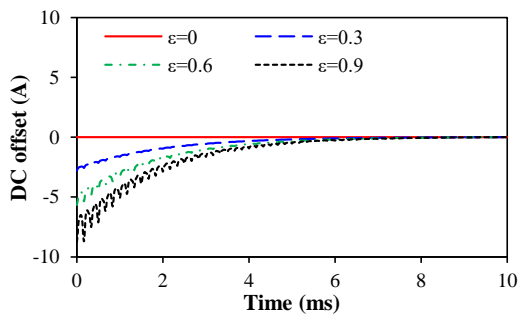
(b) Dynamic rotor eccentricity

Fig. 5. 11. Influence of rotor eccentricity ratio on the back-EMF difference between coils A1 and A2.

With the increase of rotor eccentricity ratio, the peak-to-peak values of circulating currents and DC components increase, Fig. 5 12, due to the increased back-EMF difference between coils A1 and A2, Fig. 5. 11. However, the rotor eccentricity ratio does not change the amount of time that the DC components decrease to zero, Fig. 5. 12 (b). For the first electric cycle, the circulating currents with DC components of coil A1 in the motors with different static/dynamic rotor eccentricity ratios are shown in Fig. 5. 13. For the 30<sup>th</sup> electric cycle, the circulating currents without DC components of coil A1 in the motors with different static/dynamic rotor eccentricity ratios are shown in Fig. 5. 14.



(a) Circulating currents

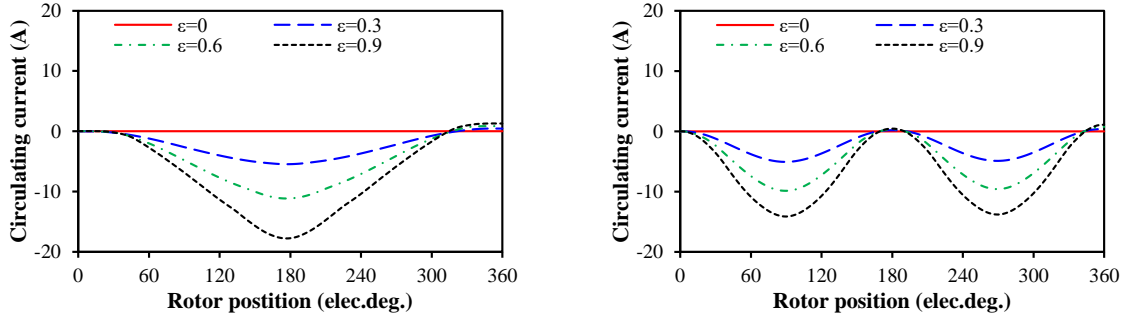


(b) DC components

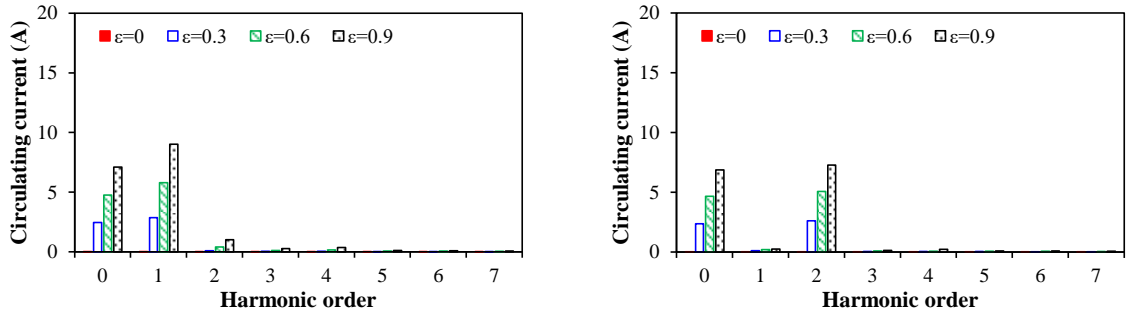
(I) Static rotor eccentricity

(II) Dynamic rotor eccentricity

Fig. 5. 12. Relationships between circulating currents and DC components of coil A1 and time under different static/dynamic rotor eccentricity ratios.



(a) Waveforms

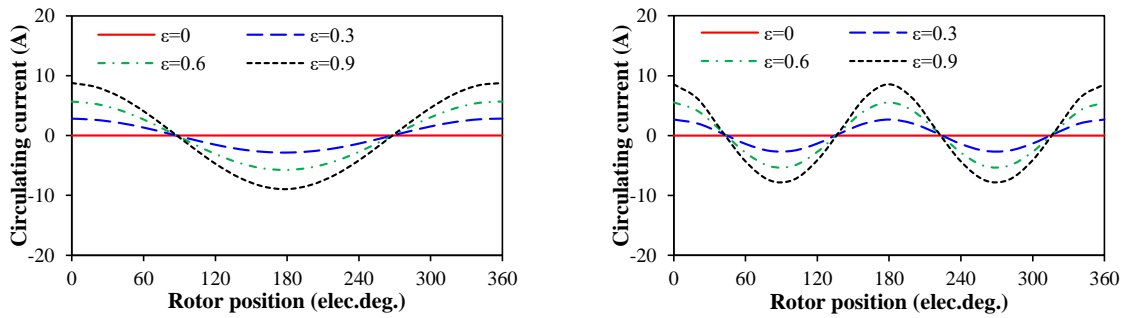


(b) Spectra

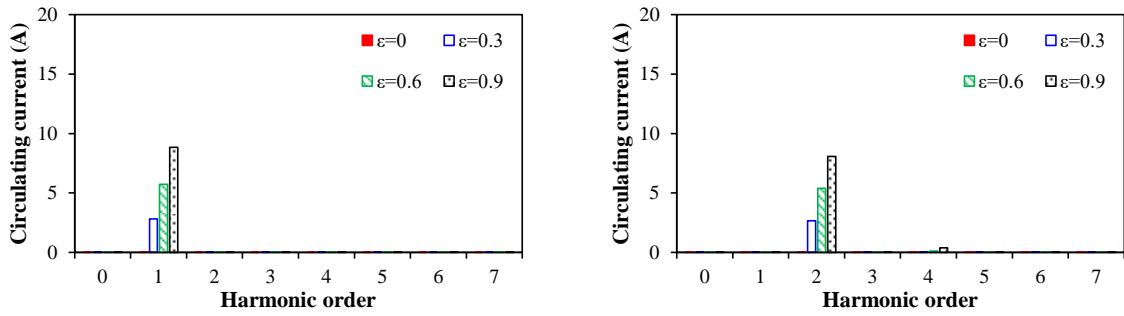
(I) Static rotor eccentricity

(II) Dynamic rotor eccentricity

Fig. 5. 13. Circulating currents with DC components of coil A1 in the motors with different static/dynamic rotor eccentricity ratios.



(a) Waveforms



(b) Spectra

(I) Static rotor eccentricity

(II) Dynamic rotor eccentricity

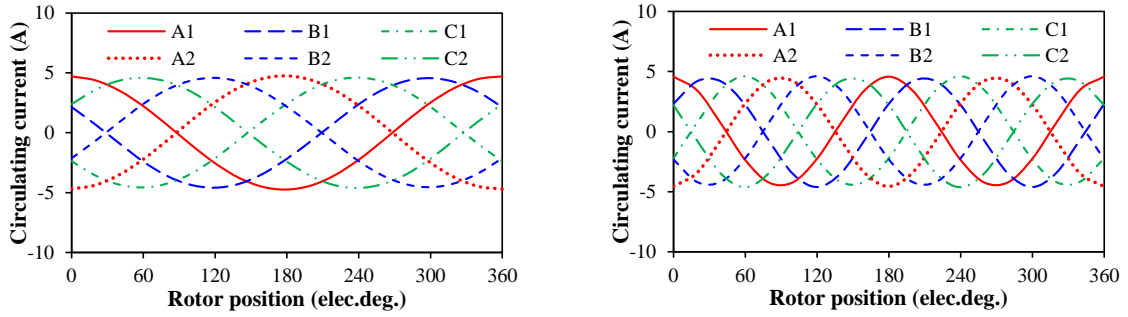
Fig. 5. 14. Circulating currents without DC components of coil A1 in the motors with different static/dynamic rotor eccentricity ratios.

#### 5.4 Steady-state Circulating Currents and Effect due to Rotor Eccentricities

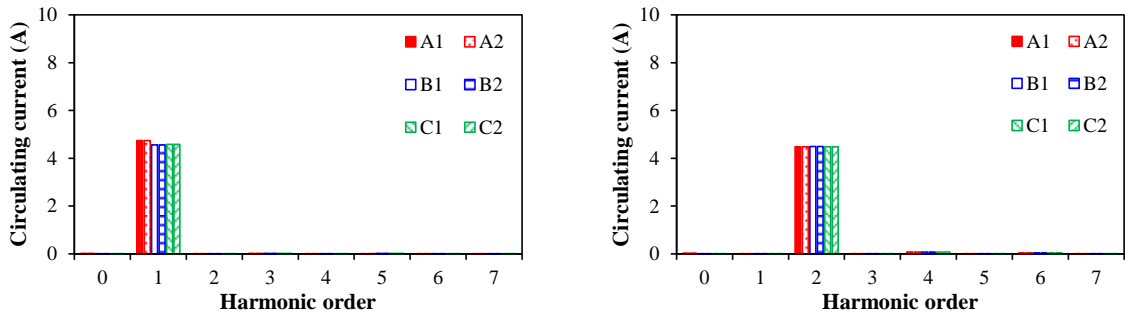
In this section, the effect of the circulating currents at steady-state operation with rotor eccentricity (in the 30th electric cycle), is investigated under open-circuit and on-load conditions.

##### 5.4.1 Open-circuit Condition

The steady-state circulating currents due to static and dynamic eccentricities result in the phase angles of circulating currents in three phases differ by 60 elec. deg., Fig. 5. 15, and the spectra show that the circulating currents due to dynamic rotor eccentricity exhibit a double frequency component compared with the circulating currents due to static rotor eccentricity, which corresponds to the back-EMFs due to static and dynamic rotor eccentricities, Fig. 5. 6. For static rotor eccentricity, the circulating currents in phase A have larger fundamental magnitudes than those in phases B and C since the rotor is offset towards phase A and the back-EMF difference between coils in phase A is the largest. For dynamic rotor eccentricity, the magnitudes of the 2<sup>nd</sup> order harmonics of the circulating currents of coils in three phase are almost the same.



(a) Waveforms



(b) Spectra

(I) Static rotor eccentricity

(II) Dynamic rotor eccentricity

Fig. 5. 15. Steady-state circulating currents caused by static/dynamic rotor eccentricities.

The induced circulating currents directly lead to the additional copper loss, Fig. 5. 16. It can be seen that the circulating currents caused by static and dynamic rotor eccentricities result in almost the same average total additional copper loss of three phase windings due to the same resistance of coils and almost the same root mean square (RMS) value of the induced circulating currents. When employing the series-connected windings, the circulating current will not be induced by rotor eccentricity and thus no additional copper loss.

The rotor eccentricity leads to an increase of stator iron loss due to the local saturation when neglecting the circulating currents, Figs. 5. 17 (a) and 5. 18. Accounting for the induced circulating currents, the motor with dynamic rotor eccentricity has the largest stator iron loss, Figs. 5. 17 (b) and 5. 18, since the circulating currents due to dynamic rotor eccentricity exhibit a double frequency component compared with the circulating currents due to static rotor eccentricity. When considering the circulating currents, the iron core losses in the motors with/without rotor eccentricity are different, Fig. 5. 19.

Under the open-circuit condition and without rotor eccentricity, the rotor magnet loss of the

6s/2p HSPM motor is small and can be neglected since only the space harmonics due to slot opening exist, e.g. the 5<sup>th</sup> and 7<sup>th</sup> order harmonics, Fig. 5. 20, but the slotting effect is relatively small due to the large air-gap. The static rotor eccentricity leads to the asymmetric air-gap distribution and significantly increases the rotor magnet loss, but the circulating currents decrease the rotor magnet loss since they decrease the magnitude of the 2<sup>nd</sup> order harmonic of air-gap flux density, Fig. 5. 21. However, the dynamic rotor eccentricity slightly increases the rotor magnet loss when neglecting the circulating currents. Accounting for circulating currents, the dynamic rotor eccentricity increases the rotor magnet loss due to the time harmonics of the circulating currents and spatial MMF harmonics.

The 6s/2p HSPM motor with symmetrical stator topology has no inherent UMF. However, the rotor eccentricity can result in the UMF due to the non-uniform air-gap distribution. When neglecting circulating currents, the UMFs caused by static/dynamic rotor eccentricities have almost the same average value, Fig. 5. 22. When considering circulating currents, the average UMFs of the motors with static/dynamic rotor eccentricities are reduced by approximately 36.3%.

Fig. 5. 23 shows the influence of rotor eccentricity on the cogging torque with/without considering circulating currents. Neglecting circulating currents, the amplitudes and harmonics contents of cogging torque increase with rotor eccentricity. The static rotor eccentricity leads to the multiples of  $(2p)$ th order harmonics of cogging torque, i.e. 2<sup>nd</sup>, 4<sup>th</sup>, 6<sup>th</sup>... and the dynamic rotor eccentricity leads to multiples of  $(N_s)$ th order harmonics of cogging torque, i.e. 6<sup>th</sup>, Fig. 5. 23 (I), where  $p$  is the number of pole pair and  $N_s$  is the number of slot. The induced circulating currents due to static/dynamic rotor eccentricities decrease the cogging torques, Fig. 5. 23 (II).

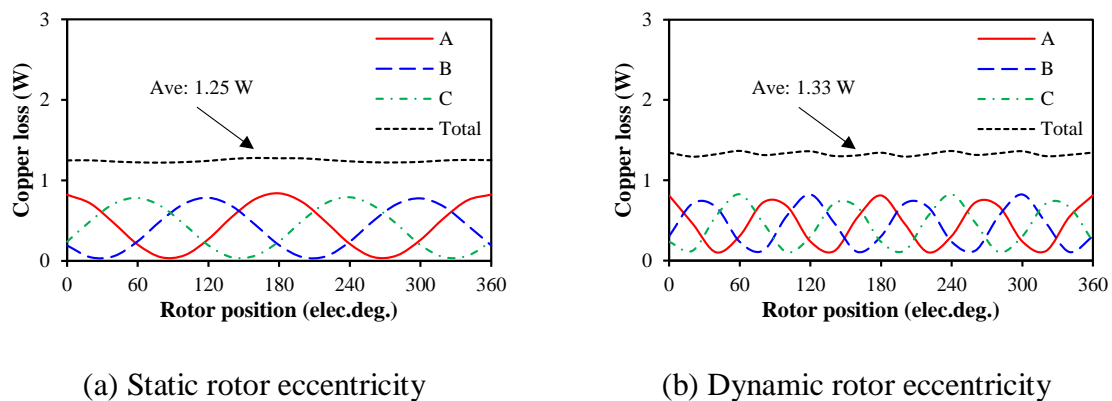
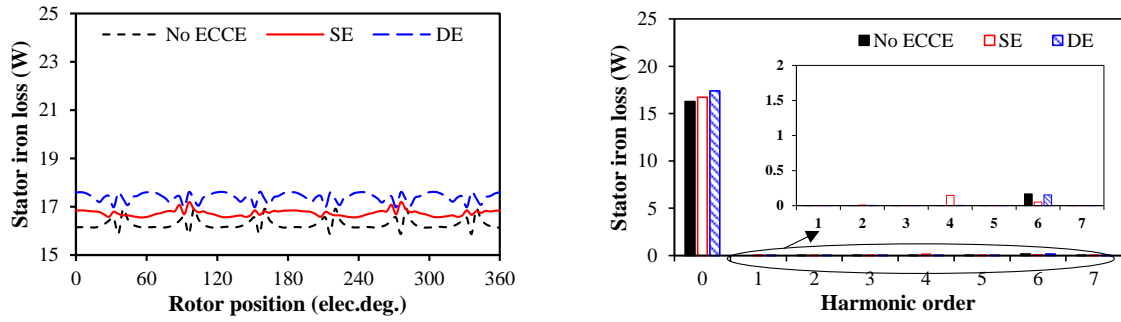
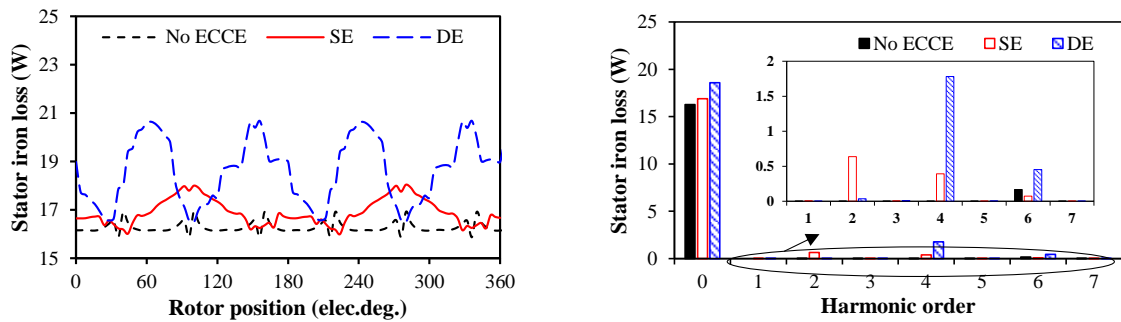


Fig. 5. 16. Open-circuit copper losses caused by circulating currents in three phase windings.



(a) Neglecting circulating currents



(b) Considering circulating currents

(I) Waveforms

(II) Spectra

Fig. 5. 17. Open-circuit stator iron loss of the motors with/without rotor eccentricity and neglecting/considering circulating currents.

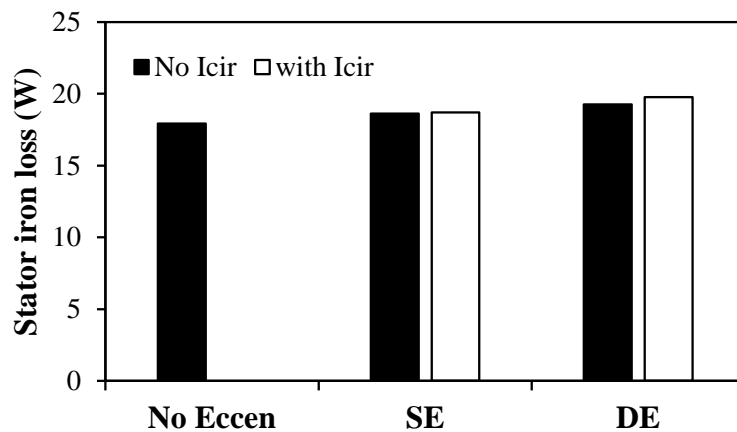
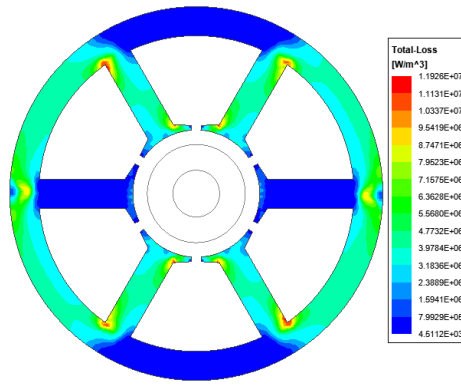
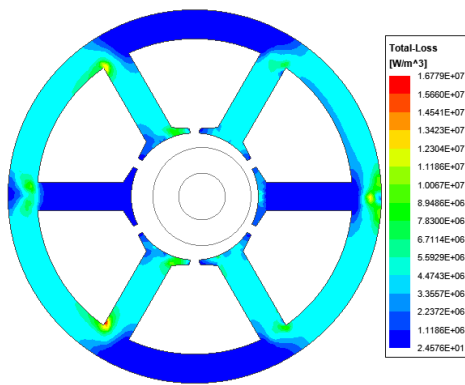


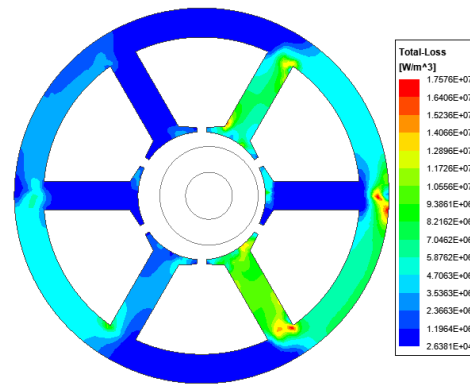
Fig. 5. 18. Open-circuit stator iron loss of the motors with/without rotor eccentricity and neglecting/considering circulating currents.



(a) Without rotor eccentricity,  $\text{Max}=1.1926 \times 10^7 \text{ W/m}^3$



(b) Static rotor eccentricity,  
 $\text{Max}=1.6779 \times 10^7 \text{ W/m}^3$



(c) Dynamic rotor eccentricity,  
 $\text{Max}=1.7576 \times 10^7 \text{ W/m}^3$

Fig. 5. 19. Stator iron loss distributions with/without rotor eccentricity.

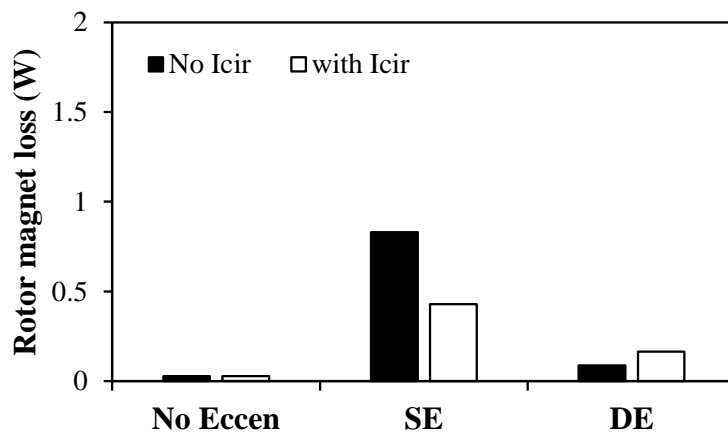
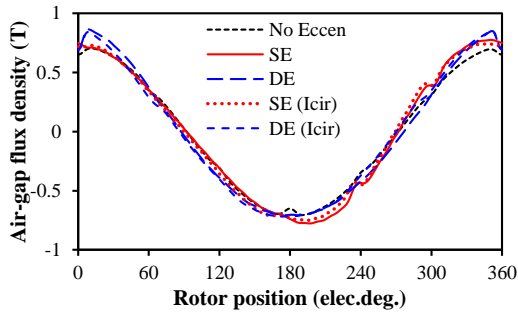
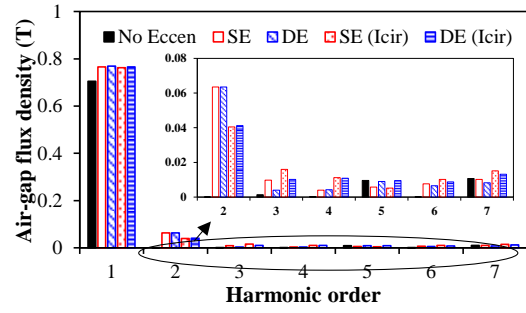


Fig. 5. 20. Rotor magnet losses of the motors with/without rotor eccentricity and neglecting/considering circulating currents.

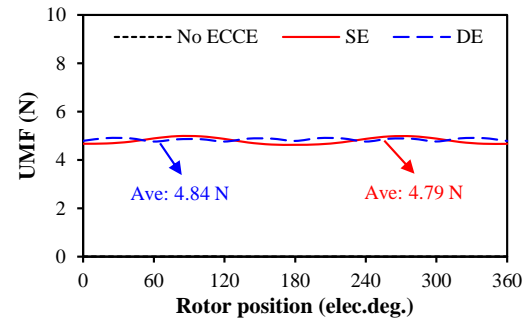
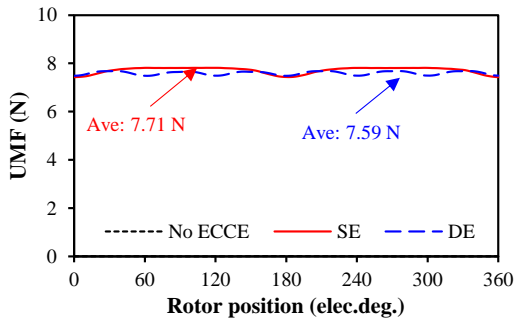


(a) Waveforms

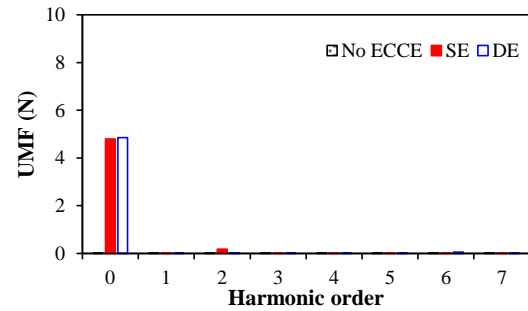
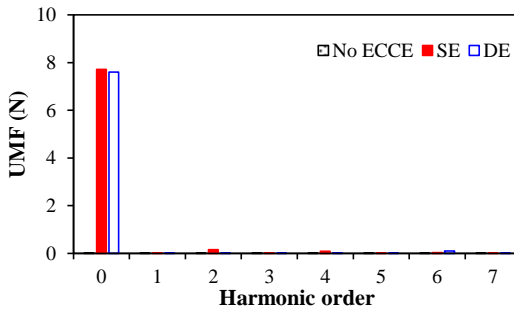


(b) Spectra

Fig. 5. 21. Air-gap field distributions of the motors with/without static/dynamic rotor eccentricities on the radial position ( $r = R_m + 0.3875$  mm) and rotor position ( $\theta = 90^\circ$ ), without/with circulating current,  $\varepsilon = 0.5$ .



(a) Waveforms



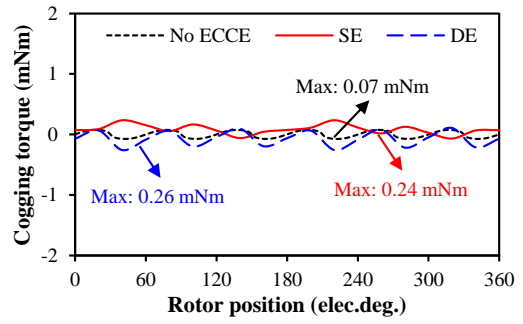
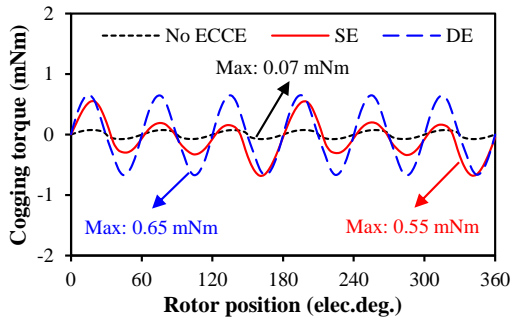
(b) Spectra

(I) Neglecting circulating current

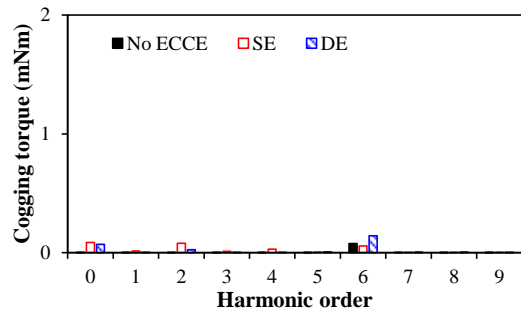
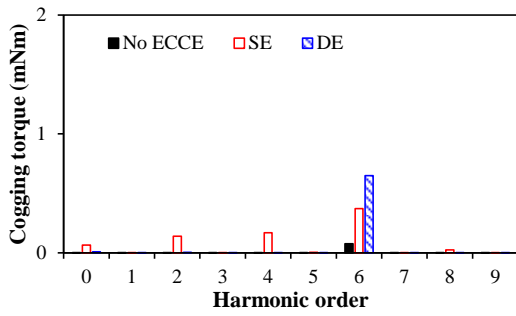
(II) Considering circulating current

Fig. 5. 22. UMF waveforms of the motors without and with static/dynamic eccentricities under open-circuit condition.





(a) Waveforms



(b) Spectra

(I) Neglecting circulating current

(II) Considering circulating current

Fig. 5. 23. Cogging torque waveforms of the motors without and with static/dynamic eccentricities under open-circuit condition.

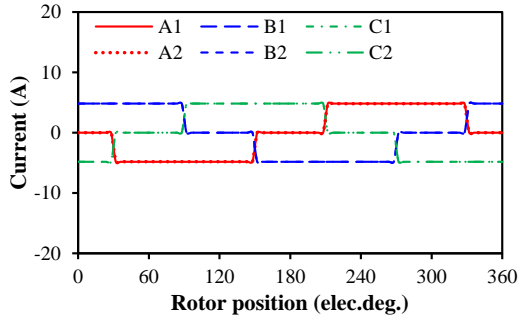
#### 5.4.2 On-load Condition

With three phase 120° electric square wave current waveforms and the rated phase current, i.e.  $I_{max}=10A$ , Fig. 5. 24, the influence of the circulating current due to rotor eccentricity on the electromagnetic performance is investigated in this section.

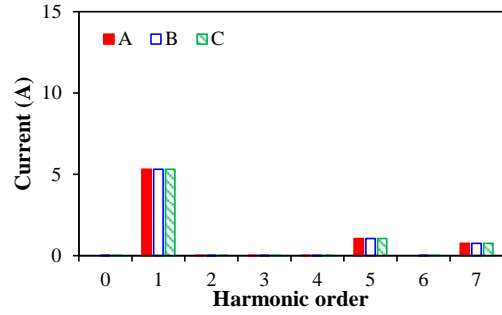
Figs. 5. 25 and 5. 26 show how the circulating currents due to static and dynamic rotor eccentricities affect the ideal square wave current of the coils in different phase windings. The steady-state circulating currents result in the different currents of two coils in the same phase since the circulating currents in two coils are opposite. It can be seen that the circulating currents due to static rotor eccentricity only increase the fundamental magnitudes of 120° electric square wave phase currents for all three phases. However, the circulating currents due to dynamic rotor eccentricity only affect the harmonic contents of three phase 120° electric square wave currents, i.e. additional 2<sup>nd</sup> order harmonic.

With the induced circulating currents due to static and dynamic rotor eccentricities, the average total copper loss increases from 2.07W to 3.30/3.40W, approximately 64.3%, Fig. 5. 27. Under on-load condition, considering circulating currents, the motor with dynamic rotor eccentricity has the largest stator iron loss since the largest armature reaction caused by the 2<sup>nd</sup> order harmonics of the circulating currents due to dynamic rotor eccentricity, Fig. 5. 28. The on-load circulating currents due to static rotor eccentricity decrease the rotor magnet loss caused by static rotor eccentricity, while the circulating currents due to dynamic rotor eccentricity slightly increase the rotor magnet loss, Fig. 5. 29.

Figs. 5. 22 and 5. 30 show that no matter neglecting or considering the circulating currents, under open-circuit or on-load conditions, the motors with static/dynamic rotor eccentricities have almost the same average UMFs. The induced circulating currents due to static/dynamic rotor eccentricities decrease the on-load average UMFs from 7.70 /7.60 N to 4.80/4.77 N, respectively. The on-load circulating currents due to static and dynamic rotor eccentricities have negligible influence on the average torque and torque ripple, Fig. 5. 31.

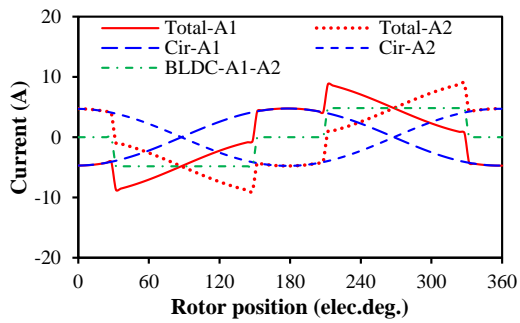


(a) Waveforms

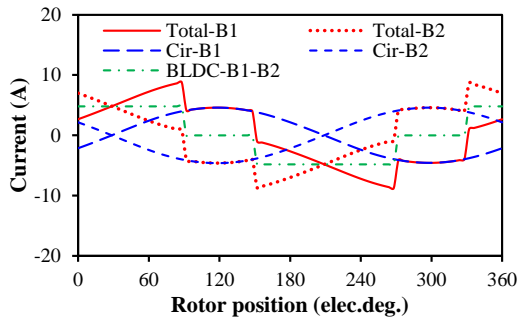
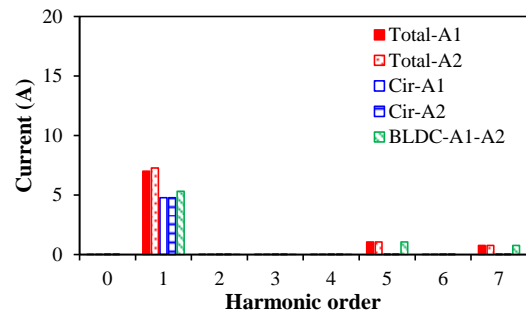


(b) Spectra

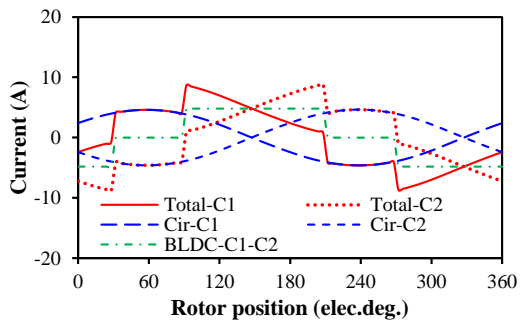
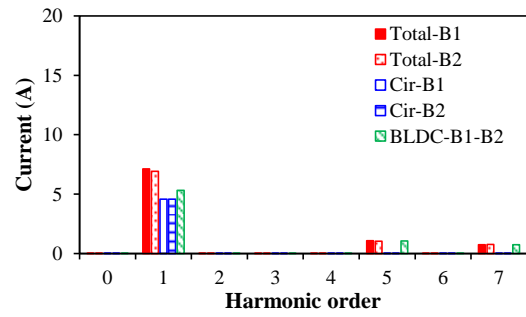
Fig. 5. 24. Current waveforms of motors without rotor eccentricity.



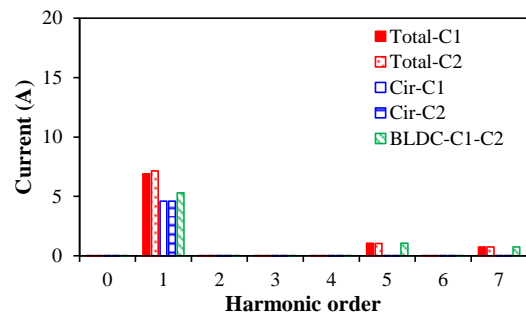
(a) Coils A1 and A2

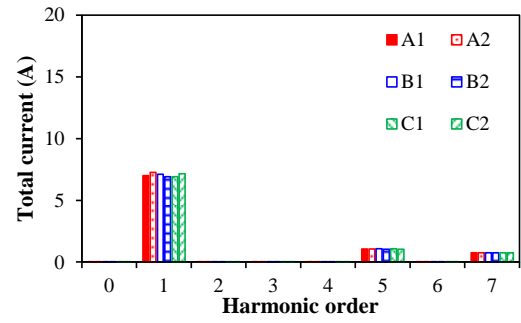
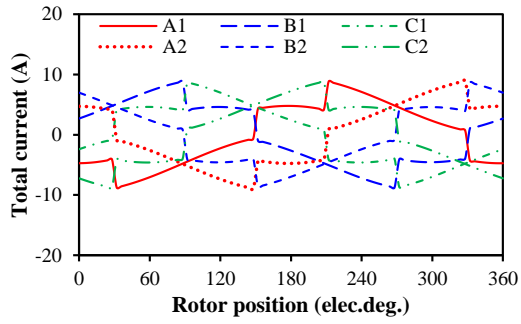


(b) Coils B1 and B2



(c) Coils C1 and C2



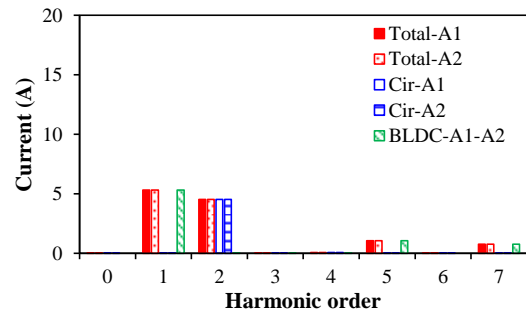
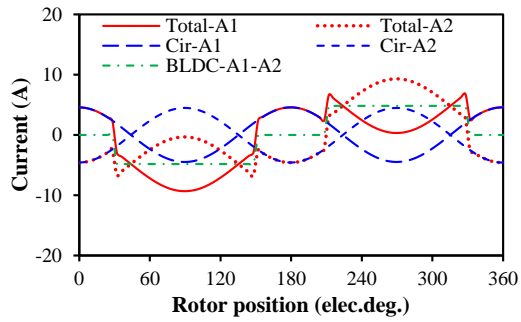


(d) Coils of three phase windings

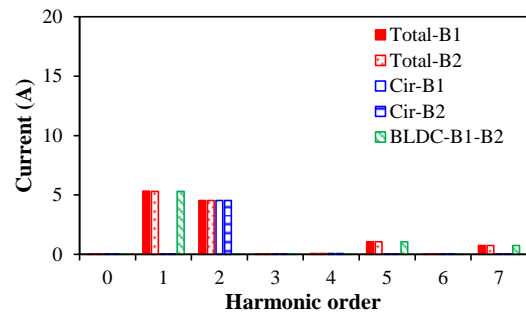
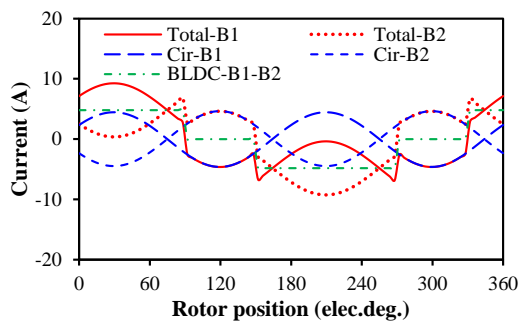
(I) Waveforms

(II) Spectra

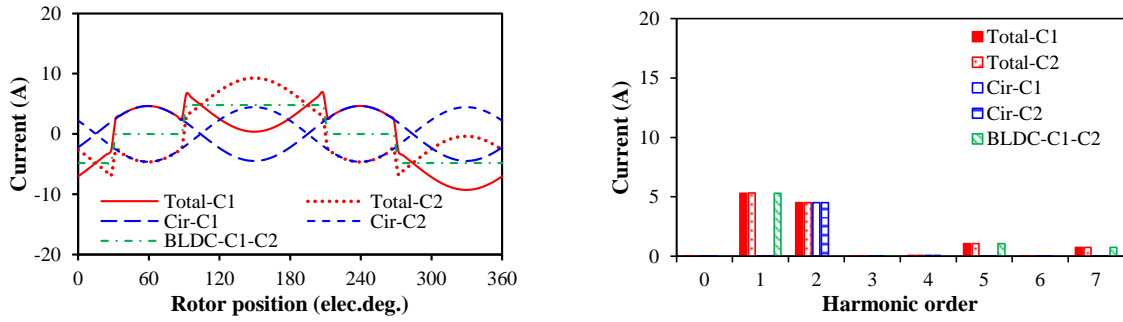
Fig. 5. 25. Currents waveforms of motors with static rotor eccentricity considering circulating current.



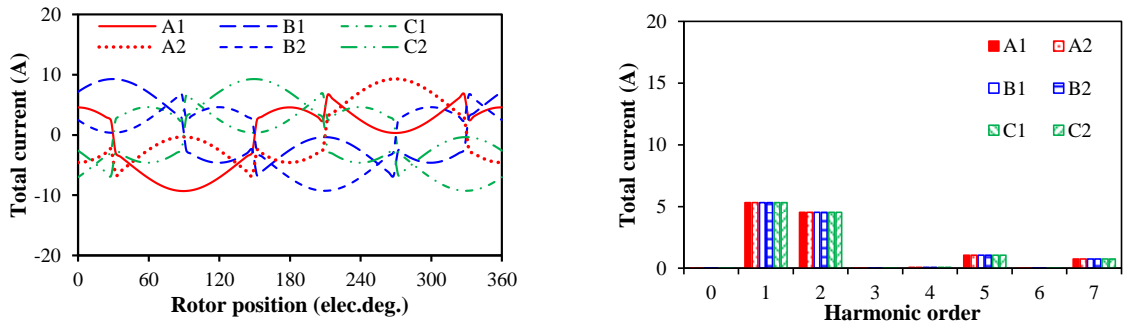
(a) Coils A1 and A2



(b) Coils B1 and B2



(c) Coils C1 and C2

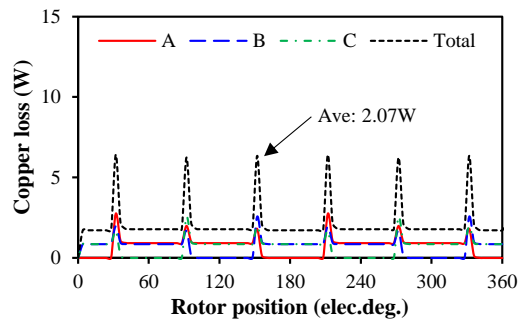


(d) Coils of three phase windings

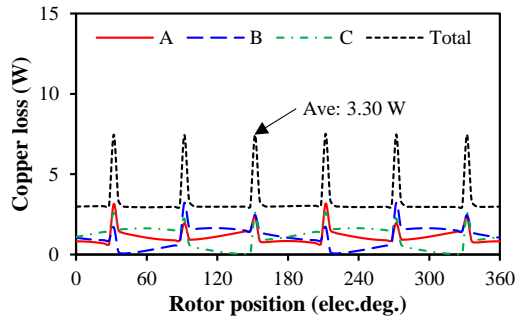
(I) Waveforms

(II) Spectra

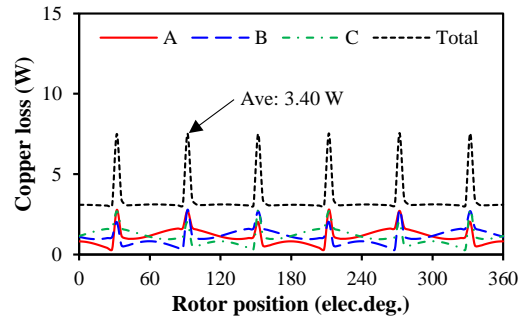
Fig. 5. 26. Currents waveforms of motors with dynamic rotor eccentricity considering circulating current.



(a) Without rotor eccentricity

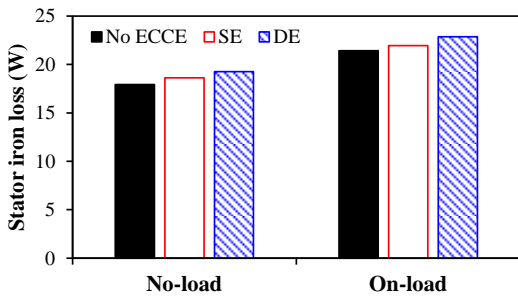


(b) Static rotor eccentricity

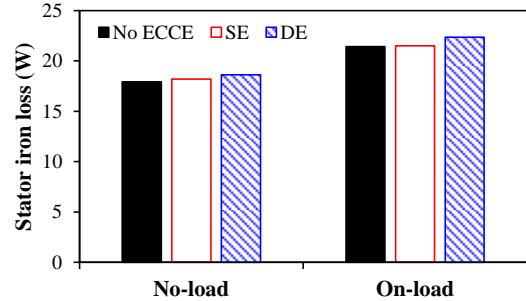


(c) Dynamic rotor eccentricity

Fig. 5. 27. Copper loss waveforms of the motors without and with static/dynamic rotor eccentricities considering circulating current.

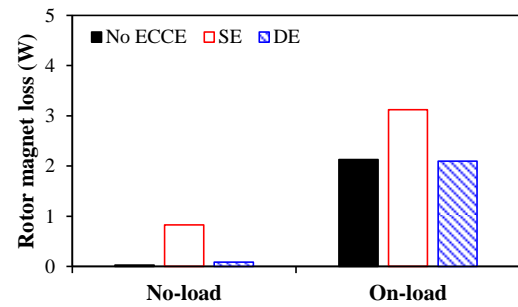


(a) Neglecting circulating current

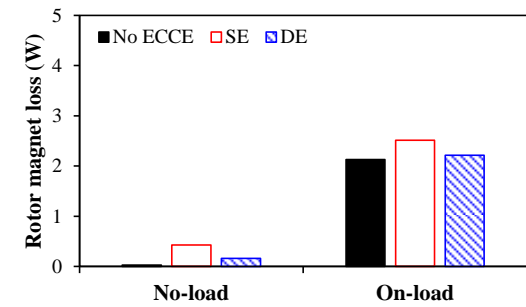


(b) Considering circulating current

Fig. 5. 28. Stator iron losses of the motors without/with rotor eccentricity and neglecting/considering circulating currents.

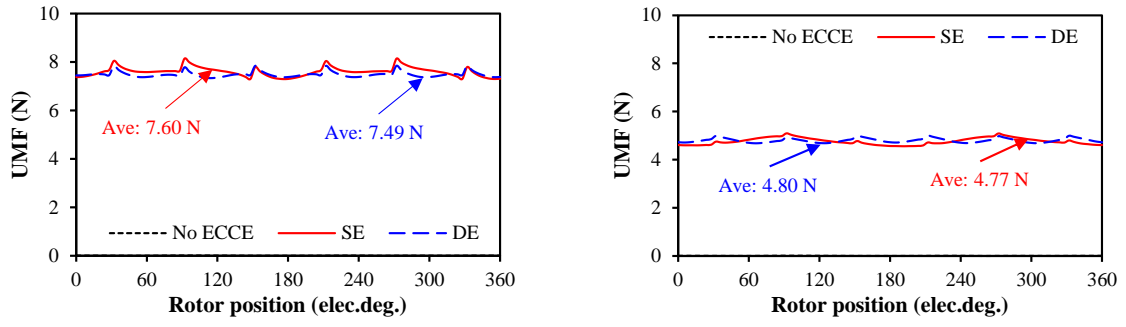


(a) Neglecting circulating current

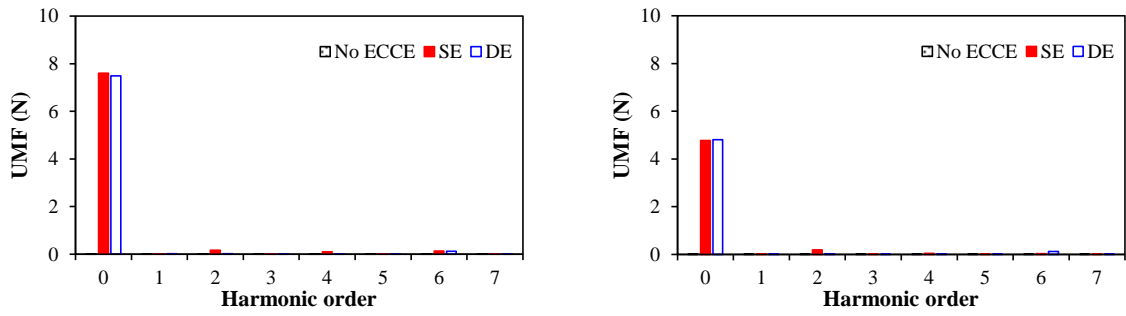


(b) Considering circulating current

Fig. 5. 29. Rotor magnet losses of the motors without/with rotor eccentricity and neglecting/considering circulating currents in three phase windings.



(a) Waveforms

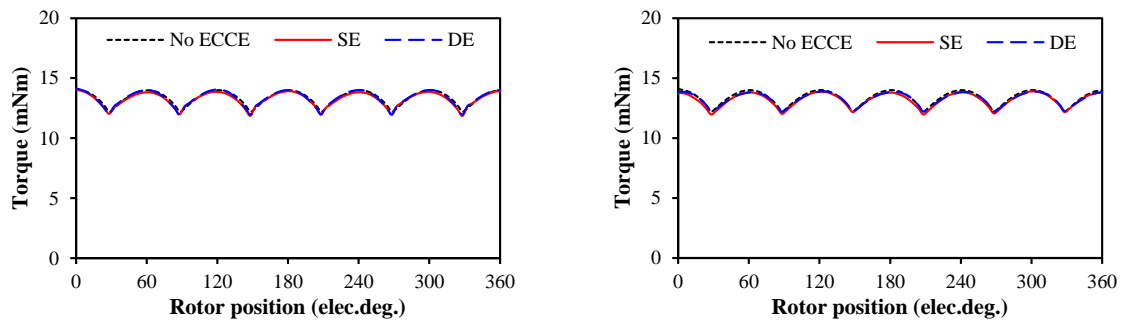


(b) Spectra

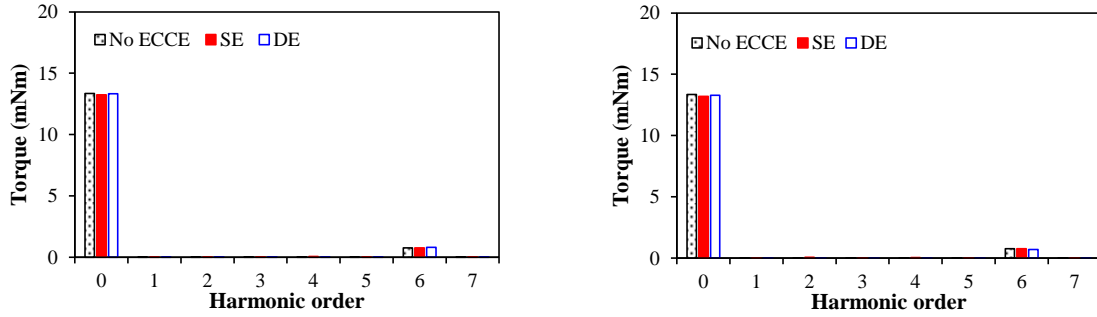
(I) Neglecting circulating current

(II) Considering circulating current

Fig. 5. 30. UMF waveforms of the motors with static/dynamic eccentricities under on-load condition.



(a) Waveforms



(b) Spectra

(I) Neglecting circulating current

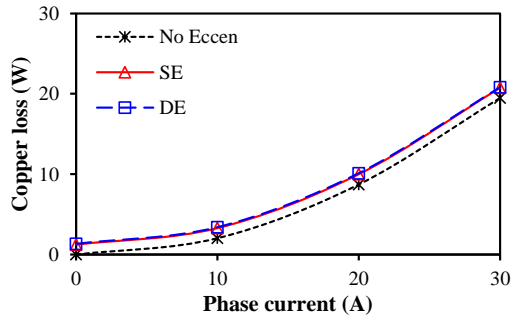
(II) Considering circulating current

Fig. 5. 31. Torque waveforms of the motors with static/dynamic eccentricities under the on-load condition.

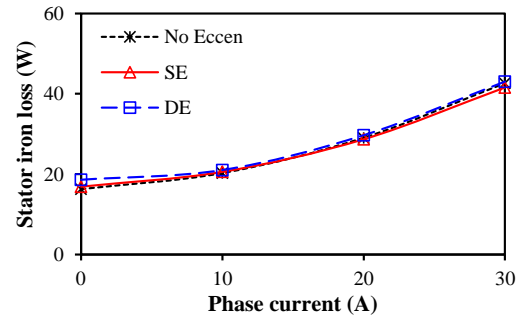
The rotor eccentricity leads to the circulating currents, which directly increase the copper loss with an approximate constant, Fig. 5. 32 (a). However, the rotor eccentricity has a small influence on the stator iron loss, Fig. 5. 32 (b). When considering circulating currents and the phase current is small, static and dynamic rotor eccentricities lead to the increases of rotor magnet losses by 18.1% and 4.0%, respectively, compared with no rotor eccentricity, Figs. 5. 29 (b) and 5. 32 (c). It is worth noting that the influence of circulating current on copper loss and rotor PM loss decreases with the increase of phase current.

The relationship between average UMF and phase current without/with static/dynamic rotor eccentricities and neglecting/considering circulating currents is presented in Fig. 5. 33. When considering the circulating current, the average UMFs of the motors with static/dynamic rotor eccentricities are decreased. In addition, the influence of the induced circulating current remains almost unchanged with the increase of phase current. As mentioned before, the circulating currents have no influence on the average torque and torque ripple. Therefore, the average torque and torque ripple increase linearly with the phase current, Fig. 5. 34, since the torque ripple is dominated by the product of rectangular current waveforms and sinusoidal back-EMF waveforms.

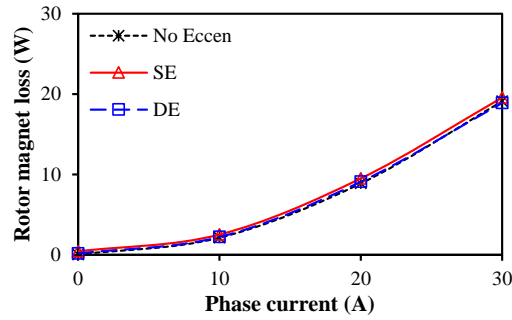




(a) Copper loss



(a) Stator iron loss



(c) Rotor PM loss

Fig. 5. 32. Influence of static/dynamic rotor eccentricities on various loss components under different phase currents, considering circulating current.

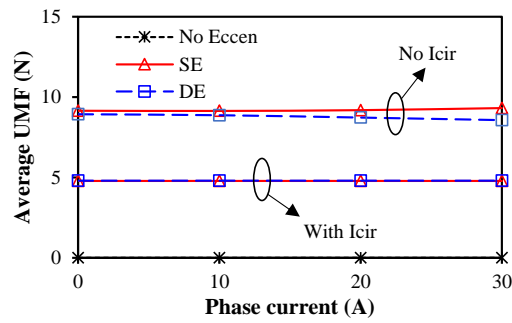


Fig. 5. 33. Relationship between average UMF and phase current with static/dynamic rotor eccentricities and neglecting/considering circulating current.

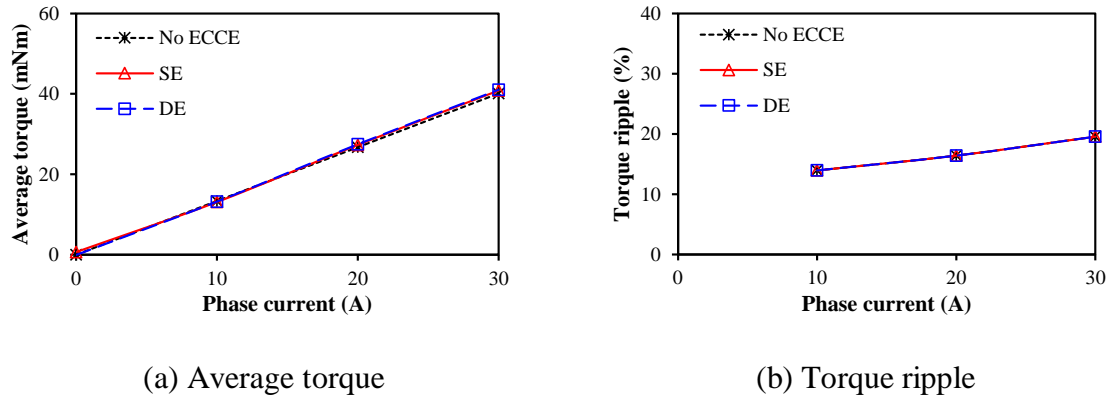


Fig. 5.34. Relationships between average torque, torque ripple, and phase current with static/dynamic rotor eccentricities considering circulating current.

## 5.5 Conclusion

In this chapter, the influence of circulating currents in the parallel-connected windings due to static and dynamic rotor eccentricities on the electromagnetic performance of the 6s/2p PM motor has been investigated by FE method, accounting for DC components in the circulating current, open-circuit/on-load conditions, and rotor eccentricity ratio. It is shown that the increased rotor eccentricity ratio leads to the increase of circulating currents which, in turn, increase the copper loss, rotor magnet loss, and stator iron loss, but reduce the cogging torque and UMF. However, as shown in the appendix, the DC components in the circulating currents at the initial transient state significantly increase the copper loss, rotor magnet loss, stator iron loss, cogging torque, and torque ripple, but reduce the UMF.

## Appendix 5. A

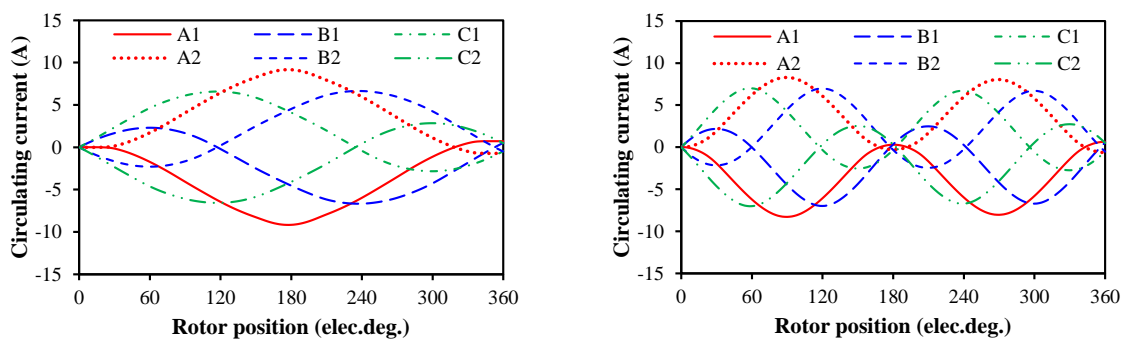
### Characteristics with Initial State of Rotor Static/Dynamic Eccentricities

As shown in section III, there exist DC components in the circulating currents at the beginning when the rotor eccentricities occur. Therefore, the circulating currents with DC components is further analyzed in this section. The circulating currents in the first electric cycle under transient state due to rotor eccentricity (designated as the circulating currents in this section for simplicity) are selected in the investigation.

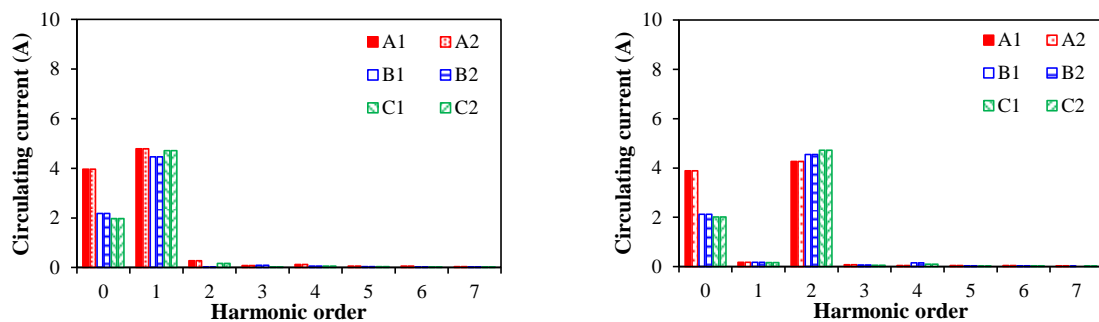
#### A. Open-circuit condition

Fig. 5. 35 shows the induced circulating currents due to static/dynamic rotor eccentricities in the first electric cycle. No matter what rotor eccentricity type, coils in phase A have the largest

peak values of the circulating currents, and coils in phases B and C have almost the same peak values. The main reason is that coil A1 facing the shortest air-gap length has the largest back-EMF, but coil A2 facing the longest air-gap length has the smallest back-EMF, which leads to the largest peak value of the back-EMF difference between two coils, Fig. 5. 7. In Fig. 5. 35, the spectra show that the largest back-EMF difference between coils A1 and A2 mainly increases the DC component in the circulating currents. Since there is no phase angle difference between two coils in phase A, the back-EMF difference of two coils in phase A equal to zero when the rotor is at the initial position, which is the rotor position when the back-EMF of phase A is zero, Fig. 5. 36.



(a) Waveforms

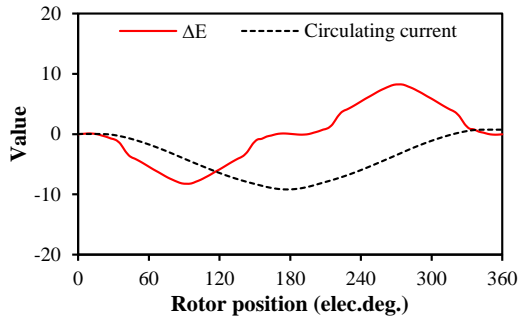


(b) Spectra

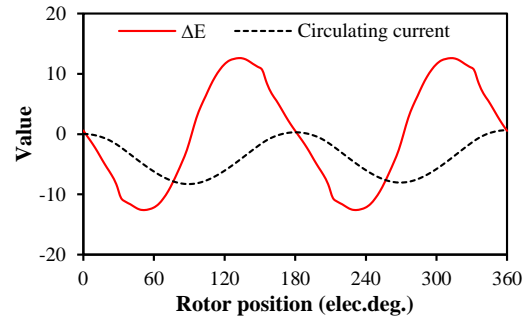
(I) Static rotor eccentricity

(II) Dynamic rotor eccentricity

Fig. 5. 35. Circulating currents of coils A1, B1, and C1 in the motors with static/dynamic rotor eccentricities,  $\varepsilon=0.5$ .



(a) Static rotor eccentricity



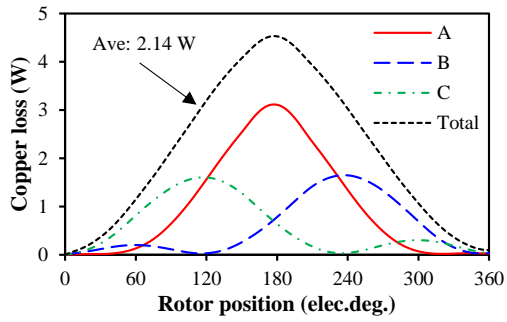
(b) Dynamic rotor eccentricity

Fig. 5. 36. Relationship between circulating current in coil A1 and the back-EMF difference between two coils in phase A,  $\varepsilon=0.5$ .

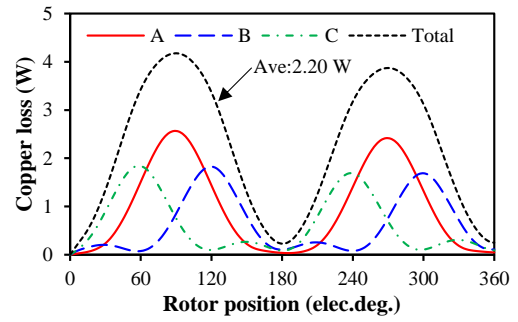
The induced circulating currents caused by static and dynamic rotor eccentricities result in the additional copper loss, i.e. 2.14W and 2.20W, respectively, Fig. 5. 37, which are almost twice of those caused by the steady-state circulating current in section IV due to DC components in the circulating currents. Figs. 5. 38 and 5. 39 show the influence of circulating currents at the initial transient state on the stator iron loss and rotor magnet loss. It indicates that the circulating currents due to dynamic rotor eccentricity slightly increase the stator iron loss due to armature reaction, and significantly increase the rotor magnet loss due to time harmonics of the circulating currents with DC components and spatial MMF harmonics.

As mentioned before, static/dynamic rotor eccentricities can cause UMFs due to non-uniform air-gap distribution. When neglecting circulating currents, the UMFs caused by static/dynamic rotor eccentricities are shown in Fig. 5. 40 (a), and they have almost the same average value. When considering circulating currents, the average UMFs of the motors with static/dynamic rotor eccentricities are reduced by approximately 33.3%. It also shows that with DC components, the minimum UMFs caused by static/dynamic rotor eccentricities are 1.93/2.43N, due to the 1<sup>st</sup> and 2<sup>nd</sup> order harmonics, respectively.

Fig. 5. 41 shows the influence of rotor eccentricity on the cogging torque with/without considering circulating currents. Neglecting circulating currents, the cogging torque increases with rotor eccentricity and but is still very small, Fig. 5. 41 (a). The induced circulating currents with DC components significantly increase the cogging torque due to the conventional cogging torque and the torque produced by the circulating current. Accounting for the circulating currents, the cogging torque caused by dynamic rotor eccentricity is larger than that caused by static rotor eccentricity.



(a) Static rotor eccentricity



(b) Dynamic rotor eccentricity

Fig. 5. 37. Additional open-circuit copper loss caused by circulating currents in three phase windings.

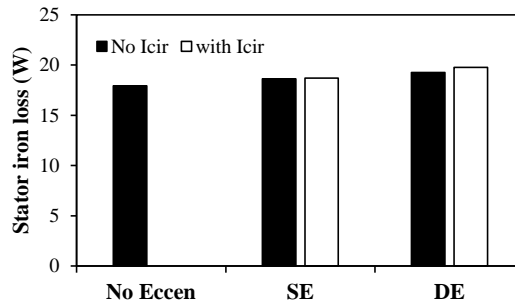


Fig. 5. 38. Open-circuit stator iron loss of the motors with/without rotor eccentricity and neglecting/considering circulating currents.

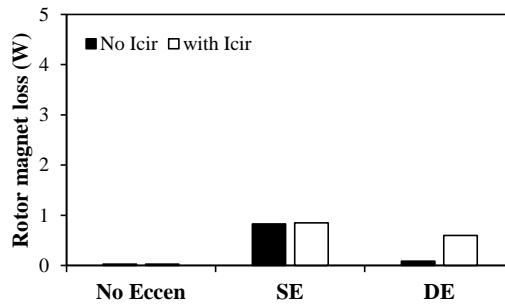
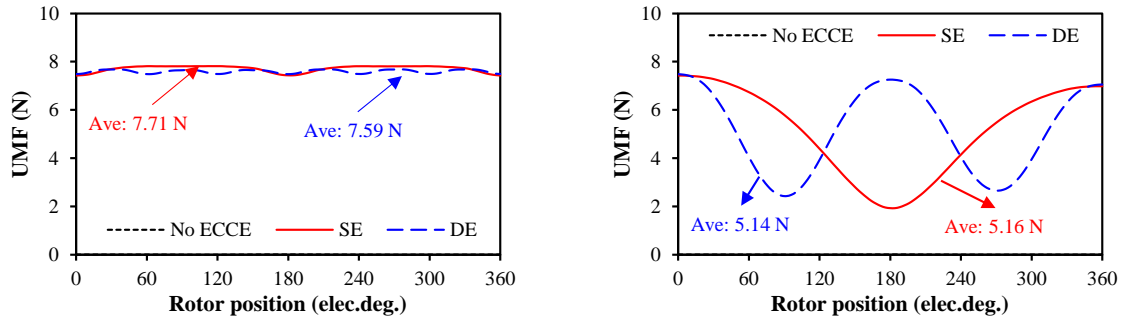
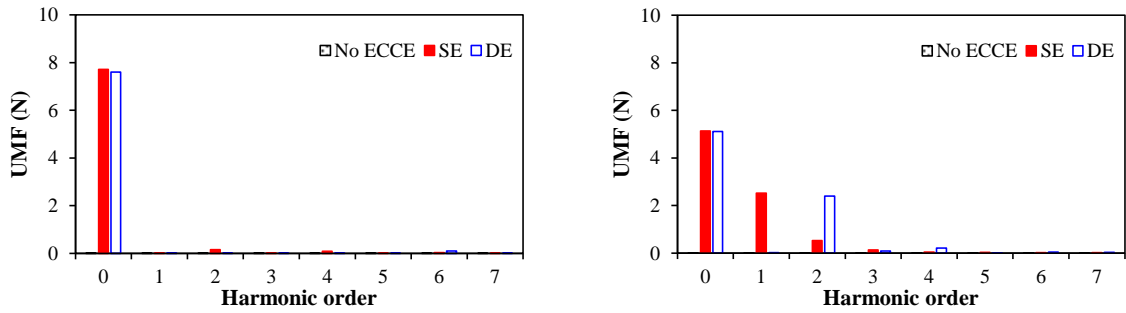


Fig. 5. 39. Open-circuit rotor magnet losses of the motors with/without rotor eccentricity and neglecting/considering circulating currents.



(a) Waveforms

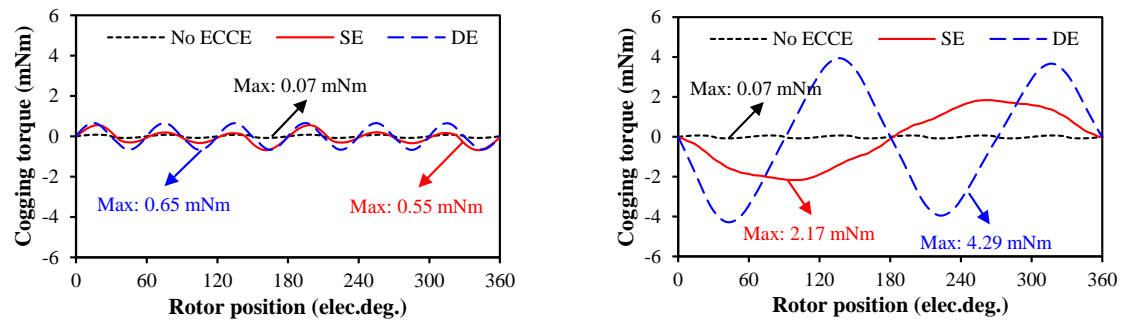


(b) Spectra

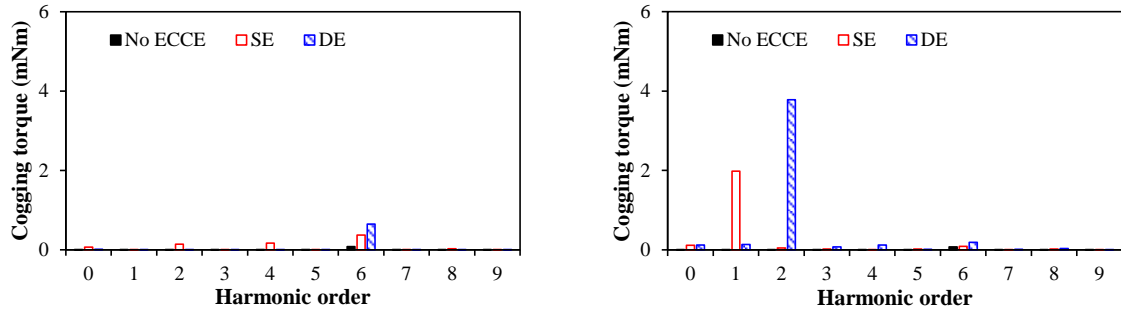
(I) Neglecting circulating current

(II) Considering circulating current

Fig. 5. 40. UMF waveforms of the motors without and with static/dynamic eccentricities under open-circuit condition.



(a) Waveforms



(b) Spectra

(I) Neglecting circulating current

(II) Considering circulating current

Fig. 5. 41. Cogging torque waveforms of the motors without and with static/dynamic eccentricities under open-circuit condition.

### B. On-load condition

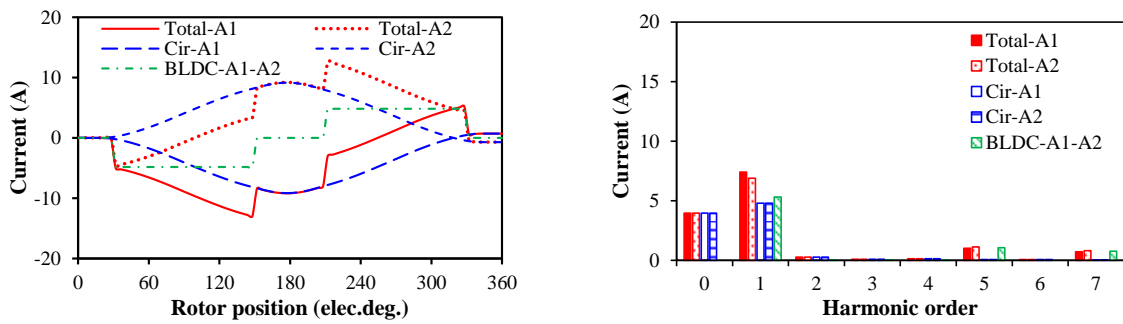
With three phase 120° electric square wave current waveforms and the rated phase current, i.e.  $I_{max}=10A$ , Fig. 5. 24, the influence of the circulating current with DC component due to rotor eccentricity on the electromagnetic performance is investigated in this section.

Figs. 5. 42 and 5. 43 show that with static rotor eccentricity, coils A1 and A2 have the same harmonic content, but the fundamental magnitude of coil A1 is slightly larger than that of coil A2 due to the local saturation in the stator tooth facing coil A1. However, in phase B or C, two coils have the same harmonic content but significantly different fundamental magnitudes, which leads to different peak values of the currents in the two coils. The DC component in phase A is larger than those in phases B and C. With dynamic rotor eccentricity, two coils in the same phase have the same magnitude of the 2<sup>nd</sup> order harmonic and have a slight difference of the fundamental magnitude.

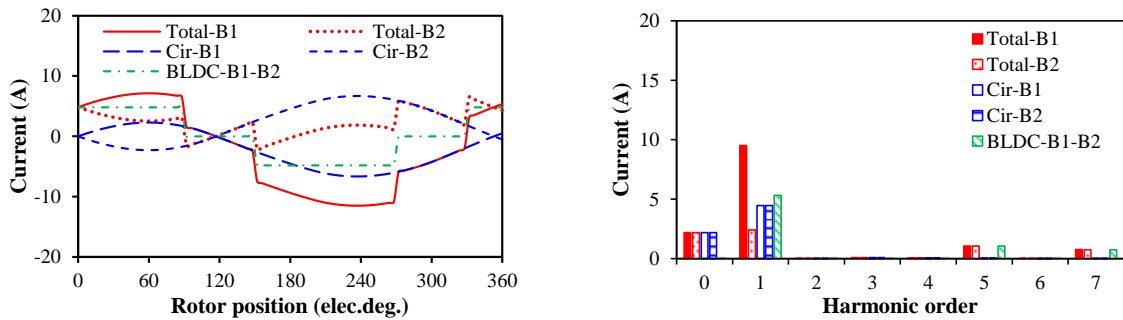
With the induced circulating currents due to static and dynamic rotor eccentricities, the average total copper loss increases from 2.07W to 4.17/4.38W, more than 100%, Fig. 5. 44. No matter on-load or no-load condition, neglecting or considering circulating currents, the motor with dynamic rotor eccentricity has the largest stator iron loss. According to the same reason under the open-circuit condition, the circulating currents due to dynamic rotor eccentricity significantly increase the rotor magnet loss under on-load condition, Fig. 5. 46 (b).

Fig. 5. 47 shows that the induced circulating currents with DC components decrease the on-load average UMFs from 7.60 /7.49 N to 5.14/5.10 N, respectively. Under the on-load

condition, the static and dynamic rotor eccentricities have negligible influence on the average torque but slightly increase the torque ripple due to the increased cogging torque, Fig. 5. 48 (I) and Table II. Accounting for the circulating currents, the rotor eccentricity does not change the average torque but significantly increases the torque ripple, especially for dynamic rotor eccentricity, Fig. 5. 48 (II) and Table II. The spectra show that the induced circulating currents due to static and dynamic rotor eccentricities exhibit the 1<sup>st</sup> and 2<sup>nd</sup> order harmonics, respectively, which result in high torque ripple. However, the influence of circulating currents decreases with the increase of phase current, Fig. 5. 49. With the large phase current, the torque ripple of the motor without rotor eccentricity is dominated by the product of rectangular current waveforms and sinusoidal back-EMF waveforms. Therefore, the rotor eccentricity has negligible influence on the torque ripple when the phase current is large.

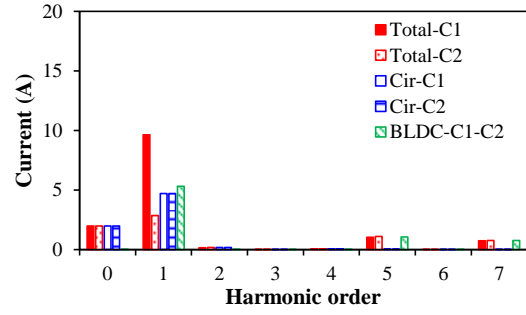
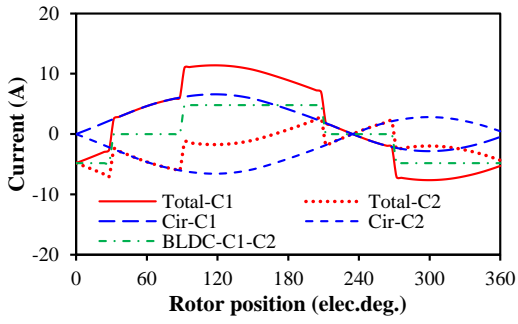


(a) Coils A1 and A2

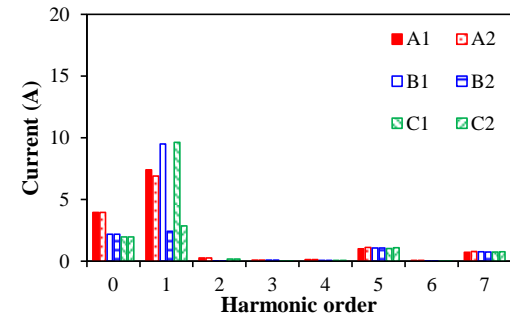
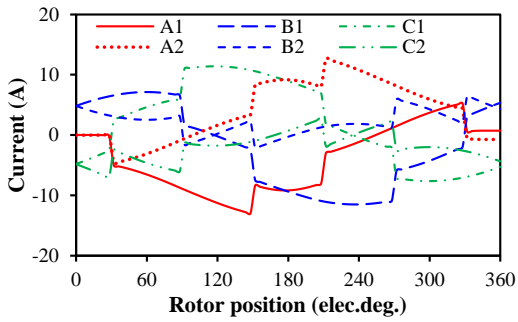


(b) Coils B1 and B2





(c) Coils C1 and C2

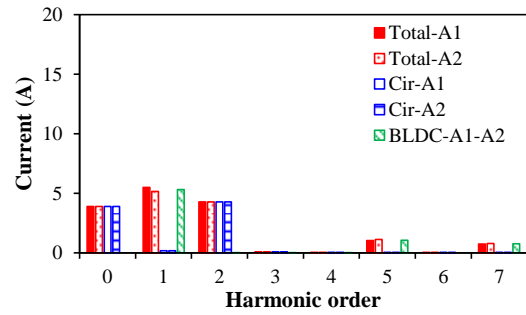
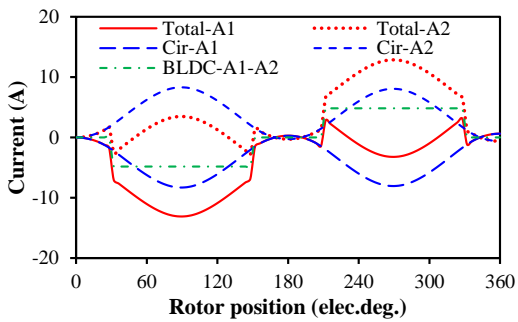


(d) Coils of three phase windings

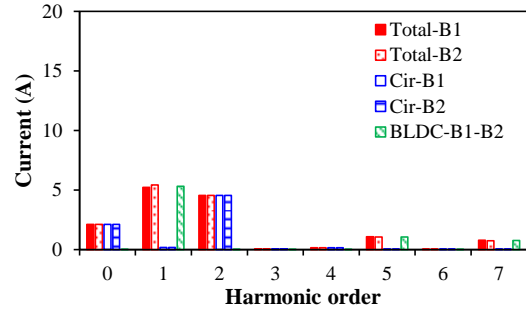
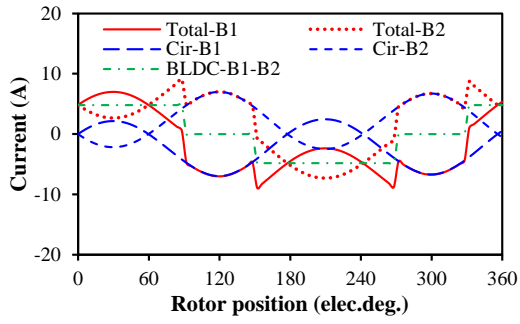
(I) Waveforms

(II) Spectra

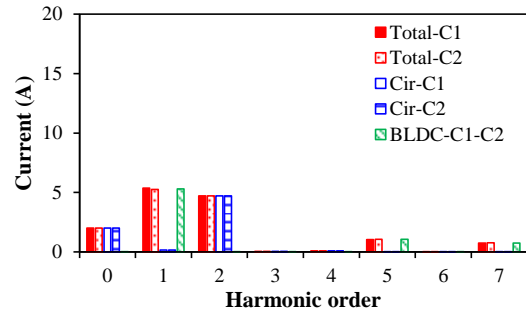
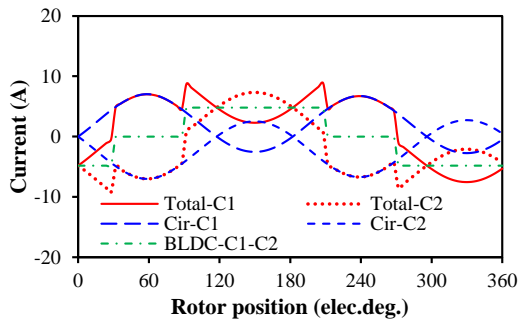
Fig. 5. 42. Currents waveforms of motors with static rotor eccentricity considering circulating current.



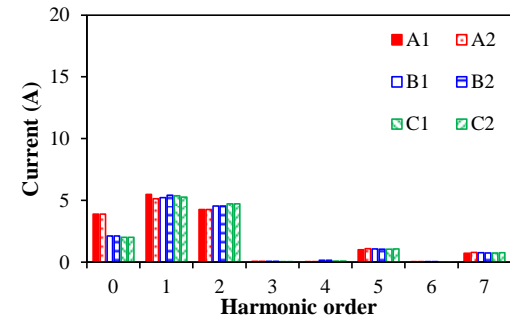
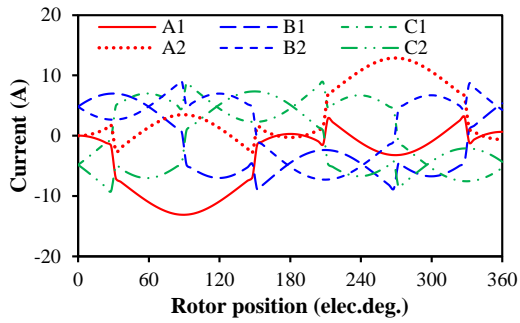
(a) Coils A1 and A2



(b) Coils B1 and B2



(c) Coils C1 and C2

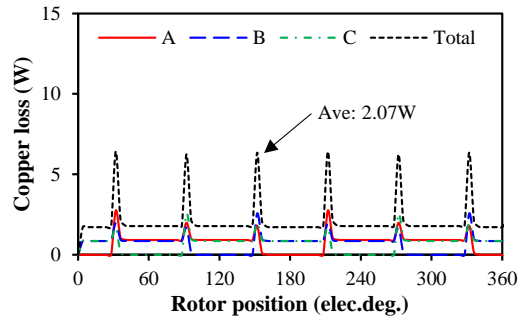


(d) Coils of three phase windings

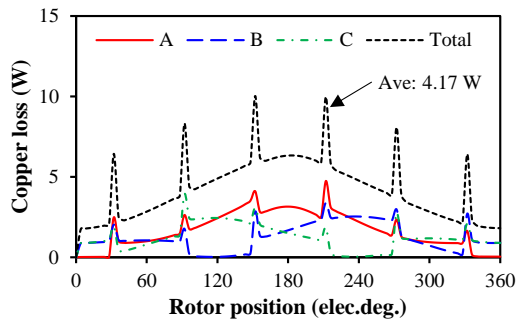
(I) Waveforms

(II) Spectra

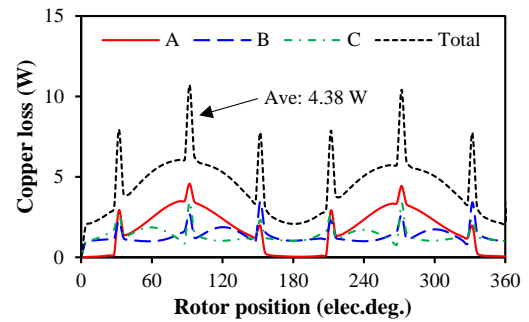
Fig. 5. 43. Currents waveforms of motors with dynamic rotor eccentricity considering circulating current.



(a) Without rotor eccentricity

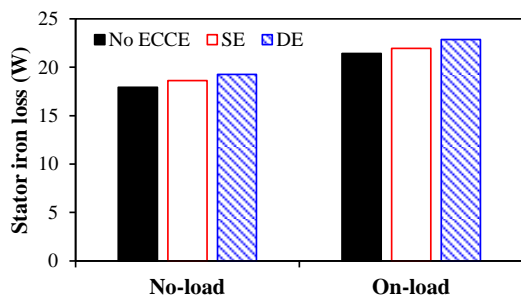


(b) Static rotor eccentricity

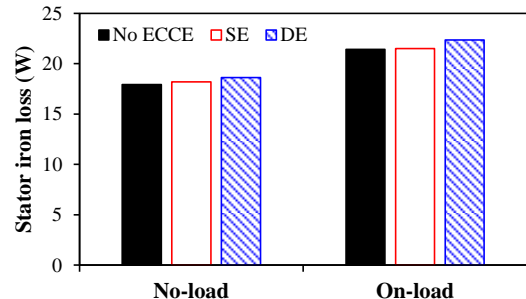


(c) Dynamic rotor eccentricity

Fig. 5. 44. Copper loss waveforms of motors without and with static/dynamic rotor eccentricities considering circulating current.

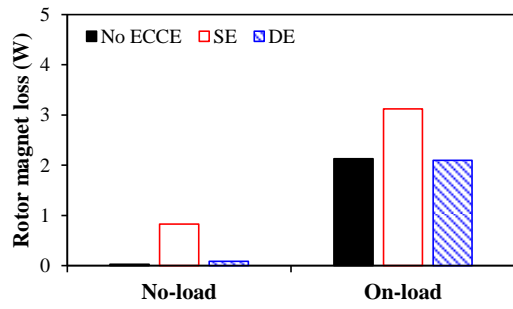


(a) Neglecting circulating current

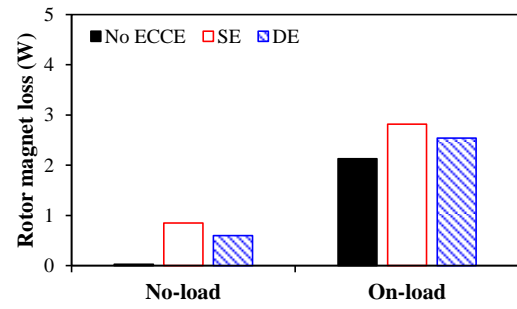


(b) Considering circulating current

Fig. 5. 45. Stator iron losses of the motors without/with rotor eccentricity and neglecting/considering circulating currents.

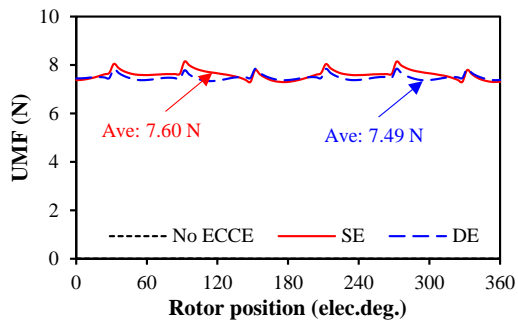


(a) Neglecting circulating current

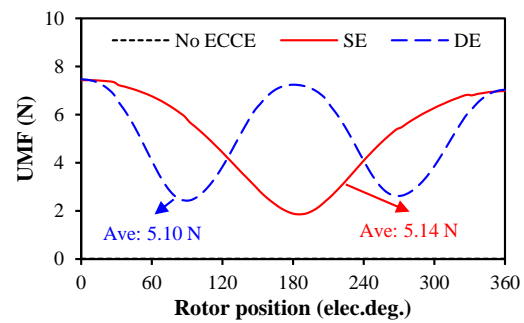


(b) Considering circulating current

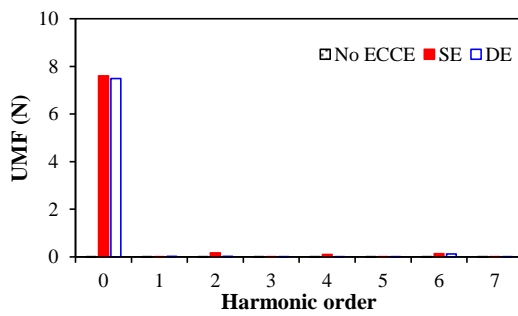
Fig. 5. 46. Rotor magnet losses of the motors without/with rotor eccentricity and neglecting/considering circulating currents in three phase windings.



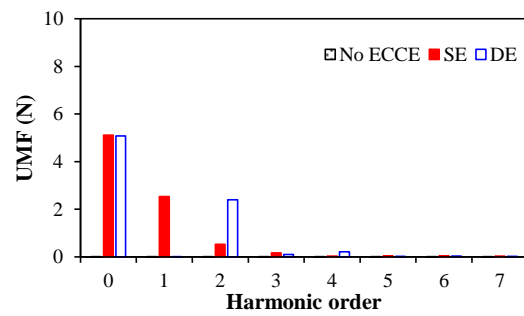
(a) Waveforms



(b) Spectra

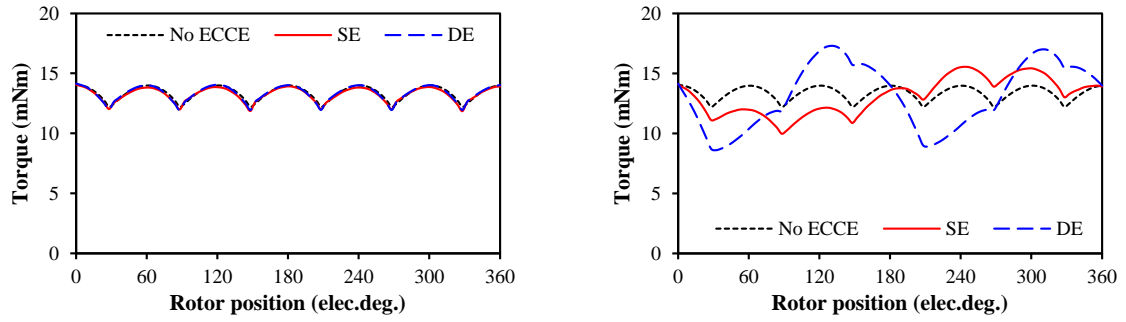


(a) Neglecting circulating current

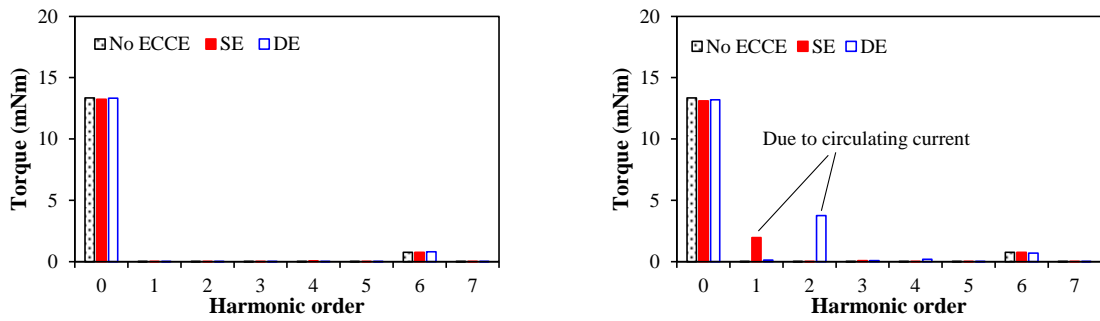


(b) Considering circulating current

Fig. 5. 47. UMF waveforms of the motors with static/dynamic eccentricities under on-load condition.



(a) Waveforms



(b) Spectra

(I) Neglecting circulating current

(II) Considering circulating current

Fig. 5. 48. Torque waveforms of the motors with static/dynamic eccentricities under the on-load condition.

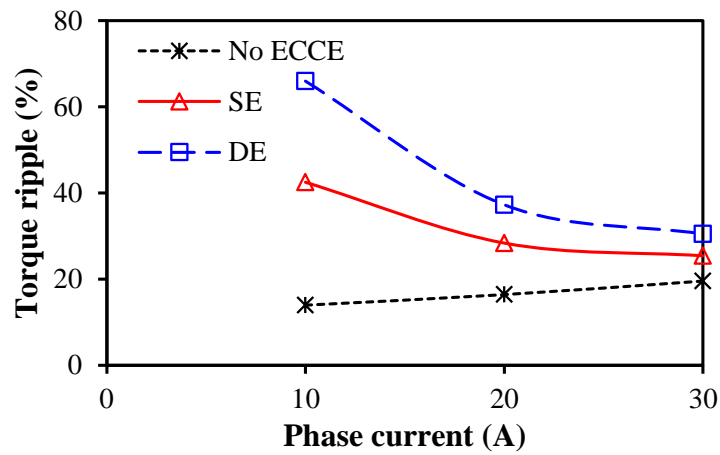


Fig. 5. 49. Variation of torque ripple with the phase current with static/dynamic rotor eccentricities considering circulating current.

Table 5. 2

## Influence of Rotor Eccentricity on Torque

	No ECCE	Without circulating current		With circulating current	
		SE	DE	SE	DE
Average torque (mNm)	13.37	13.26	13.34	13.12	13.20
Torque ripple (%)	13.96	16.79	16.59	42.47	65.95

## CHAPTER 6

### GENERAL CONCLUSIONS AND FUTURE WORK

#### 6.1. General Conclusions

##### 6.1.1 Stator Structure and Winding Configuration

Three-phase 6s/2p HSPM motors with 1, 2, and 3 slot-pitch windings are compared by FEM in Chapter 2. Then, the 6s/2p HSPM motors with two different 2 slot-pitch winding configurations are analyzed in Chapter 3. Fig. 6. 1 shows four machine topologies.

Firstly, different winding configurations lead to different end-winding structures, and thus four different 2-D and 3-D end-winding models are presented in Fig. 6. 2.

Secondly, four HSPM motors are optimized by four different optimization methods, i.e. fixed current density, fixed copper loss, fixed stator loss, i.e. fixed copper loss and iron loss of the stator, and fixed stator loss with maximum current density, Table 6.1. It shows that fixing stator loss with maximum current density due to thermal limitation is a more suitable method for optimization since it can consider the stator iron loss due to high frequency, the end-winding length, the end-winding axial length due to different slot-pitch numbers, and local overheating.

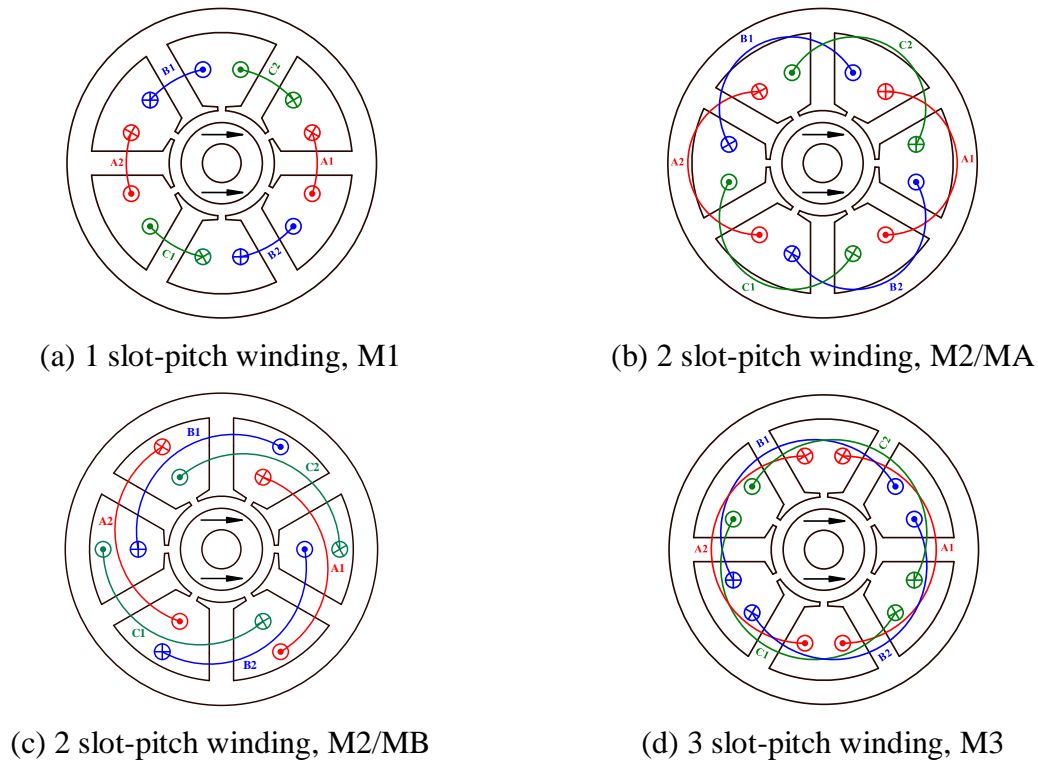
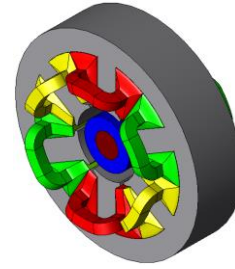
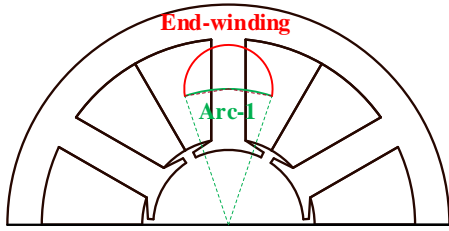
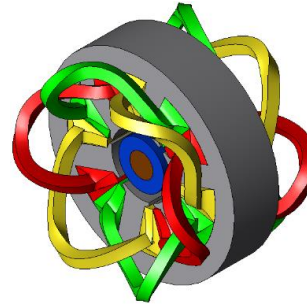
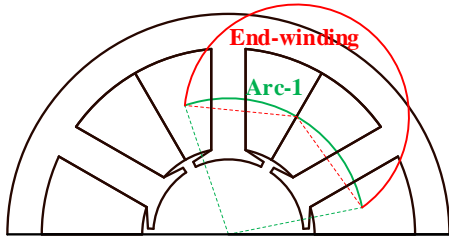


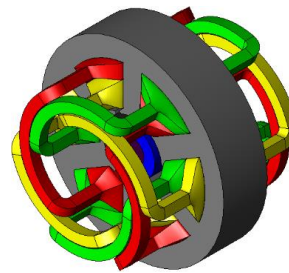
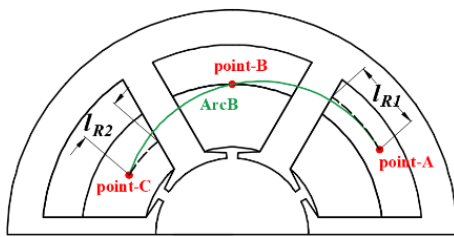
Fig. 6. 1. Machine topologies of four 6s/2p HSPM motors with different winding configurations.



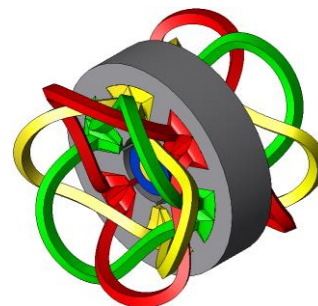
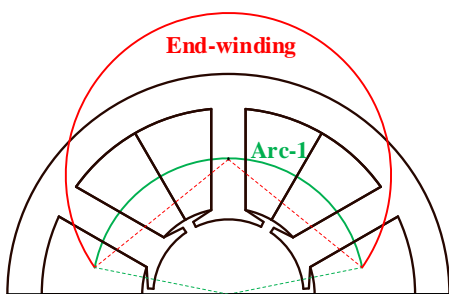
(a) 1 slot-pitch winding, M1



(b) 2 slot-pitch winding, M2/MA



(c) 2 slot-pitch winding, M2/MB



(d) 3 slot-pitch winding, M3

(I) 2-D model

(II) 3-D model

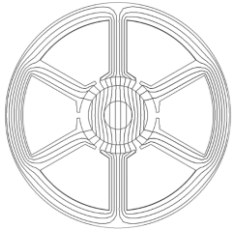
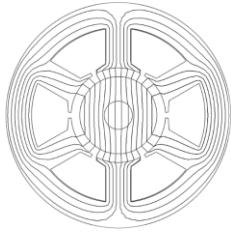
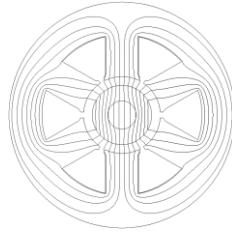
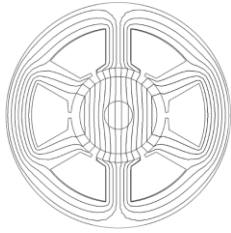
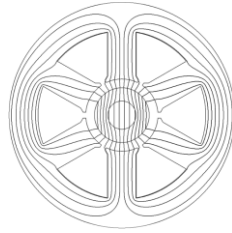
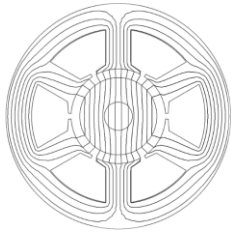
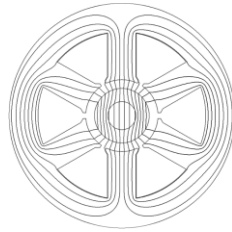
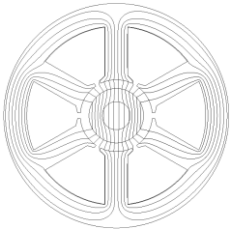
Fig. 6. 2. 2-D and 3-D end-winding models of four motors with different winding configurations.



Thirdly, the electromagnetic performances of four optimized 6s/2p HSPM motors with 1, 2, and 3 slot-pitch windings are analyzed and compared. The results indicate that for high-speed applications, compared with 1 and 3 slot-pitch windings, the motor with 2 slot-pitch windings has a good trade-off between winding factor and end-winding axial length, which is attractive for improving torque density. In addition, the 6s/2p HSPM motors with alternate layouts of 2 slot-pitch windings are analyzed. It shows that Motor B, Fig. 6. 1 (c), is an attractive motor design due to short axial length of end-winding, large torque density, and small phase inductance.

Table 6. 1

Optimized Designs of 6-Slot/2-Pole HSPM Motors by Different Optimization Methods

	Fixed current density	Fixed copper loss	Fixed stator loss	Fixed stator loss and current density
Without end-winding; Max torque				-
	$B_{max}=1.5 \text{ T}, \lambda=0.34$	$B_{max}=1.5 \text{ T}, \lambda=0.42$	$B_{max}=0.8 \text{ T}, \lambda=0.34$	
With end-winding copper loss; Max torque	-			-
		$B_{max}=1.5 \text{ T}, \lambda=0.42$	$B_{max}=0.8 \text{ T}, \lambda=0.32$	
With end-winding copper loss and axial length; Max torque density	-			
		$B_{max}=1.5 \text{ T}, \lambda=0.41$	$B_{max}=0.8 \text{ T}, \lambda=0.32$	$B_{max}=1.0 \text{ T}, \lambda=0.32$

Fourthly, the influence of end-winding axial length on the torque density of the 6s/2p HSPM motors with different stator active lengths is investigated. It found that when the stator active length is relatively long, i.e. longer than 30mm in this thesis, the motor with 2 slot-pitch windings has the largest torque and highest torque density. However, when the stator active length is relatively short, i.e. longer than 12mm in this thesis, the benefits of output torque in the motor with 2 slot-pitch windings outweigh the disadvantages of torque density, compared with the motor with 1 slot-pitch windings.

Fifthly, a conventional 3s/2p HSPM motor with non-overlapping windings is compared with the 6s/2p HSPM motor with 2 slot-pitch windings since they have the same winding factor, i.e. 0.866. The results show that compared with the 3s/2p HSPM motor, the 6s/2p HSPM motor with 2 slot-pitch windings has advantages in high torque, small phase inductance, low rotor loss, and no UMF, which is desirable for high-speed operation.

#### 6.1.2 Rotor Eccentricity

Chapter 4 analyses the electromagnetic performances of 3s/2p and 6s/2p PM motors with static and dynamic rotor eccentricities considering rotor eccentricity ratio, rotor eccentricity angle, and rotor initial angle. In Chapter 5, the circulating currents will be induced in the parallel-connected windings by rotor eccentricity in the 6s/2p PM motor. The influence of circulating currents on the electromagnetic performances, including copper loss, stator iron loss, rotor magnet loss, cogging torque, torque, and UMF, is investigated considering DC component in the circulating current, operation conditions, and rotor eccentricity ratio. The results can be summarised as follow:

##### A. 3s/2p

- Static rotor eccentricity leads to unbalanced back-EMF waveforms of three phases.
- Static rotor eccentricity results in unbalanced fundamental and phase angles of back-EMFs of three phases.
- Unbalanced ratio and offset phase angle increase with the increase of static rotor eccentricity ratio.
- Unbalanced ratio and offset phase angle changes periodically with the variation of static rotor eccentricity angle.
- Dynamic rotor eccentricity does not cause unbalance in the three phase back-EMFs.

- Dynamic rotor eccentricity does not change the fundamental magnitudes but affects the harmonic contents of three phase back-EMFs, i.e. the additional 2<sup>nd</sup> order harmonic.
- Positive and negative peak values increase with the increase of dynamic rotor eccentricity ratio.
- Dynamic rotor eccentricity leads to asymmetric positive and negative half-periods of three phase back-EMF waveforms.
- Largest asymmetric back-EMF waveforms, i.e. the maximum and minimum peak-to-peak back-EMFs, occur when the angle differences between the eccentricity angles and the rotor initial angles are equal to 0° and 90°, respectively.
- Rotor eccentricity has negligible influence on the average torque but affects the torque ripple, which increases with the increase of rotor eccentricity ratio.
- Static rotor eccentricity leads to multiples of (2*p*)th order harmonics of cogging torque, and dynamic rotor eccentricity leads to multiples of (*N<sub>s</sub>*)th order harmonics.
- Increased cogging torque and torque ripple due to dynamic rotor eccentricity are larger than those due to static rotor eccentricity.
- Rotor eccentricity results in additional UMF.

#### B. 6s/2p without circulating current

- Neglecting magnetic saturation, static and dynamic rotor eccentricities affect the magnitudes and phase angles of fundamental and the harmonic contents of coil back-EMFs, respectively, while they have negligible influence on the phase back-EMF.
- Considering magnetic saturation, the increased static rotor eccentricity ratio leads to a slight increase of unbalanced ratio and offset phase angles of back-EMFs.
- Considering magnetic saturation, the increased dynamic rotor eccentricity ratio increases the positive and negative peak values.
- The 3<sup>rd</sup> order back-EMF harmonic due to dynamic rotor eccentricity can be eliminated in 2 slot-pitch windings, and thus the peak-to-peak value remains the same with the variation of dynamic rotor eccentricity angle.
- Rotor eccentricity and slot-pitch number have no influence on average torque and torque ripple.
- Increased rotor eccentricity ratio leads to an increase of average UMF.
- Average UMF caused by rotor eccentricity decreases with the increase of phase current due to the magnetic saturation effect.

### C. 6s/2p with circulating current

- When the unbalanced back-EMFs of the parallel-connected coils in the same phase exist due to rotor eccentricity, the circulating currents are produced.
- DC components exist in the circulating currents when the rotor eccentricity occurs and then are delayed after several electric cycles.
- Frequency of sinusoidal circulating current due to dynamic rotor eccentricity is twice of that due to static rotor eccentricity.
- Rotor eccentricity leads to different peak values of circulating currents in parallel-connected coils of three phase windings.
- With DC components, circulating currents lead to the increase of copper loss, stator iron loss, rotor magnet loss, cogging torque, torque ripple. However, the average torque remains almost unchanged, and the average UMF is reduced compared with no circulating currents.
- Without DC components, circulating currents lead to the increase of various loss components. However, the torque and torque ripple remain almost unchanged, and the cogging torque and average UMF decrease compared with no circulating current.
- Rotor eccentricity ratio increases the back-EMF difference between two coils in the same phase, and thus the fundamental magnitude of circulating currents and DC offset increase.

### 6.2. Future Work

Firstly, in Chapters 2 and 3, the three-phase HSPM motors are optimized by FE method considering the effect of armature reaction on the stator iron loss, which needs a long computation time since there are three design variables, i.e. maximum stator iron flux density, split ratio, and phase current. Therefore, the analytical model can be developed considering the on-load stator iron loss, and the number of design variables can be reduced from 3 to 2, i.e. no phase current.

Secondly, since the different winding configurations result in different end-winding axial lengths and different motor axial lengths, the rotor dynamic characteristic of three 6s/2p HSPM motors with 1, 2, and 3 slot-pitch windings can be analyzed considering the variation of the L/D ratio, i.e. the ratio of rotor length to diameter, which has a close relationship with the critical speed and moment of inertia.

Thirdly, in Chapter 3, the  $6s/2p$  HSPM motors with 2 slot-pitch windings have two different winding configurations, and both of them are overlapping windings. Therefore, a non-overlapping 2 slot-pitch winding with short end-winding axial length can be employed for improving torque density.

Fourthly, although  $3s/2p$  HSPM motors with inherent UMF may lead to high vibration and noise, the relatively large winding factor and simple manufacturing make this kind of motor popular in high-speed applications. However, few papers discuss the influence of the inherent UMF on rotor vibration and noise under high-speed operation. In addition, although the method of reducing the UMF of the  $3s/2p$  [MAJ18] has been researched, the influence on the mechanical stress, the windage loss, and the vibration and noise under high-speed operation has not been investigated. Therefore, the influence of the UMF in a  $3s/2p$  motor on the rotor vibration and noise under high-speed operation, including the method of reducing the UMF, can be investigated.

## REFERENCES

- [AHN17] J. H. Ahn, J. Y. Choi, C. H. Park, C. Han, C. W. Kim, and T. G. Yoon, "Correlation between rotor vibration and mechanical stress in ultra-high-speed permanent magnet synchronous motors," *IEEE Trans. Magn.*, vol. 53, no. 11, pp. 1-6, Nov. 2017.
- [AHN18] J. H. Ahn, C. Han, C. Kim, and J. Choi, "Rotor design of high-speed permanent magnet synchronous motors considering rotor magnet and sleeve materials," *IEEE Trans. Appl. Superconduct.*, vol. 28, no. 3, pp. 1-4, Apr. 2018.
- [ALA15] F. Rezaee Alam and K. Abbaszadeh, "Magnetic field analysis in eccentric surface-mounted permanent-magnet motors using an improved conformal mapping method," *IEEE Trans. Energy Convers.*, vol. 31, no. 1, pp. 333-344, Nov. 2015.
- [ALA17] F. Rezaee Alam, B. Rezaeealam, and J. Faiz, "Unbalanced magnetic force analysis in eccentric surface permanent-magnet motors using an improved conformal mapping method," *IEEE Trans. Energy Convers.*, vol. 32, no. 1, pp. 146-154, Mar. 2017.
- [ARK05] A. Arkkio, T. Jokinen, and E. Lantto, "Induction and permanent magnet machines for high speed applications," *International Conference on Electrical Machines and Systems (ICEMS)*, Nanjing, China, 2005, pp. 871-876.
- [ARK10] A. Arkkio, B. R. Nepal, and A. Sinervo, "Electromechanical interaction in a synchronous reluctance machine," *International Symposium on Power Electronics, Electrical Drives, Automation and Motion (SPEEDAM)*, Pisa, Italy, 2010, pp. 501-506.
- [ARU16] P. Arumugam, Z. Xu, A. La Rocca, G. Vakil, M. Dickinson, E. Amankwah, T. Hamiti, S. Bozhko, C. Gerada, and St. J. Pickering, "High-speed solid rotor permanent magnet machines: concept and design," *IEEE Trans. Transp. Electrification*, vol. 2, no. 3, pp. 391-400, Sept. 2016.
- [ATA92] K. Atallah, Z. Q. Zhu, and D. Howe, "An improved method for predicting iron losses in brushless permanent magnet DC drives," *IEEE Trans. Magn.*, vol. 28, no. 5, pp. 2997-2999, Sept. 1992.

- [ATA93] K. Atallah and D. Howe, "Calculation of the rotational power loss in electrical steel laminations from measured H and B," *IEEE Trans. Magn.*, vol. 29, no. 6, pp. 3547-3549, Nov. 1993.
- [BEN18] R. Benlamine, T. Hamiti, F. Vangraefschep, and D. Lhotellier, "Electromagnetic, structural and thermal analyses of high-speed PM machines for aircraft application," *International Conference on Electrical Machines (ICEM)*, Alexandroupoli, Greece, 2018, pp. 212-217.
- [BEN99] S. Bentouati, Z. Q. Zhu, and D. Howe, "Permanent magnet brushless DC motors for consumer products," *International Conference on Electrical Machines and Drives (Conf. Publ. No. 468)*, Canterbury, UK, 1999, pp. 118-122.
- [BEN00] S. Bentouati, Z. Q. Zhu, and D. Howe, "Influence of design parameters on the starting torque of a single-phase PM brushless DC motor," *IEEE Trans. Magn.*, vol. 36, no. 5, pp. 3533-3536, Sept. 2000.
- [BER16] N. Bernard, R. Missoum, L. Dang, N. Bekka, H. Ben Ahmed, and M. E. Zaïm, "Design methodology for high-speed permanent magnet synchronous machines," *IEEE Trans. Energy Convers.*, vol. 31, no. 2, pp. 477-485, Jun. 2016.
- [BER88] G. Bertotti, "General properties of power losses in soft ferromagnetic materials," *IEEE Trans. Magn.*, vol. 24, pp. 621-630, Jan. 1988.
- [BIA04] N. Bianchi, S. Bolognani, and F. Luise, "Potentials and limits of high-speed PM motors," *IEEE Trans. Ind. Appl.*, vol. 40, no. 6, pp. 1570-1578, Nov. 2004.
- [BIA05] N. Bianchi, S. Bolognani, and F. Luise, "Analysis and design of a PM brushless motor for high-speed operations," *IEEE Trans. Energy Convers.*, vol. 20, no. 3, pp. 629-637, Sep. 2005.
- [BIN06] A. Binder, T. Schneider, and M. Klohr, "Fixation of buried and surface-mounted magnets in high-speed permanent-magnet synchronous machines," *IEEE Trans. Ind. Appl.*, vol. 42, no. 4, pp. 1031-1037, Jul./Aug. 2006.
- [BOR12] A. Borisavljevic, *Limits, Modeling and Design of High-Speed Permanent Magnet Machines*, New York: Springer, 2012.
- [BOR14] A. Borisavljevic, S. Jumayev, and E. Lomonova, "Toroidally-wound permanent magnet machines in high-speed applications," *International Conference on Electrical Machines (ICEM)*, Berlin, Germany, 2014, pp. 2588-2593.

- [BOR14a] J. B. Bartolo and C. Gerada, "The electromagnetic design of a high speed, 45kW, switched reluctance machine having a novel rotor geometry for aerospace application," *International Conference on Electrical Machines (ICEM)*, Berlin, Germany, 2014, pp. 2513-2519.
- [BUM06] J. R. Bumby, E. Spooner, and M. Jagiela, "Equivalent circuit analysis of solid-rotor induction machines with reference to turbocharger accelerator applications," *IEE Elect. Power Appl.*, vol. 153, no. 3, pp. 31–39, Jan. 2006.
- [BUR19] G. Burnand and Y. Perriard, "Very-high-speed miniaturized permanent magnet motors: design and optimization," *IEEE Energy Conversion Congress and Exposition (ECCE)*, Baltimore, USA, 2019, pp. 5258-5264.
- [CAN07] D. de Canha, W. A. Cronje, A. S. Meyer, and S. J. Hoffe, "Methods for diagnosing static eccentricity in a synchronous 2 pole generator," *IEEE Lausanne Power Tech*, 2007, pp. 2162-2167.
- [CHA18] F. Chai, Z. Li, and Y. Yu, "Analysis of AC losses in high-speed permanent magnet motors based on the equivalent modeling method," *International Conference on Electrical Machines (ICEM)*, Alexandroupoli, Greece, 2018, pp. 1061-1066.
- [CHE06] Y. Chen, S. Chen, Z. Q. Zhu, D. Howe, and Y. Y. Ye, "Starting torque of single-phase flux-switching permanent magnet motors," *IEEE Trans. Magn.*, vol. 42, no. 10, pp. 3416-3418, Oct. 2006.
- [CHE09] A. Chebak, P. Viarouge, and J. Cros, "Analytical computation of the full load magnetic losses in the soft magnetic composite stator of high-speed slotless permanent magnet machines," *IEEE Trans. Magn.*, vol. 45, no. 3, pp. 952-955, Mar. 2009.
- [CHE11] F. Cheng, H. Xu, and S. Xue, "Study on the design method of high speed permanent magnet synchronous machine," *International Conference on Electrical Machines and Systems (ICEMS)*, Beijing, China, 2011, pp. 1–6.
- [CHE13] X. Chen, J. B. Wang, P. Lazari, and L. Chen, "Permanent-magnet assisted synchronous reluctance machine with fractional-slot winding configurations," *IEEE Int. Electric Machines and Drives Conf (IEMDC)*, Chicago, IL, USA, May. 12–15, 2013, pp. 393–400.



- [CHE19] X. Cheng, W. Xu, G. Du, G. Zeng, and J. Zhu, "Novel rotors with low eddy current loss for high speed permanent magnet machines," *CES Transactions on Electrical Machines and Systems*, vol. 3, no. 2, pp. 187-194, Jun. 2019.
- [CHE98] Y.S. Chen, Z.Q. Zhu, D. Howe, and G.F. Hu, "Slotless brushless permanent magnet motor and winding topologies," *International Workshop on Rare-Earth Magnets and Their Application*, Dresden, Germany, 1998, pp.737-745.
- [CHE99] Y.S. Chen, Z.Q. Zhu, and D. Howe, "Slotless brushless permanent magnet machines: influence of design parameters," *IEEE Trans. Energy Convers.*, vol. 14, no. 3, pp. 686-691, 1999.
- [DAM16] A. Damiano, A. Floris, G. Fois, M. Porru, and A. Serpi, "Modelling and design of PM retention sleeves for high-speed PM synchronous machines," *International Electric Drives Production Conference (EDPC)*, Nuremberg, Germany, 2016, pp. 118-125.
- [DEB93] M. DeBortoli, S. Salon, D. Burow, and C. Slavik, "Effects of rotor eccentricity and parallel windings on induction machine behavior: A study using finite element analysis," *IEEE Trans. Magn.*, vol. 29, no. 2, pp. 1676–1682, Mar. 1993.
- [DON14] J. Dong, Y. Huang, L. Jin, B. Guo, H. Lin, J. Dong, M. Cheng, and H. Yang, "Electromagnetic and thermal analysis of open-circuit air cooled high-speed permanent magnet machines with gramme ring windings," *IEEE Trans. Magn.*, vol. 50, no. 11, Nov. 2014.
- [DON14a] J. Dong, Y. Huang, L. Jin, H. Lin, and H. Yang, "Thermal optimization of a high-speed permanent magnet motor," *IEEE Trans. Magn.*, vol. 50, no. 2, pp. 749-752, Feb. 2014.
- [DON14b] J. Dong, Y. Huang, L. Jin, B. Guo, T. Zhou, H. Lin, and J. Dong, "Development of an air-cooled 150 kW high speed permanent magnet motor with Gramme ring windings for turbo blowers," *International Conference on Electrical Machines and Systems (ICEMS)*, Berlin, Germany, 2014, pp. 3534-3538.
- [DON16a] M. S. Donea and D. Gerling, "Design and calculation of a 300 kW high-speed PM motor for aircraft application," *International Symposium on Power Electronics, Electrical Drives, Automation and Motion (SPEEDAM)*, Anacapri, Italy, 2016, pp. 1-6.

- [DON16c] J. Dong, Y. Huang, L. Jin, and H. Lin, "Comparative study of surface-mounted and interior permanent-magnet motors for high-speed applications," *IEEE Trans. Appl. Superconduct.*, vol. 26, no. 4, pp. 1-4, Jun. 2016.
- [DOR97] D. G. Dorrell, W. T. Thomson, and S. Roach, "Analysis of air gap flux, current, and vibration signals as a function of the combination of static and dynamic air gap eccentricity in 3-phase induction motors," *IEEE Trans. Ind. Appl.*, vol. 33, no. 1, pp.24–34, Jan./Feb. 1997.
- [DUG20] G. Du, W. Xu, J. Zhu, and N. Huang, "Effects of design parameters on the multiphysics performance of high-speed permanent magnet machines," *IEEE Trans. Ind. Electron.*, vol. 67, no. 5, pp. 3472-3483, May. 2020.
- [DYS11] Y. Chen, T. Celik, and S. Greetham, "Control of a brushless motor," U.S. Patent Appl. 20110254483A1, Apr. 13. 2011.
- [EDE01] J. D. Ede, Z. Q. Zhu, and D. Howe, "Optimal split ratio for high-speed permanent magnet brushless DC motors," *International Conference on Electrical Machines and Systems (ICEMS)*, Shenyang, China, 2001, pp. 909-912, vol. 2.
- [EDE02] J. D. Ede, Z. Q. Zhu, and D. Howe, "Rotor resonances of high-speed permanent-magnet brushless machines," *IEEE Trans. Ind. Applicat.*, vol. 38, no. 6, pp. 1542-1548, Nov./Dec. 2002.
- [ERT05] H. B. Ertan, B. Dag, and G. Capolino, "Calculation of parameters of single-phase PM motor for design optimization," *IEEE Trans. Energy Convers.*, vol. 20, no. 3, pp. 538-548, 2005.
- [FAN12] C. Fang, H. Xu, S. Xue, and S. Xue, "Research on vibration characteristics of rotor of high speed permanent magnet synchronous machine," *International Conference on Electrical Machines and Systems (ICEMS)*, Sapporo, Japan, 2012, pp. 1-5.
- [FAN17] H. Fang, R. Qu, J. Li, P. Zheng, and X. Fan, "Rotor design for high-speed high-power permanent-magnet synchronous machines," *IEEE Trans. Ind. Applicat.*, vol. 53, no. 4, pp. 3411-3419, July-Aug. 2017.
- [FER20] F. Ferrucci, M. Merdzan, F. G. Capponi, and E. Lomonova, "Evaluation of eddy current losses in the cooling sleeve of a toroidal high speed permanent magnet machine," *Global Power, Energy and Communication Conference (GPECOM)*, Izmar, Turkey, 2020, pp. 125-130.

- [FOD14] D. Fodorean, D. C. Popa, P. Minciunescu, C. Irimia, and L. Szabó, “Study of a high-speed motorization for electric vehicle based on PMSM, IM and VRSM,” *International Conference on Electrical Machines (ICEM)*, Berlin, Germany, 2014, pp. 2577-2582.
- [FOG99] A. Foggia, J. Torlay, C. Corenwinder, A. Audoli, and J. Herigault, “Circulating current analysis in the parallel-connected windings of synchronous generators under abnormal operating conditions,” *International Electric Machines and Drives Conference (IEMDC)*, Seattle, USA, 1999, pp. 634-636.
- [GER14] D. Gerada, A. Mebarki, N. Brown, C. Gerada, A. Cavagnino, and A. Boglietti, “High-speed electrical machines: technologies, trends, and developments,” *IEEE Trans. Ind. Electron.*, vol. 61, no. 6, pp. 2946–2959, Jun. 2014.
- [GIL15] A. Gilson, S. Tavernier, M. Gerber, C. Espanet, F. Dubas, and D. Depernet, “Design of a cost-efficient high-speed high-efficiency PM machine for compressor applications,” *IEEE Energy Conversion Congress and Exposition (ECCE)*, Montreal, USA, 2015, pp. 3852-3856.
- [GIL16] A. Gilson, F. Dubas, D. Depernet, and C. Espanet, “Comparison of high-speed pm machine topologies for electrically-assisted turbocharger applications,” *International Conference on Electrical Machines and Systems (ICEMS)*, Makuhari, Japan, 2016, pp. 13-16.
- [GIL17] A. Gilson, G. Verez, F. Dubas, D. Depernet, and C. Espanet, “Design of a high-speed permanent-magnet machine for electrically-assisted turbocharger applications with reduced noise emissions,” *International Electric Machines and Drives Conference (IEMDC)*, Miami, USA, 2017, pp. 1-6.
- [HAN03] D. Hanselman, *Brushless permanent-magnet motor design*. New York: McGraw-Hill, 1994.
- [HE21] T. R. He, Z. Q. Zhu, F. Xu, Y. Wang, B. Hong, and L. Gong, “Influence of rotor eccentricity on electromagnetic performance of 2-pole/3-slot PM motors,” *IEEE Trans. Energy Convers.*, 2021.
- [HES82] D.E. Hesmondhalgh and D. Tipping, “Slotless construction for small synchronous motors using samarium cobalt magnets,” *IEE Proc. Electr. Power Appl.*, vol. 129, no.5, pp.251-261, Sept.1982.

- [HES87] D. E. Hesmondhalgh, D. Tipping, and M. Amrani, "Design and construction of a high-speed high performance direct-drive handpiece," *IEE Proc. B – Elec. Power Appl.*, vol. 134, no. 6, pp. 286-296, Nov. 1987.
- [HE20] T. R. He, Z. Q. Zhu, F. Xu, H. Bin, D. Wu, L. M. Gong, and J. T. Chen, "Comparison of 6-slot/2-pole high-speed permanent magnet motors with different winding configurations," *International Conference on Ecological Vehicles and Renewable Energies (EVER)*, Monte-Carlo, Monaco, 2020, pp. 1-8.
- [HIP92] M. Hippner and R. G. Harley, "Looking for an optimal rotor for high speed permanent magnet synchronous machine," *IEEE Industry Applications Society Annual Meeting (IAS)*, Houston, USA, 1992, pp. 265-270, vol.1.
- [HON09] D. Hong, B. Woo, C. Ahn, and D. Koo, "Unbalance analysis of 15kw, 120krpm, ultra high speed permanent magnet synchronous motor," *International Conference on Electromagnetic Field Problems and Applications (ICEF)*, Dalian, China, 2012, pp. 1-4.
- [HON13] D. Hong, D. Joo, B. Woo, Y. Jeong, D. Koo, C. Ahn., and Y. CHO, "Performance verification of a high speed motor-generator for a microturbine generator," *Int. J. Precis. Eng. Manuf.*, vol. 14, no. 7, pp. 1237-1244, 2013.
- [HON18] D. Hong, T. Lee, and Y. Jeong, "Design and experimental validation of a high-speed electric turbocharger motor considering variation of the  $L/D$  ratio," *IEEE Trans. Magn.*, vol. 54, no. 11, pp. 1-4, Nov. 2018.
- [HON97] Y. Honda, S. Yokote, T. Higaki, and Y. Takeda, "Using the Halbach magnet array to develop an ultrahigh-speed spindle motor for machine tools," *IEEE Industry Applications Conference Thirty-Second IAS Annual Meeting*, New Orleans, USA, 1997, pp. 56-60, vol.1.
- [HUA16] Z. Huang, J. Fang, X. Liu, and B. Han, "Loss calculation and thermal analysis of rotors supported by active magnetic bearings for high-speed permanent-magnet electrical machines," *IEEE Trans. Ind. Electron.*, vol. 63, no. 4, pp. 2027-2035, Apr. 2016.
- [HUA16b] Z. Huang and J. Fang, "Multiphysics design and optimization of high-speed permanent-magnet electrical machines for air blower applications," *IEEE Trans. Ind. Electron.*, vol. 63, no. 5, pp. 2766-2774, May. 2016.

- [HUA18] W. Hua, X. Zhu, and Z. Wu, "Influence of coil pitch and stator-slot/rotor-pole combination on back EMF harmonics in flux-reversal permanent magnet machines," *IEEE Trans. Energy Convers.*, vol. 33, no. 3, pp. 1330-1341, Sept. 2018.
- [HUA99] D. R. Huang, C. Y. Fan, S. J. Wang, H. P. Pan, T. F. Ying, C. M. Chao, and E. G. Lean, "A new type single-phase spindle motor for HDD and DVD," *IEEE Trans. Magn.*, vol. 35, no. 2, pp. 839-844, Mar. 1999.
- [HUP04] J. Hupponen, "High-Speed solid-rotor induction machine-electromagnetic calculation and design," Ph.D. dissertation, Lappeenranta Univ. Technol., Lappeenranta, Finland, 2004.
- [HUY15] Y. Hu and T. Wu, "Comprehensive design and modeling of a super high-speed permanent magnet motor," *IEEE Workshop on Electrical Machines Design, Control and Diagnosis (WEMDCD)*, Turin, Italy, 2015, pp. 28-33.
- [HWA14] C. C. Hwang, S. S. Hung, C. T. Liu, and S. P. Cheng, "Optimal design of a high speed SPM motor for machine tool applications," *IEEE Trans. Magn.*, vol. 50, no. 1, pp. 1-4, Jan. 2014.
- [IID20] T. Iida, M. Takemoto, S. Ogasawara, K. Orikawa, I. Sato, H. Kokubun, A. Toba, and M. Syuto, "Investigation of enhancing output power density in ultra-high-speed motors with concentrated winding structure," *IEEE Energy Conversion Congress and Exposition (ECCE)*, Detroit, USA, 2020, pp. 262-269.
- [IKA14] J. Ikäheimo, J. Kolehmainen, T. Käsäkangas, V. Kivelä, and R. R. Moghaddam, "Synchronous high-speed reluctance machine with novel rotor construction," *IEEE Trans. Ind. Electron.*, vol. 61, no. 6, pp. 2969-2975, Jun. 2014.
- [ISM18] F. R. Ismagilov, V. E. Vavilov, and D. V. Gusakov, "High-Speed electric machine with a speed of 1.2 million rpm," *International Symposium on Power Electronics, Electrical Drives, Automation and Motion (SPEEDAM)*, Amalfi, Italy, 2018, pp. 1159-1164.
- [JAN01] S. Jang, S. Jeong, D. Ryu, and S. Choi, "Design and analysis of high speed slotless PM machine with Halbach array," *IEEE Trans. Magn.*, vol. 37, no. 4, pp. 2827-2830, Jul. 2001.
- [JAN04] S. Jang, H. Cho, S. Lee, H. Yang, and Y. Jeong, "The influence of magnetization pattern on the rotor losses of permanent magnet high-speed machines," *IEEE Trans. Magn.*, vol. 40, no. 4, pp. 2062-2064, Jul. 2004.

- [JAN05] K. Jang, S. Won, T. Kim, and J. Lee, "Starting and high-speed driving of single-phase flux-reversal motor for vacuum cleaner," *IEEE Trans. Magn.*, vol. 41, no. 10, pp. 3967-3969, Oct. 2005.
- [JAN07] S. Jang, H. Cho, and S. Choi, "Design and analysis of a high-speed brushless DC motor for centrifugal compressor," *IEEE Trans. Magn.*, vol. 43, no. 6, pp. 2573-2575, Jun. 2007.
- [JAN09] S. Jang, U. Lee, D. You, J. Lee, and S. Choi, "Operating torque estimation of high-speed slotless brushless DC machine considering power loss," *IEEE Trans. Magn.*, vol. 45, no. 10, pp. 4539-4542, Oct. 2009.
- [JAN11b] X. Jannot, J. Vannier, C. Marchand, M. Gabsi, J. Saint-Michel, and D. Sadarnac, "Multiphysic modeling of a high-speed interior permanent-magnet synchronous machine for a multiobjective optimal design," *IEEE Trans. Energy Convers.*, vol. 26, no. 2, pp. 457-467, Jun. 2011.
- [JAN18] G. Jang, J. Ahn, B. Kim, D. Lee, J. Bang, and J. Choi, "Design and characteristic analysis of a high-speed permanent magnet synchronous motor considering the mechanical structure for high-speed and high-head centrifugal pumps," *IEEE Trans. Magn.*, vol. 54, no. 11, pp. 1-6, Nov. 2018.
- [JAS17] R. P. Jastrzebski, P. Jaatinen, O. Pyrhönen, and A. Chiba, "Design of 6-slot inset PM bearingless motor for high-speed and higher than 100kW applications," *International Electric Machines and Drives Conference (IEMDC)*, Miami, USA, 2017, pp. 1-6.
- [JUM14] S. Jumayev, A. Borisavljevic, K. Boynov, E. A. Lomonova, and J. Pyrhönen, "Analysis of rotor eddy current losses in slotless high-speed permanent magnet machines," *European Conference on Power Electronics and Applications (ECCE Europe)*, Lappeenranta, Finland, 2014, pp. 1-10.
- [JUM16a] S. Jumayev, J. J. H. Paulides, K. O. Boynov, J. Pyrhönen, and E. A. Lomonova, "3-D analytical model of helical winding PM machines including rotor eddy currents," *IEEE Trans. Magn.*, vol. 52, no. 5, pp. 1-8, May. 2016.
- [JUM16b] S. Jumayev, K. O. Boynov, J. J. H. Paulides, E. A. Lomonova, and J. Pyrhönen, "Slotless PM machines with skewed winding shapes: 3-D electromagnetic semianalytical model," *IEEE Trans. Magn.*, vol. 52, no. 11, pp. 1-12, Nov. 2016.

- [JUM18] S. Jumayev, K. O. Boynov, E. A. Lomonova, and J. Pyrhonen, "High-speed slotless permanent magnet machines: modelling and design frameworks," *International Power Electronics Conference (IPEC)*, Niigata, Japan, 2018, pp. 161-168.
- [JUN15] H. W. Jun, J. Lee, H. W. Lee, and W. H. Kim, "Study on the optimal rotor retaining sleeve structure for the reduction of eddy-current loss in high-speed SPMSM," *IEEE Trans. Magn.*, vol. 51, no. 3, pp. 1-4, Mar. 2015.
- [JUN18] D. Jung, J. Lee, J. Kim, I. S. Jang, J. Lee, and H. Lee, "Design method of an ultrahigh speed PM motor/generator for electric-turbo compounding system," *IEEE Trans. Appl. Superconduct.*, vol. 28, no. 3, pp. 1-4, Apr. 2018.
- [KAB17] M. A. Kabir and I. Husain, "Design of synchronous reluctance motor with multilayer AC winding," *IEEE Int. Electric Machines and Drives Conf. (IEMDC)*, Miami, USA, 2017, pp. 1-7.
- [KEN85] T. Kenjo, *Permanent-magnet and brushless DC motors*. Oxford: Clarendon, 1985.
- [KIM01] K.T. Kim, K.S. Kim, S.M. Hwang, T.J. Kim, and Y.H. Jung, "Comparison of magnetic forces for IPM and SPM motor with rotor eccentricity," *IEEE Trans. Magn.*, vol. 37, no. 5, pp. 3448–3451, Sep. 2001.
- [KIM11] K. Kim, J. Hur, B. Kim and G. Kang, "Circulating current calculation using fault modeling of IPM type BLDC motor of inter-turn fault," *International Conference on Electrical Machines and Systems(ICEMS)*, Beijing, China, 2011, pp. 1-5.
- [KIM16] D. Kim, M. D. Noh, and Y. Park, "Unbalanced magnetic forces due to rotor eccentricity in a toroidally wound BLDC motor," *IEEE Trans. Magn.*, vol. 52, no. 7, pp. 1-4, July 2016.
- [KOL13] R. Kolano, K. Krykowski, A. Kolano-Burian, M. Polak, J. Szynowski, and P. Zackiewicz, "Amorphous soft magnetic materials for the stator of a novel high-speed PM BLDC motor," *IEEE Trans. Magn.*, vol. 49, no. 4, pp. 1367-1371, Apr. 2013.
- [KRA17] C. T. Krasopoulos, M. E. Beniakar, and A. G. Kladas, "Robust optimization of high-speed PM motor design," *IEEE Trans. Magn.*, vol. 53, no. 6, pp. 1-4, Jun. 2017.

- [KUR04] K. Kurihara and M. A. Rahman, "High-efficiency line-start interior permanent-magnet synchronous motors," *IEEE Trans. Ind. Applicat.*, vol. 40, no. 3, pp. 789-796, May.-Jun. 2004.
- [LAH02] J. Lahteenmaki, "Design and voltage supply of high-speed induction machines," Ph.D. dissertation, Helsinki Univ. Technol., Espoo, Finland, 2002.
- [LEE17] H. Lee, E. Lee, S. Kwon, and J. Hong, "A study on brushless PM slotless motor with toroidal winding," *Int. Electric Machines and Drives Conf. (IEMDC)*, Miami, USA, 2017, pp. 1-6.
- [LEE20] J. Lee, K. Shin, T. Bang, B. Choi, B. Kim, and J. Choi, "Experiments and design criteria for a high-speed permanent magnet synchronous generator with magnetic bearing considering mechanical aspects," *IEEE Trans. Appl. Superconduct.*, vol. 30, no. 4, pp. 1-5, Jun. 2020.
- [LEP08] L. I. Iepure, L. Tutelea, and I. Boldea, "FEM analysis and control of a tapered airgap single phase PMSM," *International Conference on Optimization of Electrical and Electronic Equipment*, Brasov, Romania, 2008, pp. 241-248.
- [LIM17] M. S. Lim, J. M. Kim, Y. S. Hwang, and J. P. Hong, "Design of an ultra-high-speed permanent-magnet motor for an electric turbocharger considering speed response characteristics," *IEEE/ASME Trans. Mechatronics*, vol. 22, no. 2, pp. 774-784, Apr. 2017.
- [LIQ15] Q. W. Li, M. F. Dou, and C. Fang, "Analytical determination of optimal split ratio for high speed permanent magnet brushless motors," *International Conference on Electrical Machines and Systems (ICEMS)*, Pattaya, Thailand, 2015, pp. 636-640.
- [LIS16] S. Li, Y. Li, W. Choi, and B. Sarlioglu, "High-speed electric machines: challenges and design considerations," *IEEE Trans. Transp. Electrification*, vol. 2, no. 1, pp. 2-13, Mar. 2016.
- [LIU18b] Y. Liu, J. Ou, M. Schiefer, P. Breining, F. Grilli, and M. Doppelbauer, "Application of an amorphous core to an ultra-high-speed sleeve-free interior permanent-magnet rotor," *IEEE Trans. Ind. Electron.*, vol. 65, no. 11, pp. 8498-8509, Nov. 2018.
- [LIU18a] Y. Liu, H. Y. Li, and Z. Q. Zhu, "A high-power factor vernier machine with coil pitch of two slot pitches," *IEEE Trans. Magn.*, vol. 54, no. 11, pp. 1-5, Nov. 2018.



- [LIW14] W. Li, H. Qiu, X. Zhang, J. Cao, and R. Yi, "Analyses on electromagnetic and temperature fields of super high-speed permanent-magnet generator with different sleeve materials," *IEEE Trans. Ind. Electron.*, vol. 61, no. 6, pp. 3056-3063, Jun. 2014.
- [LOO10] A. Looser, T. Baumgartner, C. Zwyssig, and J. W. Kolar, "Analysis and measurement of 3D torque and forces for permanent magnet motors with slotless windings," *IEEE Energy Conversion Congress and Exposition (ECCE)*, Atlanta, USA, 2010, pp. 3792-3797.
- [LUO09] J. Luomi, C. Zwyssig, A. Looser, and J. W. Kolar, "Efficiency optimization of a 100-W 500 000-r/min permanent-magnet machine including air-friction losses," *IEEE Trans. Ind. Applicat.*, vol. 45, no. 4, pp. 1368-1377, Jul.-Aug. 2009.
- [MAC67] M. Mack, "Luftreibungsverluste bei elektrischen maschinen kleiner baugrösse," Ph.D. dissertation, Universität Stuttgart, Stuttgart, Germany, 1967.
- [MAF19] M. M. Mafruddin, S. Suwarno, and A. Abu-Siada, "Finite element simulation of a 126 MW salient pole synchronous generator with rotor eccentricity," *International Conference on High Voltage Engineering and Power Systems (ICHVEPS)*, Denpasar, Indonesia, 2019, pp. 1-96.
- [MAJ17] J. Ma, L. J. Wu, and Z. Q. Zhu, "Effect of magnet thickness on electromagnetic performance of high speed permanent magnet machines," *IEEE International Electric Machines and Drives Conference (IEMDC)*, Miami, USA, 2017, pp. 1-7.
- [MAJ18] J. Ma and Z. Q. Zhu, "Mitigation of unbalanced magnetic force in a PM machine with asymmetric winding by inserting auxiliary slots," *IEEE Trans. Ind. Applicat.*, vol. 54, no. 5, pp. 4133-4146, Sept.-Oct. 2018.
- [MAJ19a] J. Ma and Z. Q. Zhu, "Magnet eddy current loss reduction in permanent magnet machines," *IEEE Trans. Ind. Applicat.*, vol. 55, no. 2, pp. 1309-1320, Mar.-Apr. 2019.
- [MAJ19b] J. Ma and Z. Q. Zhu, "Optimal split ratio in small high speed PM machines considering both stator and rotor loss limitations," *CES Trans. Electrical Machines and Systems*, vol. 3, no. 1, pp. 3-11, Mar. 2019.

- [MAR13] E. Maruyama, A. Nakahara, A. Takahashi, and K. Miyata, "Circulating current in parallel connected stator windings due to rotor eccentricity in permanent magnet motors," *Energy Conversion Congress and Exposition (ECCE)*, Raleigh, USA, 2013, pp. 2850-2855.
- [MAX] <https://www.maxongroup.co.uk/maxon/view/application/Vacuum-compatible-maxon-motors-for-extreme-conditions>.
- [MAY89] J. S. Mayer and O. Wasynczuk, "Analysis and modeling of a single-phase brushless DC motor drive system," *IEEE Trans. Energy Convers.*, vol. 4, no. 3, pp. 473-479, Sept. 1989.
- [MEL06] P. H. Mellor, R. Wrobel, and N. McNeill, "Investigation of proximity losses in a high speed brushless permanent magnet motor," *IEEE Industry Applications Conference Forty-First IAS Annual Meeting*, Tampa, FL, USA, 2006, pp. 1514-1518.
- [MER15] M. Merdzan, J. J. H. Paulides, and E. A. Lomonova, "Comparative analysis of rotor losses in high-speed permanent magnet machines with different winding configurations considering the influence of the inverter PWM," *Int. Conf. Ecological Vehicles and Renewable Energies (EVER)*, Monte Carlo, 2015, pp. 1-8.
- [MIL16] J. Millinger, J. Soulard, and O. Wallmark, "Influence of shaft relative permeability on rotor losses in 2-pole slotless high-speed motor," *International Conference on Electrical Machines (ICEM)*, Lausanne Switzerland, 2016, pp. 405-411.
- [MIL85] T. J. E. Miller, "Single-phase permanent-magnet motor analysis," *IEEE Trans. Ind. Applicat.*, vol. IA-21, no. 3, pp. 651-658, 1985.
- [MIL91] R. D. van Millingen, and J. D. van Millingen. "Phase shift torquemeters for gas turbine development and monitoring," *International Gas Turbine and Aeroengine Congress and Exposition*, Orlando, USA, 1991, pp. 91-GT-189.
- [MIR08] M. Mirzaei and A. Binder, "Permanent magnet savings in high speed electrical motors," *International Symposium on Power Electronics, Electrical Drives, Automation and Motion (SPEEDAM)*, Ischia, Italy, 2008, pp. 1276-1281.

- [MOI17] N. Moisson-Franckhauser, T. Lugand, A. Schwery, and L. Garbuio, "Effect of static or dynamic eccentricities on the unbalanced magnetic pull in Doubly-Fed induction machines," *International Conference on Electrical Machines, Drives and Power Systems (ELMA)*, Sofia, Bulgaria, 2017, pp. 383-388.
- [MOR00] L. Morel, H. Fayard, R. Vives Fos, A. Galindo, and G. Abba, "Study of ultra high speed switched reluctance motor drive," *IAS Annual Meeting and World Conference on Industrial Applications of Electrical Energy*, Rome, Italy, 2000, pp. 87-92, vol.1.
- [MUN10] G. Munteanu, A. Binder, T. Schneider, and B. Funieru, "No-load tests of a 40 kW high-speed bearingless permanent magnet synchronous motor," *International Symposium on Power Electronics, Electrical Drives, Automation and Motion (SPEEDAM)*, Pisa, Italy, 2010, pp. 1460-1465.
- [NGK96] K. Ng, Z. Q. Zhu, and D. Howe, "Open-circuit field distribution in a brushless motor with diametrically magnetized PM rotor, accounting for slotting and eddy current effects," *IEEE Trans. Magn.*, vol. 32, pp. 5070–5072, Sept. 1996.
- [NIU12] S. Niu, S. L. Ho, W. N. Fu, and J. Zhu, "Eddy current reduction in high-speed machines and eddy current loss analysis with multislice time-stepping finite-element method," *IEEE Trans. Magn.*, vol. 48, no. 2, pp. 1007-1010, Feb. 2012.
- [NOG05] T. Noguchi, Y. Takata, Y. Yamashita, Y. Komatsu, and S. Ibaraki, "220000 r/min 2kW PM motor drive for turbocharger," *IEEJ Trans. Ind. Appl.*, vol. 125, no. 9, pp. 854–861, Sep. 2005.
- [NOG07] T. Noguchi and M. Kono, "Development of 150000r/min 1.5kW permanent magnet motor for automotive supercharger," *International Conference on Power Electronics and Drive Systems (PEDS)*, Bangkok, Thailand, 2007, pp. 183–188.
- [NOG09] T. Noguchi and T. Wada, "1.5kW, 150000r/min ultra-high-speed PM motor fed by 12V power supply for automotive supercharger," *European Conference on Power Electronics and Applications (EPE)*, Barcelona, Spanish, 2009, pp. 1–9.
- [NOG15] T. Noguchi and T. Komori, "Eddy-current loss analysis of copper-bar windings of ultra high-speed PM motor," *Electrical Systems for Aircraft Railway Ship Propulsion and Road Vehicles Conference (ESARS)*, Aachen, Germany, 2015, pp. 3-5.

- [OYA03] J. Oyama, T. Higuchi, T. Abe, K. Shigematsu, X. Yang, and E. Matsuo, "A trial production of small size ultra-high speed drive system," *International Electric Machines and Drives Conference (IEMDC)*, Madison, USA, 2003, pp. 31-36, vol.1.
- [OHT00] H. Ohta, T. Sato, I. Masugane, and K. Matsuse, "Rotor pole discrimination and simple starting method of new single-phase PM motor without position sensor," *International Power Electronics and Motion Control Conference (IPEMC)*, Beijing, China, 2000, pp. 616-621, vol.2.
- [PAN06] Y. Pang, Z. Q. Zhu, and D. Howe, "Analytical determination of optimal split ratio for permanent magnet brushless motors," *IEE Proceedings - Electric Power Applications*, vol. 153, no. 1, pp. 7-13, 1 Jan. 2006.
- [PAN14] Y. Pang and Z. Q. Zhu, "Reduction of unbalanced magnetic force in 2-pole 3-slot permanent magnet machine," *IET International Conference on Power Electronics, Machines and Drives (PEMD)*, Manchester, UK, 2014, pp. 1-6.
- [PAT14] V. I. Patel, J. Wang, W. Wang, and X. Chen, "Six-phase fractional-slot-per-pole-per-phase permanent-magnet machines with low space harmonics for electric vehicle application," *IEEE Trans. Ind. Appl.*, vol. 50, no. 4, pp. 2554-2563, July-Aug. 2014.
- [PER19] J. J. Pérez-Loya, C. J. D. Abrahamsson, and U. Lundin, "Electromagnetic losses in synchronous machines during active compensation of unbalanced magnetic pull," *IEEE Trans. Ind. Electron.*, vol. 66, no. 1, pp. 124-131, Jan. 2019.
- [PFI10] P. D. Pfitser and Y. Perriard, "Very high speed slotless PM motors: analytical modelling, optimization, design and torque measurement methods," *IEEE Trans. Ind. Electron.*, vol. 57, no. 1, pp. 296-303, Jan. 2010.
- [POL00] H. Polinder and M. J. Hoeijmakers, "Effect of a shielding cylinder on the rotor losses in a rectifier-loaded PM machine," *IAS Annual Meeting and World Conference on Industrial Applications of Electrical Energy*, Rome, Italy, 2000, pp. 163-170, vol.1.
- [POP13] M. Popescu and D. G. Dorrell, "Proximity losses in the windings of high speed brushless permanent magnet ac motors with single tooth windings and parallel paths," *IEEE Trans. Magn.*, vol. 49, no. 7, pp. 3913-3916, July 2013.

- [PYR10] J. Pyrhonen, J. Nerg, P. Kurronen, and U. Lauber, “High-speed, high-output, solid-rotor induction motor technology for gas compression,” *IEEE Trans. Ind. Electron.*, vol. 57, no. 1, pp. 272–280, Jan. 2010.
- [PYR96] J. Pyrhonen and J. Hupponen, “A new medium speed solid rotor induction motor for a high speed milling machine,” *International Symposium on Power Electronics, Electrical Drives, Automation and Motion, (SPEEDAM)*, Taormina, Italy, 1996, pp. B5-1–B5-8.
- [REI13] T. Reichert, T. Nussbaumer, and J. W. Kolar, “Split ratio optimization for high-torque PM motors considering global and local thermal limitations,” *IEEE Trans. Energy Convers.*, vol. 28, no. 3, pp. 493-501, Sept. 2013.
- [RIC97] E. Richter and C. Ferreira, “Performance evaluation of a 250 kW switched reluctance starter generator,” *IEEE Industry Applications Conference Thirtieth IAS Annual Meeting*, Phoenix, USA, 1995, pp. 434-440, vol. 1.
- [ROD13] P. Rodriguez, P. Rzeszucinski, M. Sulowicz, R. Disselnkoetter, U. Ahrend, C. T. Pinto, J. R. Ottewill, and S. Wildermuth., “Stator circulating currents as media of fault detection in synchronous motors,” *International Symposium on Diagnostics for Electric Machines, Power Electronics and Drives (SDEMPED)*, Valencia, Spain, 2013, pp. 207-214.
- [SCH17] M. Schuck, A. Da Silva Fernandes, D. Steinert, and J. W. Kolar, “A high speed millimeter-scale slotless bearingless slice motor,” *International Electric Machines and Drives Conference (IEMDC)*, Miami, USA, 2017, pp. 1-7.
- [SCH20] C. Schepe, E. Haschen, and B. Ponick, “Calculation of circulating currents in parallel branches of salient pole synchronous machines,” *International Conference on Electrical Machines (ICEM)*, Gothenburg, Sweden, 2020, pp. 2582-2588.
- [SHA09] M. R. Shah and A. M. EL-Refáie, “Eddy-current loss minimization in conducting sleeves of surface PM machine rotors with fractional-slot concentrated armature windings by optimal axial segmentation and copper cladding,” *IEEE Trans. Ind. Applicat.*, vol. 45, no. 2, pp. 720-728, Mar.-Apr. 2009.

- [SHA96] N. D. Sharma, R. Anbarasu, J. Nataraj, A. Y. Dangore, and B. Bhattacharjee, "Experimental investigations on high speed solid and composite rotor induction motor," *International Conference on Power Electronics, Drives and Energy Systems for Industrial Growth (PEDES)*, New Delhi, India, 1996, vol. 2, pp. 913–919.
- [SHE13] J. X. Shen, H. Hao, M. J. Jin, and C. Yuan, "Reduction of rotor eddy current loss in high speed PM brushless machines by grooving retaining sleeve," *IEEE Trans. Magn.*, vol. 49, no. 7, pp. 3973-3976, Jul. 2013.
- [SHE18] J. X. Shen, X. Qin, and Y. Wang, "High-speed permanent magnet electrical machines – applications, key issues and challenges," *CES Transactions on Electrical Machines and Systems*, vol. 2, no. 1, pp. 23-33, Mar. 2018.
- [SHI04] K. Shigematsu, J. Oyama, T. Higuchi, T. Abe, and Y. Ueno, "The study of eddy current in rotor and circuit coupling analysis for small size and ultra-high-speed motor," *International Power Electronics and Motion Control Conference (IPEMC)*, Xi'an, China, 2004, pp. 275–279.
- [SPA15] S. Spas, G. Dajaku, and D. Gerling, "Eddy current loss reduction in PM traction machines using two-tooth winding," *IEEE Vehicle Power and Propulsion Conf. (VPPC)*, Montreal, Canada, 2015, pp. 1-6.
- [TAK10] R. Takahata, S. Wakui, K. Miyata, K. Noma, and M. Senoo, "Analysis of rotor eccentricity on permanent magnet synchronous motor characteristics," *International Power Electronics Conference - ECCE ASIA -*, Sapporo, Japan, 2010, pp. 1306-1311.
- [TAN03] X. Tang and C. R. Sullivan, "Stranded wire with uninsulated strands as a low cost alternative to Litz wire," *Annual IEEE Conference on Power Electronics Specialists (PESC)*, 2003, pp. 1–7.
- [TEN03] A. Tenhunen, T. P. Holopainen, and A. Arkkio, "Effects of equalizing currents on electromagnetic forces of whirling cage rotor," *International Electric Machines and Drives Conference (IEMDC)*, Madison, USA, 2003, pp. 257-263 vol.1.
- [THO14] A. S. Thomas, Z. Q. Zhu, and G. J. Li, "Electromagnetic loss investigation and mitigation in switched flux permanent magnet machines," *International Conference on Electrical Machines (ICEM)*, Berlin, Germany, 2014, pp. 1146-1152.

- [TOD05] D. Todd and K. Y. Lee, "Electric propulsion with the sensorless permanent magnet synchronous motor: model and approach," *IEEE Trans. Energy Convers.*, vol. 20, No. 4, pp. 818-825, Dec. 2005.
- [TON20] W. Tong, S. Li, X. Pan, S. Wu, and R. Tang, "Analytical model for cogging torque calculation in surface-mounted permanent magnet motors with rotor eccentricity and magnet defects," *IEEE Trans. Energy Convers.*, vol. 35, no. 4, pp. 2191-2200, Dec. 2020.
- [TUY14] A. Tüysüz, C. Zwysig, and J. W. Kolar, "A novel motor topology for high-speed micro-machining applications," *IEEE Trans. Ind. Electron.*, vol. 61, no. 6, pp. 2960-2968, Jun. 2014.
- [UZH14] N. Uzhegov, N. Uzhegov, J. Nerg, and J. Pyrhönen, "Design of 6-slot 2-pole high-speed permanent magnet synchronous machines with tooth-coil windings," *International Conference on Electrical Machines (ICEM)*, Berlin, Germany, 2014, pp. 2537-2542.
- [UZH16] N. Uzhegov, E. Kurvinen, J. Nerg, J. Pyrhönen, J. T. Sopenan, and S. Shirinskii, "Multidisciplinary design process of a 6-slot 2-pole high-speed permanent-magnet synchronous machine," *IEEE Trans. Ind. Electron.*, vol. 63, no. 2, pp. 784-795, Feb. 2016.
- [VEE97] J. L. F. Van der Veen, L. J. J. Offringa, and A. J. A. Vandenput, "Minimising rotor losses in high-speed high-power permanent magnet synchronous generators with rectifier load," *IEE Proceedings – Electric Power Applications*, vol. 144, no. 5, pp. 331-337, Sep 1997.
- [WAL09] O. Wallmark, P. Kjellqvist, and F. Meier, "Analysis of axial leakage in high-speed slotless PM motors for industrial hand tools," *IEEE Trans. on Ind. Applicat.*, vol. 45, no. 5, pp. 1815-1820, Sept.-Oct. 2009.
- [WAL11] M. Wallin, M. Ranlof, and U. Lundin, "Reduction of unbalanced magnetic pull in synchronous machines due to parallel circuits," *IEEE Trans. Magn.*, vol. 47, no. 12, pp. 4827–4833, 2011.
- [WAN03] F. Wang, M. Zong, W. Zheng, and E. Guan, "Design features of high speed PM machines," *International Conference on Electrical Machines and Systems (ICEMS)*, Beijing, China, 2003, pp. 66-70, vol. 1.

- [WAN05] S. Wan, H. Li, Y. Li, and F. Meng, "Analysis of stator winding parallel-connected branches circulating current and its application in generator fault diagnosis," *IEEE Industry Applications Society Annual Meeting (IAS)*, Hong Kong, China, 2005, pp. 42-45, vol. 1.
- [WAN09] F. Wang, D. Zhang, J. Xing, and Y. Xu, "Study on air friction loss of high speed PM machine," *International Conference on Industrial Technology (ICIT)*, Melbourne, Australia, 2009, pp. 1-4.
- [WAN10] K. Wang, M. J. Jin, J. X. Shen, and H. Hao, "Study on rotor structure with different magnet assembly in high-speed sensor-less brushless DC Motors," *IET Elec. Power Appl.*, vol. 4, no. 4, pp. 241–248, Sept. 2010.
- [WAN10K] X. Wang, X. Zhang, S. Yan, X. Wang, and C. Zhang, "The analysis of high speed slotless permanent magnet brushless DC motor based on soft magnetic ferrite," *International Conference on Electrical Machines and Systems (ICEMS)*, Incheon, Korea (South), 2010, pp. 1061-1064.
- [WAN14a] J. Wang, V. I. Patel, and W. Wang, "Fractional-slot permanent magnet brushless machines with low space harmonic contents," *IEEE Trans. Magn.*, vol. 50, no. 1, pp. 1-9, Jan. 2014.
- [WAN14b] K. Wang, Z. Q. Zhu, and G. Ombach, "Synthesis of high performance fractional-slot PM machines with coil-pitch of two slot-pitches," *IEEE Trans. Energy Convers.*, vol. 29, no. 3, pp. 758-770, Sept. 2014.
- [WAN18] Y. Wang, J. H. Feng, S. Y. Guo, Y. F. Li, Z. C. Chen, Y. Wang, and Z. Q. Zhu, "Investigation of optimal split ratio for high-speed permanent-magnet brushless machines," *IEEE Trans. Magn.*, vol. 54, no. 11, pp. 1-5, Nov. 2018.
- [WAN21] Y. Wang, Z. Q. Zhu, J. Feng, S. Guo, Y. Li, and Y. Wang, "Rotor stress analysis of high-speed permanent magnet machines with segmented magnets retained by carbon-fibre sleeve," *IEEE Trans. Energy Convers.*, vol. 36, no. 2, pp. 971-983, Jun. 2021.
- [WON06] S. H. Won, T. H. Kim, K. B. Jang, S. K. Choi, W. S. Oh, and J. Lee, "Effect of design variables on starting torque of single phase flux-reversal machine," *Journal of Applied Physics*, vol. 99, no. 8, pp. 08R312, 2006.
- [WRO10] R. Wrobel, A. Mlot, and P. H. Mellor, "Investigation of end-winding proximity losses in electromagnetic devices," *International Conference on Electrical Machines (ICEM)*, Rome, Italy, 2010, pp. 1-6.



- [WUL13] L. J. Wu, Z. Q. Zhu, and M. L. M. Jamil, "Unbalanced magnetic force in permanent magnet machines having asymmetric windings and static/ rotating eccentricities," *International Conference on Electrical Machines and Systems (ICEMS)*, Busan, Korea (South), 2013, pp. 937-942.
- [XIN10] J. Xing, F. Wang, T. Wang, and Y. Zhang, "Study on anti-demagnetization of magnet for high speed permanent magnet machine," *IEEE Trans. Appl. Superconduct.*, vol. 20, no. 3, pp. 856-860, Jun. 2010.
- [XUE12] S. Xue, H. Xu, and C. Fang, "The effect of stator slot and air gap length on high speed brushless PM motor," *International Power Electronics and Motion Control Conference (IPEMC)*, Harbin, China, 2012, pp. 281-285.
- [XU20] F. Xu, T. R. He, Z. Q. Zhu, Y. Wang, S. Cai, H. Bin, D. Wu, L. M. Gong, and J. T. Chen, "Influence of slot number on electromagnetic performance of 2-pole high-speed permanent magnet motors with toroidal windings," *International Conference on Ecological Vehicles and Renewable Energies (EVER)*, Monte-Carlo, Monaco, 2020, pp. 1-7.
- [XUJ11] J. Xu and C. Liu, "Research on high-speed permanent magnet generator for a miniature turbojet," *IEEE Conference on Industrial Electronics and Applications*, Beijing, China, 2011, pp. 2783-2786.
- [YAN81] S.J. Yang, *Low noise electric motors*, Oxford University Press, 1981.
- [ZHA07] L. Zhao, C. Ham, L. Zheng, T. Wu, K. Sundaram, J. Kapat, and L. Chow, "A highly efficient 200,000 rpm permanent magnet motor system," *IEEE Trans. Magn.*, vol. 43, no. 6, pp. 2528-2530, Jun. 2007.
- [ZHA15a] F. Zhang, G. Du, T. Wang, G. Liu, and W. Cao, "Rotor retaining sleeve design for a 1.12-MW high-speed PM machine," *IEEE Trans. Ind. Applicat.*, vol. 51, no. 5, pp. 3675-3685, Sept.-Oct. 2015.
- [ZHA15d] J. Zhang, W. Chen, X. Huang, Y. Fang, J. Zhang, J. Ma, and W. Cao, "Evaluation of applying retaining shield rotor for high-speed interior permanent magnet motors," *IEEE Trans. Magn.*, vol. 51, no. 3, pp. 1-4, Mar. 2015.
- [ZHA15e] X. Zhang, W. Li, B. Kou, J. Cao, H. Cao, C. Gerada, and H. Zhang, "Electrothermal combined optimization on notch in air-cooled high-speed permanent-magnet generator," *IEEE Trans. Magn.*, vol. 51, no. 1, pp. 1-10, Jan. 2015.

- [ZHA15H] H. Zhang, X. Zhang, C. Gerada, M. Galea, D. Gerada, and J. Li, "Design considerations for the tooth shoe shape for high-speed permanent magnet generators," *IEEE Trans. Magn.*, vol. 51, no. 11, pp. 1-4, Nov. 2015.
- [ZHA16a] F. Zhang, G. Du, T. Wang, F. Wang, W. Cao, and J. L. Kirtley, "Electromagnetic design and loss calculations of a 1.12-MW high-speed permanent-magnet motor for compressor applications," *IEEE Trans. Energy Convers.*, vol. 31, no. 1, pp. 132-140, Mar. 2016.
- [ZHA16b] F. G. Zhang, G. H. Du, T. Y. Wang, and G. W. Liu, "Review on development and design of high speed machines," *Transactions of China electrotechnical society*, vol.31, no.7, Apr. 2016.
- [ZHA16c] X. C. Zhang, W. L. Li, H. Zhang, C. Gerada, M. Galea, and J. Li, "Topology investigation on high speed PM generator with back wound windings," *International Symposium on Industrial Electronics (ISIE)*, Santa Clara, USA, 2016, pp. 234–239.
- [ZHA17a] Y. Zhang, S. McLoone, and W. Cao, "High speed permanent magnet motor design and power loss analysis," *IEEE Transportation Electrification Conference and Expo, Asia-Pacific (ITEC Asia-Pacific)*, Harbin, China, 2017, pp. 1-6.
- [ZHA17b] Y. Zhang, S. McLoone, W. Cao, F. Qiu, and C. Gerada, "Power loss and thermal analysis of a MW high speed permanent magnet synchronous machine," *IEEE Trans. Energy Convers.*, vol. 32, no. 4, pp. 1468-1478, Dec. 2017.
- [ZHA18b] W. Zhao, X. Wang, C. Gerada, H. Zhang, C. Liu, and Y. Wang, "Multi-physics and multi-objective optimization of a high speed PMSM for high performance applications," *IEEE Trans. Magn.*, vol. 54, no. 11, pp. 1-5, Nov. 2018.
- [ZHA19] Z. Zhang, Z. Deng, C. Gu, Q. Sun, C. Peng, and G. Pang, "Reduction of rotor harmonic eddy-current loss of high-speed PM BLDC motors by using a split-phase winding method," *IEEE Trans. Energy Convers.*, vol. 34, no. 3, pp. 1593-1602, Sept. 2019.
- [ZHA21] J. Zhao, W. Fu, X. Liu, L. Yang, and L. Yang, "Research on performances of slotted/slotless high-speed PM BLDC motors with different PM magnetizations," *International Electrical and Energy Conference (CIEEC)*, Wuhan, China, 2021, pp. 1-6.

- [ZHE05] L. Zheng, T. X. Wu, D. Acharya, K. B. Sundaram, J. Vaidya, L. Zhao, L. Zhou, C. H. Ham, N. Arakere, J. Kapat, and L. Chow, "Design of a super high speed cryogenic permanent magnet motor," *IEEE Trans. Magn.*, vol. 41, no. 10, pp. 3823–3825, Oct. 2005.
- [ZHO06] F. Z. Zhou, J. X. Shen, W. Fei, and R. Lin, "Study of retaining sleeve and conductive shield and their influence on rotor loss in high-speed PM BLDC motors," *IEEE Trans. Magn.*, vol. 42, no. 10, pp. 3398-3400, Oct. 2006.
- [ZHO07] F. Z. Zhou, J. X. Shen, and R. G. Lin, "Influence on rotor eddy-current loss in high-speed PM BLDC motors," *Journal of Zhejiang University (Engineering Science)*, vol. 41, no. 9, pp. 1587-1591, Sept. 2007.
- [ZHU01] Z. Q. Zhu, J. D. Ede, and D. Howe, "Design criteria for brushless dc motors for high-speed sensorless operation," *Int. J. Appl. Electromagn. Mech.*, vol. 15, pp. 79–87, 2001/2002.
- [ZHU01b] Z. Q. Zhu, K. Ng, and D. Howe, "Analytical prediction of stator flux density waveforms and iron losses in brushless DC machines, accounting for load condition," *International Conference on Electrical Machines and Systems (ICEMS)*, Shenyang, China, 2001, pp. 814-817 vol.2.
- [ZHU04] Z. Q. Zhu, K. Ng, N. Schofield, and D. Howe, "Improved analytical modelling of rotor eddy current loss in brushless machines equipped with surface mounted permanent magnets," *Proc. Inst. Elect. Eng.*, vol. 151, no. 6, pp. 641–650, Nov. 2004.
- [ZHU07] Z. Q. Zhu, D. Ishak, D. Howe, and J. Chen, "Unbalanced magnetic forces in permanent-magnet brushless machines with diametrically asymmetric phase windings," *IEEE Trans. Ind. Appl.*, vol. 43, no. 6, pp. 1544-1553, Nov.-dec. 2007.
- [ZHU09] Z. Q. Zhu, "A simple method for measuring cogging torque in permanent magnet machines," *IEEE Power Energy Soc. General Meeting, Calgary, AB, Canada*, 2009, pp. 1–4.
- [ZHU13] Z. Q. Zhu, L. J. Wu, and M. L. M. Jamil, "Distortion of back-EMF and torque of PM brushless machines due to eccentricity," *IEEE Trans. Magn.*, vol. 49, no. 8, pp. 4927-4936, Aug. 2013.

- [ZHU13b] Z. Q. Zhu, M. L. Mohd Jamil, and L. J. Wu, "Influence of slot and pole number combinations on unbalanced magnetic force in PM machines with diametrically asymmetric windings," *IEEE Trans. Ind. Applicat.*, vol. 49, no. 1, pp. 19-30, Jan.-Feb. 2013.
- [ZHU14] Z. Q. Zhu, L. J. Wu, and M. L. M. Jamil, "Influence of pole and slot number combinations on cogging torque in permanent-magnet machines with static and rotating eccentricities," *IEEE Trans. Ind. Appl.*, vol. 50, no. 5, pp. 3265-3277, Sept.-Oct. 2014.
- [ZHU97] Z. Q. Zhu, K. Ng, and D. Howe, "Design and analysis of high-speed brushless permanent magnet motors," *International Conference on Electrical Machines and Drives (Conf. Publ. No. 444)*, Cambridge, UK, 1997, pp. 381-385.
- [ZWY05] C. Zwyssig, J. W. Kolar, W. Thaler, and M. Vohrer, "Design of a 100W, 500, 000 rpm permanent-magnet generator for mesoscale gas turbines," *IEEE Industry Applications Society Annual Meeting (IAS)*, Hong Kong, China, Sep. 2005, pp. 253-260.
- [ZWY09] C. Zwyssig, J. W. Kolar, and S. D. Round, "Megasppeed drive systems: pushing beyond 1 Million r/min," *IEEE/ASME Trans. Mechatronics*, vol. 14, no. 5, pp. 564-574, Oct. 2009.

## APPENDIX I

### PUBLICATION RESULTED FROM PHD STUDY

#### Journal Publications:

- [1] **T. R. He**, Z. Q. Zhu, F. Xu, H. Bin, D. Wu, L. M. Gong, and J. T. Chen, “Comparative study of 6-slot/2-pole high-speed permanent magnet motors with different winding configurations,” *IEEE Transactions on Industry Applications*, doi:10.1109/TIA.2021.3108115.
- [2] **T. R. He**, Z. Q. Zhu, F. Xu, Y. Wang, H. Bin, and L. M. Gong, “Influence of rotor eccentricity on electromagnetic performance of 2-pole/3-slot PM motors,” *IEEE Transactions on Energy Convers.*, doi: 10.1109 / TEC.2021.3098669.
- [3] **T. R. He**, Z. Q. Zhu, F. Xu, Y. Wang, H. Bin, and L. M. Gong, “Electromagnetic performance analysis of 6-slot/2-pole high-speed permanent magnet motors with coil-pitch of two slot-pitches,” *IEEE Transactions on Industry Applications*. Revised.
- [4] F. Xu, **T. R. He**, Z. Q. Zhu, Y. Wang, S. Cai, H. Bin, D. Wu, L. M. Gong, and J. T. Chen, “Influence of slot number on electromagnetic performance of 2-pole high-speed permanent magnet motor with toroidal winding,” *IEEE Transactions on Industry Applications*.
- [5] F. Xu, Z. Q. Zhu, **T. R. He**, Y. Wang, H. Bin, D. Wu, L. M. Gong, and J. T. Chen, “Influence of stator gap on electromagnetic performance of 6-slot/2-pole modular high speed permanent magnet motor with toroidal windings,” *IEEE Access*, vol. 9, pp. 94470-94494, 2021, doi:10.1109/ACCESS.2021.3092053.

#### Conference Publications:

- [1] **T. R. He**, Z. Q. Zhu, *et al.*, “Comparison of 6-slot/2-pole high-speed permanent magnet motors with different winding configurations,” *2020 Fifteenth International Conference on Ecological Vehicles and Renewable Energies (EVER)*, Monte-Carlo, Monaco, 2020, pp. 1-8.
- [2] Fan Xu, **T. R. He**, Z. Q. Zhu, *et al.*, “Influence of slot number on electromagnetic performance of 2-pole high-speed permanent magnet motors with toroidal windings,” *2020 Fifteenth International Conference on Ecological Vehicles and Renewable Energies (EVER)*, Monte-Carlo, Monaco, 2020, pp. 1-7.